AFRL-VA-WP-TR-2005-3035

CONSISTENT STRUCTURAL INTEGRITY AND EFFICIENT CERTIFICATION WITH ANALYSIS

Volume 3: Appendices of Verification and Validation Examples, Correlation Factors, and Failure Criteria

Craig Collier

Collier Research Corporation 2 Eaton Street, Suite 504 Hampton, VA 23669



MAY 2005

Final Report for 27 June 2002 – 27 June 2004

THIS IS A SMALL BUSINESS INNOVATION RESEARCH (SBIR) PHASE II REPORT.

Approved for public release; distribution is unlimited.

STINFO FINAL REPORT

AIR VEHICLES DIRECTORATE AIR FORCE RESEARCH LABORATORY AIR FORCE MATERIEL COMMAND WRIGHT-PATTERSON AIR FORCE BASE, OH 45433-7542

NOTICE

Using Government drawings, specifications, or other data included in this document for any purpose other than Government procurement does not in any way obligate the U.S. Government. The fact that the Government formulated or supplied the drawings, specifications, or other data does not license the holder or any other person or corporation; or convey any rights or permission to manufacture, use, or sell any patented invention that may relate to them.

This report was cleared for public release by the Air Force Research Laboratory Wright Site (AFRL/WS) Public Affairs Office (PAO) and is releasable to the National Technical Information Service (NTIS). It will be available to the general public, including foreign nationals.

PAO Case Number: AFRL-WS 05-2761, 12 Dec 2005

THIS TECHNICAL REPORT IS APPROVED FOR PUBLICATION.

//S//

DUANE E. VELEY
Aerospace Engineer
Structural Design & Development Branch

//S//

MICHAEL L. ZEIGLER
Branch Chief
Structural Design & Development Branch

//S//

MICHAEL D. PILKENTON, LtCol, USAF Deputy Chief Structures Division

This report is published in the interest of scientific and technical information exchange and its publication does not constitute the Government's approval or disapproval of its ideas or findings.

REPORT DOCUMENTATION PAGE

Form Approved OMB No. 0704-0188

The public reporting burden for this collection of information is estimated to average 1 hour per response, including the time for reviewing instructions, searching existing data sources, searching existing data sources, gathering and maintaining the data needed, and completing and reviewing the collection of information. Send comments regarding this burden estimate or any other aspect of this collection of information, including suggestions for reducing this burden, to Department of Defense, Washington Headquarters Services, Directorate for Information Operations and Reports (0704-0188), 1215 Jefferson Davis Highway, Suite 1204, Arlington, VA 22202-4302. Respondents should be aware that notwithstanding any other provision of law, no person shall be subject to any penalty for failing to comply with a collection of information if it does not display a currently valid OMB control number. PLEASE DO NOT RETURN YOUR FORM TO THE ABOVE ADDRESS.

1.	REPORT DATE (DD-MM-YY)	2. REPORT TYPE	3. DATES	COVERED (From - To)
	May 2005	Final	06/27	7/2002 – 06/27/2004
4.	TITLE AND SUBTITLE CONSISTENT STRUCTURAL I			5a. CONTRACT NUMBER F33615-02-C-3216
	CERTIFICATION WITH ANALY	5b. GRANT NUMBER		
	Volume 3: Appendices of Verifica Factors, and Failure Criteria	on	5c. PROGRAM ELEMENT NUMBER 0605502	
6.	AUTHOR(S)			5d. PROJECT NUMBER
	Craig Collier			A01V
				5e. TASK NUMBER
				5f. WORK UNIT NUMBER
				0A
7.	PERFORMING ORGANIZATION NAME(S) A Collier Research Corporation 2 Eaton Street, Suite 504 Hampton, VA 23669	AND ADDRESS(ES)		8. PERFORMING ORGANIZATION REPORT NUMBER
9.	SPONSORING/MONITORING AGENCY NA	AME(S) AND ADDRESS(ES)		10. SPONSORING/MONITORING AGENCY ACRONYM(S)
	Air Vehicles Directorate			AFRL/VASD
	Air Force Research Laboratory Air Force Materiel Command Wright-Patterson AFB, OH 45433	3-7542		11. SPONSORING/MONITORING AGENCY REPORT NUMBER(S) AFRL-VA-WP-TR-2005-3035
	·	·		

12. DISTRIBUTION/AVAILABILITY STATEMENT

Approved for public release: distribution is unlimited.

13. SUPPLEMENTARY NOTES

This is a Small Business Innovation Research (SBIR) Phase II report. Report contains color.

This is Volume 3 of a three-volume work. See also Volume 1 (AFRL-VA-WP-TR-2005-3033) and Volume 2 (AFRL-VA-WP-TR-2005-3034).

14. ABSTRACT

Report developed under SBIR contract for topic AF01-239.

This SBIR report maintains that reliable pretest predictions and efficient certification are suffering from inconsistent structural integrity that is prevalent throughout a project's design maturity. Eight primary inconsistencies practiced in aerospace structural analysis are identified. This SBIR proposes solutions for these inconsistencies and documents software implementation and real world examples. Volume 3 provides a collection of verification and validation examples, mostly for composite laminate strength and bonded joints.

15. SUBJECT TERMS

SBIR Report, HyperSizer, certification, analysis, structures, aerospace, bonded joints, composite materials

16. SECURITY	CLASSIFICATI	ON OF:	17. LIMITATION	18. NUMBER	19a.	NAME OF RESPONSIBLE PERSON (Monitor)
a. REPORT Unclassified		c. THIS PAGE Unclassified	of abstract: SAR	OF PAGES 304		Duane E. Veley TELEPHONE NUMBER (Include Area Code) (937) 255-8286

Table of Contents

<u>Secti</u>	<u>ion</u>	<u>Page</u>
LIST	T OF FIGURES	viii
ACK	NOWLEDGMENTS	xiv
1	SUMMARY OF CORRELATION CATEGORIES, FACTORS (CF), PDFS, AND HISTOGRA	MS1
	1.1.1 Correlation Factors	2
	1.1.2 Correlation Equations.	
1.2		
	1.2.1 Panel Buckling, Curved	
	1.2.2 Panel Buckling, Flat; Beam Buckling	13
	1.2.3 Local Buckling	15
	1.2.4 Crippling	
	1.2.5 Isotropic Strength	
	1.2.6 Composite Strength	
	1.2.7 Sandwich Failure Modes	
	1.2.8 Bonded Joint Failures	
1 3	3 SUMMARY OF HISTOGRAMS BEFORE AND AFTER CORRELATIONS	
2	VALIDATION - SANDWICH WRINKLING PANEL FAILURE TEST DATA AND CFS	28
3	VALIDATION - COMPOSITE MATERIAL STRENGTH FAILURE ENVELOPES OF WOR	RLD
WID	DE FAILURE EXERCISES (WWFE) TEST DATA AND OTHER PUBLISHED DATA	29
3.1	1 Case 1: unidirectional E-glass/LY556 epoxy σ _y vs. τ _{xy} failure envelope	21
3.1	3.1.1 WWFE Test Data	
	3.1.2 Failure Envelopes: HyperSizer Generated and WWFE Published	
3.2		
3.2	3.2.1 WWFE Test Data $3.2.1$ which is the second of the s	
	3.2.2 Failure Envelopes: HyperSizer Generated and WWFE Published	
3.3	* **	
	3.3.1 WWFE Test Data	
	3.3.2 Failure Envelopes: HyperSizer Generated and WWFE Published	37
3.4		
	3.4.1 WWFE Test Data	
	3.4.2 WWFE Published Analytical Failure Envelopes	
3.5	,	
	3.5.1 WWFE Test Data	
2	3.5.2 WWFE Published Analytical Failure Envelopes	
3.6	L 15 / A 1	
	3.6.1 WWFE Test Data 3.6.2 WWFE Published Analytical Failure Envelopes	
3.7	*	
3.	CASE 7. $[0/-43/+43/90]_S$ AS4/3501-0, G_X VS G_Y FAILURE ENVELOPE	
	3.7.2 WWFE Published Analytical Failure Envelopes.	
	3.7.3 HyperSizer Progressive Failure	
3.8		
2.0	3.8.1 HyperSizer Generated Analytical Failure Envelopes	
3.9	**	
	3.9.1 HyperSizer Generated Analytical Failure Envelopes	
3.1		
3.1		
2 1	12 I AMERICAN PROPERTY AND LOAD PROCE	57

	3.13	References:	58
4 H		IDATION – COMPOSITE MATERIAL STRENGTH CORRELATION FACTORS AND	
	4.1	SUMMARY OF COMPOSITE HISTOGRAMS BEFORE AND AFTER CORRELATIONS	
5	VAL	IDATION - CYLINDRICAL PANEL BUCKLING FAILURE TEST DATA AND CFS	74
	5.1	VERIFICATION EXAMPLE: CYLINDRICAL BUCKLING OF A GRID-STIFFENED TANK WALL	74
6	VER	IFICATION - BONDED JOINT HOMOGENOUS ISOTROPIC AND ORTHOTROPIC D	ELALE
&		GAN PUBLICATION (SIX EXAMPLES)	
	6.1	INTRODUCTION AND SUMMARY	84
	6.2	PROBLEM DEFINITION	
	6.3	COMPARISON TO FINITE ELEMENT ANALYSIS AND PUBLISHED RESULTS	
		Condition 1 – Aluminum-BrEp Tensile Load	
		Condition 2 – Aluminum-BrEp Applied Moment	
		Condition 3 – Aluminum-Aluminum Tensile Load	
		Condition 4 – Aluminum-Aluminum Applied Moment	
		Condition 5 – Aluminum-BrEp In-Service Panel	
	6.4	EFFECT OF ELIMINATING TRANSVERSE SHEAR DEFORMATION IN THE FEA	
	6.5	REFERENCES	
7	VER	IFICATION - BONDED JOINT [0/±45/90] LAMINATE STRESSCHECK FEA	110
	7.1	INTRODUCTION AND SUMMARY	110
	7.2	PROBLEM DEFINITION	
	7.2.1	Physical Dimensions and Material Properties	112
		HyperSizer Setup	
	7.3	COMPARISON TO FINITE ELEMENT ANALYSIS	
		Desired FEA Results Comparisons	
		Simplifying Assumptions for FEA Comparisons Quality of FEA Comparison Plots	
		Peak Stresses Comparisons	
		Case 1: Applied Tensile Force ($Nx = 5.71 \text{ lb/in}$)	
		Case 2 – Applied Moment ($Mx = 0.2248$ lb.in/in)	
	7.4	SUPPLEMENTAL RESULTS.	
	7.4.1	HyperSizer Screenshots for Applied Tensile Load Case	130
	7.4.2	Stresscheck Results Presented in Powerpoint Format	138
8	VER	IFICATION – BONDED JOINT[0/±30/±60] LAMINATE MORTENSEN EXAMPLES	147
	8.1	BONDED DOUBLER JOINT EXAMPLE	
		Problem Definition	
		Comparison to Published Results	
	8.2	SINGLE LAP JOINT EXAMPLES Problem Definition	
		Comparison to Published Results	
		Linear Versus Non-Linear Adhesive Comparison	
	8.3	REFERENCES	
	8.4	SUPPLEMENTAL RESULTS.	
		Supplemental Results for the Bonded Doubler Example	
		Supplemental Results for the Single Lap Joint Example	
	8.4.3	Supplemental Single Lap Joint Results for Linear Versus Non-Linear Adhesive Comparison	167
9 PI		IDATION – BONDED DOUBLER JOINT, WOVEN FABRIC LAMINATE, TONG TION	174
- 1	9.1	SUMMARY OF RESULTS	
	9.1	PROBLEM DEFINITION	
	9.2	FYPERIMENTAL RESULTS	176

9.3.1 Visualization of Joint Failure	176
9.3.2 Test Data	
9.4 HS-BondJo Prediction	
9.4.1 Linear analysis	178
9.4.2 Nonlinear analysis	180
9.5 CONCLUSIONS	182
9.6 References	183
9.7 SUPPLEMENTAL RESULTS	
9.7.1 HS-BondJo Stress Analysis Results Using Linear Adhesive (P = 13 kN)	
9.7.2 HS-BondJo Calculation of MS in the Adherends using Linear Adhesive ($P = 13 \text{ kN}$)	
9.7.3 HS-BondJo Stress Analysis Results Using Nonlinear Adhesive ($P = 14 \text{ kN}$)	
9.7.4 HS-BondJo Calculation of MS in the Adherends using Nonlinear Adhesive ($P = 14 \text{ kN}$))192
10 VALIDATION – BONDED DOUBLER TEST [0/±45/90] LAMINATE WITH STEP TAPUBLICATION	
10.1 SUMMARY OF RESULTS	
10.2 PROBLEM DEFINITION	
10.3 EXPERIMENTAL RESULTS	
10.3.1 Visualization of Joint Failure	
10.3.2 Test Data	
10.4 HS-BondJo Prediction	
10.4.1 HS-BondJo model for analysis	
10.4.2 Linear analysis	
10.4.3 Nonlinear analysis	
10.5 DISCUSSION	
10.5.1 Comparison of HS-BondJo and NASA Prediction of Damage Onset	204
10.6 References	
SUPPLEMENTAL RESULTS	
10.6.1 Linear Stress Analysis Results at Predicted Failure Load $P_0 = 24.3 \text{ kN} \dots$	
10.6.2 HS-BondJo Calculation of MS in the adherends at Predicted Failure Load $P_0 = 24.3$	kN209
11 VALIDATION - SINGLE LAP JOINT, WOVEN FABRIC LAMINATE, TONG PUBL	LICATION211
11.1 Summary of Results	211
11.2 PROBLEM DEFINITION	
11.3 EXPERIMENTAL RESULTS	
11.3.1 Visualization of Joint Failure	
11.3.2 Test Data	
11.4 HS-BondJo Prediction	216
11.4.1 Linear Analysis	
11.4.2 Nonlinear Analysis	217
11.5 DISCUSSION	219
11.6 Conclusions	219
11.7 References	219
11.8 SUPPLEMENTAL RESULTS	
11.8.1 HS-BondJo Stress Analysis Results for Single-lap Joints under Tension $N_{xx} = 6.85 \text{ kN}$	
Adhesive	
11.8.2 HS-BondJo Stress Analysis Results for Single-lap Joints under Tension $N_{xx} = 6.82 \text{ kN}$	
Adhesive	222
12 FAILURE CRITERIA FOR BONDED JOINTS	225
12.1 BONDED JOINT FAILURE THEORY CLASSIFICATIONS	225
12.2 ADHEREND FAILURE METHODS	
12.2.1 Sectional Fracture	
12.2.2 Interlaminar Delamination	227
12.2.3 Matrix Cracking	
12.3 ADHESIVE FAILURE METHODS	
12.3.1 Cohesive Failures	
12.4 ADHESIVE – ADHEREND BONDLINE FAILURES	230

	12.5	JOINT FAILURE LOCATION CHECKS	
	12.6	SYMBOLS	232
	12.7	REFERENCES	232
13	FAI	LURE CRITERIA FOR SANDWICH PANELS	234
	13.1	Wrinkling	234
	13.1.	1 Approach Summary	234
	13.1.	2 Symbols	235
		tions	
		3 References	
		4 Interaction Equation for Wrinkling due to Biaxial Loads with Shear	
	13.2	DIMPLING	
		1 Summary approach	
		2 Symbols	
		3 Equations	
	13.2. 13.3	4 References	
		Shear Crimping	
		2 Symbols	
		3 Equations	
		4 References	
	13.3.	Core Crushing	
		1 Approach Summary	
		2 Symbols	
		3 References	
	13.5	SHEAR STRENGTH	
	13.5.	1 Summary approach	
		2 Symbols	
	13.5.	3 Shear Strength Correction Factor	251
	13.5.	4 Equations	252
	13.5.	5 References	252
14	FAI	LURE CRITERIA FOR LAMINATES	253
15	нол	V TO COMPUTE MARGIN-OF-SAFETY FOR COMPLEX LOADING AND FAILURE	
		CTIONS	254
	15.1	INTERACTIVE FORM OF FAILURE CRITERIA	254
	15.2	DEFINITION OF MARGIN OF SAFETY (MOS)	
	15.3	CALCULATION OF MARGIN OF SAFETY EXAMPLES	
	15.4	SUMMARY	262
	15.5	References	262
16	НОУ	V TO BACK OUT MARGIN-OF-SAFETY FROM %RELIABILITY, AND %RELIABILI	ГΥ
FR		S	
17	HYP	PERSIZER AND AUTOMATION THROUGH WEB SERVICES	263
	17.1	MEETING NOTES AND DESIGN DOCUMENT FOR HYPERSIZER WEB SERVICES	263
	17.2	BACKGROUND AND PURPOSE OF PROTOTYPE	263
	17.3	AFRL/VA BACKGROUND AND INTEREST	263
	17.4	AFRL/VA GRAND VISION	
	17.5	ADVANTAGES OF .NET FOR DISTRIBUTED ENGINEERING ANALYSIS	
	17.6	SERVICE ORIENTED OR PEER-TO-PEER (P2P) COMPUTING	
		SIZER SPECIFIC PROPOSED TASKS AND DATA FLOW	
		1 Scenario Level 1: Demonstrate a web service using simple functions that can be called from a c	
		2 Scenario Level 2: Demonstrate Peer-to-Peer, WSFL/Scripting file to control the process	
		3 Scenario Level 3: BJSFM legacy bolt program web service	
		4 Scenario Level 4: HyperSizer as web service5 Scenario Level 5: HyperSizer as web service calling BJSFM as a web service	
		5 Scenario Level 5: Hypersizer as web service calling BJSFM as a web service 6 Practice Level 6: Learn how to use the FEMAP COM/API	
	17.0.	O I TWO WOOD ELVEL OF ELWIN WOW WOOD WILL I EMMIN COM/IN I	

1/.0	6.7 Scenario Level 7: Develop the process we need for automated HyperSizer FEA iteration **	*
Dei	nonstrate FEMAP/NASTRAN web service	271
17.0	6.8 Scenario Level 8: Establish iterative HyperSizer-NASTRAN procedure using WSFL	271
17.7	OVERVIEW OF TECHNOLOGIES	271
17.	7.1 Web Services	271
17.	7.2 Web Services Description Language (WSDL)	273
17.	7.3 Web Services Flow Language (WSFL)	273
	7.4 Universal Description, Discovery, and Integration (UDDI)	
10 113		
18 HY	PERAUTOFEA/AUTONASTRAN	275
18 HY	PERAUTOFEA/AUTONASTRAN Introduction	
		275
18.1	Introduction	275
18.1 18.2	Introduction	275 275
18.1 18.2 18.3	INTRODUCTIONAUTONASTRAN INTERFACEEXAMPLE PROBLEM	275 275 276
18.1 18.2 18.3 18.4	INTRODUCTION AUTONASTRAN INTERFACE EXAMPLE PROBLEM PROCESS.	

List of Figures

FIGURE		PAGE
1.1	All HyperSizer current analysis PDFs normalized by the ratio of	3
	Experimental / Predicted	
1.2	All HyperSizer current analysis PDFs normalized by the ratio of	3
	Experimental/Theoretical (normalization to theoretical)	
1.3	HyperSizer current analysis PDFs with test data. (normalized to predicted)	4
1.4	HyperSizer current analysis PDFs with test data. (normalized to theoretical)	4
1.5	HyperSizer current analysis PDFs that DO NOT have test data, assumed	5
	values. (normalized to predicted)	
1.6	HyperSizer current analysis PDFs that DO NOT have test data, assumed	5
	values. (normalized to theoretical)	
1.7	HyperSizer Composite Strength analysis PDFs (normalized to predicted)	6
1.8	HyperSizer Composite Strength analysis PDFs (normalized to theoretical)	6
1.9	HyperSizer Composite Bonded Joint analysis PDFs (normalized to	7
	predicted)	_
1.10	HyperSizer Composite Bonded Joint analysis PDFs (normalized to	7
	theoretical)	
1.11	HyperSizer instability/buckling analysis PDFs (normalized to predicted)	8
1.12	HyperSizer instability/buckling analysis PDFs (normalized to theoretical)	8
1.2.1	A typical curved structural panel	10
1.2.2	Curved panel buckling knockdown factor from Ref. [1.2.1]	11
1.2.3	Knockdown factor, γ_{μ} , for HyperSizer "predicted" buckling allowable as a	12
	function of width to thickness ratio for various radius to thickness ratios	
1.2.4	Knockdown factor, γ_{μ} , for HyperSizer "predicted" buckling allowable as a	14
	function of length to thickness ratio	
1.3.1	Panel Buckling, Curved, Simple, Fixed, or Free BC, Biaxial stiffness panel	22
	correlation category. Top image before correlation. Bottom image after	
	correlation factors applied	
1.3.2	Sandwich Wrinkling, Isotropic or Honeycomb Core (Top image before	23
	correlation. Bottom image after correlation factors applied)	
1.3.3	Sandwich Wrinkling, Wrinkling, Honeycomb Core. Top image before	24
	correlation, Bottom image after correlation factors applied	
1.3.4	Joint, Bonded, Adherend Fracture. Top image before correlation. Bottom	25
	image after correlation factors applied	
1.3.5	Joint, Bonded, Adherend Delamination. Top image before correlation.	26
	Bottom image after correlation factors applied.	
3.0	A representative failure envelope generated by HyperSizer plotted with	29
	WWFE test data	
3.1.1	The black solid squares are the unidirectional (UD) allowable stresses	31
	provided to the invited contributors. The open circles are the test data	
	values. Note the discrepancy between the provided compressive transverse	
2.1.2	strength (σ_2) and the test avg, $\sim 20\%$	22
3.1.2	Biaxial σ_y - τ_{xy} failure envelopes of 0° E-glass/LY556 lamina	32
3.1.3	Biaxial σ_y - τ_{xy} failure envelopes of 0° E-glass/LY556 lamina	33
3.1.4	Comparison of LaRC03 to Sun, Hashin 73,80, and maximum stress criteria	34

FIGURE		PAGE
3.2.1	Unidirectional (UD) allowable stresses provided to the invited contributors	35
3.2.2	Biaxial σ_{x} - τ_{xy} failure envelopes of 0° T300/BSL914C lamina. Same test	36
	data shown as filled circles in both graphics. These failure envelopes use	
	the unidirectional data as originally provided to contributors	
3.3.1	The black solid squares are the unidirectional (UD) allowable stresses	37
	provided to the invited contributors. The open circles are test data values	
3.2.2	Biaxial σ_x - σ_y failure envelopes of 0° E-glass/MY750 epoxy lamina	38
3.4.1	Progressive Failure Case 4	40
3.4.2	Image taken directly from WWFE reference 3.1, (MPa)	41
3.5.1	Progressive Failure Case 5	42
3.5.2	Image taken directly from WWFE reference 3.1, (MPa)	43
3.6.1	Progressive Failure Case 6	44
3.6.2	Image taken directly from WWFE reference 3.1, (MPa)	45
3.7.1	Progressive Failure Case 7	46
3.7.2	Image taken directly from WWFE reference 3.1, (MPa)	47
3.7.3	Progressive failure modeled on the fiber/matrix constituent (micro) level	48
3.8.2	Biaxial σ_y - τ_{xy} failure envelopes of 0° AS4/55A lamina	50
3.9.1	Biaxial σ_y - τ_{xy} failure envelopes of 0 ° T800/3900-2 lamina	52
4.1	Composite Strength, Max Strain 1 Direction	60
4.2	Composite Strength, Max Strain 2 Direction	61
4.3	Composite Strength, Max Strain 12 Direction	62
4.4	Composite Strength, Max Stress 1 Direction	63
4.5	Composite Strength, Max Stress 2 Direction	64
4.6	Composite Strength, Max Stress 12 Direction	65
4.7	Composite Strength, Tsai-Hill	66
4.8	Composite Strength, Tsai-Wu	67
4.9	Composite Strength, Tsai-Hahn	68
4.10	Composite Strength, Hoffman	69
4.11	Composite Strength, Hashin Matrix Cracking	70
4.12	Composite Strength, Hashin Fiber Failure	71
4.13	Composite Strength, LaRC03 Matrix Cracking	72
4.14	Composite Strength, LaRC03 Fiber Failure	73
5.1	Problem statement for curved panel buckling comparison between	74
	HyperSizer with Raleigh Ritz and MSC/NASTRAN FEA	
5.2	The unit weight for the isogrid shown in the left figure is 2.044 (lb/ft2)	75
5.3	Eigenvalue comparison between HyperSizer with Raleigh-Ritz and MSC/	75
	NASTRAN FEA	
5.4	Buckling results can change depending on stiffeners	76
6.2.1	Solution domain of stiffened plate (bonded doubler)	85
6.3.1	Ansys 3D solid finite element model developed for verification of BondJo	87
6.3.2	Adhesive stress comparisons between BondJo, Ansys solid model FEA and	88
	Delale and Erdogan plate theory	
6.3.3	Displacements and force comparisons for condition 1	89
6.3.4	Out-of-plane stress comparisons for condition 1	90
6.3.5	In-plane stress comparisons for condition 1	91
6.3.6	Adhesive stress comparisons between BondJo, Ansys solid model FEA and	92
	Delale and Erdogan plate theory	

FIGURE		PAGE
6.3.7	Displacements and force comparisons for condition 2	93
6.3.8	Out-of-plane stress comparisons for condition 2	94
6.3.9	In-Plane stress comparisons for condition 2	95
6.3.10	Adhesive stress comparisons between BondJo, Ansys solid model FEA and Delale and Erdogan plate theory	96
6.3.11	Displacements and force comparisons for condition 3	97
6.3.12	Out-of-plane stress comparisons for condition 3	98
6.3.13	In-plane stress comparisons for condition 3	99
6.3.14	Adhesive stress comparisons between BondJo, Ansys solid model FEA and Delale and Erdogan plate theory	100
6.3.15	Displacements and force comparisons for condition 4	101
6.3.16	Out-of-plane stress comparisons for condition 4	102
6.3.17	In-plane stress comparisons for condition 4	103
6.3.18	Adhesive stress comparisons between BondJo and Ansys solid model FEA show good agreement between the codes for adhesive shear but some differences in peel stress in the stress reversal "trough" region.	104
6.3.19	Adhesive stress comparisons between BondJo and Ansys solid model FEA show good agreement between the codes for adhesive shear but some differences in peel stress in the stress reversal "trough" region	105
6.4.1	Alum-BrEp applied force (condition 1) comparisons between BondJo and Ansys solid model FEA where transverse shear deformation has been disallowed in the FEA	106
6.4.2	Alum-BrEp applied moment (condition 2) comparisons between BondJo and Ansys solid model FEA where transverse shear deformation has been disallowed in the FEA	107
6.4.3	Alum-Alum applied moment (condition 4) comparisons between BondJo and Ansys solid model FEA where transverse shear deformation has been disallowed in the FEA6	108
7.2	Sample comparison between HyperSizer-BondJo and Stresscheck for adhesive interlaminar shear and peel stresses along the bondline	110
7.2.1	Configuration of bonded doubler joint for analysis	112
7.2.2	Coordinate systems and reference planes for the HyperSizer panel and typical academic sign conventions	113
7.2.3	Boron-Epoxy material entered through the HyperSizer Interface	114
7.3.1	Stress calculations performed by HyperSizer-BondJo through the depth of the joint	115
7.3.2	Sample comparison results between HyperSizer-BondJo and Stresscheck illustrating that the jagged FEA lines	117
7.3.3	Stresscheck results as received in PowerPoint chart results	117
7.3.4	Stresscheck verification example, a small area around the reentrant corner was defined inside of which the FEA results are ignored	118
7.3.5	As the number of points chosen from the FEA increases from 75 to 500 points, the shape of curve remains same, however the peak stress increases	119
7.3.6	Comparisons of adherend displacement between HyperSizer-BondJo and Stresscheck show very close agreement	120
7.3.7	Interlaminar shear and peel stresses in the adhesive layer	121
7.3.8	Plots of interlaminar shear and peel stresses through-the-thickness of the adherend laminates	122

FIGURE		PAGE
7.3.9	Comparisons of ply in-plane stresses between HyperSizer-BondJo and Stresscheck show an almost identical match all along the joint	123
7.3.10	The out-plane stress distribution along x-axis has generally good match	124
7.3.11	Comparisons of adherend displacement between HyperSizer-BondJo and Stresscheck show very close agreement on both the vertical displacement and displacement in the x direction	125
7.3.12	Interlaminar shear and peel stresses in the adhesive layer (top) and through the thickness of the laminated adherends and adhesive at x=0.89"	126
7.3.13	Plots of interlaminar shear and peel stresses through-the-thickness of the adherend laminates and the adhesive at x=0.9575	127
7.3.14	Comparisons of ply in-plane stresses between HyperSizer-BondJo and Stresscheck show an almost identical match all along the joint	128
7.3.15	The out-plane stress distribution along x-axis in this location has generally good match with BondJo	129
8.1.1	Comparison of adhesive stresses between BondJo and Mortensen for the bonded doubler joint example. The results between the two codes are virtually identical, which is not surprising because BondJo's theory was adapted and expanded from from theory originally developed by Mortensen	147
8.1.3	Result comparisons between BondJo and Mortensen[8.1] for the bonded doubler joint example	149
8.2.1	Comparison of adhesive stresses between BondJo and Mortensen for the single lap joint example.	150
8.2.2	Result comparisons between BondJo and Mortensen[8.1] for the single lap joint example	152
8.2.3	Comparison of BondJo to original Mortensen results from [8.1] shows a very large discrepancy in the plot of horizontal displacement, v0	153
8.2.4	Comparison of BondJo to corrected results sent by the author [8.1] show very close agreement between BondJo and Mortensen's results	153
8.2.5	Non-linear stress-strain curve of epoxy AY103 adhesive with equivalent representation of that curve using several non-linear models implemented in BondJo	154
8.2.6	BondJo results compared with those of [8.1] for stresses in non-linear adhesives show some differences	154
8.2.7	Sample result comparison between linear and non-linear adhesive solutions for the Mortensen thesis single lap joint example	155
8.4.1	Supplemental BondJo results for the bonded doubler joint example problem from [8.1]	158
8.4.2	Supplemental BondJo results for the single lap joint with linear adhesive example problem verified against [8.1]	163
8.4.3	Supplemental BondJo results for the stepped lap joint with linear adhesive example	165
8.4.4	Supplemental BondJo results for the single lap joint example from [8.1	165
8.4.5	Supplemental BondJo results for the single lap joint example linear to non- linear adhesive comparison	167
8.4.6	Adhesive stresses in the single-lap joint under tension of $Nxx = 200 \text{ N/mm}$ using the Ramberg-Osgood model	171
8.4.7	Adhesive stresses in the single-lap joint under tension of $Nxx = 200 \text{ N/mm}$	171

FIGURE		PAGE
	using the exponential law model	
9.1.1	Experiment and HS-BondJo models for bonded doubler specimens studied by Cheuk and Tong [9.2]	174
9.2.1	Schematics of bonded doubler test specimens examined by Cheuk and Tong.	175
9.2.2	The nonlinear stress-strain experimental data for FM 300-K adhesive	176
9.3.1	Sectional failure of bonded doubler joint specimen	177
9.4.1	In-plane stresses in the surface ply of adherend 1; through-the-thickness	178
<i>y</i> . 1.1	distribution of out-of-plane stresses	170
9.4.2	Adhesive stresses due to yielding of adhesives under the predicted failure load of 14 kN	180
10.1	Experiment results and HS-BondJo models for bonded doubler specimen studied by Krueger et al [10.2]	194
10.2.1	Schematics of a skin/flange specimen (bonded doubler) studied by Krueger	196
10.3.1	Experimental observation of failure modes for boned doubler joint	196
10.3.2	Experiment results of load-displacement curves for bonded doubler specimens	197
10.3.3	Fatigue test data for the bonded doubler specimens	198
10.4.1	Modeling tapered skin/flange specimen by HS-BondJo	199
10.4.2	Through-the-thickness distribution of the margin of safety of skin at the bondline corner,	201
10.4.4	Experimental stress-strain data for FM 300k adhesive along with Ramberg-Osgood approximation	202
10.4.5	Linear (dashed line) and nonlinear adhesive stresses in skin/flange specimen	203
10.4.6	Margin of safety of skin obtained with nonlinear adhesive property under longitudinal tension	203
10.5.1	NASA predicted load for matrix cracking onset and experimental results.	204
11.1	Single lap joint schematic and load-displacement results for single lap joints studied by Tong	211
11.2.1	Schematic of single lap joints studied by Ton	212
11.3.1	Typical curves of applied load vs. crosshead displacement.	213
11.4.1	In-plane stresses in the surface ply of adherend 1 under tension $P = 6.85 \text{ kN}$	216
11.4.2	Through-the-thickness plot of MS at the free edge	217
11.4.3	The nonlinear stress-strain experimental data for FM 300-K adhesive	217
11.4.4	Adhesive stresses obtained from nonlinear adhesive model	218
11.4.5	Through-the-thickness plot of MS at the lead edge	218
12.1	Failure modes in adhesively bonded joints identified by Heslehurst and Hart-Smith 12.1]	226
12.2	The full stress state within the bonded joint is calculated by HyperSizer at a user-defined number of y and z locations	231
13.7.1	Compressive stress on sandwich panel from support bearing load P.	249
13.7.2	Sandwich Rampdown closeout design	249
15.2.1	Definition of MOS for a failure criterion with two interactive terms	255

List of Tables

TABLE		PAGE
1.1	Correlation Factors	2
1.2	Correlation Equations	9
1.3	Al 2024 Ultimate Tensile Strength at varying levels of reliability based on	17
	several test sample sizes	
1.4	Summary of HyperSizer CFs for Composite Failure Theorie	18
3.0	HyperSizer Failure Envelope Summary	30
3.11.1	Thermal-mechanical properties of four unidirectional laminae in WWFE	56
3.11.2	Mechanical properties of non-WWFE UD laminae	57
3.11.3	Summary of laminate types, thickness, material types and loading	57
	conditions	
6.2.1	Six material-load case verifications	85
6.2.2	Geometry and Boundary Conditions for Aluminum-Boron Epoxy Problems	85
	(1, 2, 5)	
6.2.3	Geometry and Boundary Conditions for Aluminum-Aluminum Problems	86
	(3,4,6)	
6.2.4	Material Properties	86
7.2.1	Geometry, materials and B.C of stiffened plate example 1	112
7.2.2	Material Properties of Bonded Doublers in the Analysis	112
8.1	Geometry and Boundary Conditions for	148
	Mortensen's Thesis Bonded Doubler Example	
8.2	Material Properties	148
8.3	Geometry and Boundary Conditions for	151
	Mortensen's Thesis Stepped Lap Joint Example	
8.4	Material Properties	151
9.1	Summary of predicted failure load vs. experimental result	174
9.2.1	Mechanical properties of a ply of T300/934 carbon/epoxy	176
	plain woven prepreg	
9.2.2	Mechanical properties of FM300-K adhesive	176
9.3.2	Ultimate failure load of bonded doubler joint specimens	177
10.1	Summary of predicted failure load vs. experimental result	194
10.2	Linear elastic constants of materials for skin/flange specimens	195
10.3	Initial damage load of skin/flange specimens	197
10.4	Mechanical properties of Grade 5 Fm300 adhesive	201
10.5	Comparison of HS-BondJo and NASA modeling approaches	205
11.1	Summary of predicted failure loads vs. experimental result	211
11.2	Mechanical properties of a ply of T300/934 carbon/epoxy	212
	plain woven prepreg	
11.3	Mechanical properties of FM300-K adhesive	212
11.4	Test data for failure loads and modes	215
15	Summary of margin of safety of selected interactive equations	254

Acknowledgments

This material is based upon work supported by the United States Air Force under Contract

- 1. AFRL VA SBIR Phase I contract # F33615-01-M-3125
- 2. AFRL VA SBIR Phase II contract #F33615-02-C-3216
- 3. LM Aero LRSA Contract/PO # 7067581

Preface

This appendix is a collection of verification and validation examples mostly for composite laminate strength and bonded joints.

This master table is referred to often. Refer to "Reliability Probabilistic Methods Statistical K factor converted to percent reliability. CME" for more detailed information.

Master Table
K value for a given % reliability
Based on one side of a normal distribution PDF curve

Reliability	K value - for one sided PDF
50.0	0
84.13	1
90.0	1.28
97.725	2
99.0	2.33
99.5	2.58
99.75	2.81
99.865	3

1 Summary of Correlation Categories, Factors (CF), PDFs, and Histograms

Table 1.1 lists all available HyperSizer analyses that have established Correlation Factors (CF). These factors are contained in software version 4.5 and can be customized by going to the Tools menu/Test Data Correlation drop down selection. These CFs are used with the equations defined in secion 1.1.3.

The chapter begins with a summary of all of the CFs per analysis method. Section 1.1.2 portrays these CFs graphically as PDF curves for each HyperSizer analyses. Several sets of PDFs are shown for a different grouping of analyses. In each set, the top figure shows the PDFs normalized by (experimental/predicted), and the bottom PDF figure normalized by (experimental/theoretical).

1.1.1 Correlation Factors

Table 1.1, Correlation Factors (Eqn# refers to Table 1.2)

Correlation Description	Eqn#	η	μ_1	μ_2	μ3	μ4	$3\sigma^*$
Panel Buckling, Curved, Simple, Fixed or Free, Biaxial	1.1.1	0.136	0.3956	-0.1144	0.8751		0.36
Panel Buckling, Curved, Simple, Fixed or Free, Uniaxial	1.1.1	0.136	0.3956		0.8751		0.36
Panel Buckling, Flat, Simple BC, Biaxial	1.1.2	0.06	0.4411	-0.2615		0.6	0.75
Panel Buckling, Flat, Simple BC, Uniaxial	1.1.2	0.06	0.4411			0.6	0.75
Beam Buckling	1.1.2	0.04	0.4711			0.6	0.84
Local Buckling	1.1.2	0.03	1				0.91
Crippling	1.1.4	0.1	1	-0.2615			0.7
Deformation Limit	1.1.4	0	1	0			1.0
Stiffness Requirement	1.1.4	0	1	0			1.0
Frequency Limit	1.1.4	0	1	0			1.0
Sandwich Wrinkling, Isotropic or Honeycomb Core	1.1.3	0.08	0.88	0	1.0E6		0.64
Sandwich Wrinkling, Wrinkling, Honeycomb Core	1.1.3	0.102	0.59	0	1.0E6		0.29
Sandwich Intracell Dimpling	1.1.3	0	1	0	1.0E6		1.0
Sandwich Core Shear Crimping	1.1.3	0	1	0	1.0E6		1.0
Micromechanics, Max Stress	1.1.4	0	1	0			1.0
Micromechanics, Max Strain	1.1.4	0	1	0			1.0
Micromechanics, Tsai Hill	1.1.4	0	1	0			1.0
Micromechanics, Strain Invariant Failure Theory	1.1.4	0	1	0			1.0
Composite Strength, Max Strain 1 Direction	1.1.4	0.092	0.9184	0			0.66
Composite Strength, Max Strain 2 Direction	1.1.4	0.167	0.9772	0			0.49
Composite Strength, Max Strain 12 Direction	1.1.4	0.210	1.104	0			0.41
Composite Strength, Max Stress 1 Direction	1.1.4	0.1067	0.8922	0			0.57
Composite Strength, Max Stress 2 Direction	1.1.4	0.1427	0.9305	0			0.53
Composite Strength, Max Stress 12 Direction	1.1.4	0.218	1.034	0			0.36
Composite Strength, Tsai-Hill	1.1.4	0.165	1.051	0			0.53
Composite Strength, Tsai-Wu	1.1.4	0.125	1.012	0			0.63
Composite Strength, Tsai-Hahn	1.1.4	0.099	1.013	0			0.71
Composite Strength, Hoffman	1.1.4	0.121	1.012	0			0.64
Composite Strength, Hashin Matrix Cracking	1.1.4	0.191	1.034	0			0.44
Composite Strength, Hashin Fiber Failure	1.1.4	0.143	0.9328	0			0.53
Composite Strength, LaRC03 Matrix Cracking	1.1.4	0.157	1.001	0			0.53
Composite Strength, LaRC03 Fiber Failure	1.1.4	0.1107	0.9388	0			0.61
Joint, Bonded, Adherend Fracture	1.1.4	0.1318	1.28	0			1.0
Joint, Bonded, Adherend Delamination	1.1.4	0.0819	1.32	0			1.0
Joint, Bonded, Adhesive	1.1.4	0	1	0			1.0

^{*} 3σ is a useful value for comparing the relative effective knockdown required

Correlation PDFs

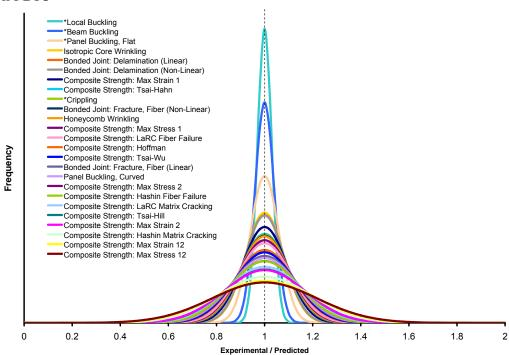


Fig. 1.1, <u>All HyperSizer current analysis PDFs</u> normalized by the ratio of Experimental/Predicted (normalization to predicted). Only when using different % reliabilities will the relative shape (flatter vs narrower) of the PDF curve will effect a change in results. Analyses with an asterick (*) do not have test data.

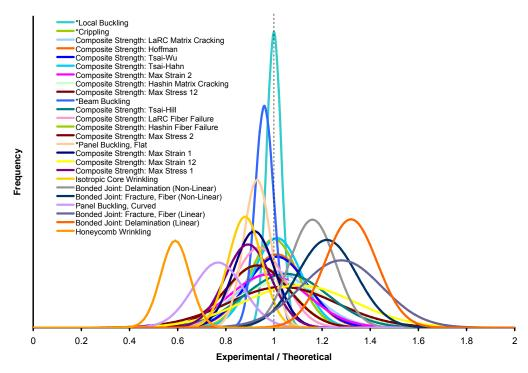


Fig. 1.2, <u>All HyperSizer current analysis PDFs</u> normalized by the ratio of Experimental/Theoretical (normalization to theoretical). The position of a PDF on the horizontal scale indicates its accuracy. Curves to the right of 1.0 underpredict failure, and curves to the lef over predict failure. Analyses with an asterick (*) do not have test data.

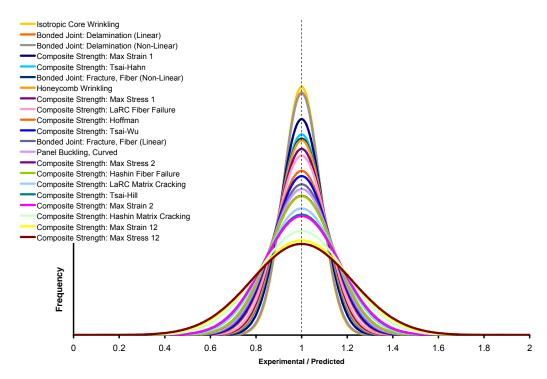


Fig. 1.3, HyperSizer current analysis PDFs that have test data. (normalized to predicted)

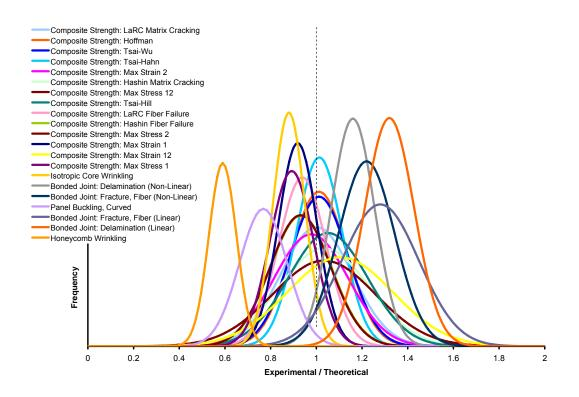


Fig. 1.4, <u>HyperSizer current analysis PDFs that have test data.</u> (normalized to theoretical)

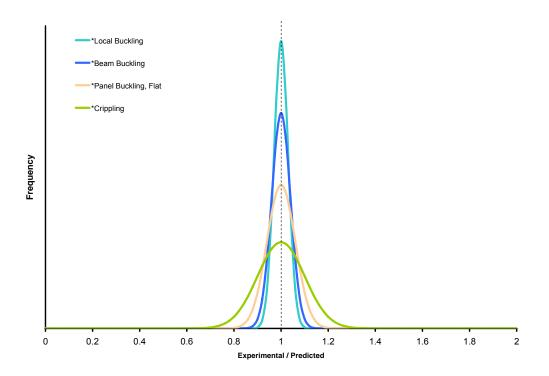


Fig. 1.5, <u>HyperSizer current analysis PDFs that DO NOT have test data, assumed values.</u> (normalized to predicted)

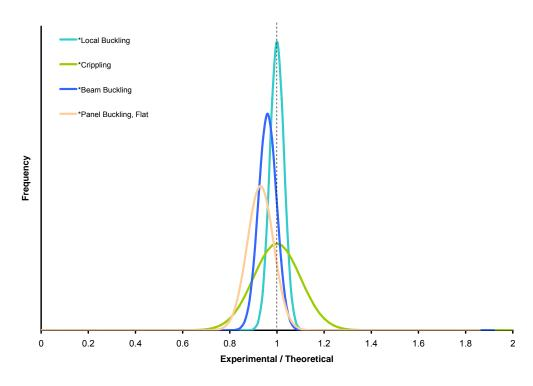


Fig. 1.6, <u>HyperSizer current analysis PDFs that DO NOT have test data, assumed values.</u> (normalized to theoretical)

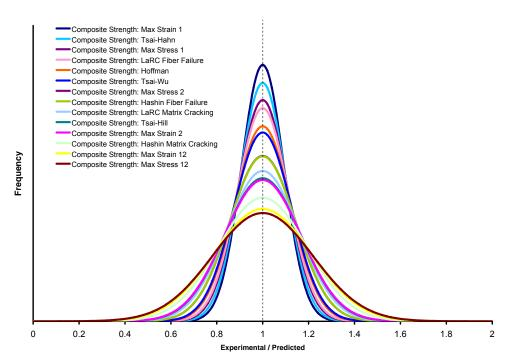


Fig. 1.7, <u>HyperSizer Composite Strength analysis PDFs</u> (normalized to predicted). Based on 130 tests of ultimate failure for unidirectional and $\pm \theta$ laminates with graphite and fiberglass material systems. Only the relative shape (flatter vs narrower) of the PDF curve will effect a change in results when using different % reliabilities.

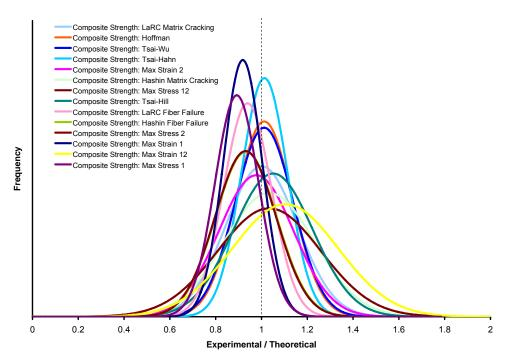


Fig. 1.8, <u>HyperSizer Composite Strength analysis PDFs</u> (normalized to theoretical) showing the relative inaccuracies of the failure criteria and their relative scatter from experimental measurements. Tsai-Hahn has the best accuracy. Though both Tsai-Hahn and LaRC03 matrix cracking failures have the same average accuracy, Tsai-Hahn can be more confidently used due to its narrower PDF and therefore will have less knockdown for a given reliability.

Probability Density Functions

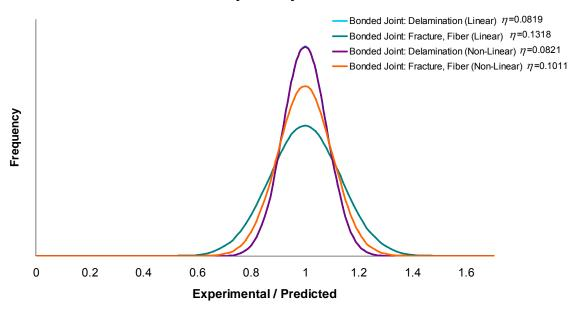


Fig. 1.9, <u>HyperSizer Composite Bonded Joint analysis PDFs</u> (normalized to predicted). Delamination linear and non-linear have the same PDF shape and only one can be seen at a time.

Probability Density Functions

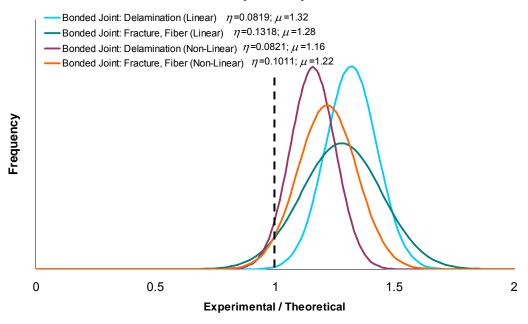


Fig. 1.10, <u>HyperSizer Composite Bonded Joint analysis PDFs</u> (normalized to theoretical). Non-linear analyses are shown to be more accurate than linear as they are closer to the 1.0 vertical dash.

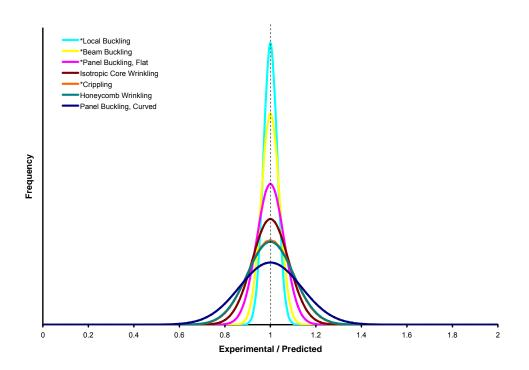


Fig. 1.11, <u>HyperSizer instability/buckling analysis PDFs</u> (normalized to predicted).

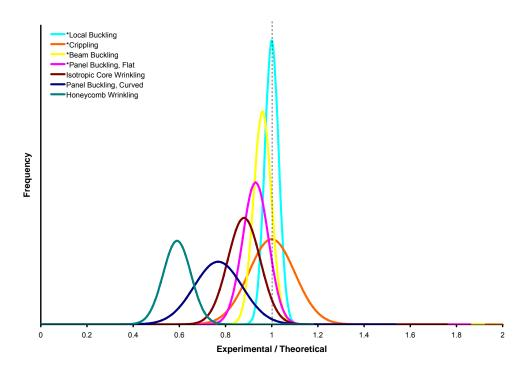


Fig. 1.12, <u>HyperSizer instability/buckling analysis PDFs</u> (normalized to theoretical).

1.1.2 Correlation Equations

This section summarizes analysis specific correlation equations that are used with the CFs defined in Table 1.1. More detailed derivation of these equations is provided in the next section.

Table 1.2, Correlation Equations

	Table 1.2, Correlation Equations					
Eqn#	Equation Description	Equation				
1.1.1	Curved Panel Buckling	$\gamma_{\mu} = \frac{\mu_{1} + \mu_{2} \frac{ D_{13} + D_{23} }{D_{11} + D_{22}} + \mu_{3} \gamma_{nasa}}{\sqrt[8]{\frac{4b}{3r}}}$ $\gamma_{nasa} = 1 - 0.901 (1 - e^{-\phi}) \qquad \phi = \frac{1}{16} \sqrt{\frac{r}{t_{eff}}}$				
1.1.2	Flat Panel/Beam Buckling	$\gamma_{\mu} = \mu_{1} + \mu_{2} \frac{ D_{13} + D_{23} }{D_{11} + D_{22}} + \mu_{4} \gamma_{l/t}$ $\gamma_{l/t} = 15168 (1 - e^{-\phi}) \qquad \phi = \frac{1}{18.744} \sqrt{\frac{l}{t_{eff}}}$				
1.1.3	Honeycomb Facesheet Wrinkling and Dimpling	$\gamma_{\mu} = \mu_1 + \mu_2 \frac{ D_{13} + D_{23} }{D_{11} + D_{22}} + \frac{1}{1 + \mu_3 R}$ $R = \frac{(0.25 - t_f)E_c}{t_c F_c}$				
1.1.4	All Other Failure Modes	$\gamma_{\mu} = \mu_1 + \mu_2 \frac{\left D_{13}\right + \left D_{23}\right }{D_{11} + D_{22}}$				

1.2 Correlation Equation Descriptions

1.2.1 Panel Buckling, Curved

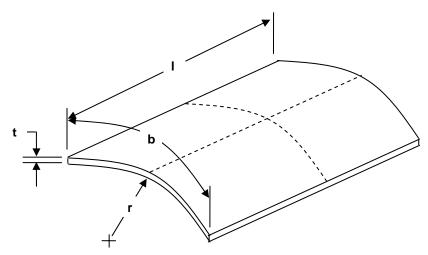


Fig. 1.2.1, A typical curved structural panel. The parameters that control knockdown for curved panels are the length, l, the width, b, the radius, r, and the thickness, t.

The correlation equation used for curved panel buckling is dependent on the relative strength of the off-diagonal D terms, the radius to thickness ratio (r/t), and the effective width to radius ratio (b/r). The equation for computing the correlation factors is Equation 1.1.1, repeated here from Section 1.1,

$$\gamma_{\mu} = \frac{\mu_{1} + \mu_{2} \frac{\left|D_{13}\right| + \left|D_{12}\right|}{D_{11} + D_{22}} + \mu_{3} \gamma_{nasa}}{\sqrt[8]{\frac{4b}{3r}}}$$

$$\gamma_{nasa} = 1 - 0.901 \left(1 - e^{-\phi}\right), \quad \phi = \frac{1}{16} \sqrt{\frac{r}{t_{eff}}}$$

For isotropic plates, t_{eff} is the actual plate thickness. For orthotropic plates or stiffened panels, the effective thickness, t_{eff} , is determined from the following relation:

$$t_{eff} = \sqrt[4]{144 \frac{D_{11}D_{22}}{A_{11}A_{22}}} \tag{1.2.1.1}$$

The purpose of the denominator, $\sqrt[8]{\frac{4b}{3r}}$, in Equation 1.1.1 is to reduce the amount of knockdown for very short curved panels. However, if the panel width becomes very large, this

denominator can cause the knockdown to become unrealistically large. For this reason, the denominator is never allowed to be greater than 1.0 or less than 0.7.

 γ_{nasa} is the cylindrical panel knockdown factor from NASA SP-8007 [1.2.1] and relates the knockdown factor to the panel r/t ratio as shown in the Fig. 1.2.2.

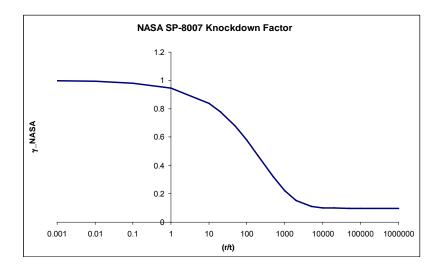


Fig. 1.2.2, Curved panel buckling knockdown factor from Ref. [1.2.1] plotted as a function of the panel r/t ratio.

The correlations for curved panel buckling are further broken down between panels that are: a) biaxial in nature, such as laminates, sandwich structures, bi-grid or isogrid stiffened; and b) those that are uniaxial in nature, such as hat stiffened or I, T, or Z stiffened. For the latter category, the dependence on the off-diagonal D terms is removed by setting $\mu_2 = 0$.

For an isotropic panel (i.e. D_{12} and $D_{13}=0$), the overall knockdown factor as a function of r/t ratio and b/t ratio takes on the shape shown in Fig. 1.2.3. This plot was generated assuming μ_1 =0.3956 and μ_3 =0.8751 as shown in Table 1.1 for curved panel buckling. Note that because the denominator of Equation 1.1.1 is restricted to 0.7 to 1.0, as the b/t ratio is increased, the denominator will reach the 1.0 threshold, meaning that further increases in b/t will not change the overall knockdown factor. This is in the curves in Fig. 1.2.3 as they become horizontal. The knockdown for flat panel buckling is shown for comparison.

The curved panel buckling γ_{μ} knockdown factor is never allowed to be greater than 1.0.

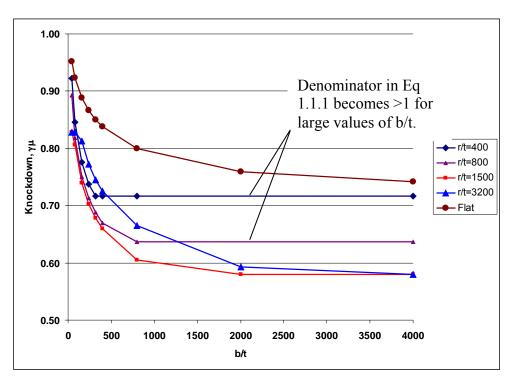


Fig. 1.2.3, Knockdown factor, $\gamma_{\mu\nu}$ for HyperSizer "predicted" buckling allowable as a function of width to thickness ratio for various radius to thickness ratios. Note that these curves are restricted by the denominator in Equation 1.1.1 not being allowed outside the range 0.7 to 1.0. As b/t increases for each curve, the denominator reaches this threshold, and the curve becomes constant as a function of b/t.

1.2.2 Panel Buckling, Flat; Beam Buckling

The correlation equation used for flat panel or beam buckling is dependent on the relative strength of the off-diagonal D terms and the effective length to thickness ratio (l/t). The equation for the flat panel knockdown correlation factor is Equation 1.1.2, repeated here,

$$\begin{split} \gamma_{\mu} &= \mu_1 + \mu_2 \frac{\left|D_{13}\right| + \left|D_{12}\right|}{D_{11} + D_{22}} + \mu_4 \gamma_{l/t} \\ \gamma_{l/t} &= 1 - .5168 \Big(1 - e^{-\phi}\Big) \qquad \phi = \frac{1}{18.744} \sqrt{\frac{l}{t_{eff}}} \end{split}$$

For flat panels, l is the average of the panel width and length, and for beams, l is the total beam length. For isotropic plates, t_{eff} is the actual plate thickness. For beams, t_{eff} is the overall beam height. For orthotropic plates or stiffened panels, the effective thickness, t_{eff} , is determined from the following relation:

$$t_{eff} = \sqrt[4]{144 \frac{D_{11}D_{22}}{A_{11}A_{22}}} \tag{1.2.2.2}$$

The correlations for flat panel buckling are further broken down between panels that are: a) biaxial in nature, such as laminates, sandwich structures, bi-grid or isogrid stiffened; and b) those that are uniaxial in nature, such as hat stiffened or I, T, or Z stiffened. For the latter category, the dependence on the off-diagonal D ratio is removed by setting $\mu_2 = 0$.

For an isotropic panel (i.e. D_{12} and $D_{13} = 0$), the knockdown as a function of l/t ratio takes on the form shown in Fig. 1.2.4. This plot was generated assuming μ_1 =0.4411 and μ_4 =0.6 as shown in Table 1.1 for flat panel buckling.

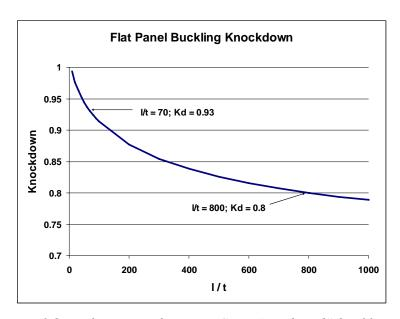


Fig. 1.2.4, Knockdown factor, γ_{μ} for HyperSizer "predicted" buckling allowable as a function of length to thickness ratio. This curve and the values correlation factors that generated it were "tuned" such that the overall knockdown is 0.8 at l/t=800.

1.2.3 Local Buckling

The knockdown correlation for local buckling uses the same form as that for flat panel buckling presented in Section 1.2.2. Instead of using overall stiffened panel properties for D_{11} , D_{22} , and effective thickness, these properties are taken from individual panel objects such as the span between stiffeners, the web, or the free span where local buckling calculations are performed.

1.2.4 Crippling

The equations for crippling are empirical in nature and therefore already based on test data. For this reason, the base predicted knockdown factor for isotropic panels is set to 1.0, and the overall knockdown is mainly a function of the test scatter knockdown factor, η which is set to 0.1. In addition, the assumption is that the knockdown for crippling will also be dependent on large off-axis D13 and D23 terms. The equation, repeated here, is Equation 1.1.4,

$$\gamma_{\mu} = \mu_1 + \mu_2 \frac{\left|D_{13}\right| + \left|D_{12}\right|}{D_{11} + D_{22}}$$

1.2.5 Isotropic Strength

The statistical knockdown for isotropic strength calculations is based on statistical data (i.e. material BASIS) provided by material references such as MIL-HDBK-5J [1.2.2]. For example, in MIL-HDBK-5J, material strength properties are generally provided as either A-basis, B-basis, S-basis or all three. The S-basis value is a "minimum property value specified by a governing industry specification", however the statistical assurance of this value is not known. Therefore, the S-basis has limited value in the statistical knockdown calculation presented here.

The A- and B- basis for a property, however are statistically calculated. At least 99% of the samples in a population of a given material are expected to exceed A-basis properties and at least 90% of the samples in a population are expected to exceed B-Basis properties (in both cases with 95% confidence). Using these two values, a mean or "typical" value for each property, as well as a standard deviation, can be backed out for use in HyperSizer.

Example: Ultimate Tensile Strength (Ftu) for Aluminum 2024 (T81)

MIL-HDBK-5 lists the A and B basis for this property as:

A-basis: 67 ksi B-basis: 68 ksi

Assuming a normal distribution, design properties will be calculated from:

$$Ftu = \mu_{Ftu} - K\sigma_{Ftu} \tag{1.2.5.1}$$

From MIL-HDBK-17 (Volume 1, Tables 8.5.10 and 8.5.11) [1.2.3], we find that for a 95% confidence based on sample size n, K is determined from the following table.

	n=10	100	∞
90%	2.355	1.527	1.282
99%	3.981	2.684	2.326

For this example, assuming the data is derived from a very large population of samples $(n=\infty)$,

A-basis:
$$67 = \mu - 2.326 \sigma$$

B-basis: $68 = \mu - 1.282 \sigma$

Solving the above two equations for mean and standard deviation, μ and σ ,

$$\mu = 69.23 \text{ ksi}$$

 $\sigma = 0.9579 \text{ ksi}$

Now, using these values for typical strength and standard deviation, HyperSizer can solve for material strength for any level of reliability.

Reliability	K	Ftu _{design}
99.865	3.00	66.35
99.00	2.326	67.0*
90.00	1.282	68.0**
84.13	1.00	68.27

^{*} A-Basis Property

If the actual sample size is given with the A and B basis test data, then the sample mean and standard deviation must be modified accordingly. For example if the sample size is known to be 100, then the mean and standard deviation could be backed out from:

A-basis:
$$67 = \mu - 2.684 \sigma$$

B-basis: $68 = \mu - 1.527 \sigma$

$$\mu = 69.32 \text{ ksi}$$

 $\sigma = 0.8643 \text{ ksi}$

and using these K values from the above table gives

99% reliability Ftu_{design} =
$$69.32 - (2.684) (0.8643) = 67$$
 ksi 90% reliability Ftu_{design} = $69.32 - (1.527) (0.8643) = 68$ ksi

A summary of typical values, standard deviations, and design values for several levels of reliability are shown in the table below.

^{**} B-Basis Property

Table 1.3, Al 2024 Ultimate Tensile Strength at varying levels of reliability based on several test sample sizes

n	Ftu _{typical}	σ	99.865%	A (99%)	B(90%)	84.13%
10	69.44	.6150		67	68	
100	69.32	.8643		67	68	
∞	69.23	.9579	66.35	67	68	68.27

The above calculations assume that the A and B basis data are available and used for the analysis. If instead, the S-basis values are used, which are the required minimum values provided by some governing specification, HyperSizer will use the lower of the S-basis properties or the statistically calculated properties.

Future Work

Currently, reliability based failure has only been implemented in HyperSizer assuming large (or infinite) sample sizes. In the future, modifications will be made to account for finite sample sizes. Several other distributions are used to represent test data scatter including Weibull distributions and Analysis of Variance (ANOVA) methods and these will also be included for material property adjustments in HyperSizer where appropriate.

1.2.6 Composite Strength

1.2.6.1 Uncertainty in Material Strength Allowables

One aspect of the statistical knockdown for composite strength calculations is based on statistical data (i.e. material BASIS) provided by material references such as MIL-HDBK-17. For example, in MIL-HDBK-17, material strength properties are generally provided as typical (or mean), minimum, maximum and Coefficient of Variation (CV) for each population sample. In addition, the B-basis values are specified along with the appropriate distribution type, and the parameters that represent this distribution.

For samples that can be represented with a normal distribution, the design material data for a given property can be determined from:

$$F = \mu_F - K\sigma_F \tag{1.2.6.1}$$

where σ_F is the standard deviation of the sample which is equal to μ_F multiplied by CV. The value of K is a function of the sample size and the required reliability.

Example: F₂^t for AS4-3502 (MIL-HDBK-17-2E, p. 4-70)

Find the A and B basis values for this property based on the given sample size (30), the mean population value (7.76) and the coefficient of variation (0.107).

For n = 30, from tables, 8.5.10 and 8.5.11,

A-Basis, 99%: K = 3.064B-Basis, 90%: K = 1.778

	Mean	7.76
	Minimum	6.26
	Maximum	10.2
	C.V.(%)	10.7
	B-value	6.28
	Distribution	Normal
F_2^t	C,	7.76
(ksi)	C ₂	0.832
	No. Specimens	30
	No. Batches	5
	Approval Class	Fully Approved

The design values are then:

A-Basis: $F_2^t = 7.76 - (3.064) (0.832) = 5.21 \text{ ksi}$ B-Basis: $F_2^t = 7.76 - (1.778) (0.832) = 6.28 \text{ ksi}$

Future Work

Currently, reliability based failure has only been implemented in HyperSizer assuming large (or infinite) sample sizes. In the future, modifications will be made to account for finite sample sizes. Several other distributions are used to represent test data scatter including Weibull distributions and Analysis of Variance (ANOVA) methods and these will also be included for material property adjustments in HyperSizer where appropriate.

1.2.6.2 Uncertainty with Interaction of Biaxial and Biaxial with Shear Loads

Unlike failure in isotropic materials, where failure theories such as Von-Mises are universally accepted for predicting failure, there are no criteria that are universally accepted criteria for predicting failure of composite laminates under combined loadings. Many failure criteria have been developed such as max stress, max strain, Tsai-Hill, Puck, LaRC03 and Hashin and each has strengths and weaknesses for various materials and loading environments. Our belief is that the proper procedure, in addition to statistically processing the design-to allowables as discussed in the Section 1.2.6.1, is to derive individual correlation factors for each criteria and each material system based on available test data. In this way, analyses can be performed for each failure criterion to a consistent level of reliability.

In Section 3, this procedure is demonstrated for several different material systems based on hundreds of test data points from the World-Wide Failure Exercises.

Table 1.4, Summary of HyperSizer CFs for Composite Failure Theories

Failure Theory	η	μ_{I}
Max Strain 1	0.092	0.9184
Max Strain 2	0.167	0.9772
Max Strain 12	0.210	1.104
Max Stress 1	0.1067	0.8922
Max Stress 2	0.1427	0.9305
Max Stress 12	0.218	1.034
Tsai-Hill	0.165	1.051
Tsai-Wu	0.125	1.012
<u>Tsai-Hahn</u>	<u>0.099</u>	<u>1.013</u>
Hoffman	0.121	1.012
Hashin Matrix Cracking	0.191	1.034
Hashin Fiber Failure	0.143	0.9328
LaRC03 Matrix Cracking	0.157	1.001
LaRC03 Fiber Failure	0.1107	0.9388
average	0.1469	0.9893

1.2.7 Sandwich Failure Modes

1.2.7.1 Facesheet Wrinkling

The equation for knockdown of panel facesheet wrinkling is based on those presented in MIL-HDBK-23 [1.2.4] and also in Ley [1.2.5] that attempt to account for facesheet initial imperfections in relation to core stiffness and strength. This equation is:

$$Factor = \frac{1}{1 + C_1 R} \qquad R = \frac{\delta E_c}{t_c F_c}$$
 (1.2.7.1)

where δ is the panel imperfection, E_c is the through thickness stiffness of the core, t_c is the core thickness and F_c is the core crush strength. Reference [1.2.4] recommends a constant C_I value of 0.65, while [1.2.5] suggests $C_I = 1.0$. In practice however, δ is rarely measured or known, therefore our suggestion is to replace δ with a function of the facesheet thickness. The constant, C_I is then modified through the HyperSizer database based on available test data (the database entry for this constant is μ_3). The knockdown correlation is Equation 1.1.3, repeated here,

$$\gamma_{\mu} = \mu_1 + \mu_2 \frac{|D_{13}| + |D_{23}|}{D_{11} + D_{22}} + \frac{1}{1 + \mu_3 R}$$

$$R = \frac{(0.25 - t_f)E_c}{t_c F_c}$$

This equation works well if it is "tuned" to a particular honeycomb design, including the core and facesheet material choices, the manufacturing process used, and the relative core and facesheet thicknesses. However, in general use, when trading different sandwich configurations with different material systems, it can lead to either very over or very under conservative results. Therefore it is recommended for general use to remove the effect of the 'R' term in Equation 1.1.3 and just use a straight knockdown using μ_1 only. To remove the effect of this term (the third term of Equation 1.1.3), the value of μ_3 should be set to a very high value (e.g. 1,000,000) so that the overall term approaches zero.

An example of assigning correlation factors for a particular honeycomb configuration is presented in detail in Section 2.2.

1.2.7.2 Facesheet Dimpling

The knockdown correlation for facesheet dimpling uses the same form as that for facesheet wrinkling presented in Section 1.2.7.1.

1.2.7.3 Facesheet Shear Crimping

The knockdown correlation for facesheet shear crimping uses the same form as that for facesheet wrinkling presented in Section 1.2.7.1.

1.2.7.4 Core Crushing; Shear Strength

Core crushing and Shear Strength failures are primarily functions of the core crushing and shear strength material properties. The statistical knockdown for these failure modes is based on statistical data (i.e. material BASIS) provided by material references such as MIL-HDBK-23 or vendor data. The design knockdowns are achieved by varying the strength as described for isotropic data and composite data in Sections 1.2.5 and 1.2.6.

1.2.8 Bonded Joint Failures

1.2.8.1 Uncertainty in Material Strength Allowables

One aspect of the statistical knockdown for bonded joint strength calculations is based on statistical data (i.e. material BASIS) provided by material references such as MIL-HDBK-17. The same statistical procedure discussed in Section 1.2.6.1 for composite material strength allowables is used in bonded joint analysis to determine the design-to material allowables in bonded joints.

1.2.8.2 Uncertainty with Bonded Joint Failure Analyses

Just as with the composite failure theories described in Section 1.2.6.2, the proper failure criteria for bonded joints are not well understood or universally accepted. This uncertainty is even more of a problem with joint failure analyses than with composite strength. The problem is compounded by the fact that there is very little public test data available for these structures. As part of this SBIR effort, 19 failure methods were implemented from a variety of sources attempting to predict failure of these joints. Just as with the various composite failure theories, the recommendation is to derive individual correlation factors for each of these joint failure theories.

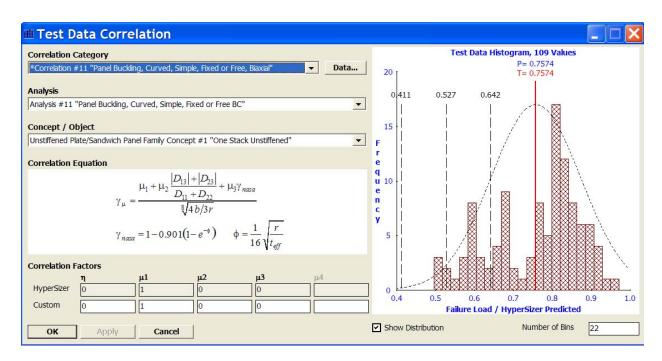
Derivation of these correlation factors was not completed as part of this SBIR. One of the primary reasons for this was lack of relevant public test data. This was especially true for the primary joint type that was implemented within the commercial HyperSizer software. That is, the bonded doubler joint representing the flange to facesheet joint of a stiffened panel.

1.2.9 References

- 1.2.1 NASA SP-8007, Buckling of Thin-Walled Circular Cylinders, NASA Space Vehicle Design Criteria (Structures), August 1968
- 1.2.2 Department of Defense Handbook, Metallic Materials And Elements For Aerospace Vehicle Structures, MIL-HDBK-5J, April 2003.
- 1.2.3 Department of Defense Handbook, Polymer Matrix Composites, MIL-HDBK-17E, January 1997.
- 1.2.4 Department of Defense Handbook, Structural Sandwich Composites, MIL-HDBK-23A, December 1968.
- 1.2.5 Ley, R. P., Lin, W., Mbanefo, U., "Facesheet Wrinkling in Sandwich Structures", NASA CR-1999-208994, 1999.

1.3 Summary of Histograms Before and After Correlations

This section lists all non-composite strength failure analysis histograms . The composite material strength histograms are not included here but are summarized in Vol 3, Ch 4.



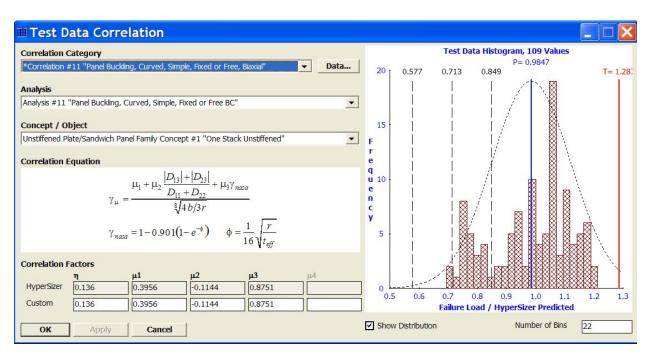
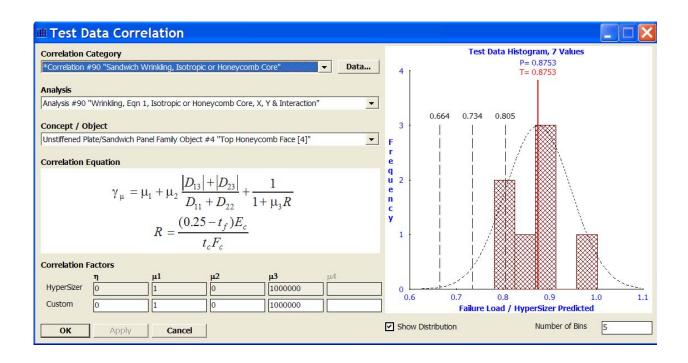


Fig. 1.3.1, <u>Panel Buckling, Curved, Simple, Fixed, or Free BC, Biaxial stiffness panel</u> correlation category. Top image before correlation. Bottom image after correlation factors applied.



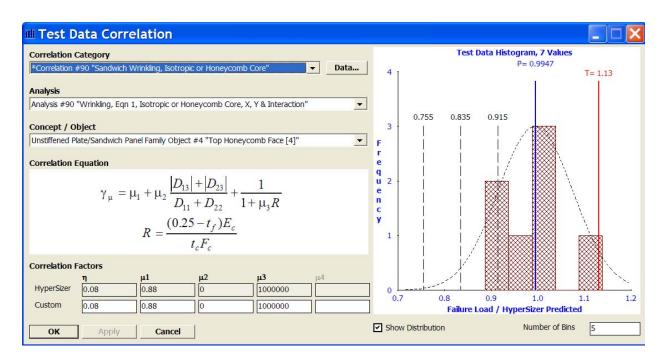
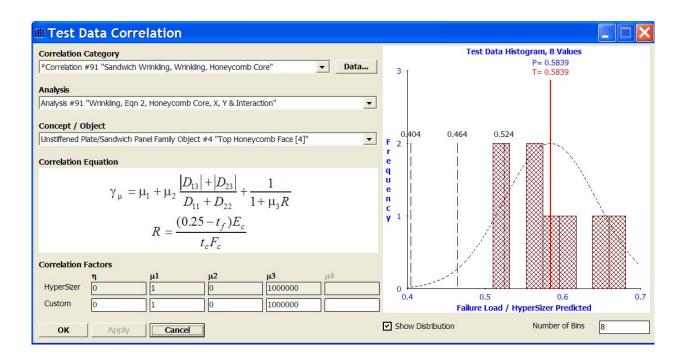


Fig. 1.3.2, <u>Sandwich Wrinkling</u>, <u>Isotropic or Honeycomb Core</u>.

Top image before correlation. Bottom image after correlation factors applied.



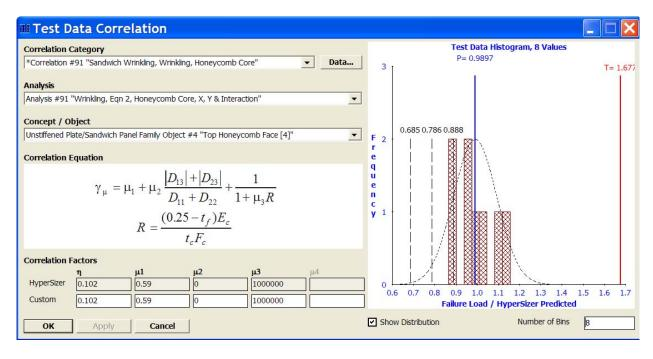
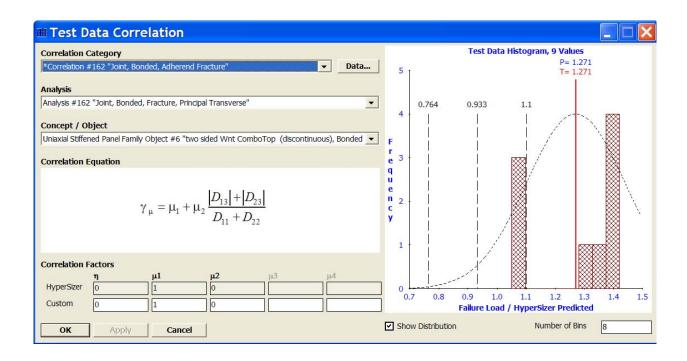


Fig. 1.3.3, <u>Sandwich Wrinkling, Wrinkling, Honeycomb Core</u>.

Top image before correlation. Bottom image after correlation factors applied.



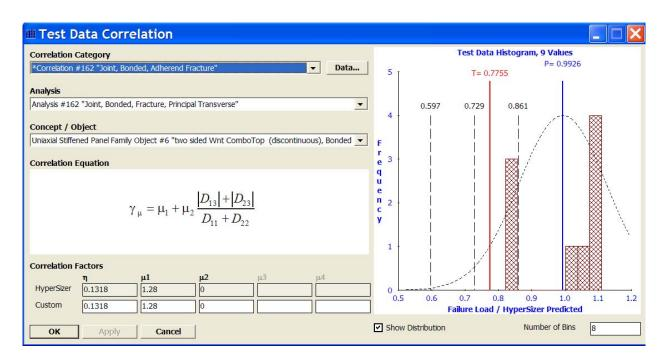
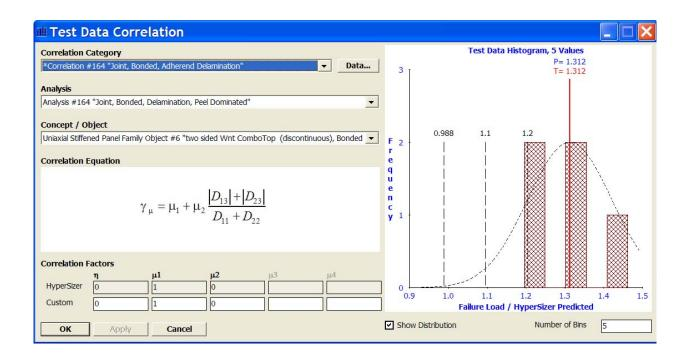


Fig. 1.3.4, <u>Joint, Bonded, Adherend Fracture</u>.

Top image before correlation. Bottom image after correlation factors applied.



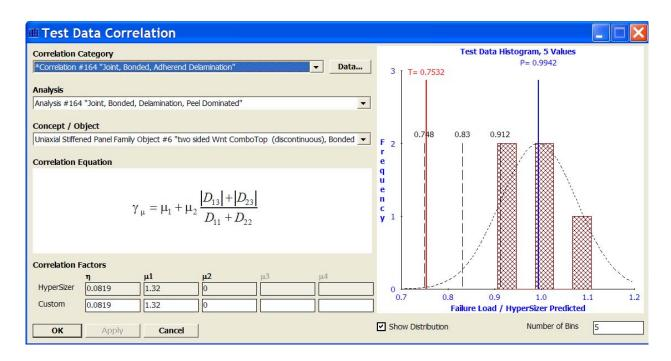


Fig. 1.3.5, <u>Joint, Bonded, Adherend Delamination</u>.

Top image before correlation. Bottom image after correlation factors applied.

--VALIDATIONS---

2 Validation - Sandwich Wrinkling Panel Failure Test Data and CFs

This section was moved to Volume 2, Chapter 2.

3 Validation – Composite Material Strength Failure Envelopes of World Wide Failure Exercises (WWFE) Test Data and Other Published Data

The validation cases included in this chapter are from the World Wide Failure Exercises (WWFE), [3.1] and from other published data [3.2]. The illustrated, laminate failure envelop strengths in the following figures are calculated using ply strengths and ply based failure criteria. The published test data are for final failure instead of initial failure, which is also referred to as damage initiation, and as first-ply-failure. However for unidirectional laminates and for $[\pm \theta]$ layups where all plies fail at the same time the first ply fails, initial failure is final failure, as in cases 1, 2, 3, 8, 9, and 10. Some of the invited WWFE contributors developed degradation models or revised their models post test (Part B) to account for progressive failure. HyperSizer will include macro (ply level) and micro (fiber/matrix level) progressive failure in the near future. Shown in Section 3.7 are preliminary HyperSizer micromechanics progressive failure predictions that illustrate close comparison to test final failures. For now though, the emphasis is the HyperSizer initial first ply failure envelopes generated for cases 1, 2, 3, 8, and 9.

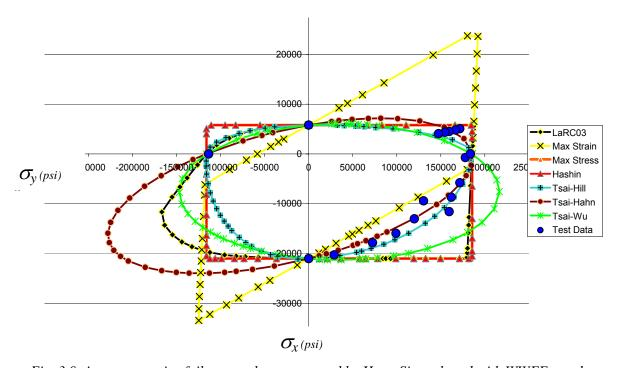


Fig. 3.0, A representative failure envelope generated by HyperSizer plotted with WWFE test data.

The theoretical composite strengths presented here as failure envelopes are for pristine laminates, that is without damage. The assumption is the test data is also for undamaged laminates. For an airframe design, damage tolerance and survivability allowables would be determined and used as additional limiting strength requirements. Note, that the unidirectional (UD) material allowable strengths provided by the WWFE are "a given" and provided for uniaxial tension, uniaxial compression, or pure shear. As such, they serve as anchor points that all failure theory pass through, as depicted on the four axes of Fig. 3.0. Differences in failure theories will be observed for biaxial and shear loading interactions. The included failure envelopes are: Max Strain, Max Stress, Tsai-Hill, Tsai-Wu, Tsai-Hahn, Hoffman, Hashin Matrix Cracking, Hashin Fiber Failure,

LaRC03 Matrix Cracking, and LaRC03 Fiber Failure. Refer to Vol2, Ch7 for detail on these failure criteria.

Section 3.10 lists the WWFE failure load test data numbers used to plot the blue filled points on the failure envelopes. Section 3.11 identifies the material properties, with Table 3.11.1 listing the UD material properties for WWFE test cases. Material properties for other validation cases listed in Table 3.11.2. Section 3.12 lists the layups, thicknesses, materials, and loadings for each case.

Table 3.0, HyperSizer Failure Envelope Summary

Case	WWFE	Layup	Loading Interaction	Prog. Failure	Material	Failure Envelope Figure	HyperSizer Workspace
1	✓	Unidirectional [0°]	σ_{y} - $ au_{xy}$		E-glass/LY556/HT907	Fig. 3.1.2 and 3.1.3	Α
2	✓	Unidirectional [0°]	σ_{x} - τ_{xy}		Gr/Ep T300/BSL914C	Fig. 3.2.2	Α
3	\checkmark	[±85°]	σ_{x} - σ_{y}		E-glass/MY750	Fig. 3.3.2	Α
4	✓	[-30/+30/90]s	σ_{x} - σ_{y}	✓	E-glass/LY556/HT907		Α
5	✓	[-30/+30/90]s	σ_{x} - τ_{xy}	✓	E-glass/LY556/HT907		Α
6	\checkmark	[+55/-55]s	σ_{x} - σ_{y}		E-glass/MY750		Α
7	✓	[0/-45/+45/90]s	σ_{x} - σ_{y}	✓	Gr/Ep AS4/3501-6	Fig. 3.7.3*	Α
8		Unidirectional [0°]	σ_{v} - τ_{xv}		Gr/Ep AS4_55A	Fig. 3.8.2	В
9		Unidirectional [0°]	σ_{v} - τ_{xv}		Gr/Ep T800_3900-2	Fig. 3.9.2	В
10		[±θ]	Loading on $[\pm \theta]$		Gr/Ep AS4/3502	none	В

A= WWFE test data, HyperSizer Workspace: World Failure Exercise Composite Failure

B= Non-WWFE test data, HyperSizer Workspace: <u>LaRC03 Workspace</u>

3.1 Case 1: unidirectional E-glass/LY556 epoxy σ_y vs. τ_{xy} failure envelope

3.1.1 WWFE Test Data

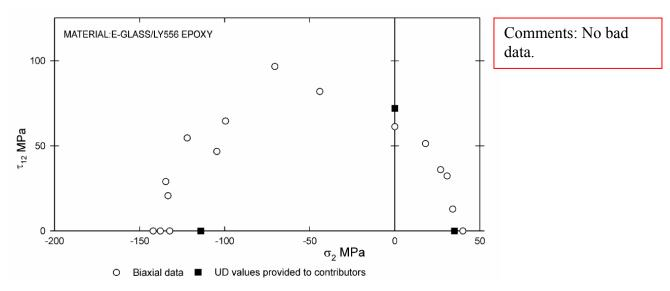


Fig. 3.1.1, The black solid squares are the unidirectional (UD) allowable stresses provided to the invited contributors. The open circles are the test data values. Note the discrepancy between the provided compressive transverse strength (σ_2) and the test average, about 20%.

This is Test Case 1 of WWFE. It is for unidirectional E-glass/LY556 under combined biaxial stresses σ_{22} and σ_{12} . Fig. 3.1.1 plots the test data results. Note the scatter and the fact that the measured 'in-situ' compressive σ_2 is much different than the provided unidirectional (UD) allowable. For this reason, we show two different sets of failure envelopes. Fig. 3.1.2 uses the provided UD allowable, and Fig. 3.1.3 and Fig. 3.1.4 uses the measured average stress as the allowable.

3.1.2 Failure Envelopes: HyperSizer Generated and WWFE Published

Figs. 3.1.2 and 3.1.3 show failure envelopes plotted in an Excel spreadsheet generated automatically with HyperSizer's object model. For Case 1, Tsai-Wu and Tsai-Hahn are producing the same envelope, and in general match test data better than the other criteria. Note the trend in the test data that shows shear strength increasing as σ_{22} goes into compression. LaRC03 captures this behavior as plotted in Figs. 3.1.2 and 3.1.3.

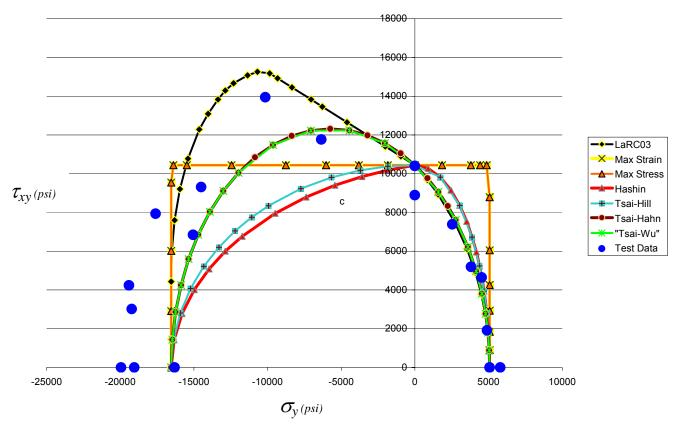
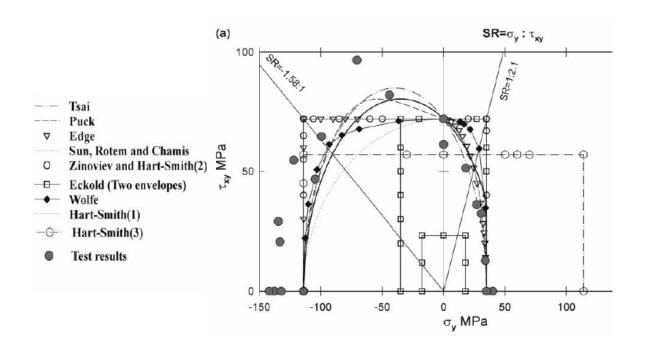


Fig. 3.1.2, Biaxial σ_y - τ_{xy} failure envelopes of 0° **E-glass/LY556** lamina. Same test data is shown in both top and bottom graphics as filled circles. Note the scatter in measured failure. These plots use the unidirectional data as originally provided to contributors. $Y^c = 114$ MPa, S=72 MPa.

(a) Top graphic; HyperSizer generated, units of (psi)

(b)Bottom graphic, image taken directly from reference 3.1, units of (MPa)



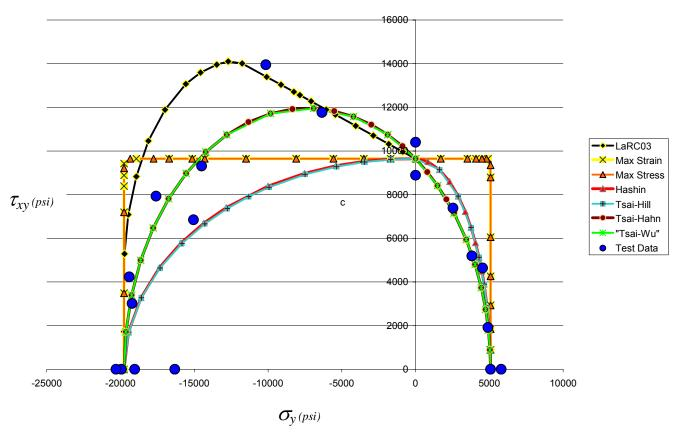
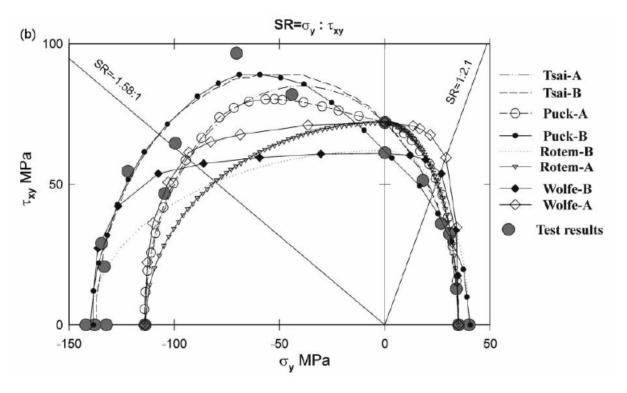


Fig. 3.1.3, Biaxial σ_y - τ_{xy} failure envelopes of 0° **E-glass/LY556** lamina. Same test data shown as filled circles in both graphics.

These plots use inidirectional strengths based on test results. $Y^c = 136.2 \text{ MPa}$, S=65 MPa.

- (a) Top graphic; HyperSizer generated, units of (psi)
- (b)Bottom graphic, image taken directly from WWFE reference 3.1, units of (MPa)



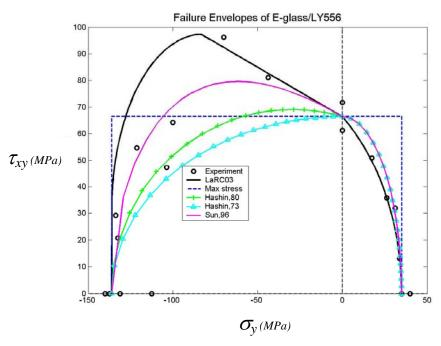


Fig. 3.1.4, Comparison of LaRC03 to Sun, Hashin 73,80, and maximum stress criteria.

The LaRC03 failure envelope is also included on Fig. 3.1.4 for the purpose of comparing to Sun, Hashin, 80, Hashin, 73, and maximum stress criteria. In the first quadrant where the UD ply fails in matrix tension, all the failure theories match well with the experiment except the maximum stress failure criterion whose envelope is rectangular because it does not prescribe interaction between stress components.

In the second quadrant where the UD ply is under transverse compression, the test data shows that the trend of shear strength increase as σ_{22} goes into compression. Traditional failure theories, like Hashin'73 and Hashin'80, however, gives an elliptical envelope with diminishing τ_{12} as the absolute value of compressive σ_{22} increases. "One important feature of the experimental results was that the shear strength appeared to increase significantly in the presence of longitudinal tension. As this was contradicted by nearly all of the theoretical predictions, further experimental work is clearly needed in this area," [3.1]. LaRC03 models this behavior.

Puck's envelope shown in Fig. 3.1.3, from the 2002 [3.1] appears to be the most accurate, but it relies on fitting parameters based on the same test data. The LaRC03 curve uses the stiffnesses and strengths shown in Table 3.11.1, an assumed α_0 =53°, and no other empirical or fitting parameter. The failure envelope for Sun's criterion was calculated using η^L =0.336. The results indicate a significant improvement over Hashin's criteria. An even better fit would have been achieved using a higher value for η^L .

3.2 Case 2: unidirectional T300/BSL914C; σ_x vs. τ_{xy} failure envelope

Graphite/Epoxy

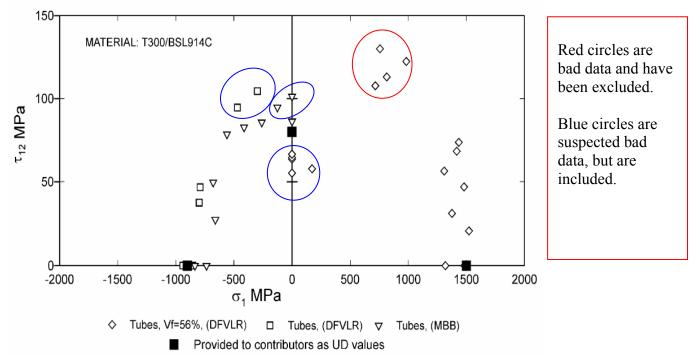


Fig. 3.2.1, The black solid squares are the unidirectional (UD) allowable stresses provided to the invited contributors.

3.2.1 WWFE Test Data

This is Test Case 2 of WWFE unidirectional T300/BSL914C; σ_x vs. τ_{xy} . Fig. 3.2.1 plots the test data results. Note the scatter particularly for the pure shear measured value. In contrast to Fig. 3.1.1, the measured 'in-situ' τ_{xy} is in the middle of the provided unidirectional (UD) allowable. The blue circles are suspect bad data, but are included. The red circles are excluded bad data based on the WWFE report.

Fig. 3.2.2 shows failure envelopes plotted in an Excel spreadsheet generated automatically with HyperSizer's object model.

For Case 2, Tsai-Wu and Tsai-Hahn are again producing the same envelope, and in general match test data better than the other criteria. LaRC03, max stress, and max strain match the 1st quadrant of tension fiber loading with shear better than any other theories. The other criteria under-predict in this quadrant. In the second quadrant, LaRC03 is apparently under-predicting the occurrence of fiber compressive failure due to the supporting matrix collapse under compression.

3.2.2 Failure Envelopes: HyperSizer Generated and WWFE Published

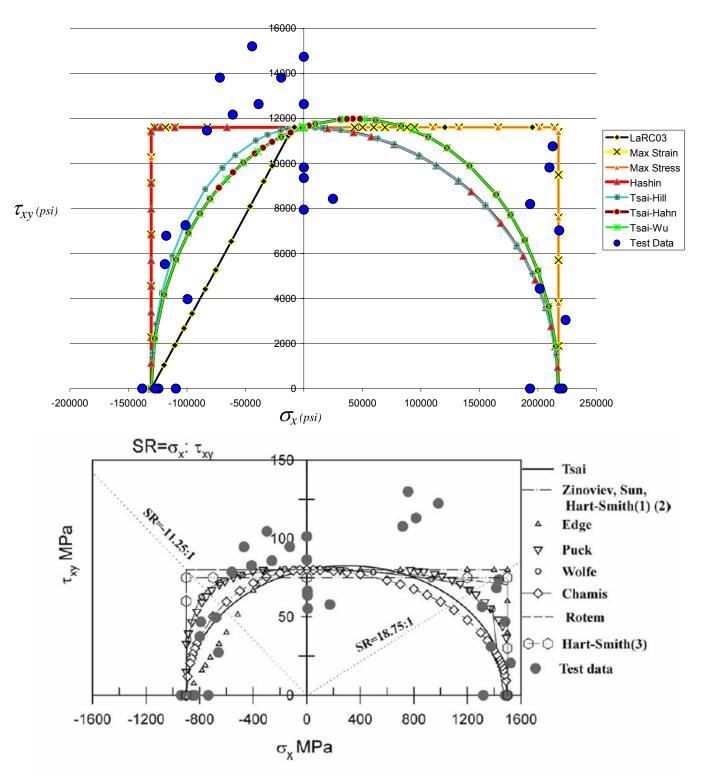
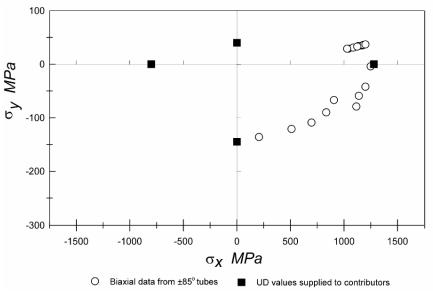


Fig. 3.2.2, Biaxial σ_x - τ_{xy} failure envelopes of 0° **T300/BSL914C** lamina. Same test data shown as filled circles in both graphics. These failure envelopes use the unidirectional data as originally provided to contributors.

- (a) Top graphic; HyperSizer generated, units of (psi)
- (b)Bottom graphic, image taken directly from WWFE reference 3.1, units of (MPa)

3.3 Case 3: $[\pm 85^{\circ}]$ E-glass/MY750 epoxy; σ_x vs σ_y failure envelope

3.3.1 WWFE Test Data



Comments: No bad data was found for this case. Instead there is not enough data in the 1st, 2nd, 3rd quadrant.

Fig. 3.3.1,The black solid squares are the unidirectional (UD) allowable stresses provided to the invited contributors. The open circles are the test data values.

3.3.2 Failure Envelopes: HyperSizer Generated and WWFE Published

Failure envelope of unidirectional E-glass/MY750 epoxy under combined biaxial stresses σ_x vs. σ_y is plotted in Fig. 3.3.2. Since the comparison is σ_x vs. σ_y , all four quadrants of the failure envelopes are illustrated, to capture the influence of compressive vs. tensile strength differences. The experimental data is not sufficient to judge the theories in all the four quadrants, because most of the data points are located in the first and fourth quadrant. All tests are tensile in the X direction.

For case 3, Tsai-Hahn matches the test data very well as does Tsai-Hill. Tsai-Wu does poor in the 4th quadrant of tension-compression. At first glance, it appears that max strain matches very poorly. Max strain depicts an extreme increase in tensile σ_y capability as tensile σ_x increases, and case 3 has limited test data in this quadrant, as a consequence, this helpful biaxial loading interaction cannot be confirmed or refuted. However, the provided data does shows max strain to be fairly accurate in the 4th quadrant, better than max stress, Puck, and LaRC03.

Note that Tsai-Hahn is predicting much greater biaxial strengths in the 3rd quadrant (compression-compression) than any other failure criteria. Since data is not available at these loads, this helpful biaxial loading interaction also cannot be confirmed or refuted. To a lesser extent LARC03 and Tsai-Wu also depict this helpful superposition.

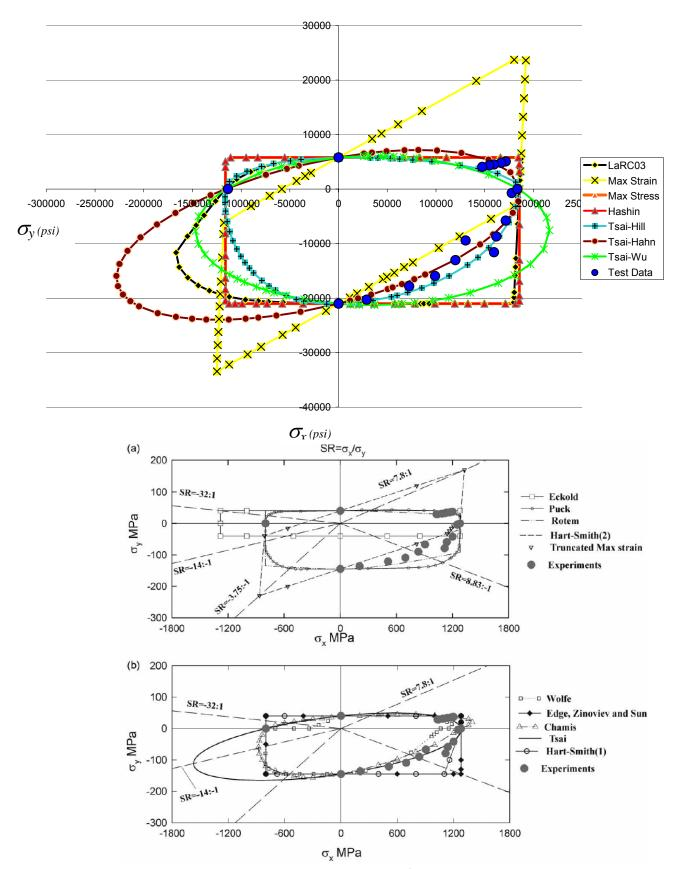


Fig. 3.2.2, Biaxial σ_x - σ_y failure envelopes of 0° **E-glass/MY750** epoxy lamina. (a) Top graphic; HyperSizer generated, units of (psi) (b)Bottom graphic; image taken directly from WWFE reference 3.1, units of (MPa)

Testing for biaxial loads presents a number of complexities, and experimental results are rare. For example, Waas et al.[3.4] reports a number of references in which multiaxial loading was studied by superposing a hydrostatic pressure in addition to the compressive loading. For all materials considered, there was a significant increase in compressive strength with increasing pressure. In particular, the results of Wronsky and Parry [3.5] on glass/epoxy show a longitudinal strength increase of 3.3 MPa per MPa of hydrostatic pressure, which means a compressive strength increase of 4.3 MPa per MPa of applied transverse biaxial stress. More recently, Sigley et al.[3.6] found a 32% to 71% increase in compressive strength per 100 MPa superposed pressure.

3.4 Case 4: $(-30/30/90)_s$ E-glass/LY556 epoxy; σ_x vs σ_y failure envelope

3.4.1 WWFE Test Data

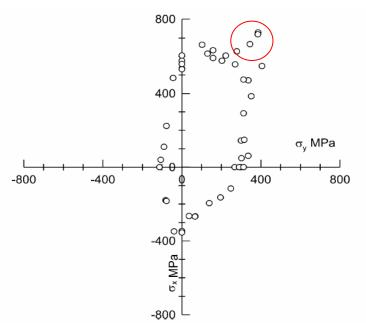


Fig. 3.4.1, Progressive Failure Case 4

Comments: No bad data was found (the circled are suspect). Progressive failure occurred in these tests.

These tests exhibit progressive failure. Failure envelopes for this case will be done later after HyperSizer implements macro (ply level) and micro (fiber/matrix level) progressive failure. Shown in Section 3.7 are preliminary HyperSizer micromechanics progressive failure predictions for Case 7, that illustrate close comparison to test final failures.

3.4.2 WWFE Published Analytical Failure Envelopes

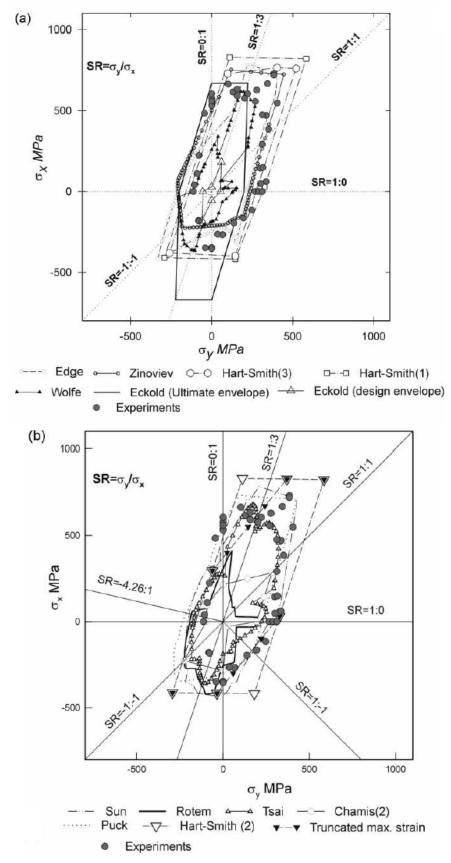
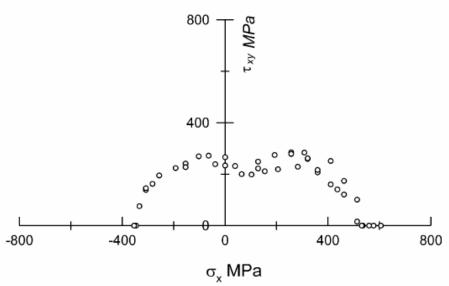


Fig. 3.4.2, Image taken directly from WWFE reference 3.1, (MPa)

3.5 Case 5: (-30/30/90)s E-glass/LY556 epoxy; σx vs σxy failure envelope

3.5.1 WWFE Test Data



Comments: No bad data . Progressive failure occurred in the tests.

Fig. 3.5.1, Progressive Failure Case 5

These tests exhibit progressive failure. Failure envelopes for this case will be done later after HyperSizer implements macro (ply level) and micro (fiber/matrix level) progressive failure. Shown in Section 3.7 are preliminary HyperSizer micromechanics progressive failure predictions for Case 7, that illustrate close comparison to test final failures.

3.5.2 WWFE Published Analytical Failure Envelopes

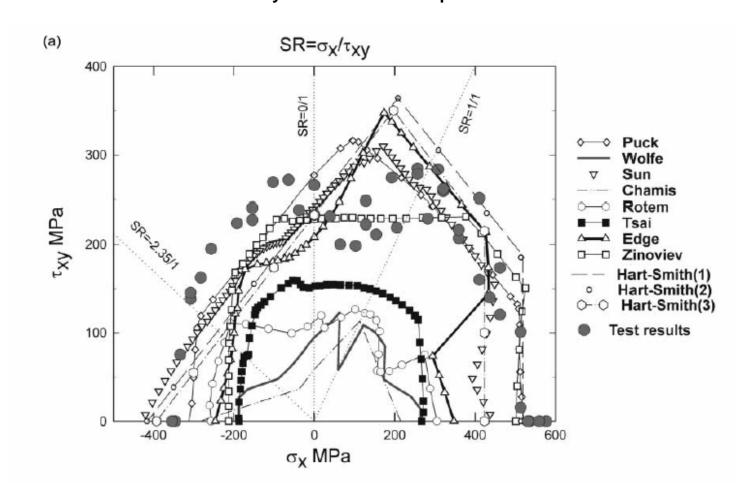


Fig. 3.5.2, Image taken directly from WWFE reference 3.1, (MPa)

3.6 Case 6: [+55/-55]_s E-glass/MY750 epoxy; σ_x vs σ_y failure envelope

3.6.1 WWFE Test Data

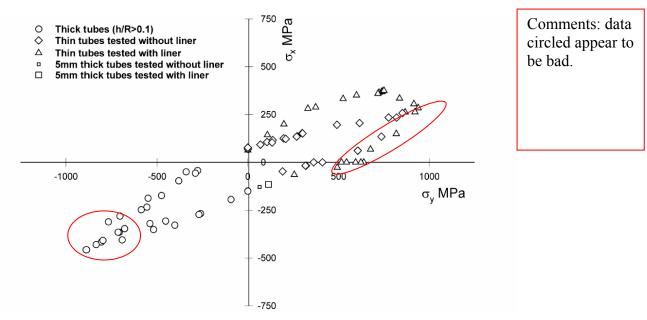
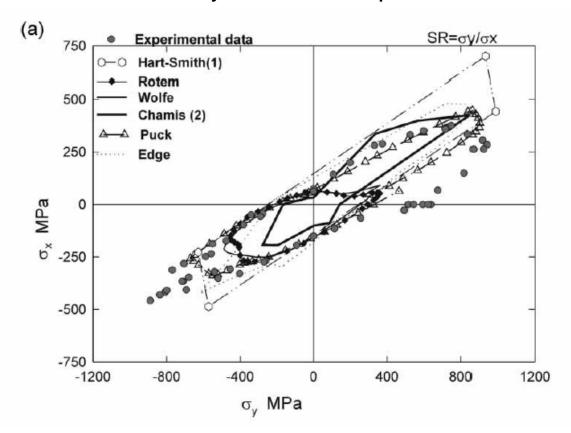


Fig. 3.6.1, Progressive Failure Case 6

These tests exhibit progressive failure. Failure envelopes for this case will be done later after HyperSizer implements macro (ply level) and micro (fiber/matrix level) progressive failure. Shown in Section 3.7 are preliminary HyperSizer micromechanics progressive failure predictions for Case 7, that illustrate close comparison to test final failures.

3.6.2 WWFE Published Analytical Failure Envelopes



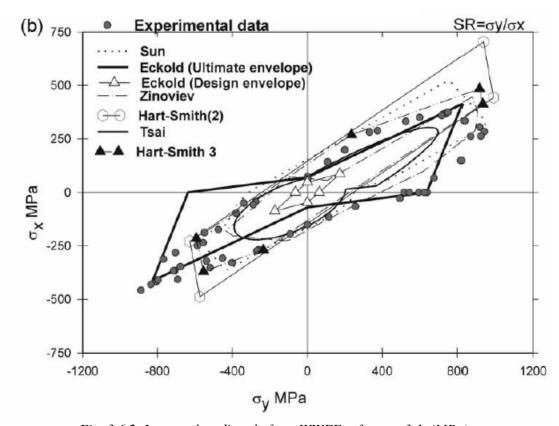
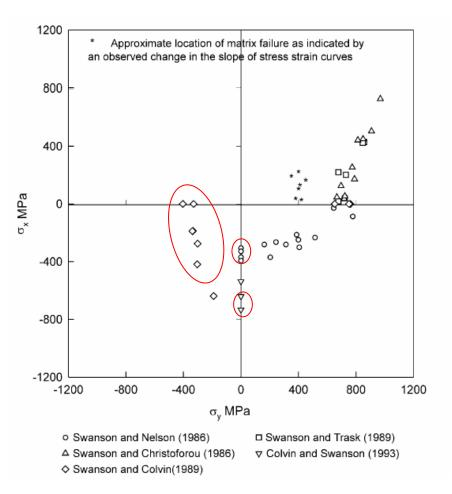


Fig. 3.6.2, Image taken directly from WWFE reference 3.1, (MPa)

3.7 Case 7: $[0/-45/+45/90]_s$ AS4/3501-6; σ_x vs σ_y failure envelope

3.7.1 WWFE Test Data



Comments: the data circled are not applicable to composite failure analysis because failure was shell buckling, which was reported by the organizer and was confirmed by HyperSizer buckling analysis.

Fig. 3.7.1, Progressive Failure Case 7

This test exhibits progressive failure. More complete failure envelopes for this case will be done later after HyperSizer implements macro (ply level) and micro (fiber/matrix level) progressive failure. Shown for this Case 7 are preliminary HyperSizer micromechanics progressive failure predictions that illustrate close comparison to test final failures.

3.7.2 WWFE Published Analytical Failure Envelopes

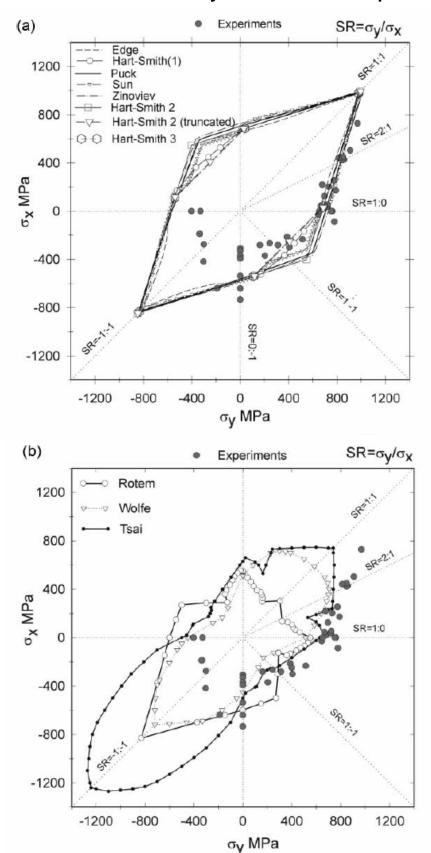


Fig. 3.7.2, Image taken directly from WWFE reference 3.1, (MPa)

3.7.3 HyperSizer Progressive Failure

Composite laminated material may continue to carry additional loading after a ply fails. Post damage initiation strength can be analyzed and is often referred to as progressive failure. Traditional aerospace design margins-of-safety for laminate strength are based on first ply failure. This may change in the future with the availability of reliable progressive failure methods. When performing test article failure prediction, progressive failure analyses, in conjunction with typical material properties, are likely needed in order to match ultimate final laminate failure.

Progressive damage can be modeled recursively with any failure criteria to: a) identify a damage initiation, b) increment a load increase until another failing event, and c) continue until eventual final collapse. Physically based failure criteria, due to distinguishing between fiber/matrix constituent failures, may prove to be better suited for progressive analysis than interaction type failure criteria such as Tsai series.

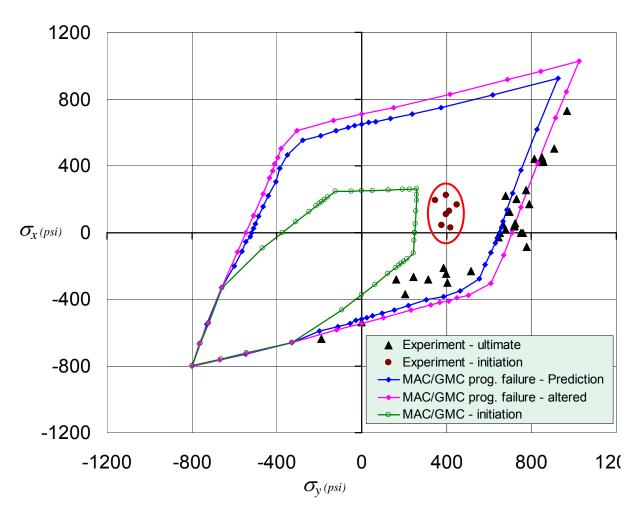


Fig. 3.7.3, Progressive failure modeled on the fiber/matrix constituent (micro) level. Failure data from the WWFE AS4/3501-6 (Case 7) MAC/GMC is a HyperSizer micromechanics module.

Progressive failure may also be modeled on the ply (macro) and fiber/matrix constituent (micro) levels. Fig. 3.7.3 shows computed failure envelopes for the WWFE AS4/3501-6 (Case 7) based

on the micromechanics progressive failure approach. MAC/GMC, shown in the legend, is the HyperSizer micromechanics module.

In Fig. 3.7.3, the red circle dots are damage initiation failures provided by the WWFE authors, and the black triangles are the ultimate final failures. In the figure are obvious large differences in load magnitudes between damage initiation and final failure, hence the need for progressive failure. Two different attempts at predicting progressive failure at the micromechanics level are shown. The first in blue was performed by fully removing a subcell when its stress level goes beyond its material allowable. An effect that is missing from the model used for this progressive failure prediction is shear-lag between subcells. It is believed that this effect would cause a portion of the load to be redistributed after a subcell failure. While a version of the micromechanics code that includes shear lag coupling HFGMC (higher theory of the general method of cells) is developed, it was not yet available to do progressive failure for this analysis. Until this code is available, the expedient solution was deemed to only remove 50% of the subcells stiffness, until all subcells fail. In this manner, a much better comparison to test ultimate failure was achieved as shown in magenta, which also compares very favorably to the progressive failure theories plotted in the WWFE Fig. 3.7.2(a).

3.8 Case 8: Unidirectional AS4-55A; σ_y vs. τ_{xy} failure envelope

Graphite/Epoxy Non WWFE Test Data from reference [3.7].

3.8.1 HyperSizer Generated Analytical Failure Envelopes

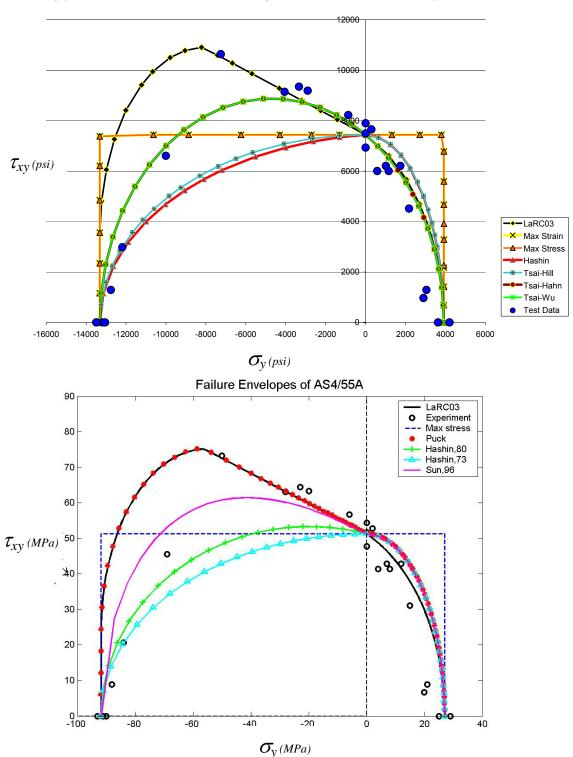


Fig. 3.8.2, Biaxial σ_y - τ_{xy} failure envelopes of 0° AS4/55A lamina.

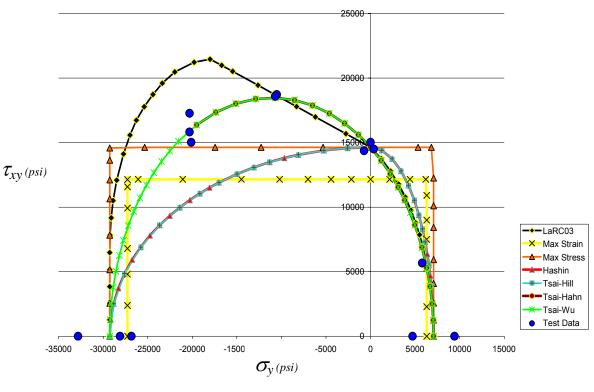
Fig. 3.8.1 illustrates a very close fit between test data and failure prediction with the Tsai-Hahn failure criteria. Only one data point fails at a higher load than the Tsai-Hahn failure envelope, but the LaRC03 failure envelope captures it. However, the LaRC03 failure criteria over predicts the strength of another test data point that Tsai-Hahn captures.

Shown in the bottom of Fig. 3.8.1 are additional failure criteria: Sun 96, Hashin 73, Hashin 80, and Puck. A special (non-production) version of HyperSizer implements these failure criteria, except Puck. The Puck data was not generated by HyperSizer, but was rather provided by a NASA Langley researcher, Davila [3.3].

3.9 Case 9: Unidirectional T800/3900-2; $\sigma_{\rm Y}$ vs. $\tau_{\rm xy}$ failure envelope

Graphite/Epoxy Non WWFE Test Data from reference [3.8].

3.9.1 HyperSizer Generated Analytical Failure Envelopes



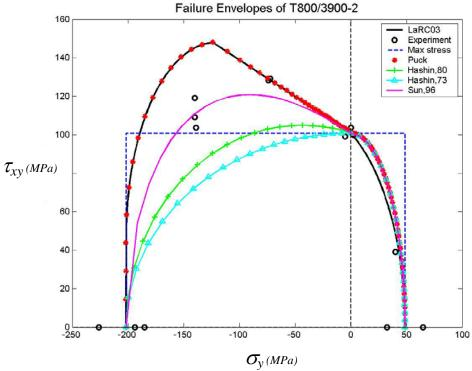


Fig. 3.9.1, Biaxial σ_y - τ_{xy} failure envelopes of 0° T800/3900-2 lamina.

Fig. 3.9.1 illustrates a very close fit between test data and failure prediction with the Tsai-Hahn failure criteria.

Shown in the bottom of Fig. 3.9.1 are additional failure criteria: Sun 96, Hashin 73, Hashin 80, and Puck. A special (non-production) version of HyperSizer implements these failure criteria, except Puck. The Puck data was not generated by HyperSizer, but was rather provided by a NASA Langley researcher, Davila [3.3].

In the top of Fig. 3.9.1, it appears that max strain has an incorrect allowable, for its predictions should follow the Max stress prediction.

Because of the scale of the failure envelope, Fig. 3.9.1, it is not readily apparent the vast difference in the two tensile σ 22 test data points. However, this difference is readily apparent when HyperSizer generates CFs and the resulting histogram. Refer to Vol3, Ch 4 for detailed information on correlation to this case. The difference is 9426 psi vs. 4713 psi, which is nearly a 100% difference between these two unidirectional values. The 4713 psi test data point causes HyperSizer to compute a MS = 0.5015. This in turn causes the ratio of (test/predicted) to be a low 0.67 value, which is beyond the 3 sigma range.

3.10 WWFE Failure Load Test Data Numbers

Case 1:

sigma_yy = [40.0 26.9 30.7 34.0 18.0 -137.8 -142.0 -132.3 -104.6 - 134.6 -99.4 -70.5 -122.0 -44.1 -133.3 0.00] (MPa)

sigma_xy = [0.0 36.0 32.3 12.8 51.3 0.0 0.0 0.0 46.7 28.9 64.5 96.6 54.6 81.9 20.7 61.2] (MPa)

Case 2:

sigma_yy = [1318.9 1481.1 1500.7 1522.8 1376.1 1480.6 1309.8 1417.3
1435.4 983.4 815.6 716.2 756.9 172.2 0 0 0 0 -297.8 -469.4 -790.1 798.7 -854.8 -939.3 0.0 0.0 -126.0 -260.3 -412.4 -559.6 -678.3 -659.9
-735.6 -835.7] (MPa)

sigma_xy = [0.0 0.0 0.0 20.4 31.0 46.9 56.4 68.4 73.7 122.3 113.0 107.7 129.9 57.8 55.2 63.5 64.6 66.5 104.5 94.6 46.7 37.4 0.0 0.0 86.3 101.3 94.7 85.7 82.7 78.6 49.6 27.2 0.0 0.0](MPa)

Case 3:

sigma_xx =[0.0 1280.0 -800.0 1170.0 1041.0 1134.0 1086.0 1181.0 1029.0
1200.0 1124.0 1249.0 1200.0 1138.0 1115.0 906.0 834.0 696.0 510.0
206.0 0](MPa)

sigma_yy =[40.0 0.0 0.0 35.0 29.0 34.0 31.0 36.0 29.0 37.0 33.0 -4.0 - 42.0 -59.0 -79.0 -67.0 -90.0 -109.0 -121.0 -136.0 145.0] (MPa)

Case 4:

sigma_xx = [292.3 592.3 730.8 557.7 720.5 548.7 -266.7 -268.0 -264.6 628.2 605.1 664.1 39.9 -179.2 223.8 110.3 -183.3 -348.5 483.7 144.4 61.6 667.3 148.8 616.0 471.0 -164.2 -195.1 -115.5 48.7 633.9 577.5 385.0 474.8 577.2 535.2 531.3 559.5 605.7 531.3 559.5 -346.5 -354.2 0.0 0.0 0.0 0.0 0.0 [MPa]

Case 5:

Sigma_xx = [577.2 531.3 282.3 436.3 513.3 462.0 410.7 64.2 128.3 128.3 192.5 256.7 -346.5 -354.2 0.0 320.8 320.8 38.5 256.7 102.6 154.0 205.3 308.0 359.3 359.3 410.7 462.0 513.3 535.2 -256.7 0.0 -64.2 -154.0 -

308.0 -333.7 -38.5 -102.7 -154.0 -192.5 -282.3 -308.0 531.3 559.5 605.7];

Sigmaxy=[0.0 0.0 228.9 140.1 100.8 173.4 251.2 199.9 222.1 248.6 274.2 284.5 0.0 0.0 233.2 258.9 261.4 231.5 278.5 198.2 211.0 218.7 283.6 206.7 216.2 159.8 120.5 15.4 0.0 194.8 265.7 271.7 240.9 138.4 75.2 238.4 269.1 227.3 223.8 162.3 145.2 0.0 0.0 0.0]

Case 6:

sigma_yy = [69.0 106.0 137.0 134.0 197.0 209.0 300.0 271.0 302.0 268.0
491.0 615.0 852.0 775.0 820 736.0 605.0 362.0 410.0 321.0 318.0 191.0
0.0 0.0 0.0 0.0 107.0 198.0 331.0 374.0 525.0 599.0 723.0 736.0 741.0
717.0 750.0 835.0 803.0 914.0 939.0 867.0 921.0 817.0 761.0 676.0
516.0 594.0 638.0 622.0 544.0 492.0 256.0](MPa)

sigma_xx = [92 106.0 116.0 103.0 124.0 122.0 151.0 135.0 151.0 134.0 196.0 205.0 257.0 234.0 234.0 133.0 0.0 0.0 0.0 -17.0 -17.0 -47.0 69.0 76.0 74.0 62.0 143.0 198.0 280.0 288.0 332.0 349.0 365.0 368.0 370.0 358.0 375.0 334.0 321.0 305.0 283.0 262.0 263.0 148.0 138.0 67.0 0.0 0.0 0.0 0.0 0.0 -27.0 -65.0](MPa)

Case 7:

sigma_xx = [-305.82 -328.40 -368.43 -393.06 -281.19 -369.45 -264.77 - 281.19 -213.46 -248.35 -300.69 -232.96 -87.23 -28.73 428.7 423.5 38.70 220.0 202.0 18.1 46.90 172.2 35.80 124.08 54.5 254.0 450.0 442.0 504.0 728.0 -733 -537 -640 0.0 0.0 0.0](MPa)

sigma_yy =[0.0 0.0 0.0 0.0 161.97 203.73 243.46 312.73 387.10 399.32
405.43 514.44 777.26 644.83 857.4 847.1 721.9 677.1 730.5 677.6 667.0
790.0 718.0 696.0 723.0 774.0 849.0 813.0 908.0 969.0 0.0 0.0 0.0
652.0 761.0 752.0](MPa)

3.11 Material Properties

 $Table \ 3.11.1, Thermal-mechanical \ properties \ of four \ unidirectional \ laminae \ in \ WWFE$

	AS4/3501-6 carbon/epoxy	T300/BSL914C epoxy	Eglass/LY556/ HT907/DY063 epoxy	Silenka E-glass MY750/HY917
Fiber volume fraction V _f	0.60	0.60	0.62	0.60
Longitudinal modulus E ₁ (GPa)	126	138	53.5	45.6
Transverse modulus E ₂ (GPa)	11	11	17.7	16.2
In-plane shear modulus G ₁₂ (GPa)	6.6	5.5	5.83	5.83
Major Poisson's ratio, v_{12}	0.28	0.28	0.278	0.278
Through thickness Poisson's ratio, v_{23}	0.40	0.4	0.4	0.4
Longitudinal tensile strength F _{1t} , (MPa)	1950	1500	1140	1280
Longitudinal compressive strength F _{1c}	1480	900	570	800
In-plane shear strength F ₆ (MPa)	79	80	72	73
Transverse tensile strength F _{2t} (MPa)	48	27	35	40
Transverse compressive strength F _{2c}	200	200	114	145
Ultimate longitudinal tensile strain $\epsilon_{lt}^{\ u}$	0.0138	0.01087	0.02132	0.02807
Ultimate transverse tensile strain ϵ_{2t}^{u}	0.00436	0.00245	0.00197	0.00246
Ultimate longitudinal compressive strain ε_{1c}^{u}	0.01175	0.00652	0.01065	0.01754
Ultimate transverse compressive strain ϵ_{2c}^{u}	0.02	0.01818	0.00644	0.012
In-plane shear failure strain, γ ₆	0.02	0.04	0.038	0.04
Longitudinal CTE α ₁ , 10 ⁻⁶ /°C	-1	-1	8.6	8.6
Transverse CTE α ₂ , 10 ⁻⁶ /°C	26	26	26.4	26.4

Table 3.11.2, Mechanical properties of non-WWFE UD laminae

	AS4/55A [3.7]	T800/3900-2 [3.8]	Scotch tape 1002 [3.9]	AS4-3502 [3.10]
Longitudinal modulus E ₁ (GPa)	126	155	53.5	127.6
Transverse modulus E ₂ (GPa)	11	8.5	17.7	11.3
In-plane shear modulus G ₁₂ (GPa)	6.6	5.5	5.83	6.0
Major Poisson's ratio, v_{12}	0.28	0.30	0.278	0.278
Through thickness Poisson's ratio, v_{23}	0.40	0.4	0.4	0.4
Longitudinal tensile strength F _{1t} , (MPa)	1200	1200	1108	1045
Longitudinal compressive strength F_{1c}	800	800	617.8	~
In-plane shear strength F_6 (MPa)	51.3	100.9	37.5	95.1 (in-situ)
Transverse tensile strength F_{2t} (MPa)	27	48.8	19.6	~ ~
Transverse compressive strength F_{2c}	91.8	201.7	137.3	244

3.12 Layups, thicknesses, materials, and loadings

Table 3.11.3, Summary of laminate types, thickness, material types and loading conditions

Laminate type	Ply thickness	Laminate	Material types	WWFE Case No., loading conditions.
	(mm)	thickness		
		(mm)		
0° unidirectional	0.25	2.0	E-glass/LY556/HT907	1. σ_v vs τ_{xy} failure stress envelope
lamina		2.0	T300/BSL914C	2. σ_x vs τ_{xy} failure stress envelope
		1.0	E-glass/MY750/HY917	3. $\sigma_{\rm v}$ vs $\sigma_{\rm x}$ failure stress envelope
(-30/+30/90) _s	$0.414 \text{ for } \pm 30;$	2.0	E-glass/LY556/HT907	4. σ_v vs σ_x failure stress envelope
	0.172 for 90			5. σ_x vs τ_{xy} failure stress envelope
(+55/-55)s	0.25	1	E-glass/MY750/HY917	6. σ_y vs σ_x failure stress envelope
(0/-45/+45/90) _s	0.1375	1.1	AS4/3501-6	7. σ_y vs σ_x failure stress envelope

3.13 References:

- 3.1 Soden P. D., Hinton, M. J., and Kaddour, A. S., (2002) "Biaxial test results for strength and deformation of a range of E-glass and carbon fibre reinforced composite laminates: failure exercise benchmark data," *Composite Science and Technology*, 62, pp.1489-1514.
- 3.2 Davila, C. G. and Camanho, P. P., "Failure criteria for FRP laminates in plane stress," NASA/TM-2003-212663.
- 3.3 Davila, C. G, personal communication.
- 3.4 Waas, A.M., and Schultheisz, C.R., "Compressive Failure of Composites, Part II: Experimental Studies," Progress in Aerospace Sciences, Vol. 32, No. 1, 1996, pp. 43-78.
- 3.5 Wronski, A.S., and Parry, T.V., "Compressive Failure and Kinking in Uniaxially Aligned Glass-Resin Composite under Superposed Hydrostatic Pressure," Journal of Material Science, Vol. 17, 1982, pp. 3656-3662.
- 3.6 Sigley, R.H., Wronski, A.S., and Parry, T.V., "Axial Compressive Failure of Glass-Fibre Polyester Composites under Superposed Hydrostatic Pressure: Influence of Fibre Bundle Size," Composite Science and Technology, Vol. 43, 1992, pp. 171-183.
- 3.7 Swanson, S. R., Messick, M. J. and Tian, Z., "Failure of Carbon/Epoxy Lamina Under Combined Stress," J. Composite Materials, 1987, Vol.21, pp.619-630.
- 3.8 Swanson, S. R. and Qian, Y., "Multiaxial Characterization of T800/3900-2 Carbon/Epoxy," Composite Science and Technology, 1992, Vol.43, pp.197-203.
- 3.9 Voloshin, A. and Arcan, M., "Failure of Unidirectional Fiber-reinforced Materials—New Methodology and Results," Experimental Mechanics, 1980, Vol.20, pp.280-284.
- 3.10 Shuart, M. J., "Failure of Compression-Loaded Multidirectional Composite Laminates," AIAA Journal, Vol. 27, 1989, pp.1274-1279.

4 Validation – Composite Material Strength Correlation Factors and Histogram

The complete listing of our histograms for each failure criteria is reported in this section. The data was collected, CF's were quantified, and figures are provided of the before and after resulting histograms to visually see performance of each failure theory. The presented CFs are based on 130 tests of either unidirectional ply or $[\pm \theta]$ laminates.

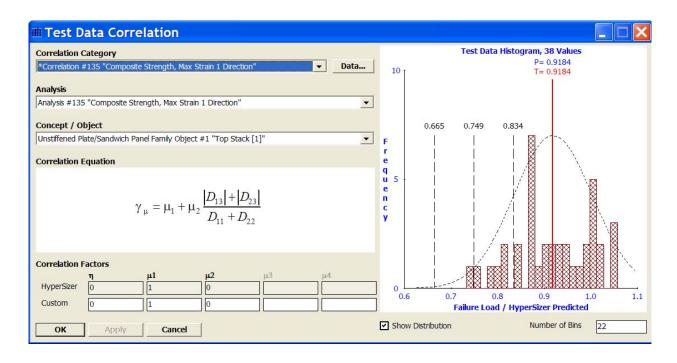
There are two primary references that should be reviewed.

- Vol 3, Ch 3: Validation Composite Material Strength Failure Envelopes of World Wide Failure Exercises (WWFE) Test Data and Other Published Data
- Vol 2, Ch 4: Correlation to Test: Composite Laminate Strength

The validation cases included in this chapter are from the World Wide Failure Exercises (WWFE), referred to as (cases 1, 2, and 3) and two additional failure envelope unidirectional cases (cases 8 and 9) from other publications, and a \pm 0 layup of AS4/3502 material (case 10) reported by] and described in detail in this section.

Failure of a laminate comprised of unidirectional or $[\pm \theta]$ layups occurs at first ply failure. Strength allowables presented here are based on damage initiation and not ultimate laminate strength which can be predicted using progressive failure techniques. The cases not included from WWFE involve progressive failure. Correlations to these progressive failure test data will come later. As a final point, the composite strengths are for pristine laminates, that is without damage. For an airframe design, damage tolerance and survivability allowables would be established and used as additional limiting strength requirements.

4.1 Summary of Composite Histograms Before and After Correlations



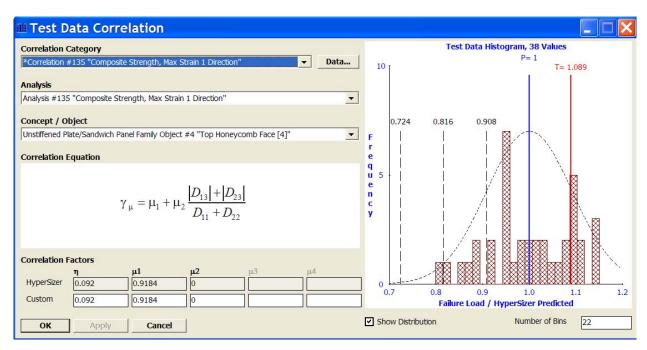
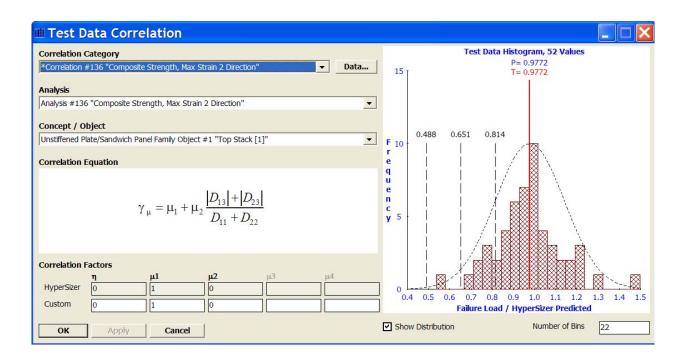


Fig. 4.1, Composite Strength, Max Strain 1 Direction.

Top image before correlation. Bottom image after correlation factors applied.



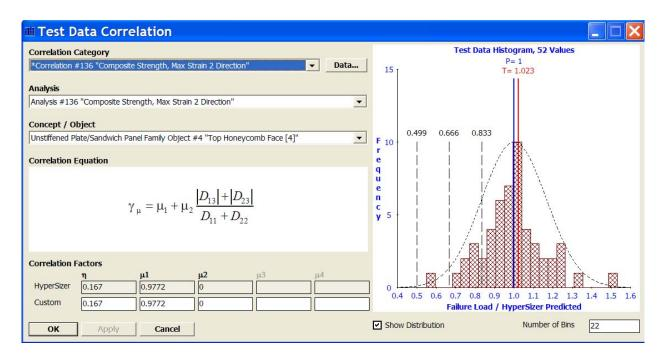
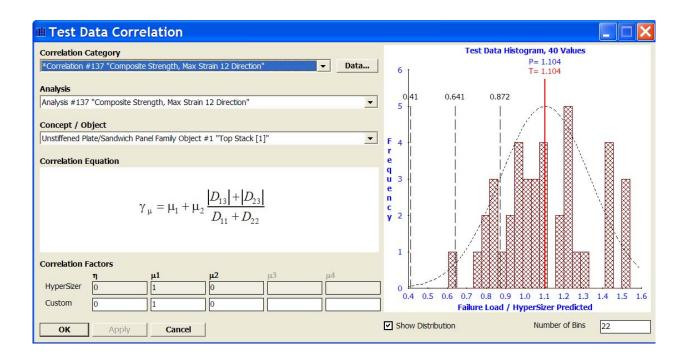


Fig. 4.2, Composite Strength, Max Strain 2 Direction.

Top image before correlation. Bottom image after correlation factors applied.



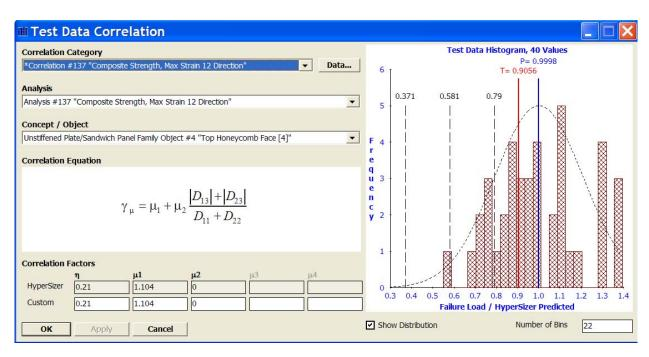
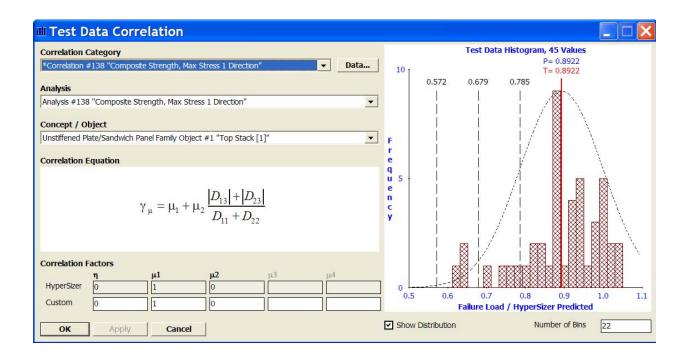


Fig. 4.3, Composite Strength, Max Strain 12 Direction.

Top image before correlation. Bottom image after correlation factors applied.



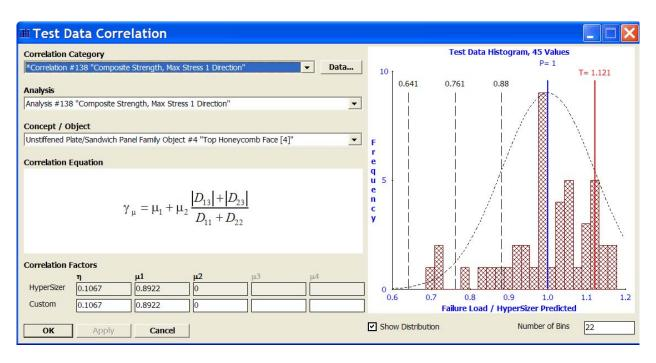
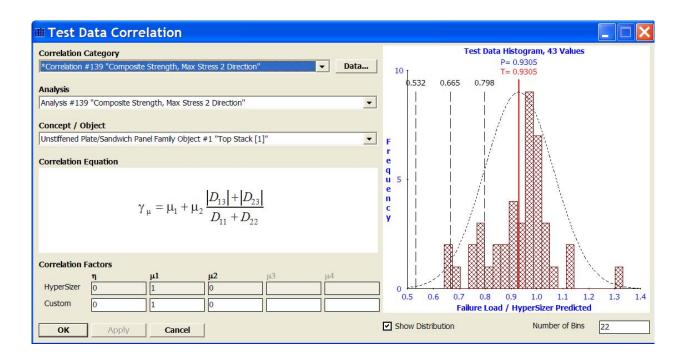


Fig. 4.4, Composite Strength, Max Stress 1 Direction.

Top image before correlation. Bottom image after correlation factors applied.



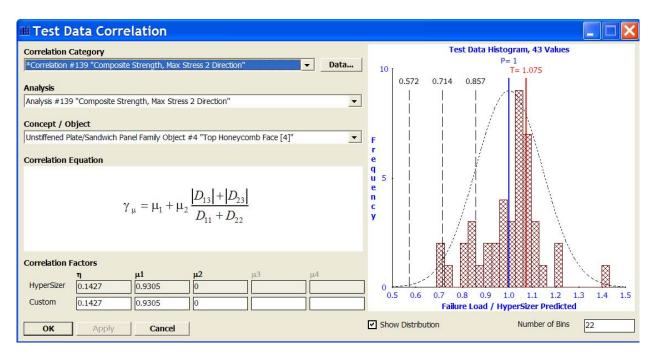
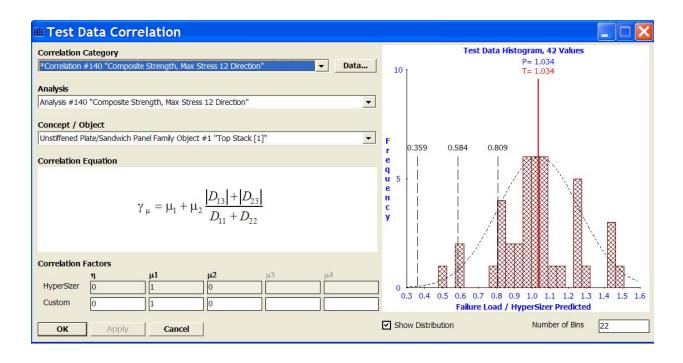


Fig. 4.5, Composite Strength, Max Stress 2 Direction.

Top image before correlation. Bottom image after correlation factors applied.



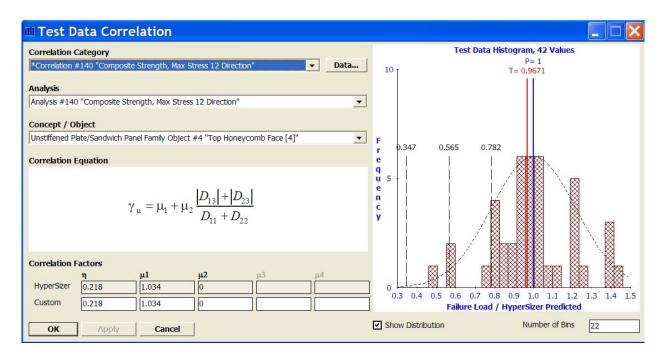
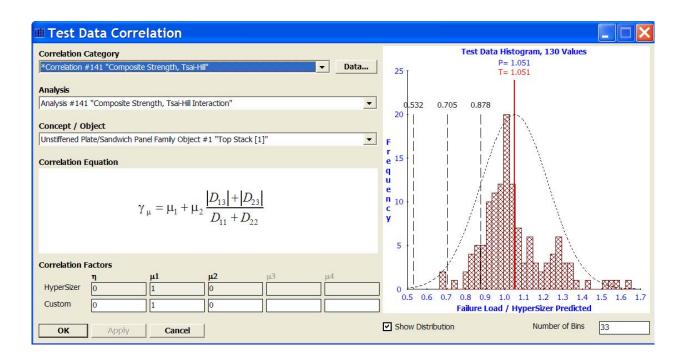


Fig. 4.6, Composite Strength, Max Stress 12 Direction.

Top image before correlation. Bottom image after correlation factors applied.



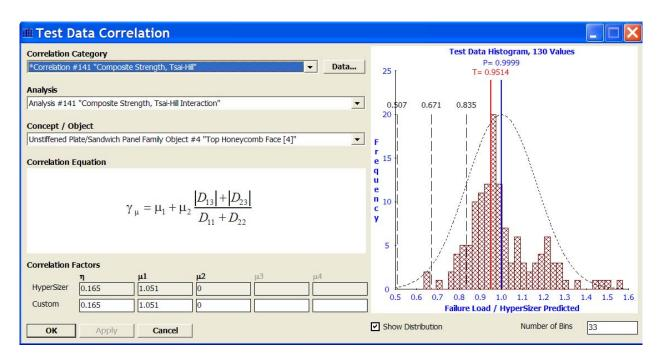
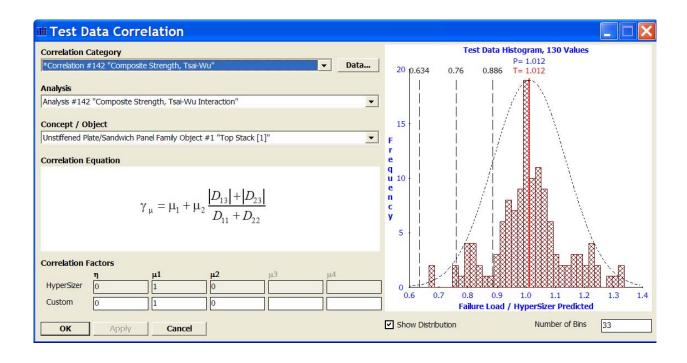


Fig. 4.7, Composite Strength, Tsai-Hill.

Top image before correlation. Bottom image after correlation factors applied.



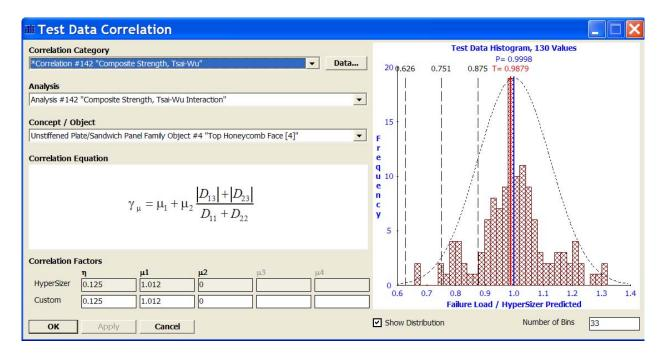
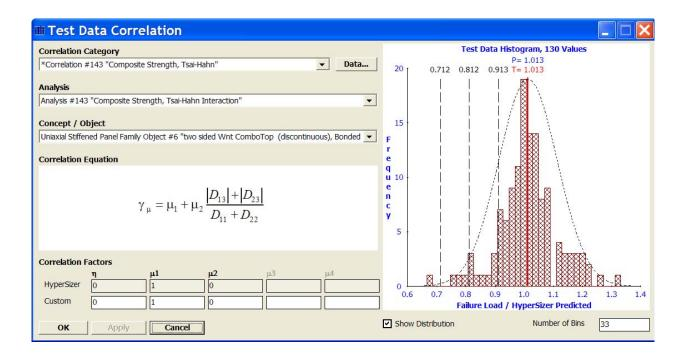


Fig. 4.8,, Composite Strength, Tsai-Wu.

Top image before correlation. Bottom image after correlation factors applied.



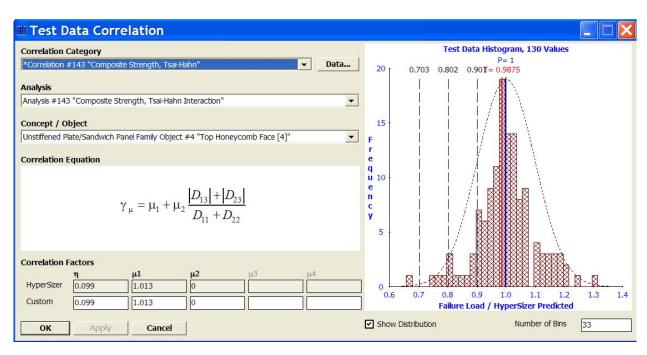
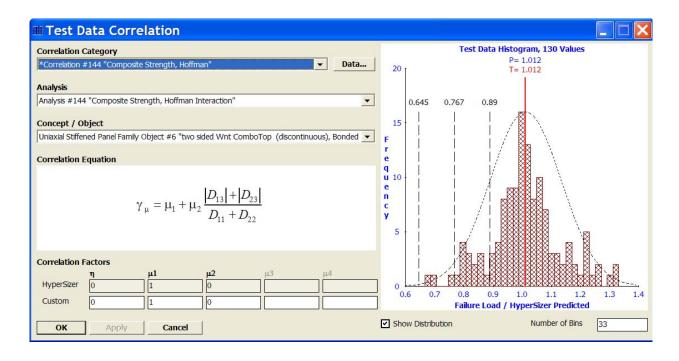


Fig. 4.9, Composite Strength, Tsai-Hahn.

Top image before correlation. Bottom image after correlation factors applied.



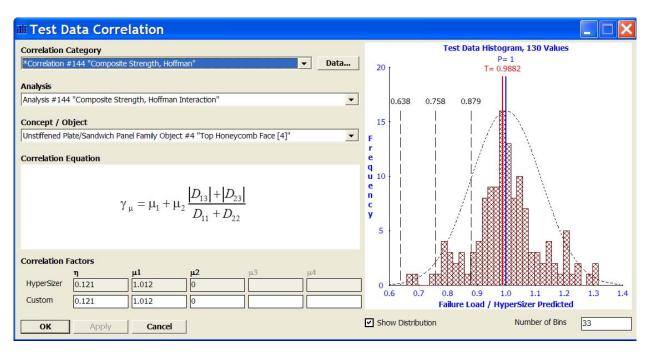
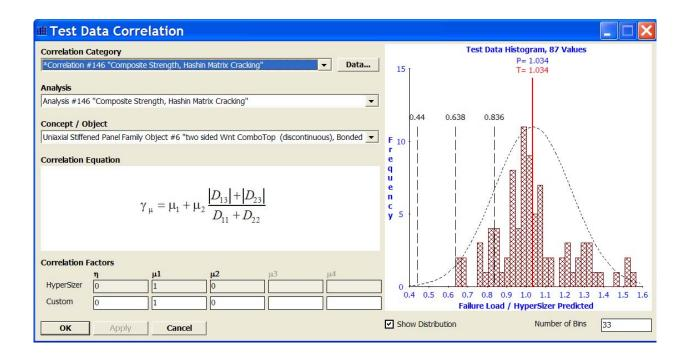


Fig. 4.10, Composite Strength, Hoffman.

Top image before correlation. Bottom image after correlation factors applied.



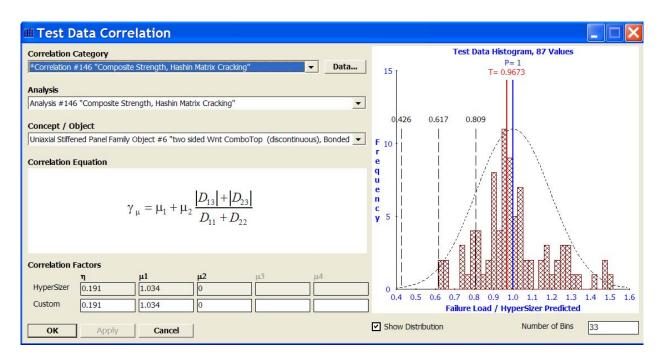
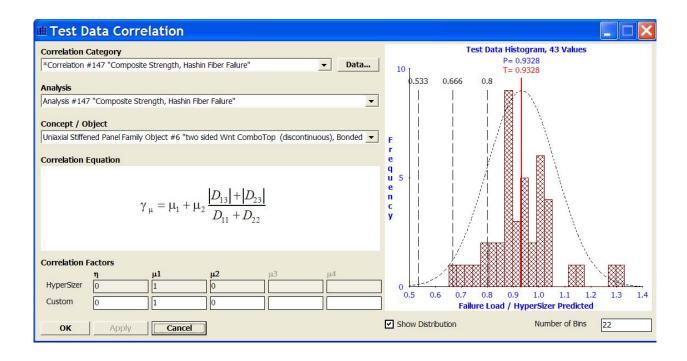


Fig. 4.11, Composite Strength, Hashin Matrix Cracking.

Top image before correlation. Bottom image after correlation factors applied.



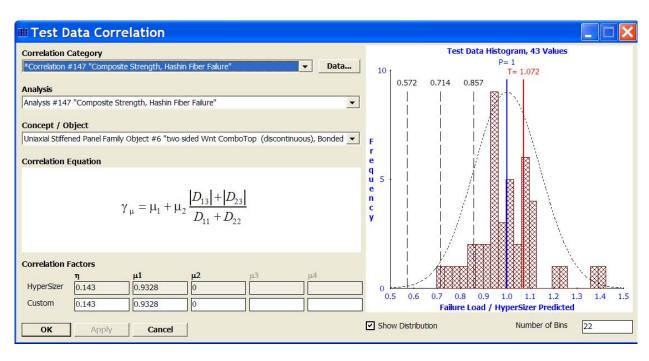
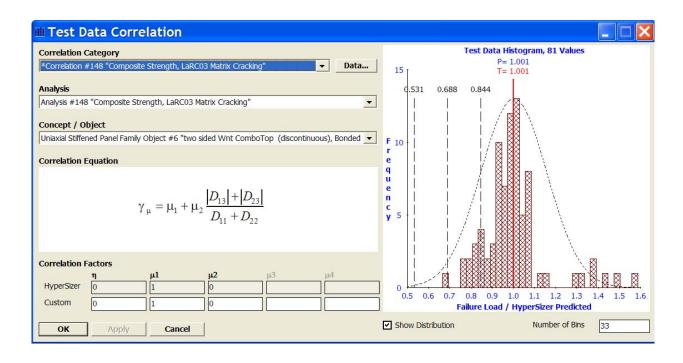


Fig. 4.12, Composite Strength, Hashin Fiber Failure.

Top image before correlation. Bottom image after correlation factors applied.



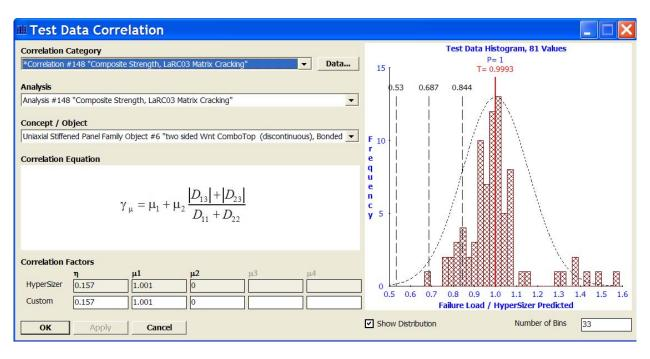
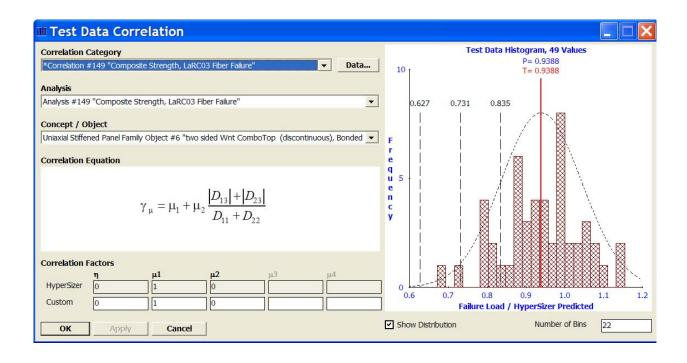


Fig. 4.13, Composite Strength, LaRC03 Matrix Cracking.

Top image before correlation. Bottom image after correlation factors applied.



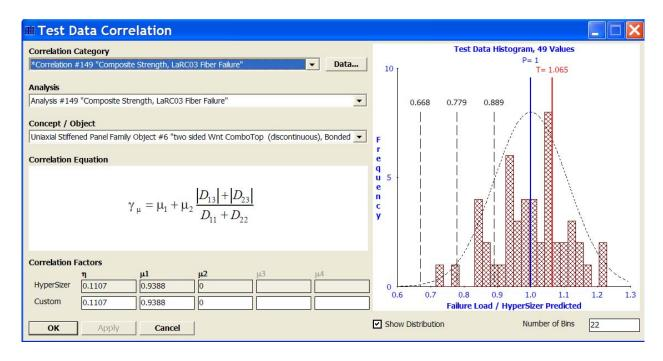


Fig. 4.14, Composite Strength, LaRC03 Fiber Failure.

Top image before correlation. Bottom image after correlation factors applied.

5 Validation - Cylindrical Panel Buckling Failure Test Data and CFs

Refer to Volume 2, Chapter 5 for many validation cases for panel buckling.

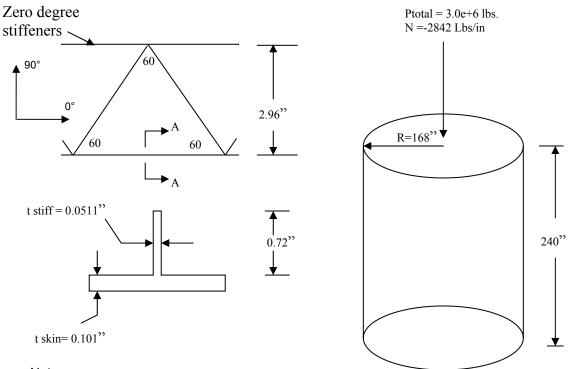
5.1 Verification Example: Cylindrical Buckling of a Grid-Stiffened Tank Wall

This section summarizes comparisons of cylindrical buckling analyses between HyperSizer and MSC/NASTRAN for a grid-stiffened curved tank wall. Six different cases are considered where stiffeners are on the inside or outside, together with combinations of stiffeners primarily oriented in axial stiffness, then in hoop stiffness. The buckling behavior of a stiffened panel is more complex than the unstiffened laminates and isotropic sheets that have been presented so far, however the cases still compare closely with the maximum difference being about 8%.

Workspace: Tank Isogrid RR3 cylindrical buckling - May02

Components: 2-13; Groups 2-3

Baseline Isogrid



Notes:

- Material is 2219 Aluminum.
- Both angled and zero degree stiffeners are the same thickness(0.0511").
- There are no 90 degree stiffeners.
- Zero degree stiffeners run in circumferential direction.
- Both top and bottom edges of cylinder are clamped.

Fig. 5.1, Problem statement for curved panel buckling comparison between HyperSizer with Raleigh Ritz and MSC/NASTRAN FEA.

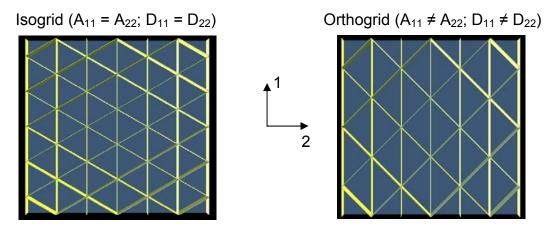


Fig. 5.2, The unit weight for the isogrid shown in the left figure is 2.044 (lb/ft2). Using the same dimensions for thickness gages and rib heights, the isogrid was converted to an orthogrid by changing the stiffener angle from 30° to 45°. The change in angle causes the panel to have a higher stiffness in one direction. This panel concept is 1.938 (lb/ft2), shown in the right figure.

Summary Results

Buckling Comparisons

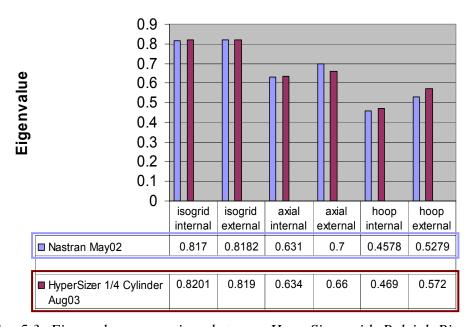


Fig. 5.3, Eigenvalue comparison between HyperSizer with Raleigh-Ritz and MSC/NASTRAN FEA. Comparisons are generally very good with the worst-case difference being about 8%, and for that case the FEA solution is suspect. Test cases include isogrid with internal and external stiffeners and orthogrid oriented both in the axial direction and the hoop direction for both internal and external stiffeners.

Observations:

- 1. HyperSizer buckling predictions match well the MSC/NASTRAN v 70.7.2 predictions.
- 2. It is difficult to achieve the correct buckling solution with the FEA because of boundary condition generality, and care must be exercised to achieve the desired response.
- 3. The isogrid has the same stiffness in the X(1) and Y(2) directions by definition.
- 4. The isogrid panel produces nearly the same buckling allowable regardless if the stiffeners are internal (inside) or external (outside) to the shell, for the given r=168. For smaller radius of curvatures a more substantial difference was demonstrated by analysis.
- 5. Four additional possibilities were investigated. These four are represented in the figures below starting from left to right: axial internal, axial external, hoop internal, hoop external.

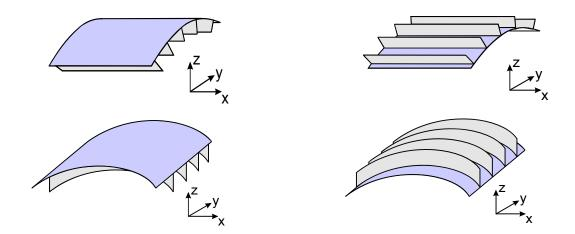
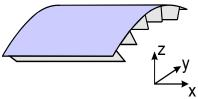


Fig. 5.4, Buckling results can change depending on whether the stiffeners are on the inside or outside of the curved panel and whether the stiffeners are aligned in the direction of the curvature or transverse to the curvature. The results show that for the isogrid panels the buckling results are nearly identical for all four of these options.

Note that the four pictures in figure 5.4 (and at the beginning of the following sections) are "representative" snapshots from the HyperSizer software and do not represent the exact panel type. They uniaxial stiffeners shown are meant to indicate the x direction. If the actual panel type used is isogrid, then the uniaxial stiffener shown corresponds to the 0° web of the isogrid panel.

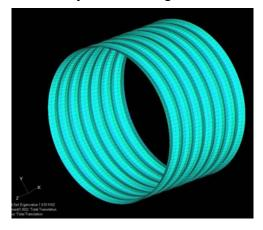
5.1.1.1 Case 1: Isogrid panel with stiffeners inside.

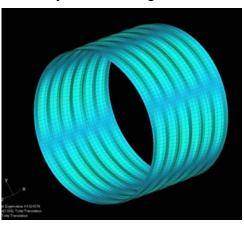
Since this was the first test case, a full cylindrical FEM was made and compared to the results obtained with a curved panel. The results indicate that all remaining investigations can be carried out with a portion of the cylinder modeled as a curved panel with a width equal to ½ the circumference.



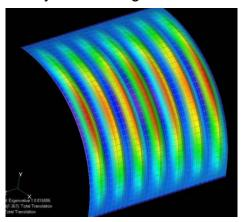
FEA Full Cylinder 1st Eigenvalue = 0.814

FEA Full Cylinder 2nd Eigenvalue = 0.824





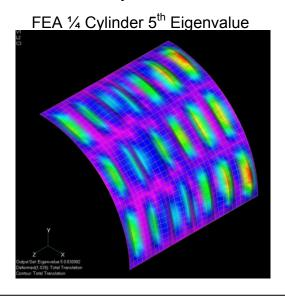
FEA 1/4 Cylinder 1st Eigenvalue = 0.817

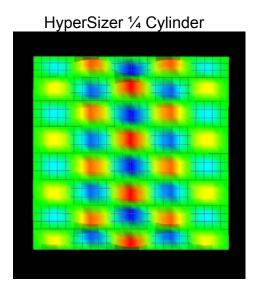


D11=D22, Stiffeners ISOGRID on inside.

The top two figures: The full cylinder Nastran 1^{st} eigenvalue = 0.814, Nastran 2^{nd} eigv = 0.824. Note that the 2^{nd} mode shape is about the same as the 1^{st} mode shape for the curved panel.

Bottom figure: Nastran curved panel 1^{st} eigv = 0.817. Axial = 13 buckling mode waves, hoop = 1 wave The FEA solution shows that there are actually many mode shapes that produce eigenvalues that are very close to each other. It is not surprising then that the actual number of mode shapes for the lowest eigenvalue predicted by the FEA may not exactly match the lowest mode shape predicted by HyperSizer. In the case shown below, the 5th eigenvalue is shown from the FEA which matches with the HyperSizer result relatively well. In this case the difference between the two solutions is only about 1%.





= 0.831.

D11=D22, Stiffeners ISOGRID on inside.

Bottom left figure: The curved panel 5th Nastran eigenvalue

Axial = 15 waves, hoop = 3 waves

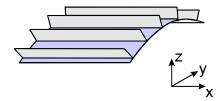
Bottom right figure: For a similar mode shape, the 1^{st} HyperSizer eigenvalue = .8201

Axial = 8 waves, hoop = 5 waves

It is more proper, however to compare the lowest eigenvalue from the HyperSizer solution (0.8201) to the lowest eigenvalue from the FEA solution (0.817) for a difference of ~4%. In all of the following results, as well as the summary results shown in Fig. 5.3, the comparisons shown are those between the lowest predicted eigenvalues from both HyperSizer and FEA, although, in most cases, the minimum energy mode shapes are not identical.

5.1.1.2 Case 2: Isogrid panel with stiffeners outside.

No pictures made, because the mode shapes were very similar to the mode shapes for the previous case of stiffeners on the inside.

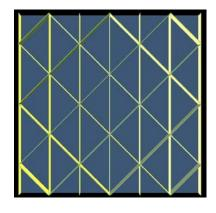


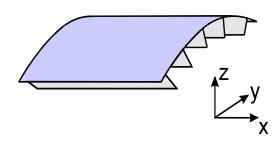
D11=D22, Stiffeners ISOGRID on outside.

Nastran eigv 1 = 0.8182

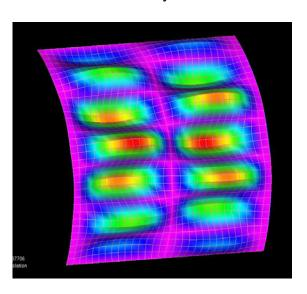
HyperSizer = 0.819

5.1.1.3 Case 3: Orthogrid panel with primary axial stiffeners inside.

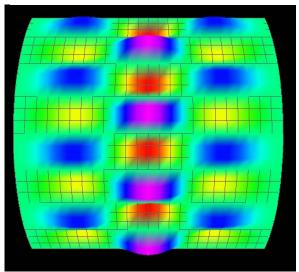




FEA 1/4 Cylinder



HyperSizer 1/4 Cylinder



Stiffeners primary in AXIAL on inside.

Bottom left figure: Nastran eigv <u>0.631</u> Axial = 2 waves, hoop = 7 waves

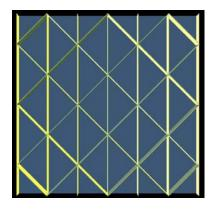
Bottom right figure: HyperSizer MS = -0.3661, Eigv = 0.634, 0.5%

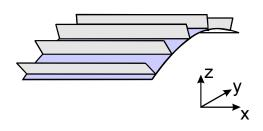
unconservative

Axial = 3 waves, hoop = 8 waves

Displayed the second mode from Nastran, nearly same eigv as the first mode.

5.1.1.4 Case 4: Orthogrid panel with primary axial stiffeners outside.





FEA 1/4 Cylinder

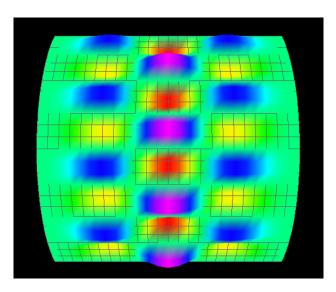
2

Output Set Eignewals 18 700189

Deformed(1.81) Total Translation

Contour Total Translation

HyperSizer 1/4 Cylinder



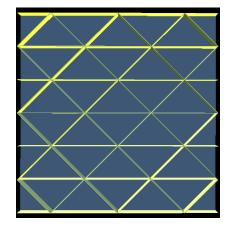
Stiffeners primary in AXIAL on outside.

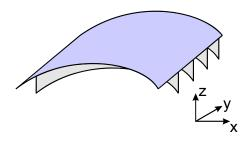
Bottom left figure: Nastran eigv <u>0.7000</u> Axial = 2 waves, hoop = 7 waves

Bottom right figure: HyperSizer MS = -0.3401, Eigv = 0.660, Axial = 3 waves, hoop = 8 waves

6.0% conservative, HyperSizer found a lower energy mode shape, with three waves in the axial direction, instead of the two waves as determined by the FEA

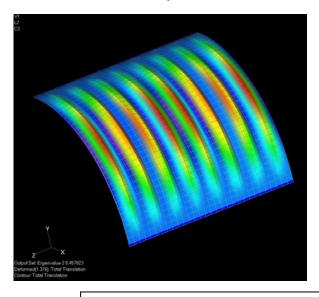
5.1.1.5 Case 5: Orthogrid panel with primary hoop stiffeners inside.

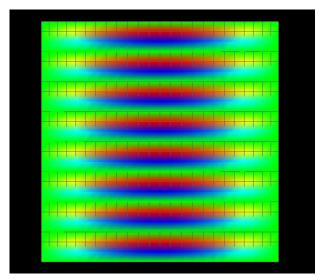




FEA 1/4 Cylinder

HyperSizer ½ Cylinder





Stiffeners primary in hoop on inside.

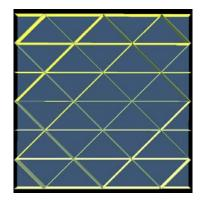
Bottom left figure: Nastran eigv 0.4578, Axial = 15 waves, hoop = 1 wave

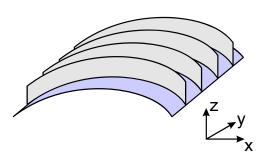
Aug 03 Update: HyperSizer MS = -0.531, Eigv = $\underline{0.469}$

Axial = 16 waves, hoop = 1 wave

2.4% unconservative

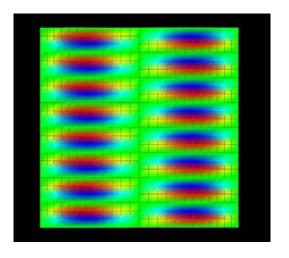
5.1.1.6 Case 6: Orthogrid panel with primary hoop stiffeners outside.





FEA 1/4 Cylinder

HyperSizer 1/4 Cylinder



Stiffeners primary in hoop on outside.

Bottom left figure: Nastran eigv $1 = \underline{0.5279}$ Axial = 16 waves, hoop = 1 wave

Aug 03 Update: HyperSizer MS = -0.4279, Eigv = 0.5721

Axial = 16 waves, hoop = 2 wave

8.4% unconservative. It appears the NASTRAN FEM was too coarse to pick up the modes shapes properly. See in the top figure on left how the buckling modes are less than the typical minimum required of 5 elements.

6 Verification - Bonded Joint Homogenous Isotropic and Orthotropic Delale & Erdogan Publication (Six Examples)

6.1 Introduction and Summary

The following verification examples are based on a classical series of examples presented by Delale et. al. [6.1] which compared a plate theory based solution to a series of FEA solutions. Delale et. al. presented results both for a stiffened plate (or bonded doubler) and for a single lap joint. The BondJo comparisons presented in this section concentrate only on the stiffened plate results.

Six material-load case combinations are given and the results compared with those of [6.1] and with a solid model FEA. The results obtained show very good consistency and accuracy with inplane and interlaminar shear stresses along the bondline and through the thickness of adherends. Some discrepancies were seen in the results for peel stress. BondJo generally predicts higher peek stresses than those of the FEA. When transverse shear deformation in the FEA was eliminated, the results between BondJo and FEA results match closer, presumably due to BondJo's assumption of classical lamination theory in the adherends (which does not include out-of-plane shear deformation). In future BondJo development, transverse shear deformation in the adherends will be included in the analysis.

6.2 Problem Definition

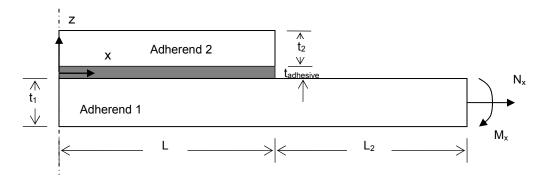


Fig. 6.2.1, Solution domain of stiffened plate (bonded doubler).

Six conditions were identified and analyzed with BondJo as shown in the following table. Conditions 1 and 2 use a unidirectional orthotropic Boron-Epoxy composite for adherend 2, while conditions 3 and 4 use Aluminum for adherend 2. Conditions 5 and 6 use the same materials and geometry as cases 1 and 3 respectively, however the boundary conditions were changed to approximate those that would be seen by an in-service panel. (See Volume 2, Section 6.2 for discussion of panel in-service boundary conditions).

Table 6.2.1, Six material-load case verifications

	Adherend 1	Adherend 1	Applied Loading	Boundary Conditions
1	Aluminum	Boron Epoxy	Tensile	Test Article
2	Aluminum	Boron Epoxy	Moment	Test Article
3	Aluminum	Aluminum	Tensile	Test Article
4	Aluminum	Aluminum	Moment	Test Article
5	Aluminum	Boron Epoxy	Tensile	In-Service panel
6	Aluminum	Aluminum	Tensile	In-Service Panel

The geometry, boundary conditions and material properties are shown in the following tables.

Table 6.2.2, Geometry and Boundary Conditions for Aluminum-Boron Epoxy Problems (1, 2, 5)

Dimensions		Materials	Loading and Boundary Conditions:
SI $L = 25.4 \text{ mm}$ $L_2 = 30 \text{ mm} *$ $t_1 = 2.29 \text{ mm}$ $t_2 = 0.762 \text{ mm}$ $t_{adhesive} =$ 0.1016 mm *not be defined in the paper	English L = 1.0 in. L ₂ = 1.181 in.* $t_1 = 0.09$ in. $t_2 = 0.03$ in. $t_{adhesive} = 0.004$ in.	Adherend 1: Aluminum Adherend 2: Boron/epoxy Adhesive: epoxy	Left Face (symmetry): Latest as specified by $u_0 = w = \beta_x = v = 0$ Right Face: 1. $N_{xx} = 1N/mm$; $Q_x = N_{xy} = 0$; $M_x = 0$; 2. $N_{xx} = 0$; $Q_x = N_{xy} = 0$; $M_x = 1$ (N.mm)/mm; Note: $1N/mm = 5.71$ lb/in. 1 N.mm /mm = 0.2248 (lb.in)/in.

Table 6.2.3, Geometry and Boundary Conditions for Aluminum-Aluminum Problems (3, 4, 6)

Dimensions:		Materials	Loading and Boundary Conditions:
$SI \\ L = 12.7 \text{ mm} \\ L_2 = 12.7 \text{ mm} \\ t_1 = 1.524 \text{ mm} \\ t_2 = 0.762 \text{ mm} \\ t_{adhesive} = \\ 0.1016 \text{ mm}$	English $L = 0.5 \text{ in.}$ $L_2 = 0.5 \text{ in.}$ $t_1 = 0.06 \text{ in.}$ $t_2 = 0.03 \text{ in.}$ $t_{adhesive} = 0.004$ in.	Adherend 1: aluminum Adherend 2: aluminum Adhesive: epoxy	Left Face (symmetry): Latest as specified by $u_0 = w = \beta_x = \nu = 0$ Right Face: 1. $N_{xx} = 1N/mm$; $Q_x = N_{xy} = 0$; $M_x = 0$; 2. $N_{xx} = 0$; $Q_x = N_{xy} = 0$; $M_x = 1$ (N.mm) /mm; Note: $1N/mm = 5.71$ lb/in. 1 N.mm /mm = 0.2248 (lb.in)/in.

Table 6.2.4, Material Properties

Aluminum		Boron/epoxy		Epoxy Adhesive		
				(assumed linear, elastic)		
SI	English	SI	English	SI	English	
$E_1 = E_2 = E_3 =$	$E_1 = E_2 = E_3 =$	$E_1 = 223.4$ GPa	$E_1 = 32.4 \text{ Msi}$	E = 3.068 GPa	E = 0.445 Msi	
68.95 GPa	10 Msi	$E_2 = E_3 = 24.13$	$E_2 = E_3 = 3.5$	G=1.138 GPa	G = 0.165 Msi	
$v_{12} = v_{13} = v_{23}$	$v_{12} = v_{13} = v_{23}$	GPa	Msi	v=0.348	v=0.348	
= 0.3	= 0.3	$v_{12} = 0.23$	$v_{12} = 0.23$			
		G_{12} =8.481 GPa	$G_{12} = 1.23 \text{ Msi}$			

6.3 Comparison to Finite Element Analysis and Published Results

In addition to comparisons between BondJo and results from the Delale and Erdogan publication, a 3D linear finite element model was constructed using the commercial finite element package ANSYS and used for further verification. The solution domain of FE models are based on the joint configuration, shown in Fig. 6.2.1, while the width (y-direction) of the joint is taken as 0.739 mm. 37312 eight-noded anisotropic solid elements (SOLID64) are used. Mesh density along the longitudinal direction gradually increases toward the adhesive leading edge from both symmetric plane and right end. The adhesive layer is modeled using 4 layers of elements to capture the through-the-thickness gradient of peel and shear stresses. To obtain accurate solution for out-of-plane (interlaminar) stresses in the adherends, 24 layers of elements are used in the through-the-thickness direction. Fig. 6.3.1 shows the 3D finite element meshes for the whole bonded doubler and details at the adhesive leading edge. The boundary conditions at the symmetric plane (y=0) is $u_y = 0$ and $u_z = 0$ at point A, as shown in Fig. 6.3.1. The front and back planes are constraint in x-direction, i.e. $u_x = 0$. The boundary conditions at right end of plate vary according to different problems, which are listed in Tables 6.2.2 and 6.2.3.

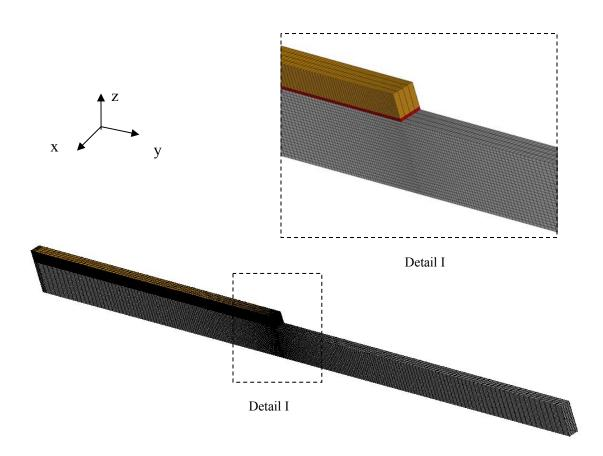


Fig. 6.3.1, Ansys 3D solid finite element model developed for verification of BondJo.

6.3.1 Condition 1 - Aluminum-BrEp Tensile Load

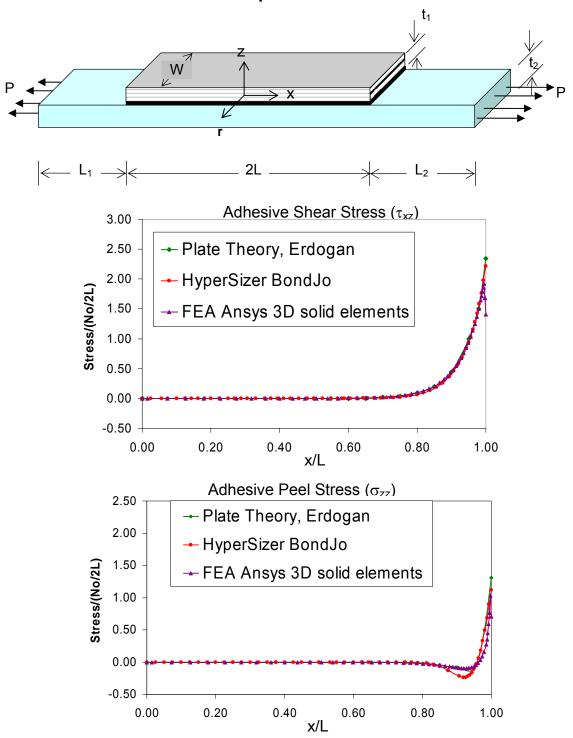


Fig. 6.3.2, Adhesive stress comparisons between BondJo, Ansys solid model FEA and Delale and Erdogan plate theory show good agreement between the codes for adhesive shear but some differences in peel stress in the stress reversal "trough" region. The analytical methods generally predict higher peak stresses at the singularity than those of the FEA.

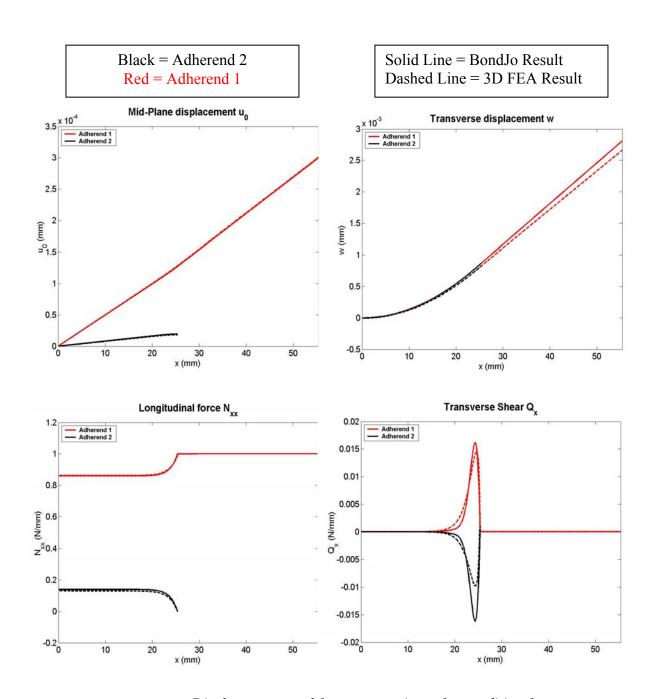


Fig. 6.3.3, Displacements and force comparisons for condition 1.

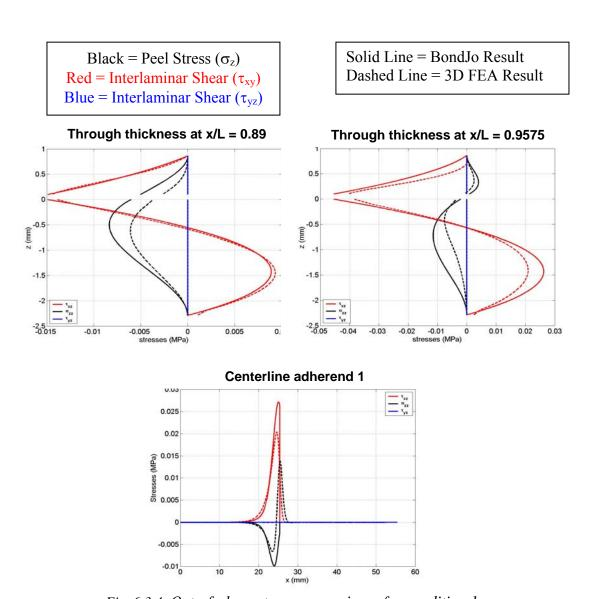
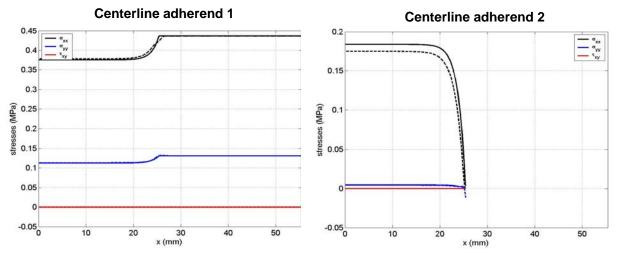


Fig. 6.3.4, Out-of-plane stress comparisons for condition 1.





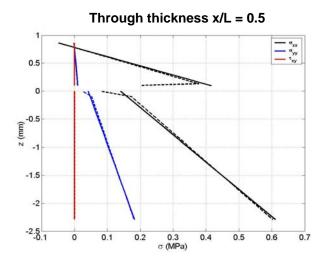


Fig. 6.3.5, In-plane stress comparisons for condition 1.

6.3.2 Condition 2 – Aluminum-BrEp Applied Moment

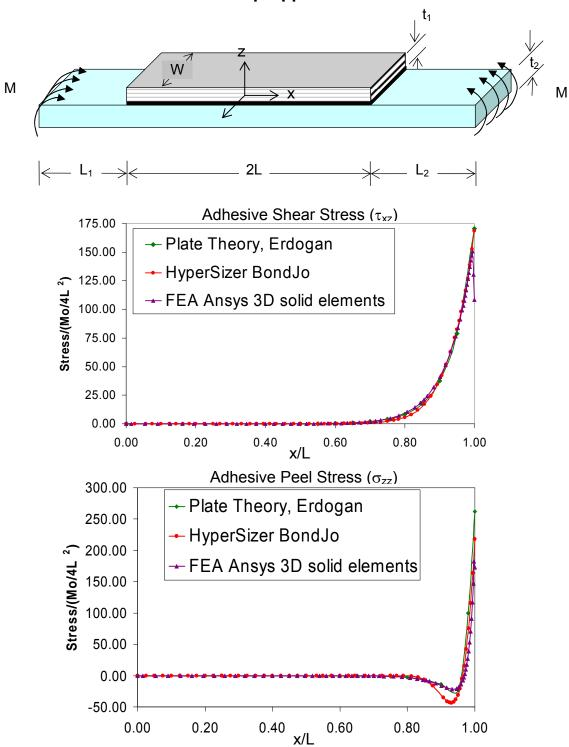


Fig. 6.3.6, Adhesive stress comparisons between BondJo, Ansys solid model FEA and Delale and Erdogan plate theory show good agreement between the codes for adhesive shear but some differences in peel stress in the stress reversal "trough" region. The analytical methods generally predict higher peak stresses at the singularity than those of the FEA.

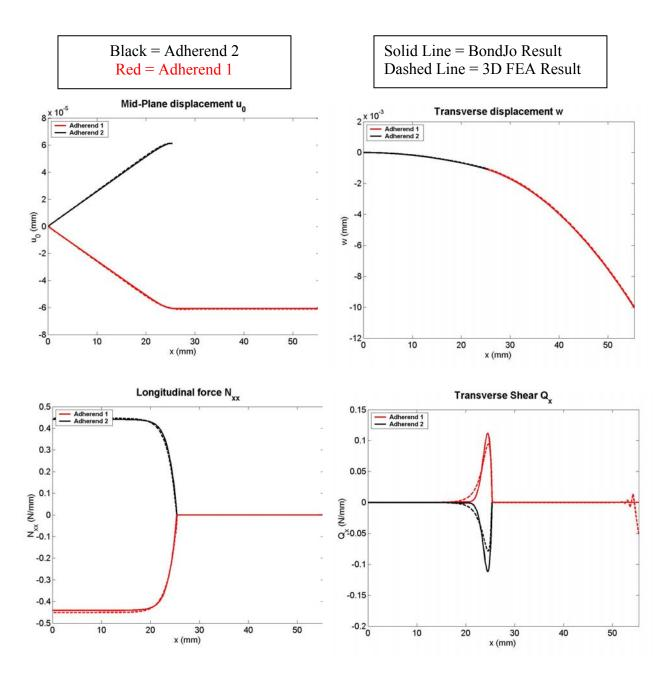
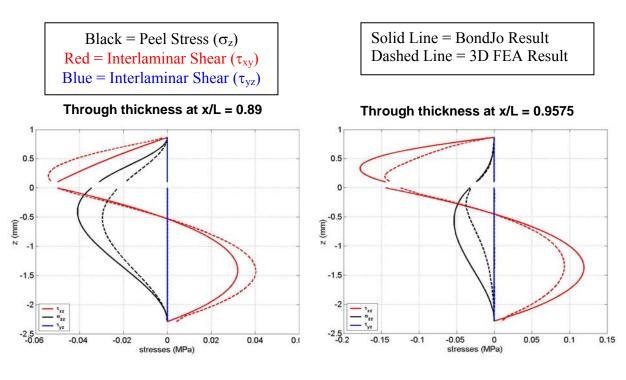


Fig. 6.3.7, Displacements and force comparisons for condition 2.



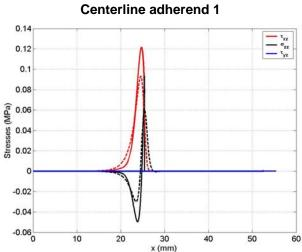
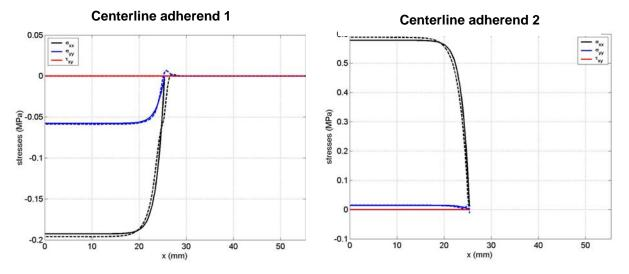


Fig. 6.3.8, Out-of-plane stress comparisons for condition 2.





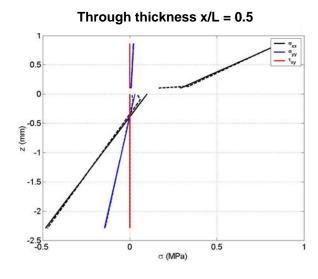


Fig. 6.3.9, In-Plane stress comparisons for condition 2.

6.3.3 Condition 3 – Aluminum-Aluminum Tensile Load

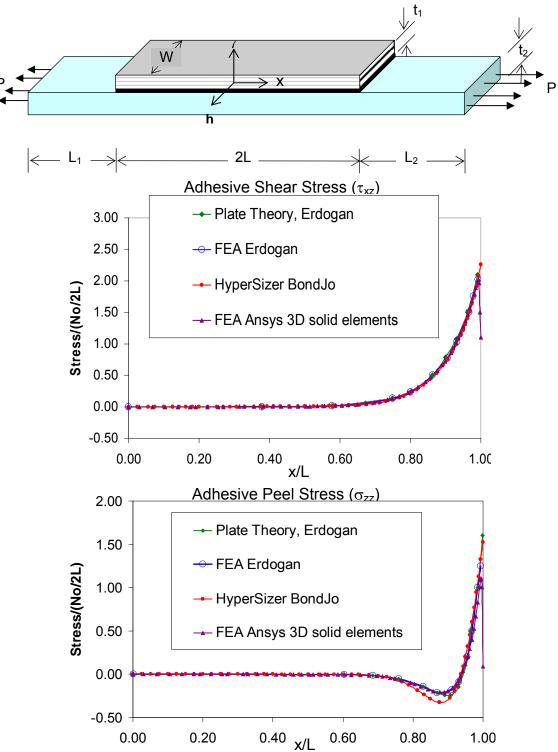


Fig. 6.3.10, Adhesive stress comparisons between BondJo, Ansys solid model FEA and Delale and Erdogan plate theory show good agreement between the codes for adhesive shear but some differences in peel stress in the stress reversal "trough" region. The analytical methods generally predict higher peak stresses at the singularity than those of the FEA.

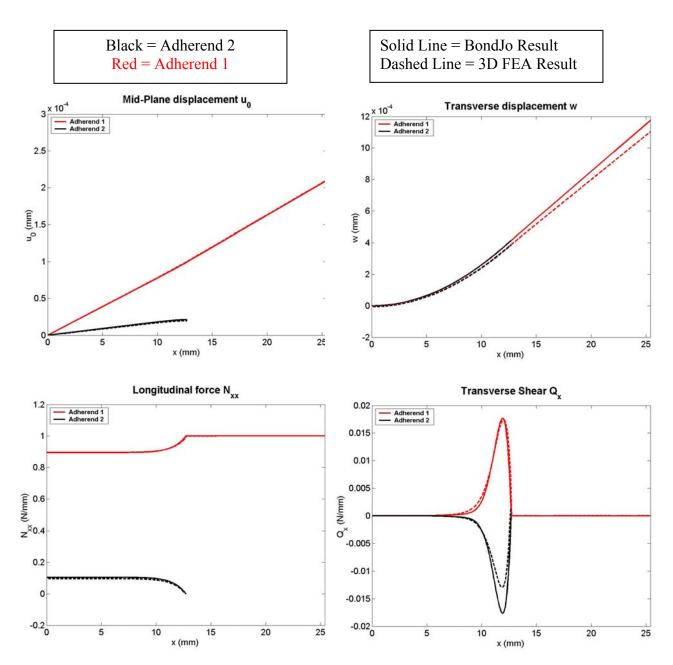
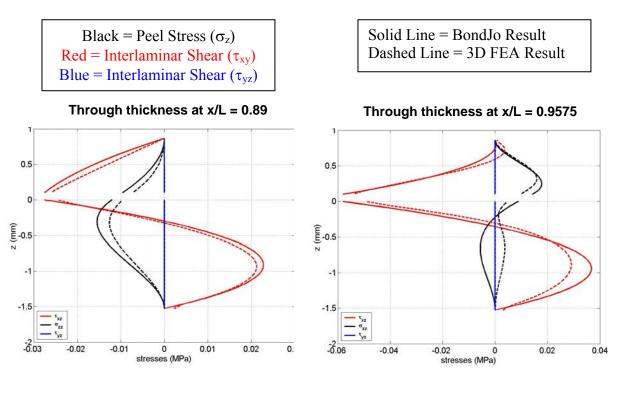


Fig. 6.3.11, Displacements and force comparisons for condition 3.



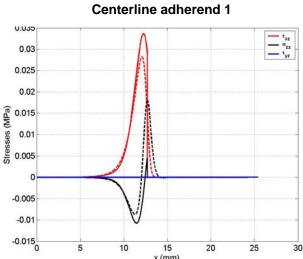


Fig. 6.3.12, Out-of-plane stress comparisons for condition 3.

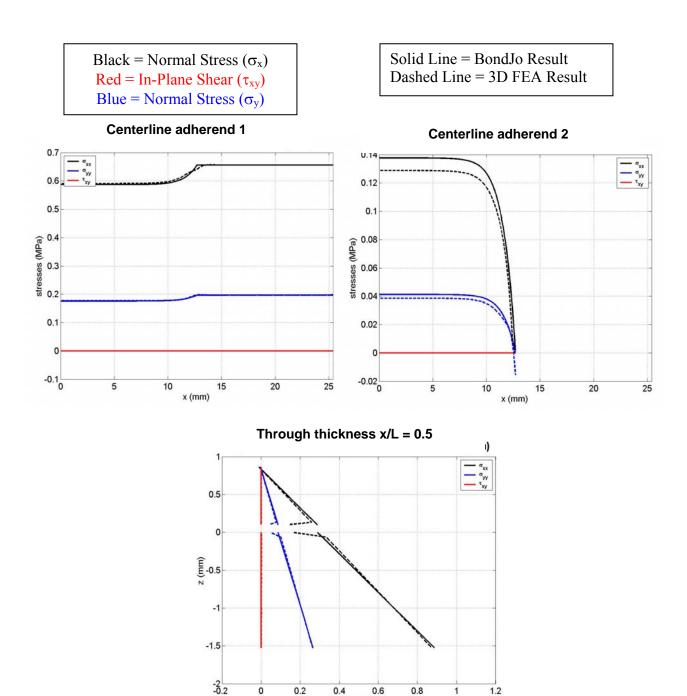


Fig. 6.3.13, In-plane stress comparisons for condition 3.

0.2

0

0.4 0.6 σ (MPa)

0.8

1.2

6.3.4 Condition 4 - Aluminum-Aluminum Applied Moment

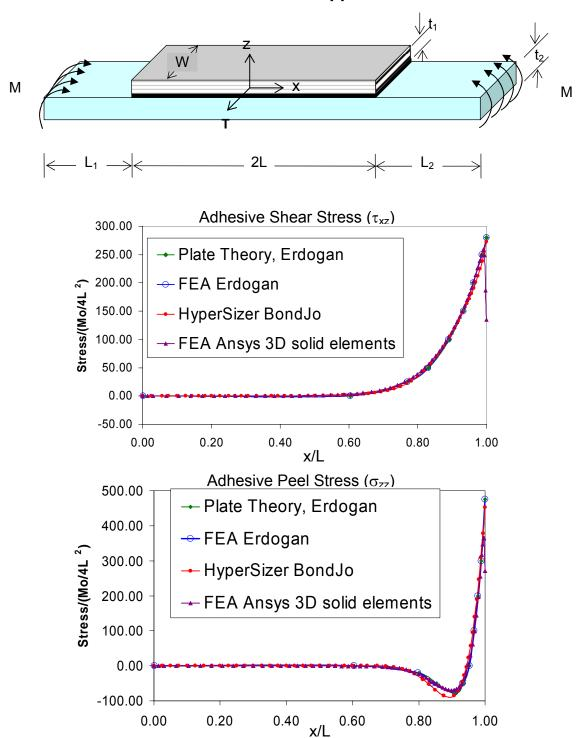


Fig. 6.3.14, Adhesive stress comparisons between BondJo, Ansys solid model FEA and Delale and Erdogan plate theory show good agreement between the codes for adhesive shear but some differences in peel stress in the stress reversal "trough" region. The analytical methods generally predict higher peak stresses at the singularity than those of the FEA.

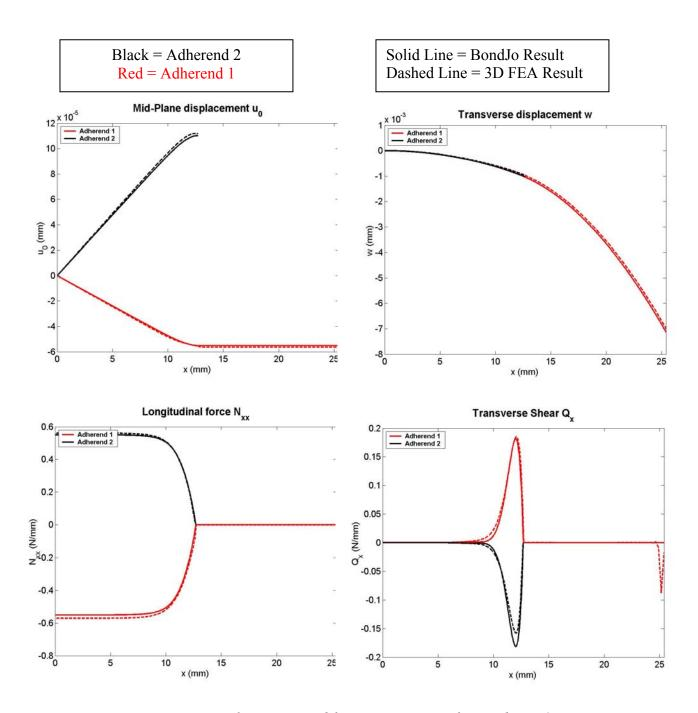
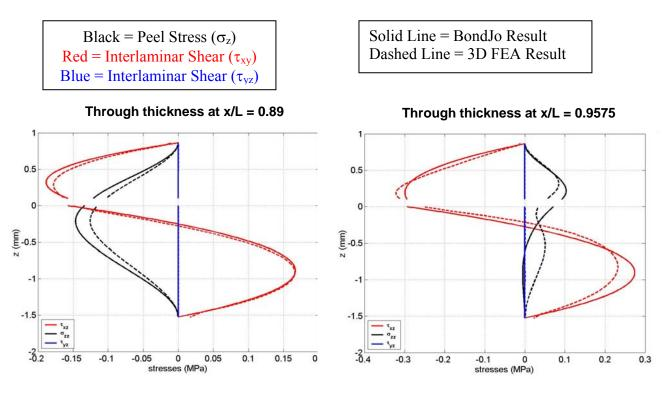


Fig. 6.3.15, Displacements and force comparisons for condition 4.



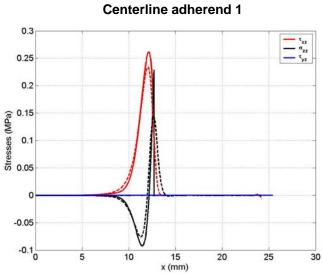
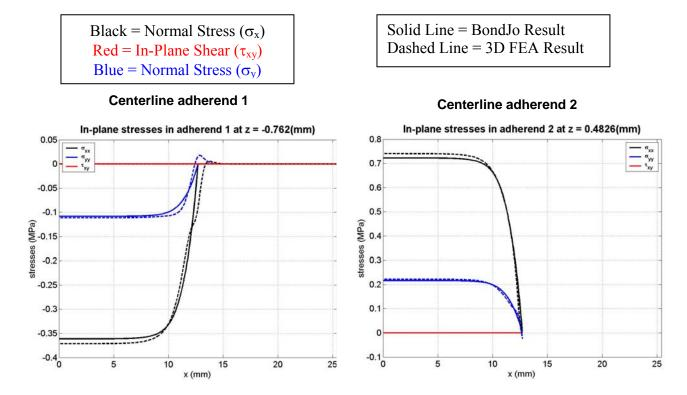


Fig. 6.3.16, Out-of-plane stress comparisons for condition 4.





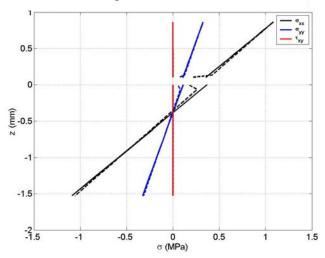


Fig. 6.3.17, In-plane stress comparisons for condition 4.

6.3.5 Condition 5 - Aluminum-BrEp In-Service Panel

The following results are presented for the case where the materials and plate dimensions are the same as those presented by Delale and Erdogan, however the boundary conditions have been changed to those that approximate a continuous in-service panel. This boundary condition case, for which BondJo was designed, shows very close agreemend between BondJo and FEA.

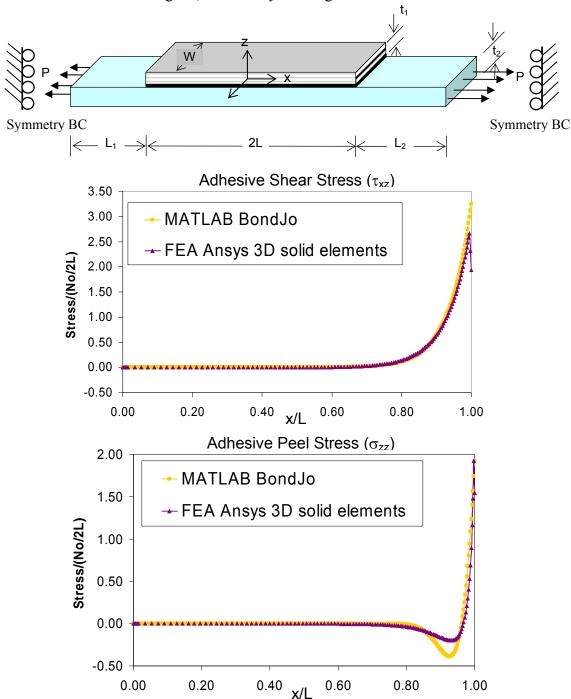


Fig. 6.3.18, Adhesive stress comparisons between BondJo and Ansys solid model FEA show good agreement between the codes for adhesive shear but some differences in peel stress in the stress reversal "trough" region. BondJo generally predicts higher peak stresses at the singularity than those of the FEA.

6.3.6 Condition 6 – Aluminum-Aluminum In-Service Panel

The following results are presented for the case where the materials and plate dimensions are the same as those presented by Delale and Erdogan, however the boundary conditions have been changed to those that approximate a continuous in-service panel. This boundary condition case, for which BondJo was designed, shows very close agreemend between BondJo and FEA.

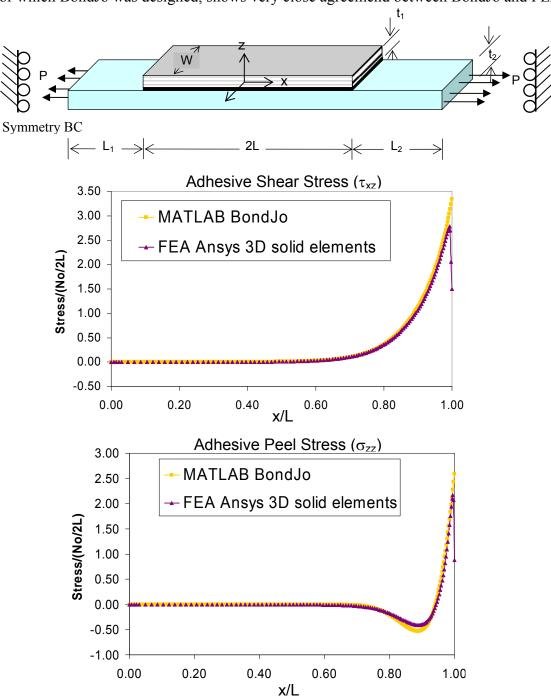


Fig. 6.3.19, Adhesive stress comparisons between BondJo and Ansys solid model FEA show good agreement between the codes for adhesive shear but some differences in peel stress in the stress reversal "trough" region. BondJo generally predicts higher peak stresses at the singularity than those of the FEA.

6.4 Effect of Eliminating Transverse Shear Deformation in the FEA

The CLT assumption employed by BondJo does not account for the shear deformation in either adherend, however this effect is included in the finite element model. As we also see that the out-of-plane stresses calculated by BondJo still have some discrepancy with FE results. This may be due to effects of transverse shear of adherends. To test this theory, the above FEMs were reanalyzed with reduced transverse shear deformation of the adherends. The transverse shear moduli, G_{yz} and G_{xz} of the adherends were increased by a factor of 100, thus the adherends become much stiffer in transverse shear. The results obtained from modified FE models then show a much better match with BondJo. The results are plotted for each case in the followings, particulary for out-of-plane stresses.

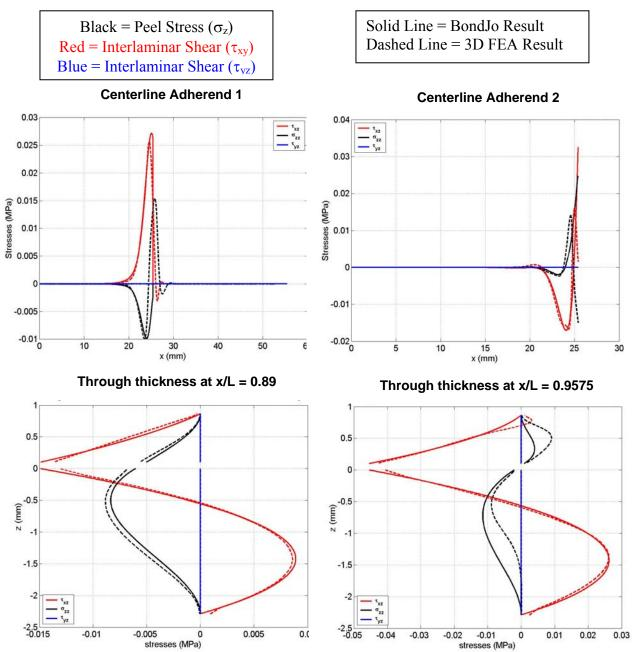


Fig. 6.4.1, Alum-BrEp applied force (condition 1) comparisons between BondJo and Ansys solid model FEA where transverse shear deformation has been disallowed in the FEA.

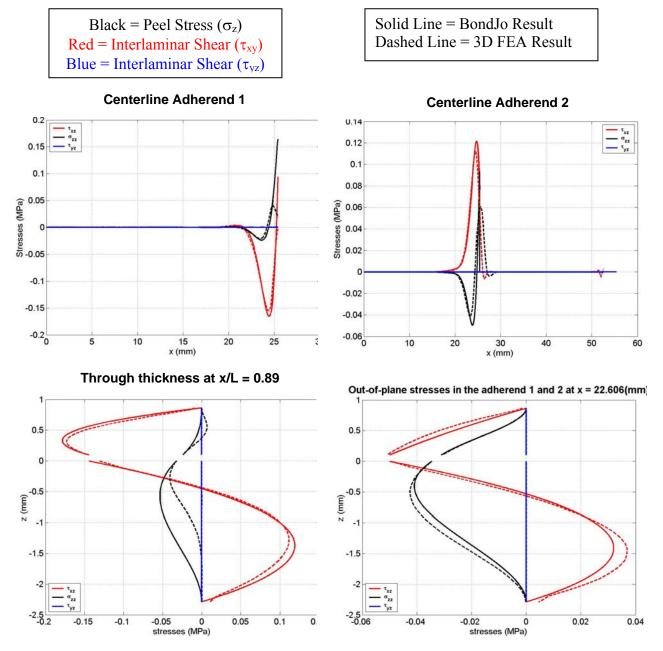


Fig. 6.4.2, Alum-BrEp applied moment (condition 2) comparisons between BondJo and Ansys solid model FEA where transverse shear deformation has been disallowed in the FEA.

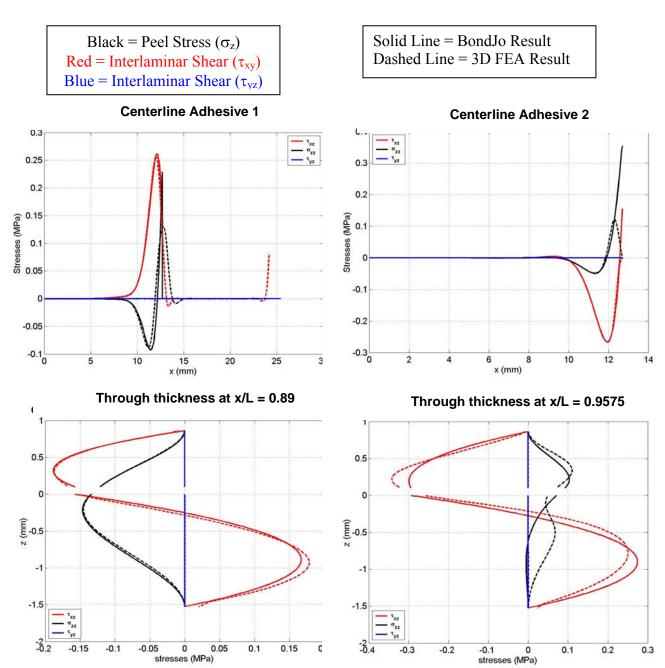


Fig. 6.4.3, Alum-Alum applied moment (condition 4) comparisons between BondJo and Ansys solid model FEA where transverse shear deformation has been disallowed in the FEA.

6.5 References

6.1 F. Delale, F., Erdogan, M. N., Aydinoglu, (1981), "Stress in Adhesively Bonded Joints: A Closed – Form solution," J. composite Materials, 15, pp 249.

7 Verification - Bonded Joint [0/±45/90] Laminate Stresscheck FEA

7.1 Introduction and Summary

In this verification example, laminated, composite joint results from HyperSizer-BondJo are compared with those from the p-based finite element analysis code, Stresscheck. The problem chosen is complex enough to test out all of the features of the software. Because the adherends are laminates, finding the through-the-thickness stress distribution requires explicit modeling of each ply in the finite element model.

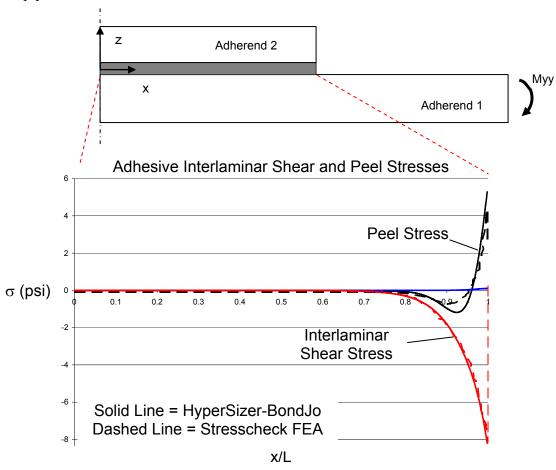


Fig.7.2, Sample comparison between HyperSizer-BondJo and Stresscheck for adhesive interlaminar shear and peel stresses along the bondline.

In the first verification attempts, the FEM was built in-house using the commercial FEA analysis package, ANSYS. After many weeks of effort to obtain good solutions from this model, this effort was abandoned. It was never determined whether problems with obtaining good results were related to limitations with ANSYS, mesh refinement, or simply our inexperience with this type of laminated solid element model. Our company contains no experts in solid FEA modeling, however in talking with others in industry, we determined that perhaps ANSYS was not the tool of choice for this type of problem. Two FEA packages have emerged as leaders for this type of detailed analysis, Abaqus and Stresscheck.

Using Stresscheck, with the help of Lockheed Martin, a robust verification model for comparison with HyperSizer-BondJo was built and analyzed. The comparison results between the two codes are very encouraging, although not identical. For the chosen boundary conditions, which were those of an in-service stiffened panel (see Volume 2, Section 6.2), predicted displacements in all directions (u, v, w) and in-plane stresses $(\sigma_x, \sigma_y, \tau_{xy})$ throughout the joints were virtually identical.

Out-of-plane stresses (σ_z , τ_{yz} , τ_{xz}) between the codes match well in the adhesive layer and through the thickness of the laminates in many locations, however in some of the through-thickness plots the results can vary substantially. The location where the results do not match, however, is not in the region of the critical stress locations, and is also thought to be a "worst case" location, not representative of the entire joint. In future work, comparisons will be made in more appropriate locations that represents the critical stresses used for failure prediction.

7.2 Problem Definition

7.2.1 Physical Dimensions and Material Properties

Note: FEA comparison results and problem definitions assume the typical academic sign convention. See Section Volume 2, Section 6.11 for details.

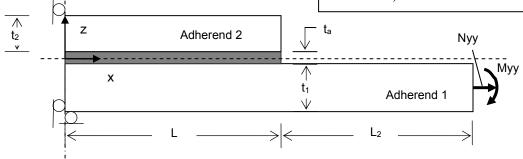


Fig.7.2.1, Configuration of bonded doubler joint for analysis.

Table 7.2.1, Geometry, materials and B.C of stiffened plate example 1

Dimensions		Layups	Loading and Boundary Conditions:	
SI Units $L = 25.4 \text{ mm}$ $L_2 = 30 \text{ mm} *$ $t_1 = 2.29 \text{ mm}$ $t_2 = 0.762 \text{ mm}$ $t_a = 0.1016 \text{ mm}$	English L = 1.0 in. L ₂ = 1.181 in.* $t_1 = 0.09$ in. $t_2 = 0.03$ in. $t_a = 0.004$ in.	Adherend 1: Boron/epoxy [45/-45/0/90/0/90/45/- 45/0] _s , 18 plies Adherend 2: Boron/epoxy [0/90/45/-45/90/0], 6 plies Adhesive: epoxy	Left Face (symmetry): Latest as specified by $u_0 = w = \beta_x = \nu_0 = 0$ Right Face: Case 1. $N_x = 5.71 \text{ lb/in (SI: } 1 \text{ N/mm})$ $Q_x = N_{xy} = M_x = 0$; Case 2. $M_x = 0.2248 \text{ lb-in/in}$ $Q_x = N_{xy} = N_x = 0$; Note: $1 \text{ N/mm} = 5.71 \text{ lb/in}$ u_0, v_0, w are the displacements of middle plane; β_x is the slope of middle plane with respect to x-axis	

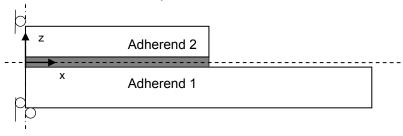
Table 7.2.2, Material Properties of Bonded Doublers in the Analysis

Aluminum		Boron/epoxy		Ероху	
	$E_1 = E_2 = E_3$ $= 10 \text{ Msi}$	$E_1 = 223.4GPa$ $E_2 = E_3 = 24.13 GPa$	$E_1 = \frac{English}{32.4 \text{ Msi}}$ $E_2 = E_3 = 3.5 \text{ Msi}$	SI Units E = 3.068 GPa G =1.138 GPa	E = 0.445 Msi $G = 0.165 Msi$
$\begin{vmatrix} v_{12} = v_{13} \\ = v_{23} = 0.3 \end{vmatrix}$	$v_{12} = v_{13}$ = $v_{23} = 0.3$	$v_{12} = 0.23$ $G_{12} = 8.481$ GPa	$v_{12} = 0.23$ $G_{12} = 1.23$ Msi	v=0.348	v=0.348

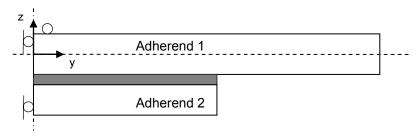
The boundary conditions for the FEA and BondJo analyses were designed to simulate the "inservice" boundary condition of a panel, as opposed to the boundary conditions of a stand-alone test article. This important distinction is described in detail in Volume 2, Section 6.2.

7.2.2 HyperSizer Setup

This problem was solved using the HyperSizer Bonded Joint Analysis implementation. When entering this problem into HyperSizer, the materials and loads must be entered in the HyperSizer sign convention as described in Volume 2, Section 6.11. As shown in the below figure, the HyperSizer sign convention uses the midplane of adhesive 1 as its z reference plane with z pointing away from adherend 2 while the academic solution uses the adhesive layer and points toward adherend 2. In addition, HyperSizer's y axis is aligned transversely to the stiffener, while in the MatLab BondJo solution, this direction is x.



a) Typical academic sign convention and reference plane



b) HyperSizer panel sign convention and reference plane

Fig.7.2.2, Coordinate systems and reference planes for the HyperSizer panel and typical academic sign conventions.

To accommodate this sign convention, and the problem definition in section 7.2.1, the material properties were rotated by 90° for entry to HyperSizer. The modified properties are shown in the table below.

HyperSizer	Traditional	Value
E_2	E_1	32.4
$E_1=E_3$	$E_2=E_3$	3.5
ν ₁₂	$v_{21} = v_{12}E_1/E_2$	0.02484
ν ₂₁	ν ₁₂	0.23

In addition to the change in material property direction, the loads were rotated by 90°. Therefore, instead of entering Nx or Mx, these loads were entered into HyperSizer as Ny or My.

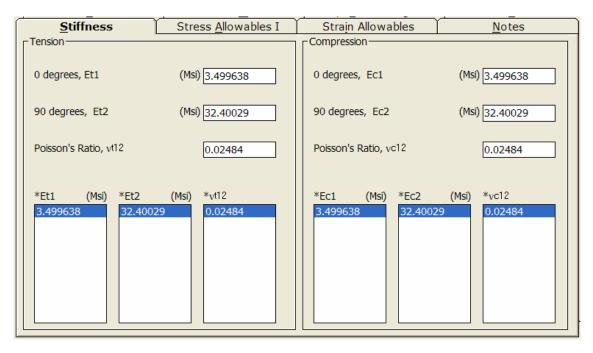


Fig.7.2.3, Boron-Epoxy material entered through the HyperSizer Interface

Beyond these changes, the layup specification and all dimensions were entered into HyperSizer exactly as shown in Section 7.2.1. Additional details for the HyperSizer specification of this problem are in Volume 2, Section 6.7. This project is stored in the HyperSizer Verification database as a Workspace with the name, "Composite Joint Verification with Stresscheck".

7.3 Comparison to Finite Element Analysis

7.3.1 Desired FEA Results Comparisons

Fig. 7.3.1 shows the out-of plane shear (red) and peel (black) stresses through the thickness of the joint as the solution marches toward the free edge of the doubler/flange. The lightest colored curves start at x/L = 0.89 (~20 ply thicknesses from the free edge) and the darkest curve at x/L = 0.998 (~½ ply thicknesses away). Notice, that not only do the stress magnitudes vary greatly, but the character of the stress field completely changes close to the free edge. HyperSizer-BondJo resolves this stress variation, and the goal of the Stresscheck comparison is to verify these results against a trusted finite element solver.

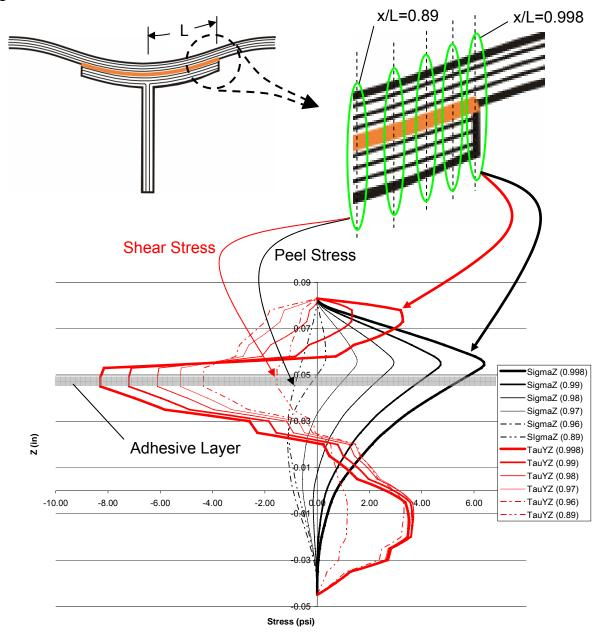


Fig. 7.3.1, Stress calculations performed by HyperSizer-BondJo through the depth of the joint show how the interlaminar shear and peel stress vary greatly as the free edge of the joint is approached.

The FEM for this comparison was generated and analyzed by Lockheed Martin. The following comparisons between HyperSizer-BondJo and Stresscheck were requested in our original problem specification.

- 1. Adhesive interlaminar and peel stress (σ_x , τ_{xz} , τ_{yz}) distribution along the bond centerline.
- 2. Through-the-thickness distribution of in-plane stresses away from the influence of the leading edge at x = 0.5".
- 3. Through-the-thickness distribution of peel and out-of-plane shear stresses, at two different locations of x. The first is approx. 22 ply thicknesses from the free edge at x=0.89" and the second is 8 ply thicknesses from the free edge at x=0.9575". (Upon viewing the results, we have determined that these may not have been the best choices for extraction of results. In a future comparison, we will attempt to get results at ½ ply thickness from the free edge, or 0.9975".)
- 4. Mid-plane displacements (*u*, *v*, *w*) for both adherends.
- 5. Would like to obtain results for two conditions:
 - a. Modify the FEM by setting the transverse shear moduli to unrealistically high values to attempt to match BondJo's CLT assumptions that do not include transverse shear (See Section 7.3.2).
 - b. Use the original, more realistic material properties of adherends to quantify the effect of these missing effects in HyperSizer-BondJo. (This analysis has not yet been performed.)

7.3.2 Simplifying Assumptions for FEA Comparisons

The classical lamination theory used by BondJo does not account for the effects of transverse shear flexibility, as discussed in Volume 2, Section 6.8.1. Therefore, to eliminate possible discrepancies this missing effect could cause between BondJo and Stresscheck results, the material properties used in the FEA were modified. The transverse shear moduli (G_{12} and G_{13}) were set to an arbitrarily high number (1.0×10^8) and the Poisson ratios that link in-plane to out-of-plane strains (v_{13} and v_{23}) were set to zero, while all other quantities were set equal to those specified in the problem definition above.

7.3.3 Quality of FEA Comparison Plots

In the comparison plots between HyperSizer and Stresscheck, notice is that the FEA plots are not smooth. This can be seen in Fig. 7.3.2. The FEA results, shown with dashed lines, are rather jagged. This does not reflect the quality of the FEA results, but rather the resolution quality of the hard copy source.

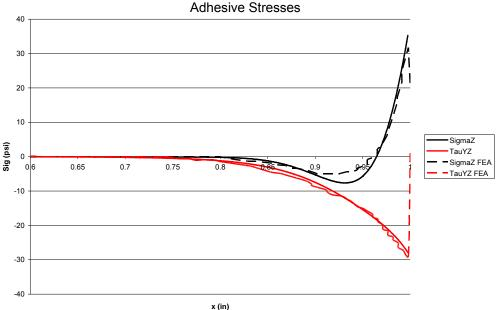


Fig. 7.3.2, Sample comparison results between HyperSizer-BondJo and Stresscheck illustrating that the jagged FEA lines are not due to an oscillating FEA solution, but rather the low resolution scans of the hard-copy results.

Unfortunately, time ran out on this project before we had a chance to fully extract results from the FEA electronically. As a result, the plots were delivered in PowerPoint charts as bitmap images as shown in Fig. 7.3.3. These images were scanned into a digitization program to extract the curves, however, as shown in the figures, the plots have relatively thick markers/lines.

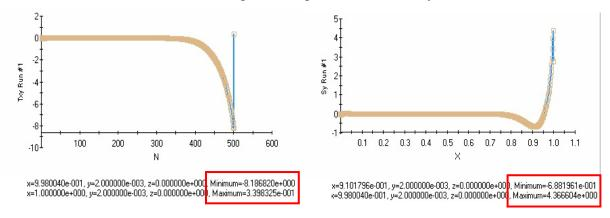


Fig. 7.3.3, Stresscheck results as received in PowerPoint chart results, the numbers in red boxes are data anchor points used to calibrate extracted results.

While the resolution of our digitized curves was inexact, each of the original received curves did supply minimum and a maximum data values (shown with red rectangles) and using these values the digitized curves were "anchored" and calibrated.

7.3.4 Peak Stresses Comparisons

At first glance, it appears that, HyperSizer-BondJo over predicts peak stresses relative to the finite element analysis in the area of the singularity at the reentrant corner. There are several reasons for this disparity but because failure prediction is not highly dependent on the actual peak stress value, but rather depends on the stress levels at some characteristic distance away, these differences may not be significant.

First of all, finite element analyses can have trouble converging in the vicinity of singularities without using a very high mesh density. In the Stresscheck solid FEA model used for BondJo verification, instead of trying to resolve the singularity itself, a small circular region surrounding the reentrant corner was defined in which the results are completely ignored. This is done because it is assumed that results in this region are "polluted". In this case, the actual peak stress, which occurs exactly at the free edge, is not known.

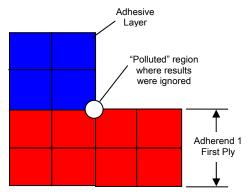


Fig. 7.3.4, In our Stresscheck verification example, a small area around the reentrant corner was defined inside of which the FEA results are ignored.

Second, when post-processing the FEA results, there is a potential disparity among the FEA results themselves. The peak stress can depend on the number of points chosen for plotting. This is shown in Fig. 7.3.5. As the number of plotting points chosen from the FEA increases from 75 to 500 points, the reported peak stress increases 60% from 2.76 to 4.37 psi. Based on this trend, perhaps even 500 points is not enough and adding more points would result in an even

higher peak stress. For this same case BondJo reports a peak stress of 5.76 psi and a stress of 5.29 psi at only ½ ply thickness away (the characteristic assumed distance), both of which are considerably higher those values returned by the FEA. In reality, the peak stress most likely somewhere in between the BondJo results and those of the FEA

Although the peak stresses reported by the two methods can be quite different, the shape of the stress curve and the integrated effect of those stresses are very similar. In HyperSizer-BondJo, failure criteria are not evaluated exactly at the free edge, but rather at all points outside of the characteristic distance. which is approx. ½ ply thickness or 0.0025" from the free edge. A discussion of different ways of evaluating failure criteria is in Volume 2. Section 6.6.

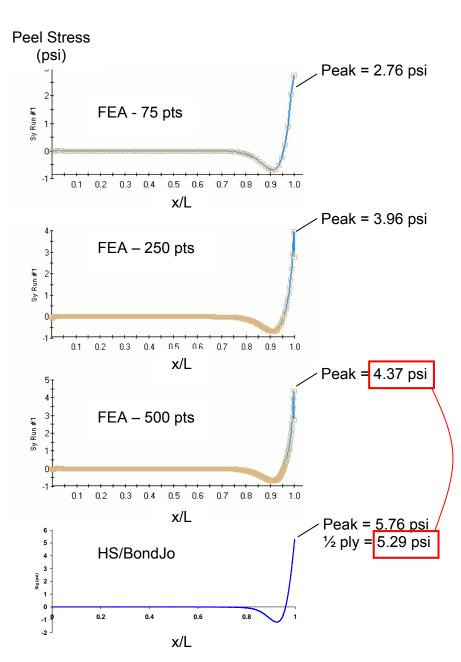


Fig. 7.3.5, As the number of points chosen from the FEA increases from 75 to 500 points, the shape of the curve remains the same, however the peak stress increases substantially. Perhaps even 500 points is not enough to retrieve the true peak stress.

7.3.5 Case 1: Applied Tensile Force (Nx = 5.71 lb/in)

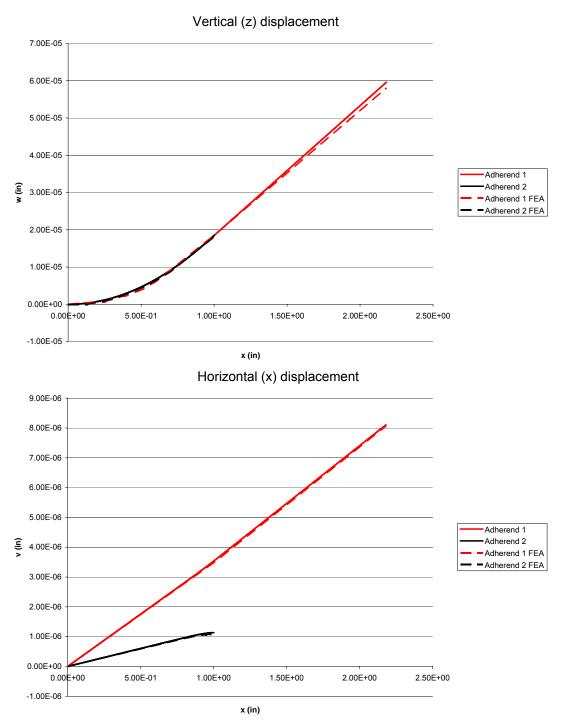
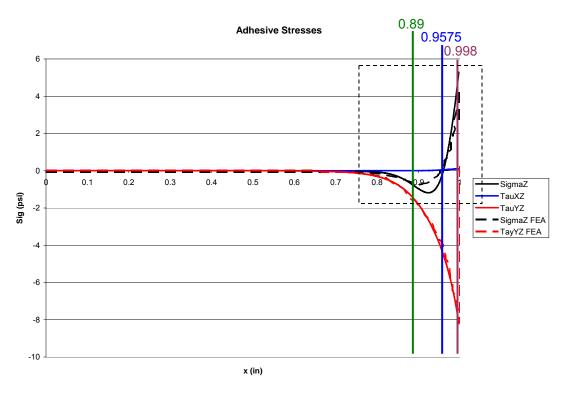


Fig. 7.3.6, Comparisons of adherend displacement between HyperSizer-BondJo and Stresscheck show very close agreement on both the vertical displacement and displacement in the x direction (that is, perpendicular to the stiffener direction).



Through Thickness out-of-plane Stresses (X=0.89)

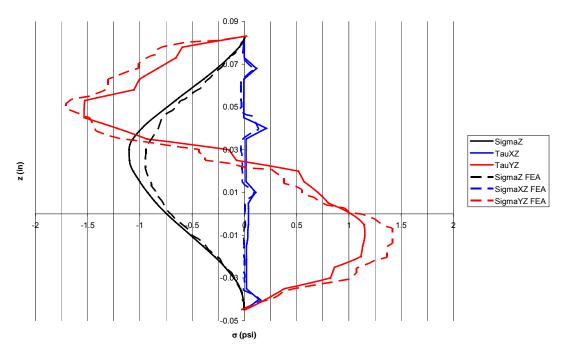


Fig. 7.3.7 Interlaminar shear and peel stresses in the adhesive layer (top) and through the thickness of the laminated adherends and adhesive at x=0.89". Stresses at this location show reasonable agreement between HyperSizer-BondJo and Stresscheck. A closeup of the adhesive stresses near the free is shown in Fig. 7.3.8.

In the extracted results shown in Fig. 7.3.8, the comparison between BondJo and Stresscheck shows a substantial disparity, especially in the peel stress. However, our belief is that this difference in results is actually magnified by our choice of x location. The locations chosen for extraction of through-thickness stress plots (x=0.89" and 0.9575") were arbitrarily chosen from a different verification problem. In this case, at x=0.9575 the stress is reversing from compression to tension and because the peel stress is very nearly zero, the difference between the two methods is magnified. In future comparisons, the key x location where comparisons should be made is at the characteristic distance of x=0.998". Our belief is that comparisons between the two methods at this location, well away from the stress reversal, will show a closer match.

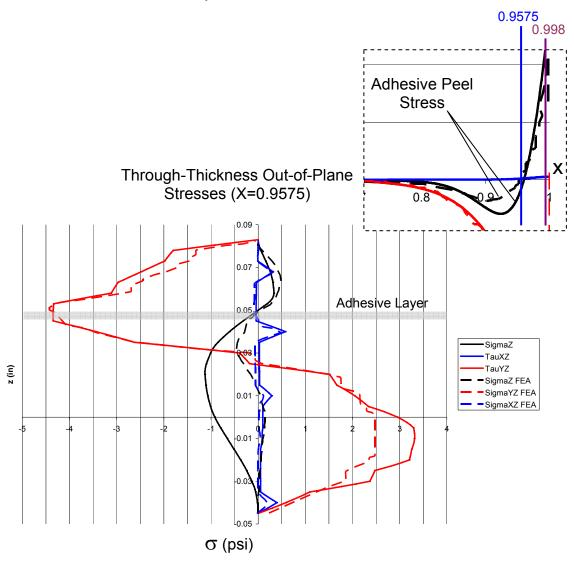


Fig. 7.3.8, Plots of interlaminar shear and peel stresses through-the-thickness of the adherend laminates and the adhesive at x=0.9575. While the interlaminar shear stresses at this location match reasonably well, the peel stress is quite different. One reason is that at this location, as seen in the adhesive stress closeup, the peel stress is reversing from compressive to tensile and the fact the the actual stress is close to zero amplifies the disparity between the HyperSizer-BondJo and FEA results.

Through Thickness in-plane Stresses (X=0.5)

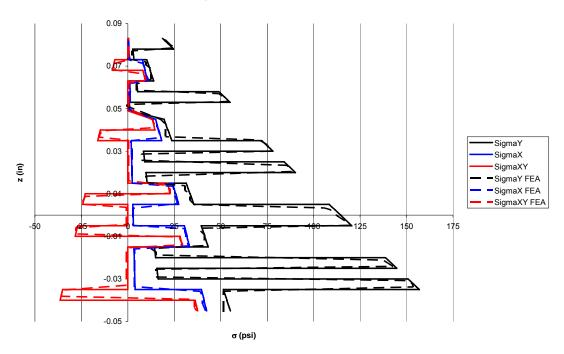
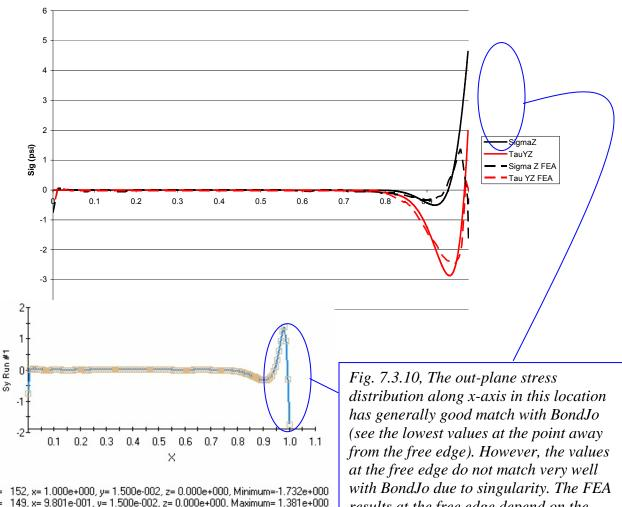
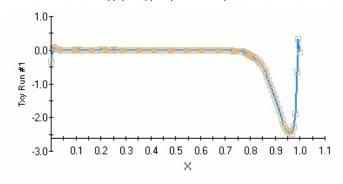


Fig. 7.3.9, Comparisons of ply in-plane stresses between HyperSizer-BondJo and Stresscheck show an almost identical match all along the joint. The only difference is that in HyperSizer-BondJo, there is an instantaneous transition in stress from ply to ply (due to the classical lamination theory formulation) whereas for Stresscheck, there is a short transition region beween each ply.

Adherend 2 Midplane Stresses



N= 152, x= 1.000e+000, y= 1.500e-002, z= 0.000e+000, Minimum=-1.732e+000 N= 149, x= 9.801e-001, y= 1.500e-002, z= 0.000e+000, Maximum= 1.381e+000



 $\begin{array}{lll} N=&147, x=9.669e\cdot001, y=1.500e\cdot002, z=0.000e+000, Minimum=\cdot2.476e+000 \\ N=&151, x=9.934e\cdot001, y=1.500e\cdot002, z=0.000e+000, Maximum=\cdot3.294e\cdot001 \end{array}$

results at the free edge depend on the number of points used when extracting from results. It appears that only a few points (75) were used in these plots. We expect that if the number of points are increased the match would be better between the two results. See the discussion that compares Stresscheck results with different number of extracted points in Fig. 7.3.5.

7.3.6 Case 2 - Applied Moment (Mx = 0.2248 lb.in/in)

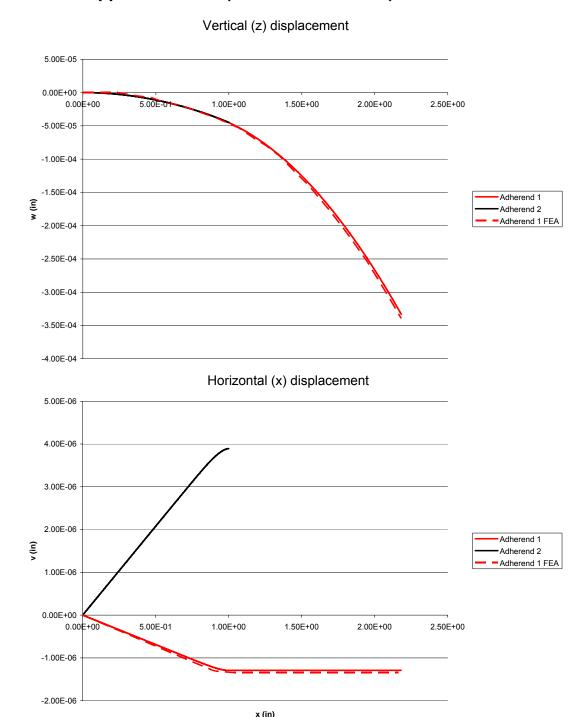


Fig. 7.3.11, Comparisons of adherend displacement between HyperSizer-BondJo and Stresscheck show very close agreement on both the vertical displacement and displacement in the x direction (that is, perpendicular to the stiffener direction).

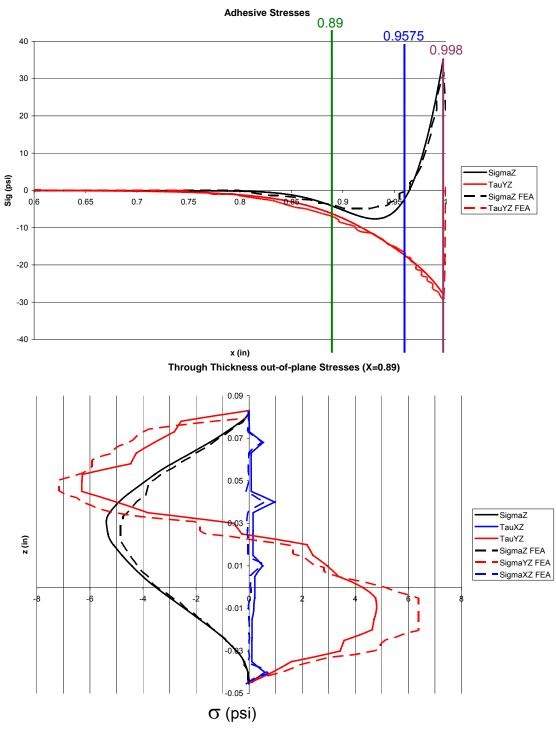


Fig. 7.3.12 Interlaminar shear and peel stresses in the adhesive layer (top) and through the thickness of the laminated adherends and adhesive at x=0.89". Stresses at this location show reasonable agreement between HyperSizer-BondJo and Stresscheck. A closeup of the adhesive stresses near the free is shown in Fig. 7.3.13.

In the extracted results shown in Fig. 7.3.13, the comparison between BondJo and Stresscheck, especially in the peel stress, shows a substantial disparity. However, our belief is that this difference in results is actually magnified by our choice of x cut location. The locations chosen for extraction of through-thickness stress plots (x=0.89" and 0.9575") were arbitrarily chosen from a different verification problem. In this case, at x=0.9575, the stress is reversing from compression to tension and because the peel stress is very nearly zero, the difference between the two methods is magnified. In future comparisons, the key x location where comparisons should be made is at the characteristic distance of x=0.998". Our belief is that comparisons between the two methods at this location, well away from the stress reversal, will show a closer match.

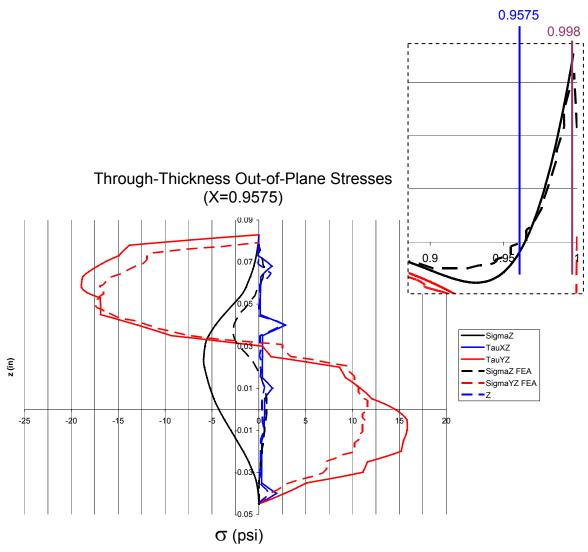


Fig. 7.3.13, Plots of interlaminar shear and peel stresses through-the-thickness of the adherend laminates and the adhesive at x=0.9575. While the interlaminar shear stresses at this location match reasonably well, the peel stress is quite different. One reason is that at this location, as seen in the adhesive stress closeup, the peel stress is reversing from compressive to tensile and the fact the the actual stress is close to zero amplifies the disparity between the HyperSizer-BondJo and FEA results.

Through Thickness in-plane Stresses (X=0.5)

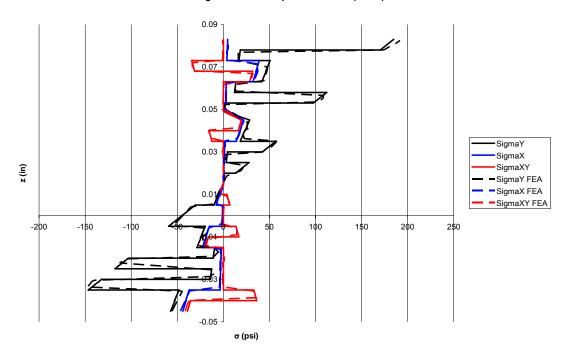
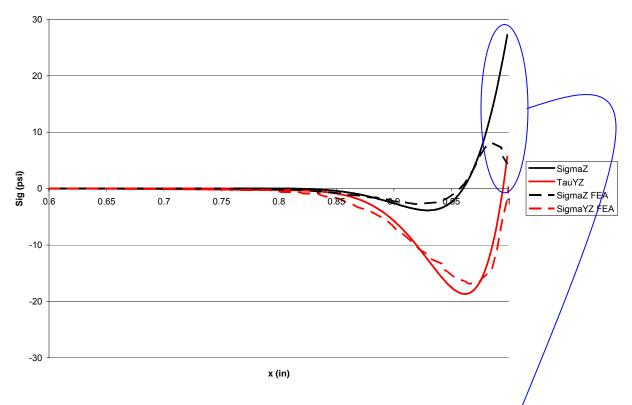
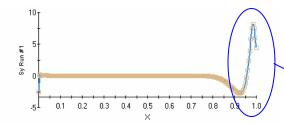


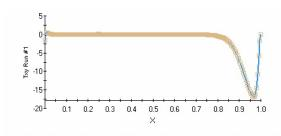
Fig. 7.3.14, Comparisons of ply in-plane stresses between HyperSizer-BondJo and Stresscheck show an almost identical match all along the joint. The only difference is that in HyperSizer-BondJo, there is an instantaneous transition in stress from ply to ply (due to the classical lamination theory formulation) whereas for Stresscheck, there is a short transition region beween each ply.

Adherend 2 Midplane Stresses





N= 187, x=9.253731e-001, y=1.500000e-002, z=0.000000e+000, Minimum=2.757422e+000 N= 199, x=9.850746e-001, y=1.500000e-002, z=0.000000e+000, Maximum=8.096576e+000



N= 195, x=9.651741e-001, y=1.500000e-002, z=0.000000e+000, Minimum=1.690016e+001
N= 2, x=4.975124e-003, y=1.500000e-002, z=0.000000e+000, Maximum=4.317053e-001

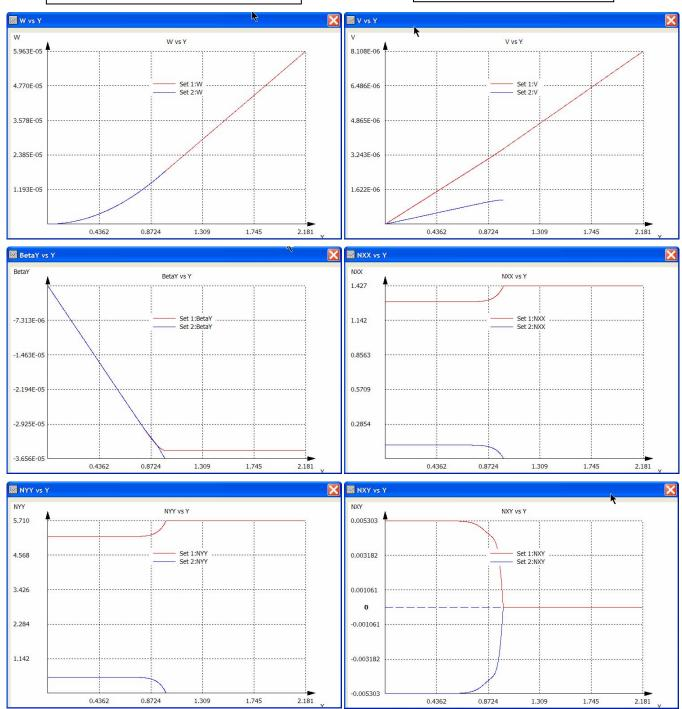
Fig. 7.3.15, The out-plane stress distribution along x-axis in this location has generally good match with BondJo (see the lowest values at the point away from the free edge). However, the values at the free edge do not match very well with BondJo due to singularity. The FEA results at the free edge depend on the number of points used when extracting from results. It appears that only a few points (75) were used in these plots. We expect that if the number of points are increased the match would be better between the two results. See the discussion that compares Stresscheck results with different number of extracted points in Fig. 7.3.5.

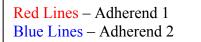
7.4 Supplemental Results

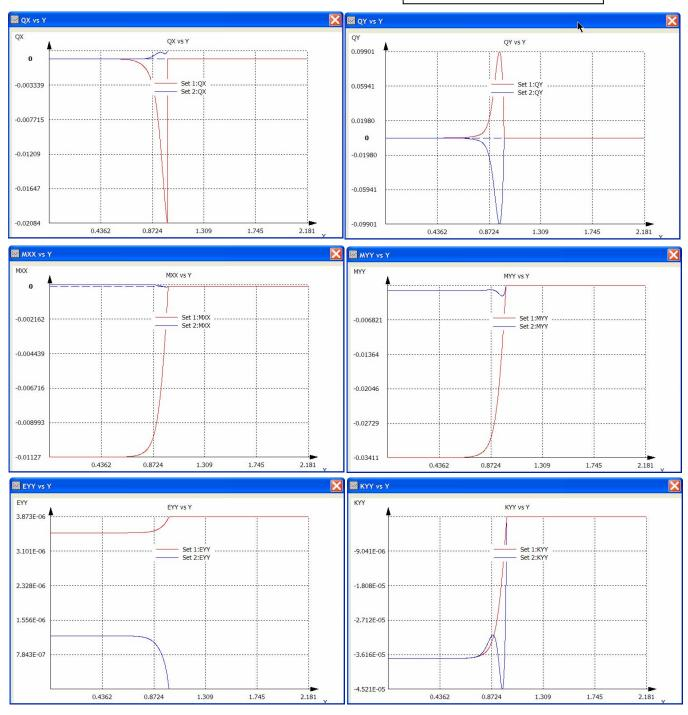
7.4.1 HyperSizer Screenshots for Applied Tensile Load Case

Note: Results shown assume the HyperSizer Panel sign convention.

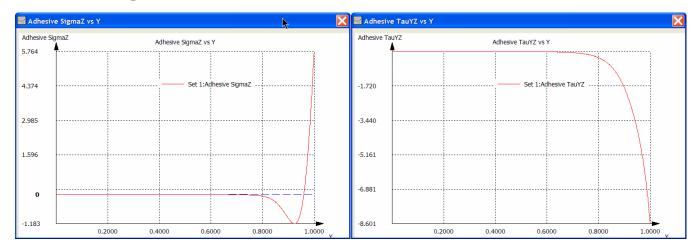
Red Lines – Adherend 1 Blue Lines – Adherend 2

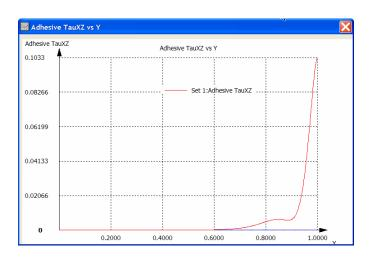




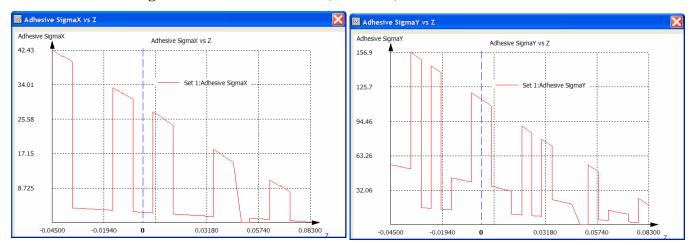


Adhesive Midplane Stresses

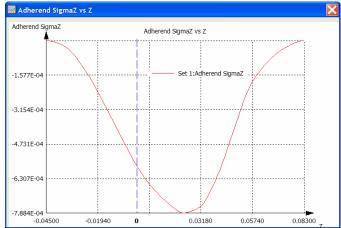


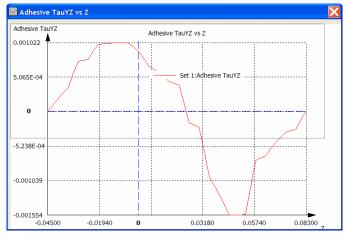


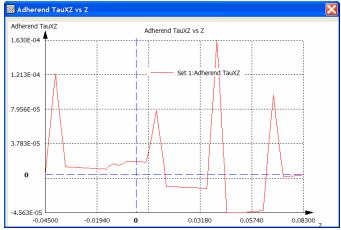
Adherend Through-Thickness Stress Plots (X/L = 0.5)



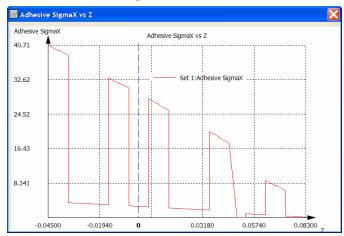


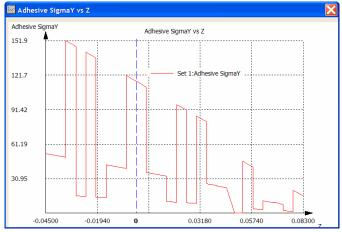


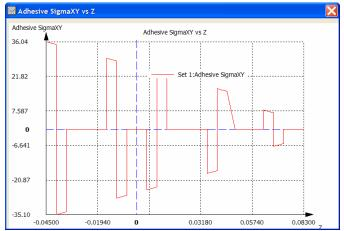


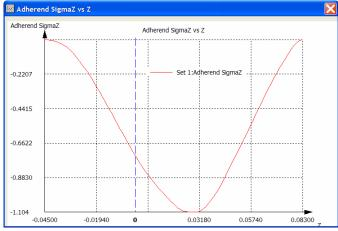


Adherend Through-Thickness Stress Plots (X/L = 0.89)

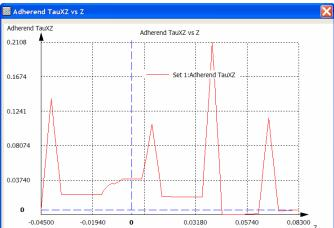




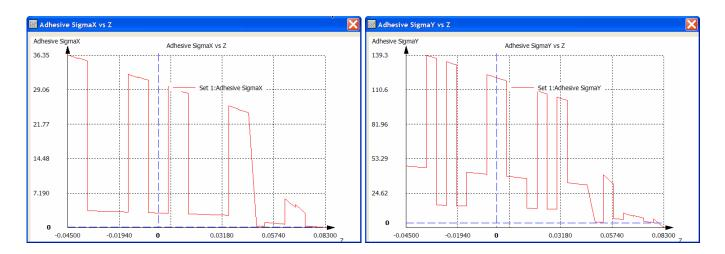


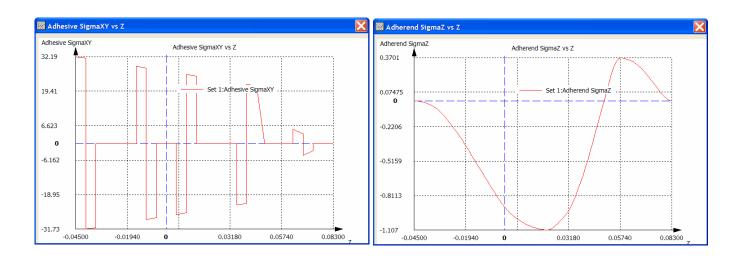


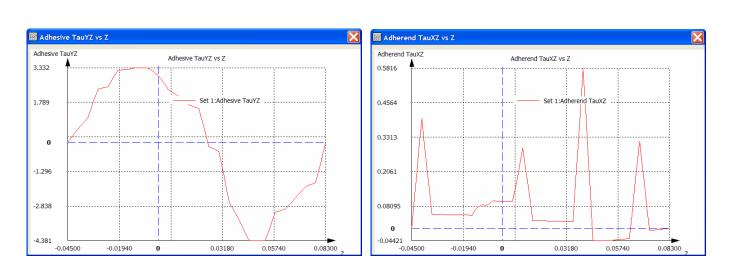




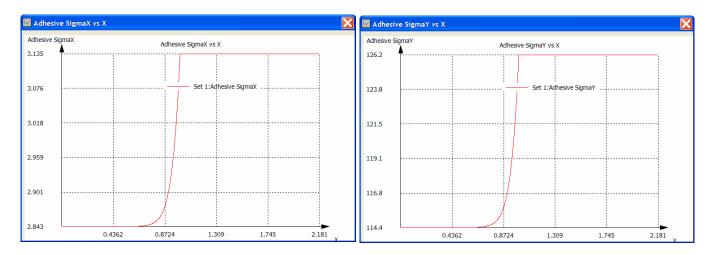
Adherend Through-Thickness Stress Plots (X/L = 0.9575)

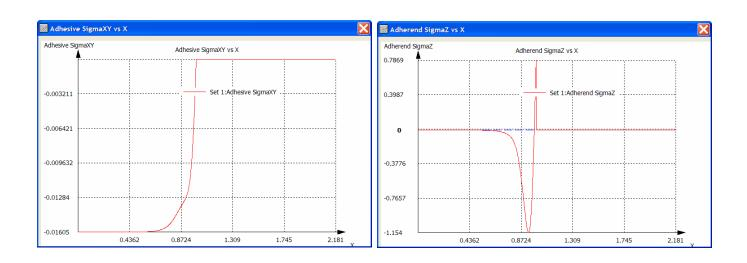


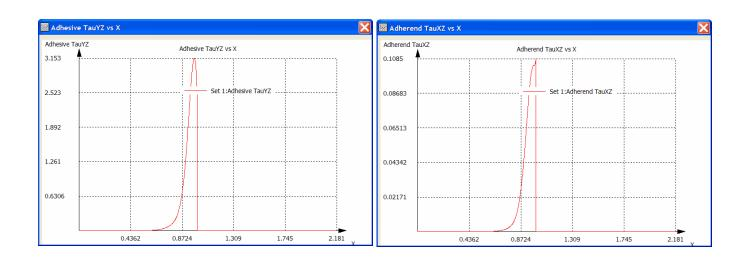




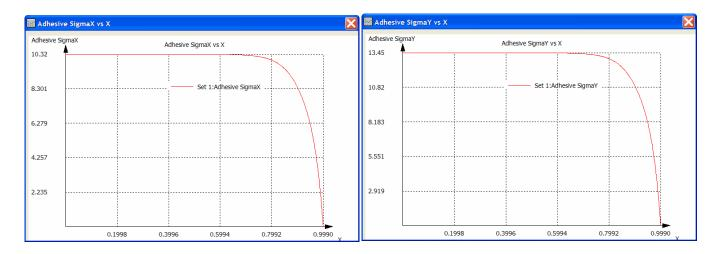
Adherend 1 Midplane Stress Plots

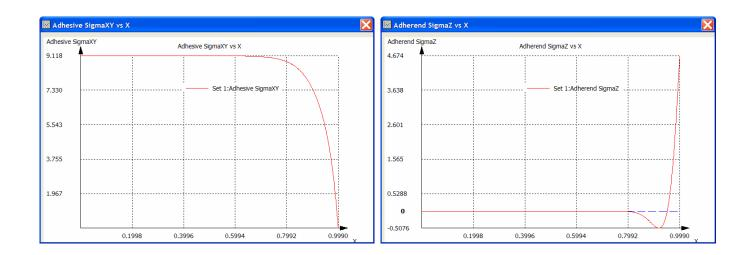


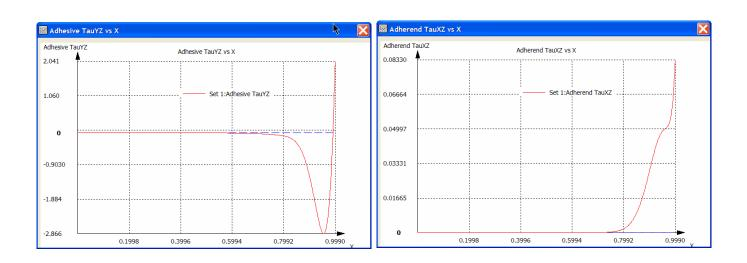




Adherend 2 Midplane Stress Plots



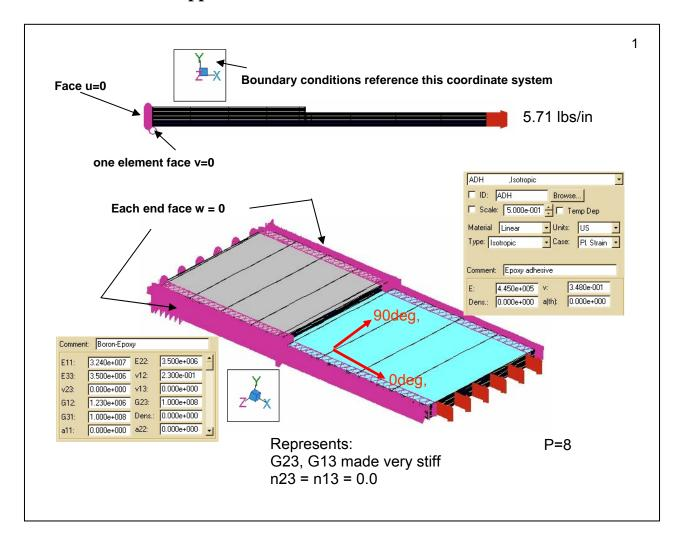


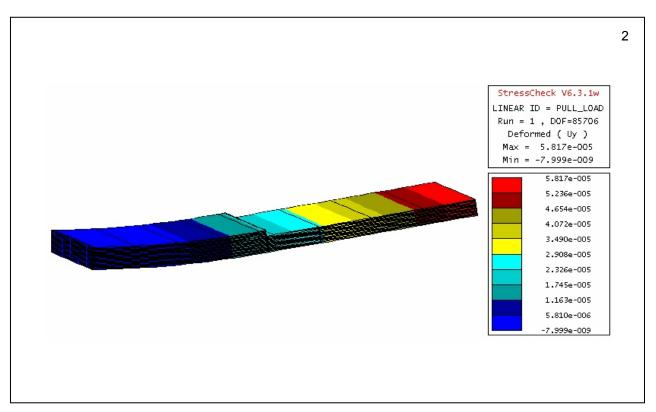


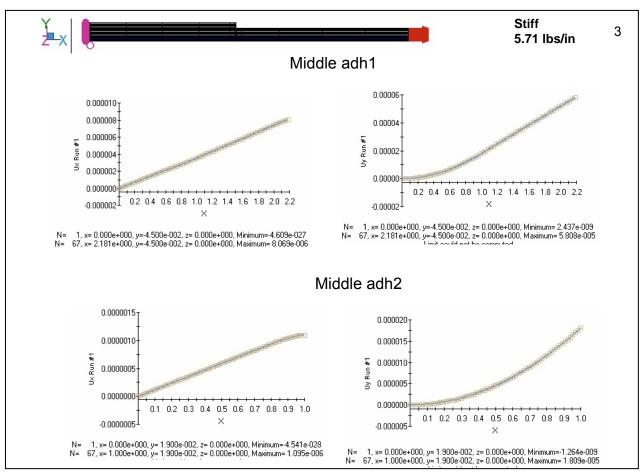
7.4.2 Stresscheck Results Presented in Powerpoint Format

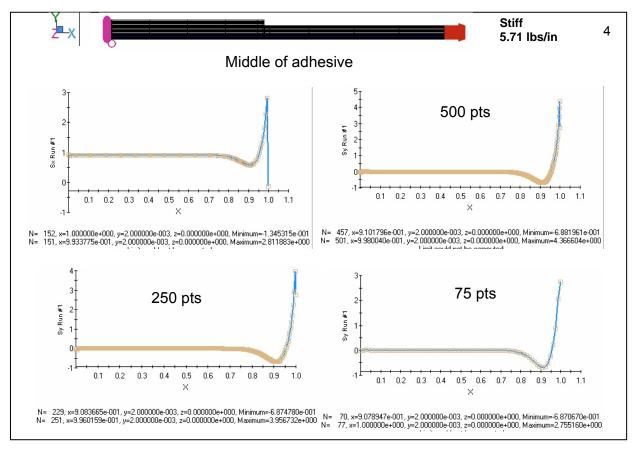
Note: The Stresscheck problem setup uses a sign convention that is different from either the HyperSizer panel or the typical academic sign conventions. Just as with the typical academic sign convention, the x direction is perpendicular to the stiffener, however the y and z axes are reversed from the typical acacemic with y being the vertical axis and z along the stiffener.

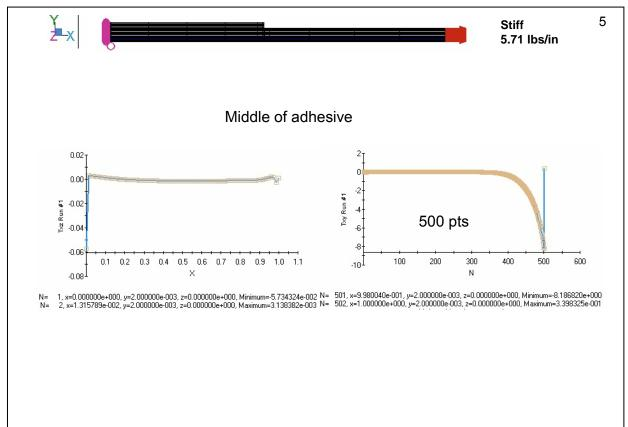
7.4.2.1 Case 1: Applied Tensile Force

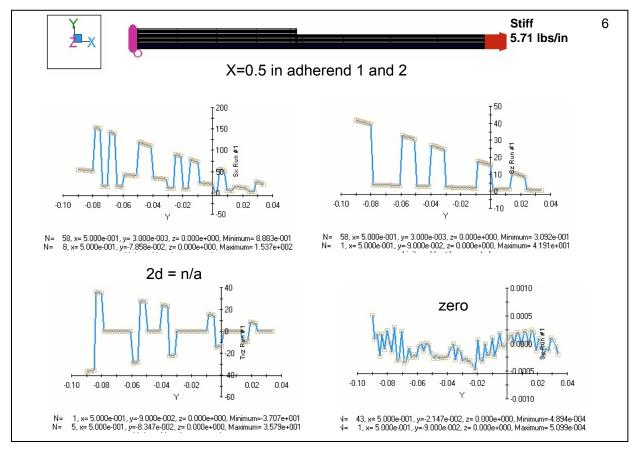


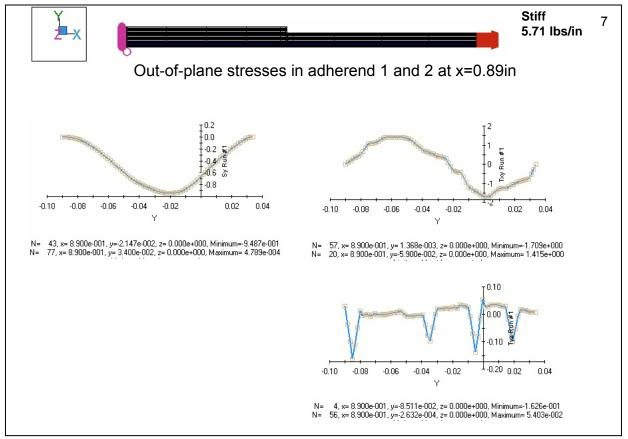


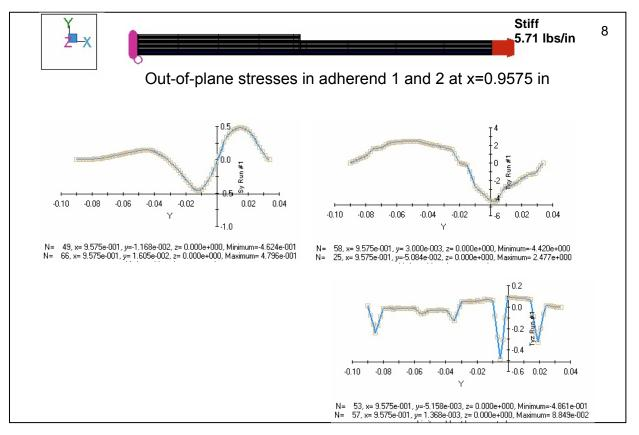


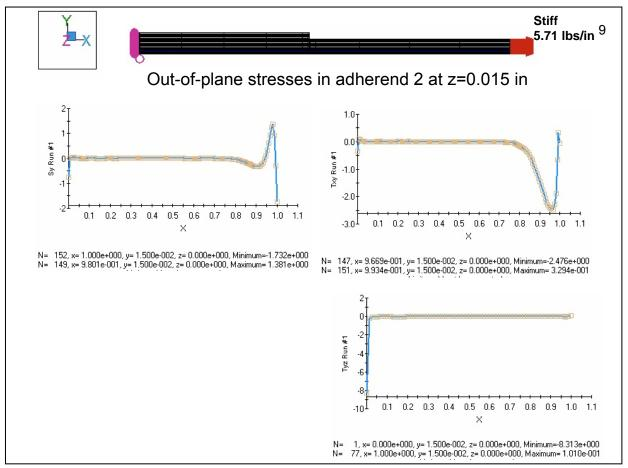




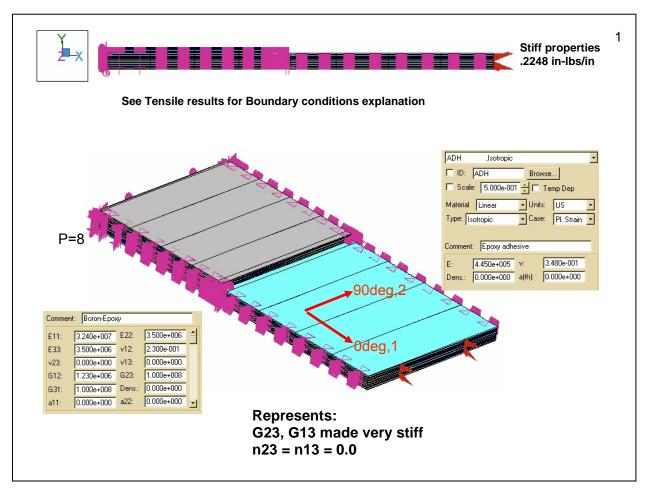


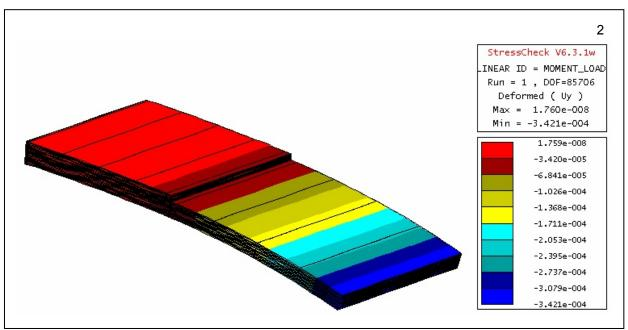


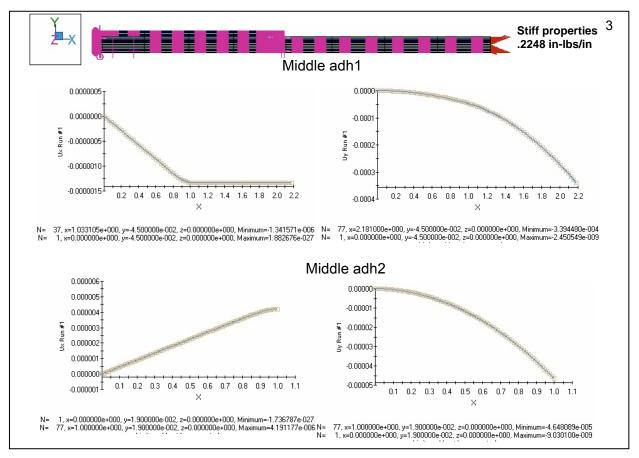


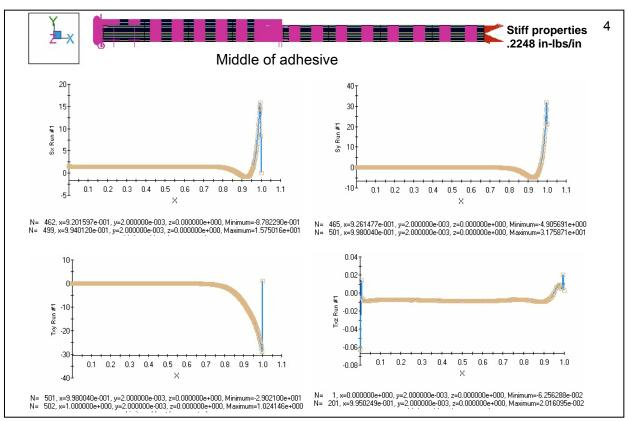


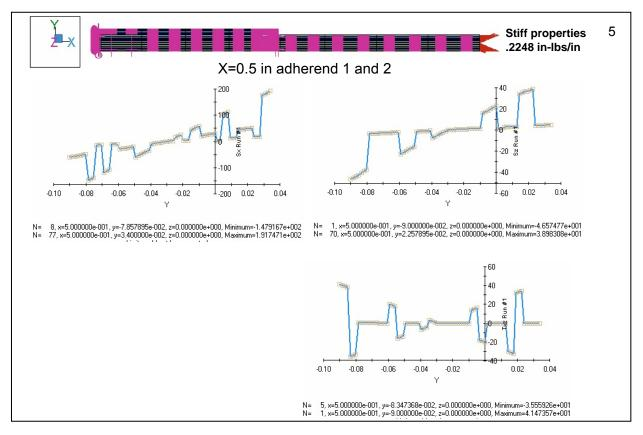
7.4.2.2 Case 2: Applied Moment

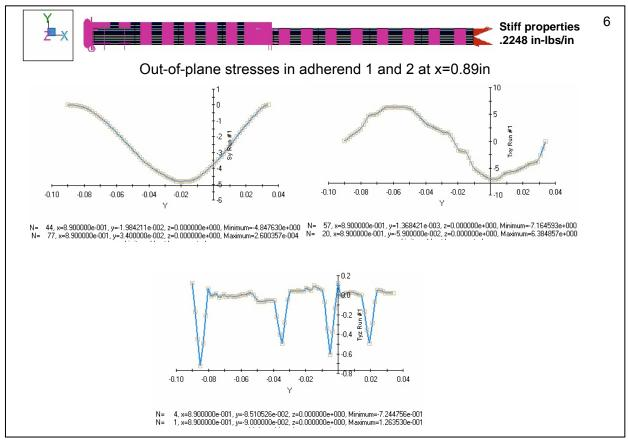


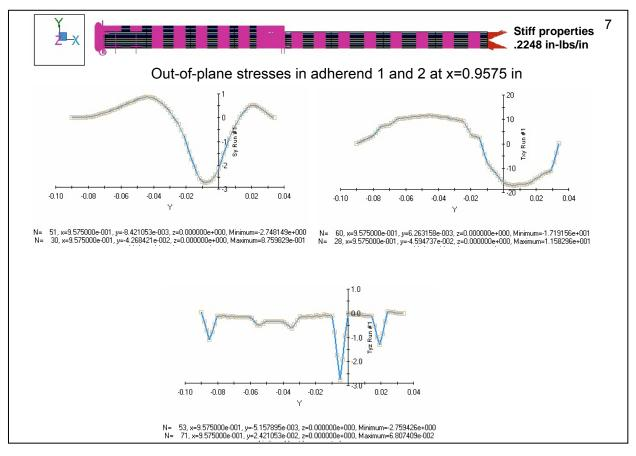


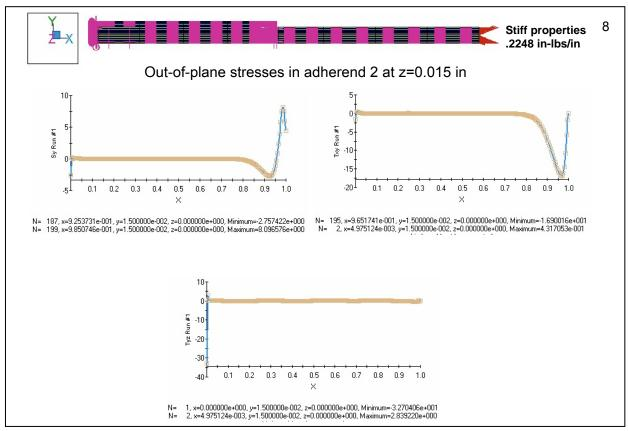












8 Verification – Bonded Joint[0/±30/±60] Laminate Mortensen Examples

8.1 Bonded Doubler Joint Example

The purpose of this all composite bonded joint example is to verify that the theory described in Volume 2, Section 6.4 was implemented correctly and consistently. The problem was presented in Mortensen [8.1] and because BondJo's theoretical development originated from that work, it is not surprising that our results match those in [8.1] exactly.

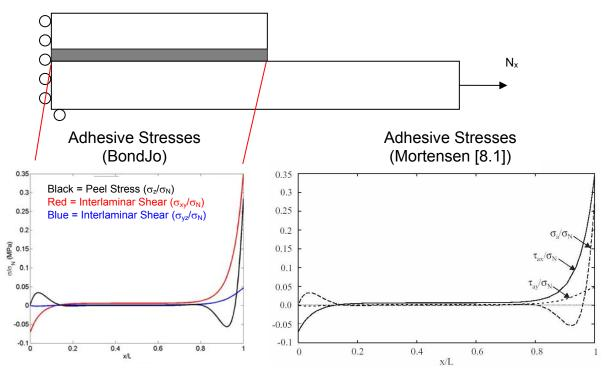


Fig. 8.1.1, Comparison of adhesive stresses between BondJo and Mortensen for the bonded doubler joint example. The results between the two codes are virtually identical, which is not surprising because BondJo's theory was adapted and expanded from from theory originally developed by Mortensen.

Note: Published comparison results and problem definitions use the typical academic sign convention. See Volume 2, Section 6.11 for details. Adherend 2 Adherend 1 Adherend 1 Adherend 1

Fig. 8.1.2, Schematic of the bonded doubler joint example from Mortensen's thesis.

Table 8.1, Geometry and Boundary Conditions for Mortensen's Thesis Bonded Doubler Example

Dimensions:		Materials	Loading and Boundary Conditions:		Conditions:
SI	English	Adherend 1: Gr/Ep	Left	Face	(symmetry):
L = 20 mm	L = 0.787"	$[0^{\circ}/30^{\circ}/60^{\circ}]_4$ (12 plies)	$\mathbf{u}_0 = \mathbf{w}$	$= \mathbf{M}_{xx} = v = 0$	
$L_2 = 30 \text{ mm}$	$L_2 = 1.181$ "	$t_{ply} = 0.125 \text{mm} (.0049'')$			
$t_1 = 1.5 \text{ mm}$	$t_1 = 0.059$ "		Right Fa	ice:	
$t_2 = 1.5 \text{ mm}$	$t_2 = 0.059$ "	Adherend 2: Gr/Ep	1. $N_{xx} = 1$	100N/mm (571	lb/in);
		[60°/30°/0°] ₄ (12 plies)	$v_o = w$	$= 0; M_x = 0$	
		$t_{ply} = 0.125 \text{mm} (.0049'')$			
		Adhesive: Epoxy			
		$t_{\text{adhesive}} = 0.05 \text{mm} (.00197'')$			

Table 8.2, Material Properties

Graphite/epoxy		Epoxy Adhesive)	
		(assumed linear, elastic)		
SI	English	SI	English	
$E_1 = 164.0$ GPa	$E_1 = 23.8 \text{ Msi}$	E = 2.8GPa	E = 0.406 Msi	
$E_2 = E_3 = 8.3 \text{ GPa}$	$E_2 = E_3 = 1.2 \text{ Msi}$	G =1.0 GPa	G = 0.145 Msi	
$v_{12} = 0.34$	$v_{12} = 0.23$	v=0.40	v=0.40	
$G_{12}=2.1 \text{ GPa}$	$G_{12} = 0.305 \text{ Msi}$			

The solution domain was defined with 10 segments for the overlap region (L) and 5 segments for the free span region (L_2). The solutions are plotted with 40 points in each segment.

The left face (or "symmetry") boundary condition used by Mortensen is not the same as that used in the HyperSizer implementation of BondJo. In this example, along the left face, M_{xx} was set to zero. In the HyperSizer implementation, M_{xx} is free to vary and the slope, β_{xx} is set to zero. In the results comparisons shown below, the boundary conditions for the Matlab version of BondJo were changed to match those of the Mortensen thesis.

8.1.2 Comparison to Published Results

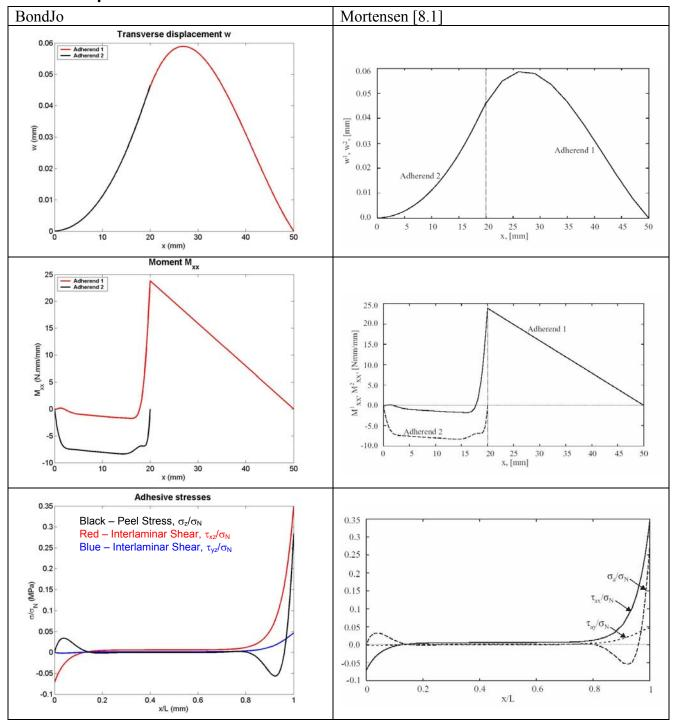


Fig. 8.1.3, Result comparisons between BondJo and Mortensen[8.1] for the bonded doubler joint example.

8.2 Single Lap Joint Examples

A second verification problem, this one for a single lap joint, was chosen from Mortensen [8.1] to verify that the theory described in Volume 2, Section 6.4 was implemented correctly and consistently. Most of the HyperSizer-BondJo results matched closely, however, some initially showed large discrepancies with the Mortensen's results. Upon contacting the author, we learned that there were errors in the author's original code and the HyperSizer-BondJo results are correct [8.2]. The corrected result supplied by the author match HyperSizer-BondJo's results exactly.

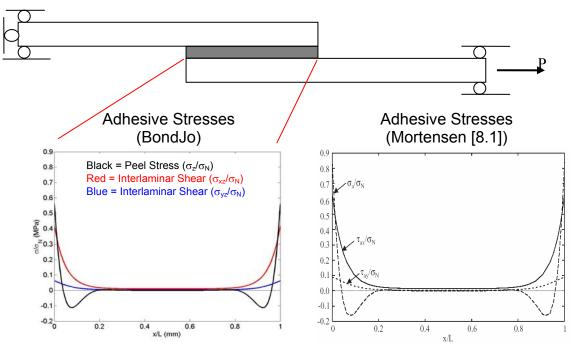


Fig. 8.2.1, Comparison of adhesive stresses between BondJo and Mortensen for the single lap joint example. Comparisons between the two codes show substantial discrepancies as seen here. Upon contacting the author, we learned that the code used to generate results in [8.1] had an unresolved bug that has since been fixed. Updated results sent to us by the author compared very close to the BondJo results.

Table 8.3, Geometry and Boundary Conditions for Mortensen's Thesis Stepped Lap Joint Example

Dimensions:		Materials	Loading and Boundary Conditions:		ditions:
SI	English	Adherend 1: Gr/Ep	Left	Face	$(x=-L_1)$:
L = 20 mm	L = 0.787"	$[0^{\circ}/30^{\circ}/60^{\circ}]_4$ (12 plies)	$v_0 = u_0 = v_0$	$= w = M_{xx} = 0$	
$L_1 = L_2$	$L_1 = L_2$	$t_{ply} = 0.125 \text{mm} (.0049'')$			
= 30 mm	= 1.18"		Right Fac	$\mathbf{e} (\mathbf{x} = \mathbf{L} + \mathbf{L}_2)$:	
$t_1 = 1.5 \text{ mm}$	$t_1 = 0.059$ "	Adherend 2: Gr/Ep	1. $N_{xx} = 10$	00N/mm (571 lb/i	in);
$t_2 = 1.5 \text{ mm}$	$t_2 = 0.059$ "	[60°/30°/0°] ₄ (12 plies)	$v_o = w =$	$= 0; M_{xx} = 0$	
		$t_{ply} = 0.125 \text{mm} (.0049'')$,	
		Adhesive: Epoxy			
		$t_{\text{adhesive}} = 0.05 \text{ mm} (.00197'')$			

Table 8.4, Material Properties

Graphite/epoxy		Epoxy Adhesive	2	
		(assumed linear, elastic)		
SI	English	SI	English	
$E_1 = 164.0$ GPa	$E_1 = 23.8 \text{ Msi}$	E = 2.8GPa	E = 0.406 Msi	
$E_2 = E_3 = 8.3 \text{ GPa}$	$E_2 = E_3 = 1.2 \text{ Msi}$	G =1.0 GPa	G = 0.145 Msi	
$v_{12} = 0.34$	$v_{12} = 0.34$	v=0.40	v=0.40	
G ₁₂ =2.1 GPa	$G_{12} = 0.305 \text{ Msi}$			

The solution domain was defined with 10 segments for the overlap region (L) and 2 segments for the each of the free span regions (L_1 and L_2). The solutions are plotted with 40 points in each segment.

8.2.2 Comparison to Published Results

8.2.2.1 Linear Adhesive

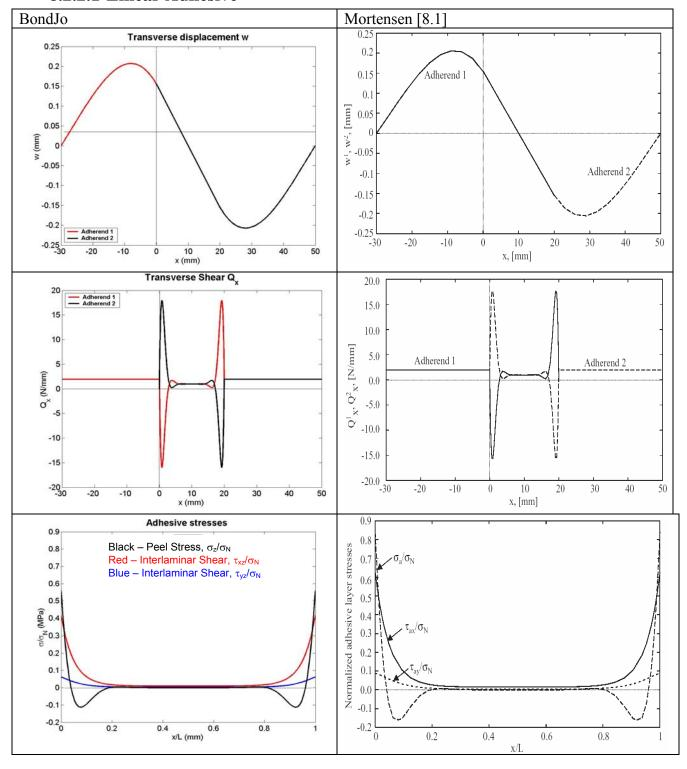


Fig. 8.2.2, Result comparisons between BondJo and Mortensen[8.1] for the single lap joint example.

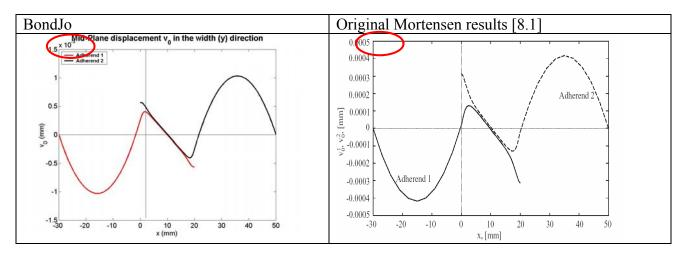


Fig. 8.2.3, Comparison of BondJo to original Mortensen results from [8.1] shows a very large discrepancy in the plot of horizontal displacement, v0.

In the BondJo-Mortensen comparisons, large discrepancies were seen in some of the results. This is most clearly seen in the plot of horizontal displacement, v_0 , shown in Fig 8.2.3, where the magnitude is off by a factor of three. Upon contacting the Dr Mortensen personally, he agreed that there were some mistakes in his thesis and BondJo's results are correct. In addition, he sent corrected results which match exactly with those of BondJo. One of these corrected results is shown in Fig. 8.2.4. The following excerpt is from an email sent by the author regarding BondJo results:

"...I have looked at your results and they are all correct. I must have found a bug in the code since I wrote my thesis, because I get the exact same results as you do now. The code has been implemented into the commercial software package ESAComp, which we completed approximately 3 years ago. It must have been in that process that I found a bug. It requires a lot of checks to release such a program. I am terrible sorry that you have been mislead by the results in my thesis. You have done a very good job, please receive my acknowledgment."

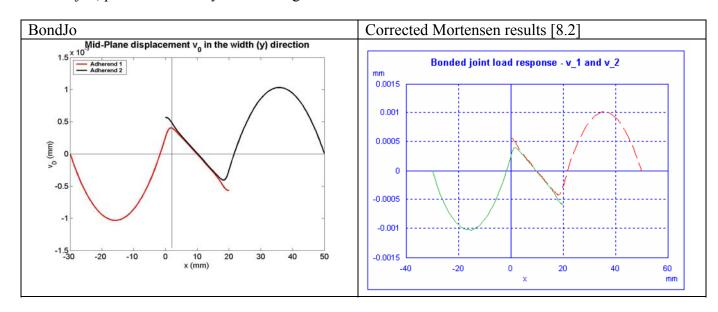


Fig. 8.2.4, Comparison of BondJo to corrected results sent by the author [8.1] show very close agreement between BondJo and Mortensen's results.

8.2.2.2 Non-linear Adhesive

In addition to the analysis using linear adhesive, [8.1] also provides results for the same problem considering the effects of nonlinear adhesive. The stress-strain curve used for the adhesive is shown in Fig. 8.2.5 along with representations using several non-linear material models. The detailed analysis procedure for nonlinear adhesives is described in Volume 2, Section 6.4.

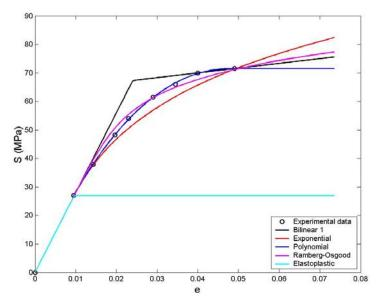


Fig. 8.2.5, Non-linear stress-strain curve of epoxy AY103 adhesive with equivalent representation of that curve using several non-linear models implemented in BondJo.

The BondJo results shown in Fig. 8.2.6 were calculated using the Ramberg-Osgood model for the adhesives. Compared to those predicted for linear adhesive, the peak interlaminar shear and peel stresses decrease due to adhesive yielding. However, it also can be seen that these results do not match those of Mortensen. This may be due to the generic mistake in Mortensen's original code, as discussed in the previous section. This has not however been verified with the author.

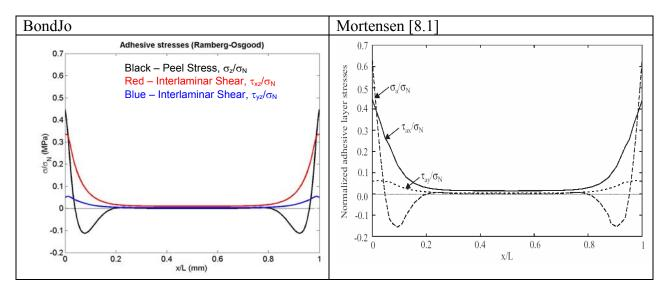


Fig. 8.2.6, BondJo results compared with those of [8.1] for stresses in non-linear adhesives show some differences that are assumed to be related to errors in Mortensen's original code as discussed in Section 8.2.2.1.

8.2.3 Linear Versus Non-Linear Adhesive Comparison

To quantify the effect of the non-linear adhesive analysis on the Mortensen single lap joint geometry, the axial load was increased to 200 N/mm to amplify the non-linear effects. The purpose of this study is to verify qualitatively the reasonability of BondJo's nonlinear adhesive results for single-lap joints, while fully quantitative verification of the results can not be completed until FE analysis is performed. The joint configuration is shown in 8.2.1 and geometry and material properties are tabulated in Tables 8.1 and 8.2.

Only small differences are seen in plots of displacement or in-plane stress between the linear and non-linear adhesive results. However, substantial differences are seen in plots of out-of-plane stress, especially near the adhesive free edge, as shown in Fig. $8.2.7 \, c) - f$). Additional results for this configuration are also shown in Section 8.3.3, Supplemental Results for Linear Versus Non-Linear Adhesive Comparison.

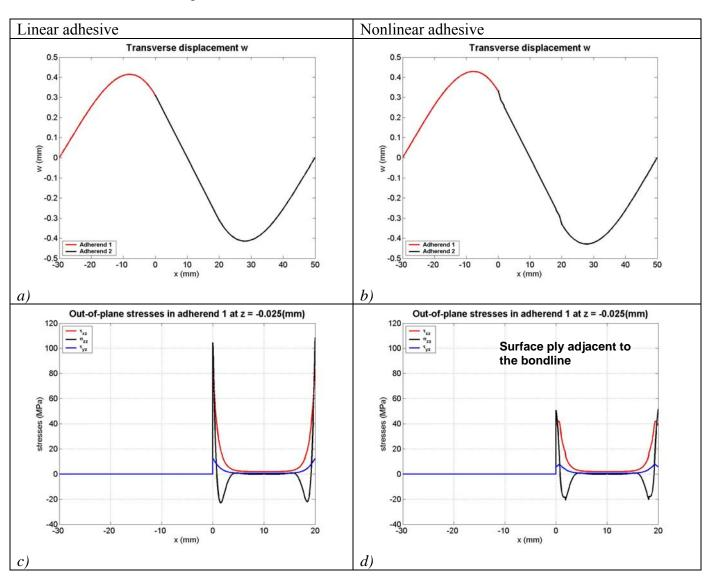


Fig. 8.2.7, Sample result comparison between linear and non-linear adhesive solutions for the Mortensen thesis single lap joint example.

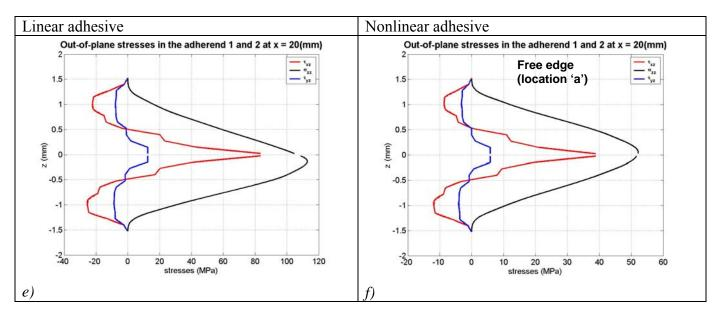


Fig. 8.2.7 (cont.), Sample result comparison between linear and non-linear adhesive solutions for the Mortensen thesis single lap joint example.

8.3 References

- 8.1 Mortensen, F., "Development of Tools for Engineering Analysis and Design of High Performance FRP-Composite Structural Elements," Ph.D. Thesis, Institute of Mechanical Engineering, Aalborg University (Denmark), Special Report no. 37, 1998.
- 8.2 ESAComp 2.0 software, personal contact.

8.4 Supplemental Results

8.4.1 Supplemental Results for the Bonded Doubler Example

In addition to the BondJo to Mortensen comparison results shown in section 8.1, BondJo also provides the following results, which were not verified against the Mortensen thesis. These results are included here for reference.

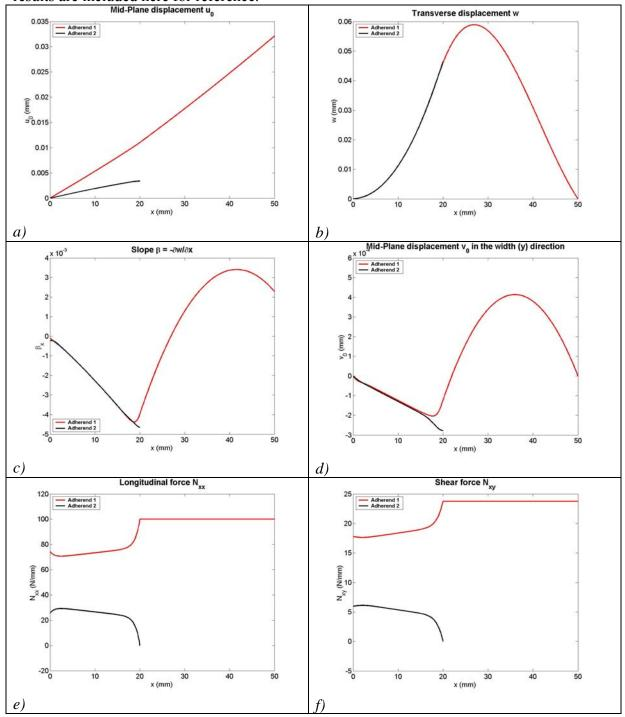


Fig. 8.4.1, Supplemental BondJo results for the bonded doubler joint example problem from [8.1]. These results are not verified but included here for reference.

Black = Adherend 2 Moment M_{xx} Transverse Shear Q Adherend 1
Adherend 2 Adherend 1
Adherend 2 20 -10 0 10 x (mm) x (mm) *h*) g)In-plane Normal force N_{yy} Moment M 25 Adherend 1
Adherend 2 (N/mm) 10 10 20 40 20 40 x (mm) x (mm) i)Twisting Moment M_{xy} Shear Force Q Adherend 1
Adherend 2 0.5 40 10 *k*) *l*)

Red = Adherend 1

Fig. 8.4.1 (cont.), Supplemental BondJo results for the bonded doubler joint example problem from [8.1]. These results are not verified but included here for reference.

Black = Peel Stress (σ_z) Red = Interlaminar Shear (τ_{xy}) Blue = Interlaminar Shear (τ_{yz})

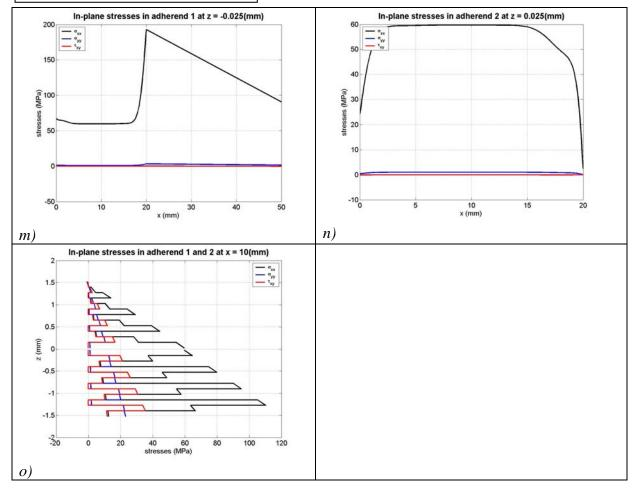


Fig. 8.4.1 (cont.), Supplemental BondJo results for the bonded doubler joint example problem from [8.1]. These results are not verified but included here for reference.

Black = Peel Stress (σ_z) Red = Interlaminar Shear (τ_{xy}) Blue = Interlaminar Shear (τ_{yz})

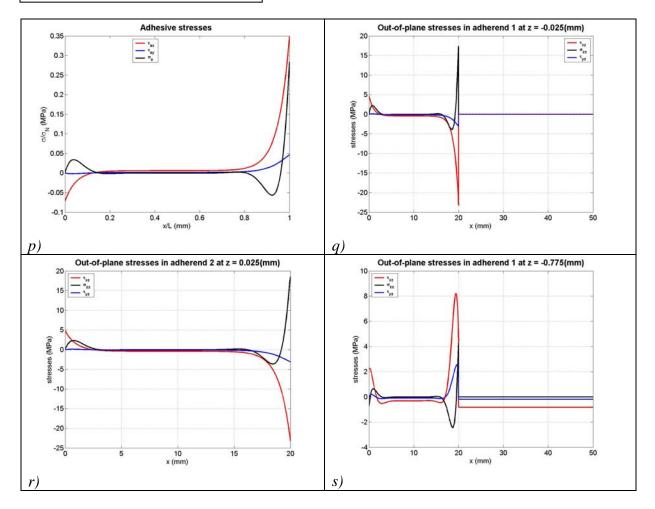


Fig. 8.4.1 (cont.), Supplemental BondJo results for the bonded doubler joint example problem from [8.1]. These results are not verified but included here for reference.

Black = Peel Stress (σ_z) Red = Interlaminar Shear (τ_{xy}) Blue = Interlaminar Shear (τ_{yz})

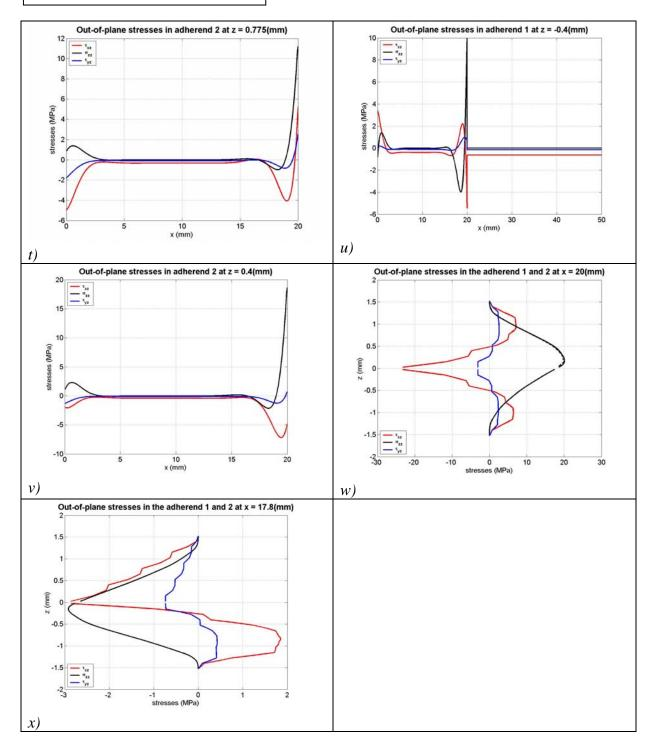


Fig. 8.4.1 (cont.), Supplemental BondJo results for the bonded doubler joint example problem from [8.1]. These results are not verified but included here for reference.

8.4.2 Supplemental Results for the Single Lap Joint Example

The following additional comparison results between BondJo and the Mortensen publication for the stepped lap joint with linear adhesive model are shown for reference.

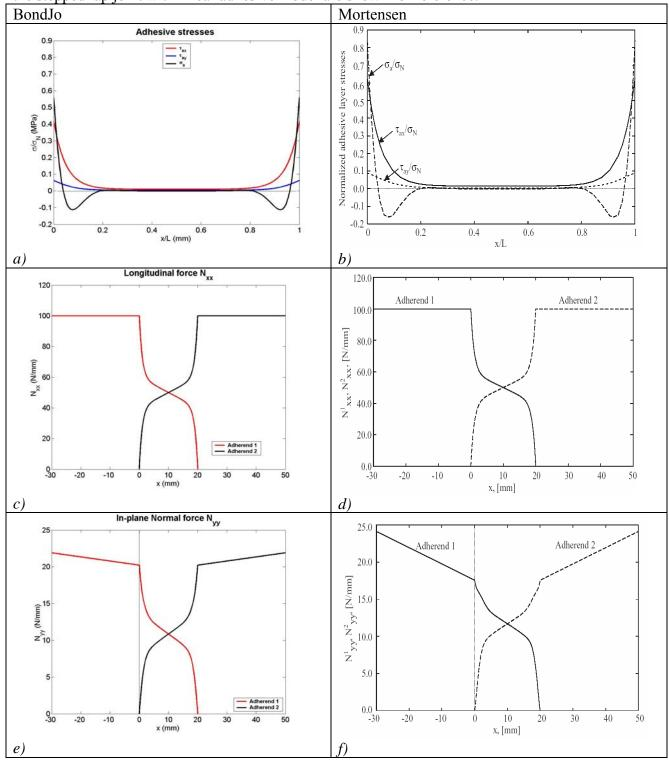


Fig. 8.4.2, Supplemental BondJo results for the single lap joint with linear adhesive example problem verified against [8.1]. See Section 8.2.2 for discussion of discrepancies between BondJo and Mortensen.

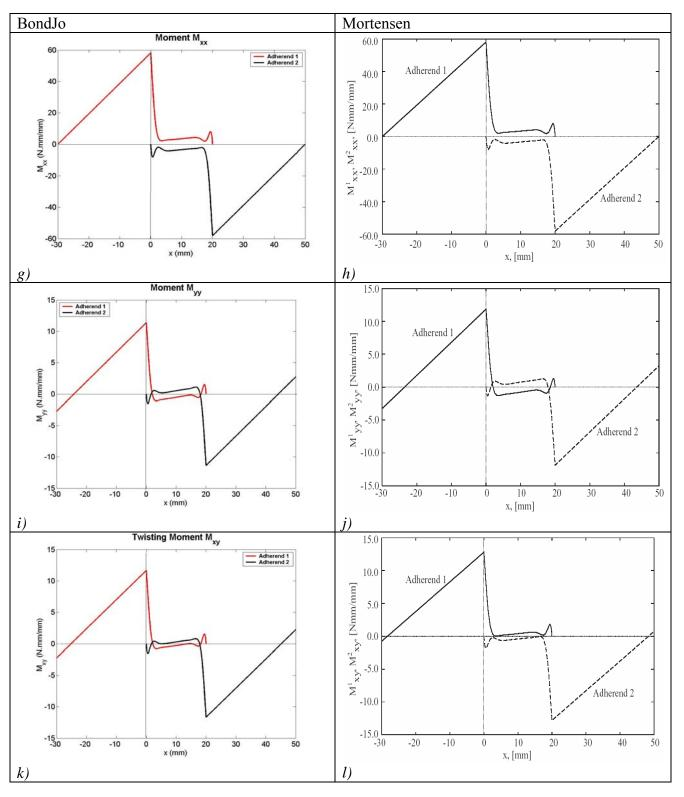


Fig. 8.4.2 (cont.), Supplemental BondJo results for the single lap joint with linear adhesive example problem verified against [8.1]. See Section 8.2.2 for discussion of discrepancies between BondJo and Mortensen.

The following "corrected" result was received from Mortensen directly [8.2] along with the v_0 displacement shown in Fig. 8.2.4.

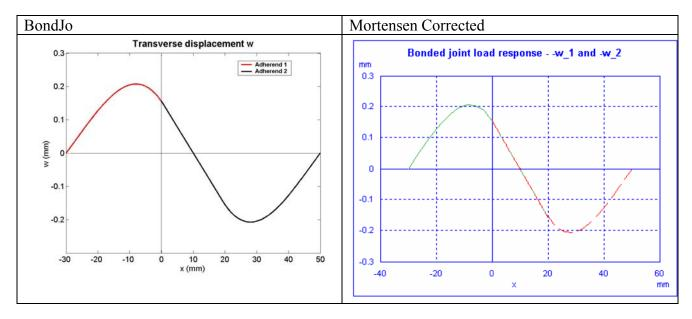


Fig. 8.4.3, Supplemental BondJo results for the stepped lap joint with linear adhesive example. Comparison of BondJo to corrected results sent by the author of [8.1] show very close agreement between BondJo and Mortensen's results.

In addition to the BondJo to Mortensen comparison results shown above, BondJo also provides solutions for the local fields, such as adherend in-plane and out-of-plane stresses. The following results are not verified by the Mortensen publication, but are included here for reference.

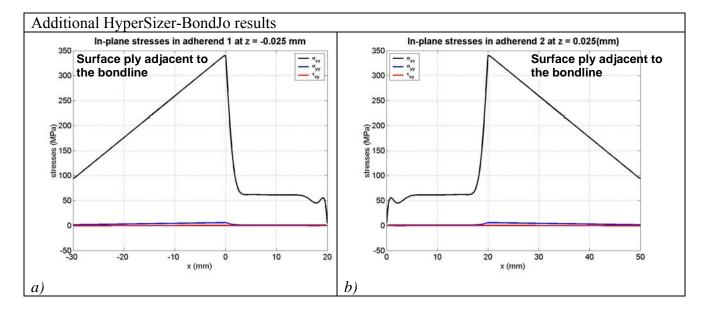


Fig. 8.4.4, Supplemental BondJo results for the single lap joint example from [8.1]. These results are not verified but included here for reference.

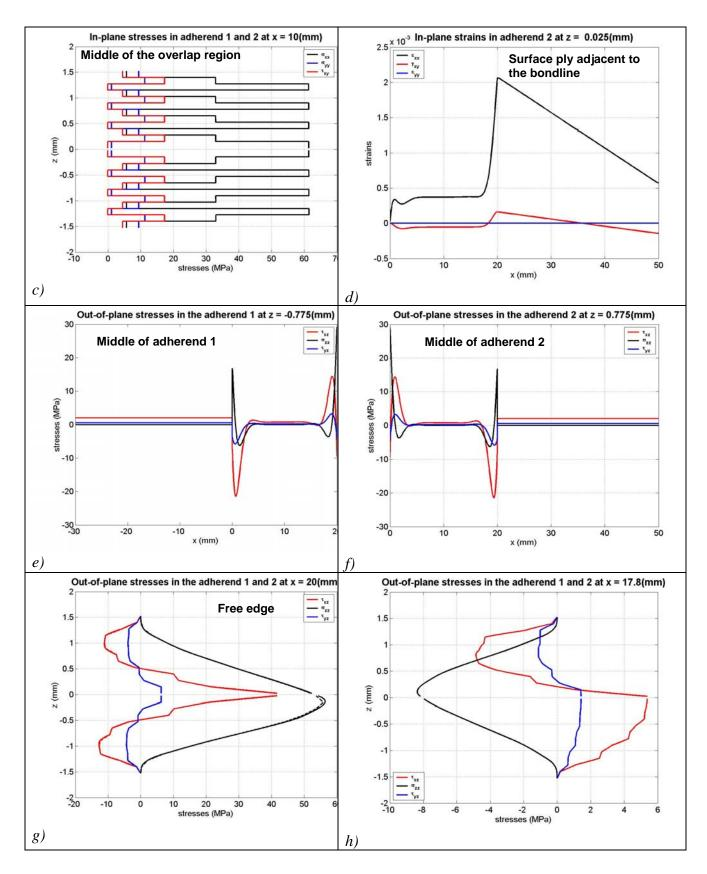


Fig. 8.4.4 (cont.), Supplemental BondJo results for the single lap joint example problem from [8.1]. These results are not verified but included here for reference.

8.4.3 Supplemental Single Lap Joint Results for Linear Versus Non-Linear Adhesive Comparison

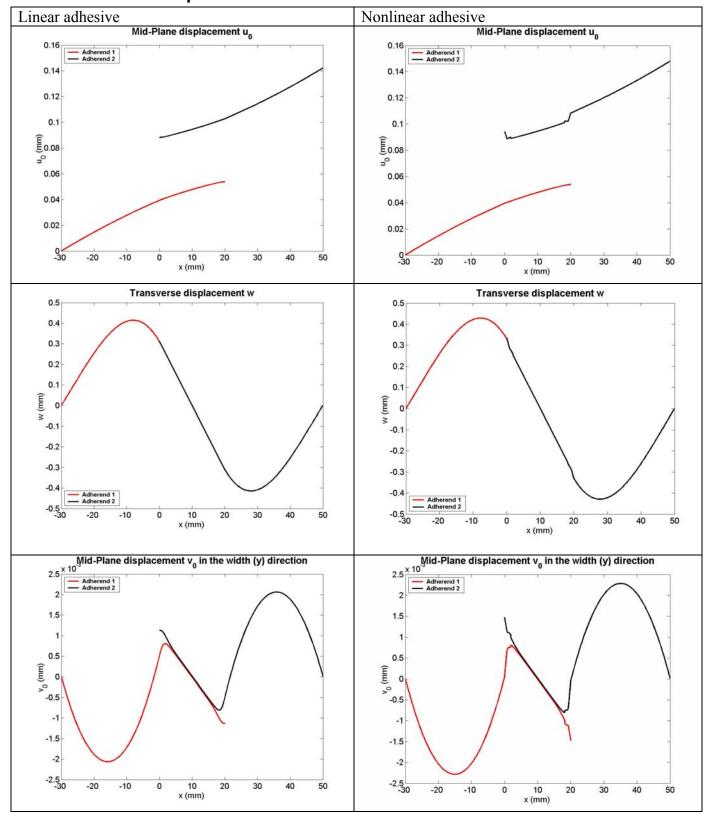


Fig. 8.4.5, Supplemental BondJo results for the single lap joint example linear to non-linear adhesive comparison. These results are not verified but included here for reference.

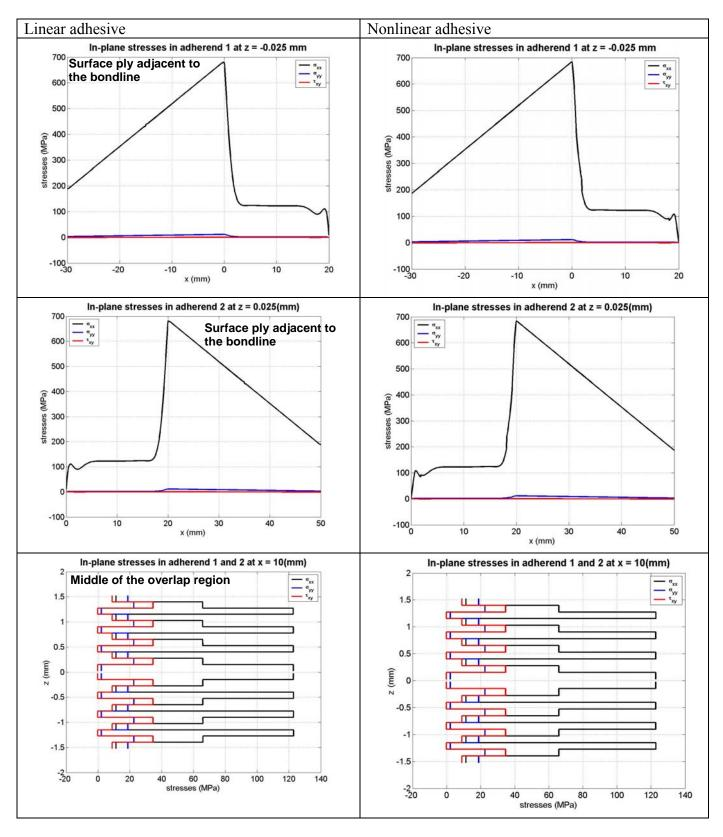


Fig. 8.4.5 (cont.), Supplemental BondJo results for the single lap joint example linear to non-linear adhesive comparison. These results are not verified but included here for

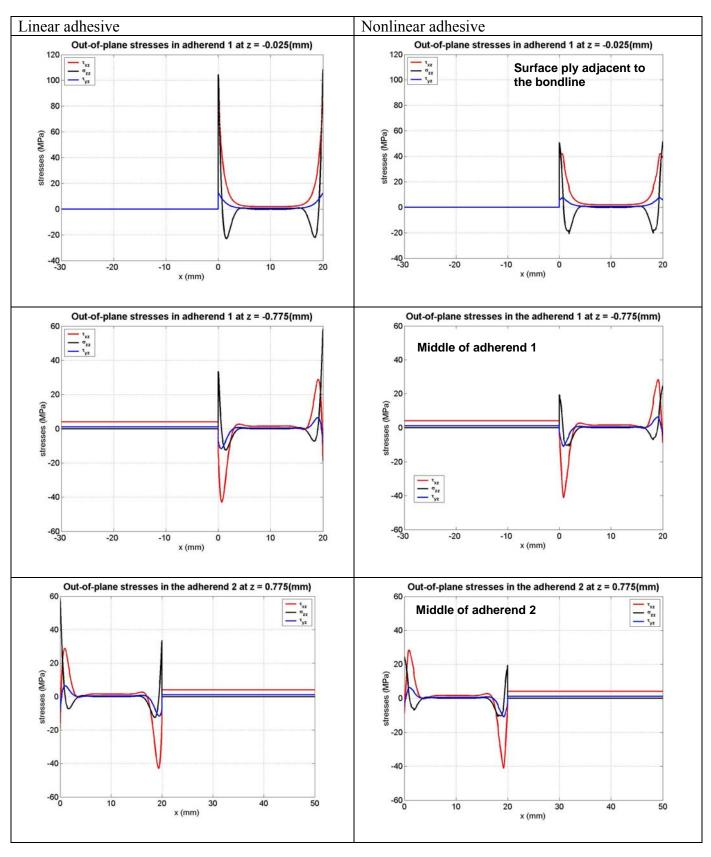


Fig. 8.4.5 (cont.), Supplemental BondJo results for the single lap joint example linear to non-linear adhesive comparison. These results are not verified but included here for

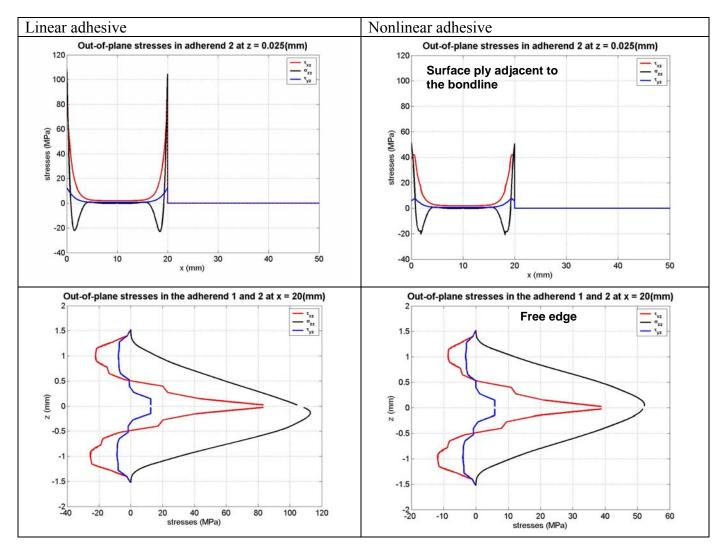


Fig. 8.4.5 (cont.), Supplemental BondJo results for the single lap joint example linear to non-linear adhesive comparison. These results are not verified but included here for

Fig. 8.4.5 plots HS-BondJo results for linear adhesive with those for nonlinear adhesive in the single-lap joint. It shows that the displacements and in-plane stresses of the adherends are not minimally affected by yielding of the adhesive, while the out-of-plane stresses are affected significantly, particularly those near the free edge. In Figs. 8.4.6–8.4.8 we show the adhesive stresses obtained with different nonlinear adhesive models, which are plotted in Fig. 8.2.5 for AY103 epoxy adhesive. It can be seen that the yield behaviors of the adhesive near the free edge are different for each model.

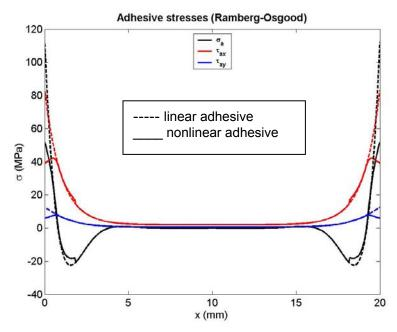


Fig. 8.4.6, Adhesive stresses in the single-lap joint under tension of Nxx = 200 N/mm using the Ramberg-Osgood model.

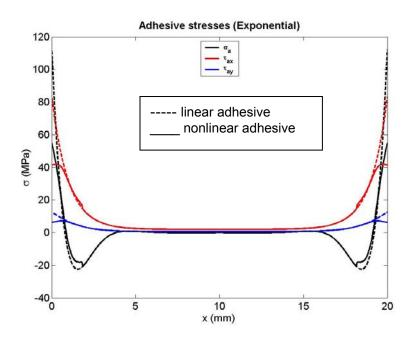


Fig. 8.4.7, Adhesive stresses in the single-lap joint under tension of Nxx = 200 N/mm using the exponential law model.

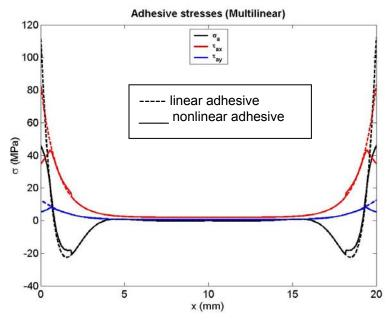


Fig. 8.4.8, Adhesive stresses in the single-lap joint under tension of Nxx = 200 N/mm using multilinear model.

---Single Test Data Validation---

9 Validation – Bonded Doubler Joint, Woven Fabric Laminate, Tong Publication

9.1 Summary of Results

The purpose of this study is to validate HyperSizer-BondJo against a series of tests conducted by Cheuk and Tong [9.2]. This series of experiments investigated interlaminar failure of bonded shear lap joints with embedded cracks. In the present study, we select the validation case from a group of experimental results for the specimen without cracks. Fig. 9.1.1 shows actual specimen failure and HS-BondJo model for this problem. The predicted results and test data are tabulated in Table 9.1.

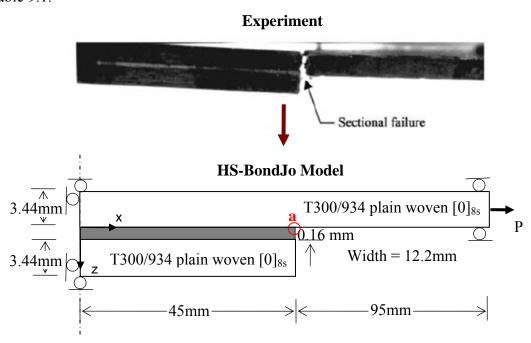


Fig. 9.1.1, Experiment and HS-BondJo models for bonded doubler specimens studied by Cheuk and Tong [9.2].

Table 9.1, Summary of predicted failure load vs. experimental result

	Experiment		BondJo prediction using linear adhesive	BondJo prediction using nonlinear adhesive	
	No.1	19.162			
Failure load (kN)	No.2	18.272			
	No.3	17.502			
	No.4	18.987			
	No.5	18.765			
	No.6	19.048			
	Average	18.623	13	14	

In this study, both linear and nonlinear analyses are performed to predict the failure load of the specimen subjected to longitudinal tension. Max principal stress criterion is used for sectional fracture of adherends. The predictions are compared to the experimental results. It shows that the location failure point predicted by *HS-BondJo* matches well with experimental observation, while the predicted failure load with linear analysis is 13 kN, which is relatively conservative compared to the measured ultimate failure load in the tests, which is 18.6 kN.

The discrepancy between prediction and test results may be due to the progressive damage involved in the experiment where the predicted failure load by *HS-BondJo* only accounts for the damage initiation. Nonlinear analysis predicts slightly higher failure load (14 kN), but is still conservative compared to the test data.

9.2 Problem Definition

Fig. 9.2.1 depicts schematically the geometrical configurations of bonded lap shear specimens used by Cheuk and Tong. The specimens have an overlap length of 45 mm and an unsupported length of 95 mm. The material used for manufacturing the composite adherends is T300/934 carbon/epoxy plain-woven, with orientation of 0-degree. Table 9.2.1 lists typical mechanical properties of a single ply of T300/934 plain-woven prepreg tape. Film adhesive FM300-K from Cytec was chosen to bond the two panels together. The mechanical properties of the FM300-K adhesive are listed in Table 9.2.2. Note S_{prop} represents the proportional limit of adhesive; S_{ult} and e_{ult} are the ultimate stress and strain respectively. λ is the ratio of compressive yield stress to the tensile yield stress of the adhesive. Fig. 9.2.2 plots the experimental data [9.1] of the actual stress-strain relation of FM300-K adhesive and the approximated stress-strain relation using the Ramberg-Osgood model.

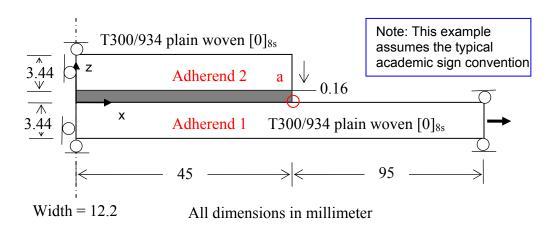


Fig. 9.2.1, Schematics of bonded doubler test specimens examined by Cheuk and Tong. Six specimens were tested and the results are summarized in Table 9.4. Point a is the location of damage initiation in adherend 1.

Table 9.2.1, Mechanical properties of a ply of T300/934 carbon/epoxy plain woven prepreg

Longitudinal modulus $E_1 = E_2$, MPa	57226
Transverse modulus E ₃ , MPa	4800
In-plane shear modulus G ₁₂ , MPa	4481
Out-of-plane shear modulus $G_{13} = G_{23}$, MPa	4400
In-plane Poisson ratio v_{12}	0.05
Out-of-plane Poisson ratio $v_{13} = v_{23}$	0.28
In-plane tensile strength X_t , MPa	518

Table 9.2.2, Mechanical properties of FM300-K adhesive

	Е	v	S_{prop}	S_{ult}	e_{ult}	λ
	(GPa)		(MPa)	(MPa)		
FM300-K	2.40	0.32	25.92	69.88	0.0685	1.0

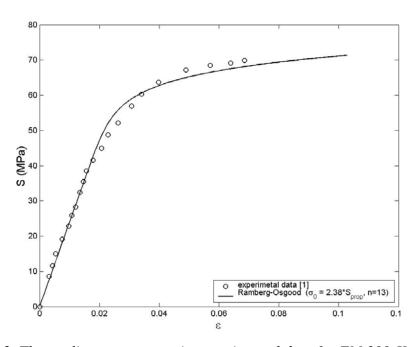


Fig. 9.2.2, The nonlinear stress-strain experimental data for FM 300-K adhesive used in the analysis along with a Ramberg-Osgood approximation of that data.

9.3 Experimental Results

9.3.1 Visualization of Joint Failure

According to the test report, the measured axial load increases almost linearly with the crosshead displacement for all specimens. Specimens failed in net sectional fracture when the respective ultimate failure load was attained, as shown in Fig. 9.3.1. Table 9.3.2 lists the ultimate failure loads of bonded lap shear joints subjected to axial tension. Note that the joint is made of woven

fabric which is prone to damage prior to ultimate failure. Thus the fracture is very likely initiated at a certain location where high stress concentration resides. As the damage grows to the critical level, the subsequent fracture of the entire adherend occurs. Unfortunately, Tong did not provide the load-displacement curves for the specimens, so the damage initiation load could not be identified.

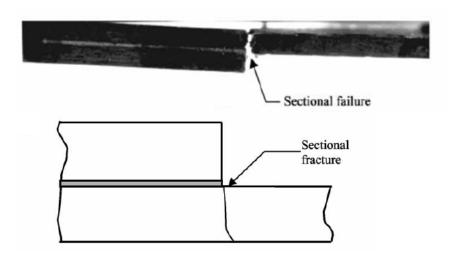


Fig. 9.3.1, Sectional failure of bonded doubler joint specimen.

9.3.2 Test Data

The test ultimate failure load of specimens under axial tension are recorded and tabulated in Table 9.4. The average test ultimate failure load for the bonded doubler joints without cracks is 18.6 kN.

Table 9.3.2, ultimate failure load of bonded doubler joint specimens

Specimen no.	0-1	0-2	0-3	0-4	0-5	0-6	average
Final Failure	19.162	18.272	17.502	18.987	18.765	19.048	18.623
load (kN)							± 0.633

9.4 HS-BondJo Prediction

HS-BondJo performs stress and failure analyses for the bonded joint specimen subjected to axial tension. The solution domain for the stress analysis is shown in Fig. 9.2.1, together with the boundary conditions applied to this problem. Based on the experimental observation, the maximum principal stress criterion is adopted herein to predict the failure loads. The margin of safety (MS) is checked at each point along the interfacial plies in adherend 1 under incremented loads. Once the MS is less than zero at any point in the adherends, the load increment stops. Note that the MS is plotted at the bottom and top of each ply because the in-plane stresses may change from one ply to the next.

9.4.1 Linear analysis

The predicted load for the problem with linear elastic adhesive properties is P_{linear} =13 kN, which is equivalent to 1066 N/mm. Figs. 9.4.1(a)-(b) show the in-plane and out-of-plane stresses in the adherends at the failure load. In this case, the in-plane stress σ_{xx} is dominant, compared to the out-of-plane stresses, σ_{zz} , τ_{yz} .

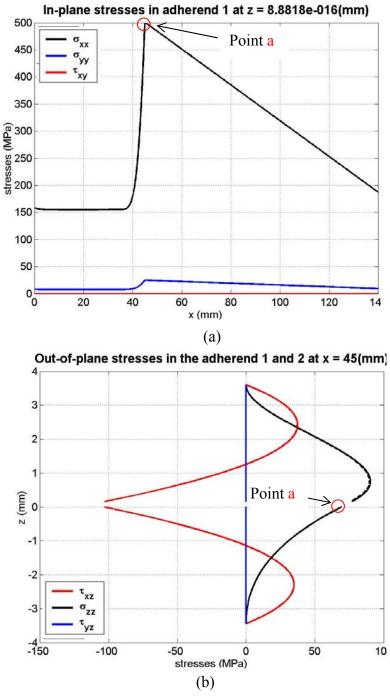


Fig. 9.4.1,(a) In-plane stresses in the surface ply of adherend 1; (b)through-the-thickness distribution of out-of-plane stresses at the free edge of bonded doubler joint with linear adhesive under the predicted failure load of 13 kN.

For the linear analysis, the margin of safety can be calculated using the stress analysis results and the failure criterion of maximum principal stress. The following demonstrates the procedure of calculation of MS at point a. First, the principal stresses is obtained from

$$(\sigma_{1}, \sigma_{2}, \sigma_{3}) = eigenvalues \begin{pmatrix} \sigma_{xx} & \tau_{xy} & \tau_{xz} \\ \tau_{yx} & \sigma_{yy} & \tau_{yz} \\ \tau_{zx} & \tau_{zy} & \sigma_{zz} \end{pmatrix} = eigenvalues \begin{pmatrix} 493.98 & 0 & -102.95 \\ 0 & 24.6988 & \\ -102.95 & 69.2197 \end{pmatrix}$$
(9.4.1.1)

$$(\sigma_1, \sigma_2, \sigma_3) = (517.6, 45.58, 24.70)$$
 (9.4.1.2)

Thus, the maximum principal stress at point a is

$$\sigma_{principal}^{\text{max}} = 517.6(\text{MPa}) \tag{9.4.1.3}$$

The MS is given by

$$MOS = \frac{X_t}{\sigma_{principal}} - 1 = \frac{518}{517.6} - 1 = 7.73 \times 10^{-4}$$
 (9.4.1.4)

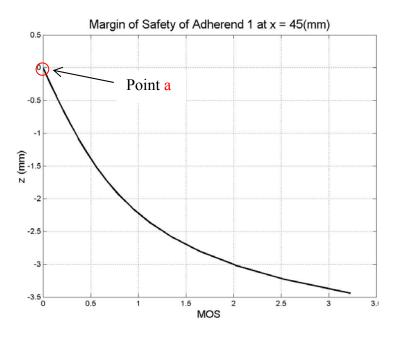


Fig. 9.4.1(c), Through-the-thickness of MS in adherend 1 near the free edge of bonded doubler joint with linear adhesive under predicted failure load of 13 kN.

The margins of safety of each ply in the adherends are shown in the section of supplemental results. The MS at point a is approximately zero, indicating that failure in adherend 1 occurs at

that point. This is consistent with experimental observations, as shown in Fig. 9.2.2. However, this predicted value is more conservative compared to the ultimate failure loads from the experiment, which is 18.6 kN average. This may be due to the progressive failure involved in sectional fracture of the plain-woven adherend, i.e. the joint can still sustain a load increment after damage initiation. The authors also implied that the damage occurs before the ultimate load is reached in the experiment, as is consistent with the evidence from other researchers that the plain woven composites are apt to be damaged under static load. It can be inferred that the damage initiation load should be much less than the ultimate failure load, 18.6 kN, thus possibly closer to BondJo's prediction. Please see section 9.7 for more stress analysis results.

9.4.2 Nonlinear analysis

Because FM 300-K adhesive shows very pronounced nonlinear behavior as shown in Fig. 9.2.2, it is necessary to perform a nonlinear analysis for this problem. The predicted failure load with nonlinear adhesive is $P_{nl} = 14$ kN, slightly higher than the 13 kN predicted for linear analysis. Fig. 9.4.2(a) shows the adhesive stresses obtained with linear and nonlinear adhesive using Ramberg-Osgood model under longitudinal tension of 14 kN. It clearly shows yielding of the adhesive layer. Figs. 9.4.2(b)-(c) show in-plane stresses in the surface ply of adherend 1 and the through-the-thickness out-of-plane stresses at the free edge. Please see section 9.7 for more stress analysis results.

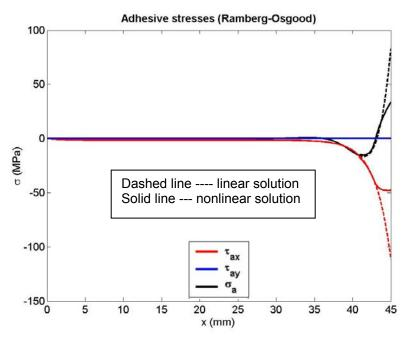
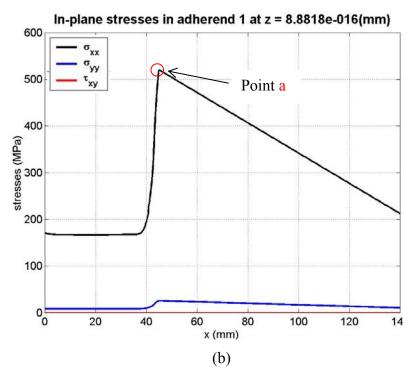


Fig. 9.4.2(a), Adhesive stresses due to yielding of adhesives under the predicted failure load of 14 kN.



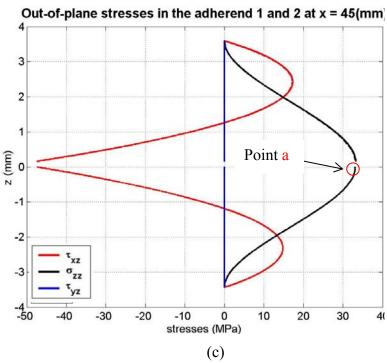


Fig. 9.4.2,(b) In-plane stresses in the surface ply of adherend 1; (c) through-the-thickness distribution of the out-of-plane stresses at the free edge of bonded doubler joint with nonlinear adhesive under predicted failure load of 14 kN.

Compared to the linear solutions, the nonlinear adhesive only slightly affects the in-plane stresses, while the out-of-plane stresses are significantly reduced, particularly near the free edges.

Similar to the procedure for the linear analysis, margin of safety can be calculated using the nonlinear stress analysis results and the failure criterion of maximum principal stress. For example, for calculation of MS at point a, we first find the maximum principal stress at point a is

$$\sigma_{principal}^{\text{max}} = 524.6(\text{MPa}) \tag{9.4.2.1}$$

The MS at point a is then given as

$$MS = \frac{X_t}{\sigma_{principal}} - 1 = \frac{518}{524.6} - 1 = -0.0126$$
 (9.4.2.2)

Fig. 9.4.2(d) shows the through-the-thickness distribution of the MS in adherend 1 the bondline leading edge (point a). The MS at the corner of the top surface ply of adherend 1 reaches zero, indicating that adherend 1 fails at that point.

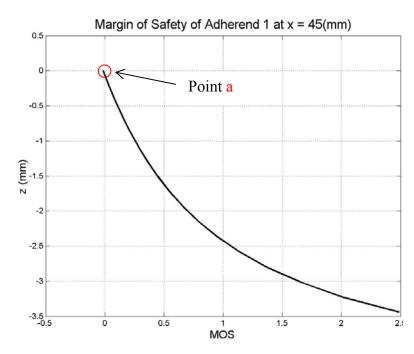


Fig. 9.4.2(d), Through-the-thickness of MS in adherend 1 near the free edge of bonded doubler joint with nonlinear adhesive under predicted failure load of 14 kN.

9.5 Conclusions

The bonded doubler joint specimen studied by Cheuk, et al [9.2] was used as a validation case for *HS-BondJo*. Analyses using linear and nonlinear adhesive were performed to predict the failure load of the specimen subjected to a longitudinal tension. Max principal stress criterion was used to predict sectional fracture of the adherends. Compared to published data, It shows that the failure location predicted by *HS-BondJo* matches well with the experimental observation, while the predicted failure load with linear analysis is relatively conservative

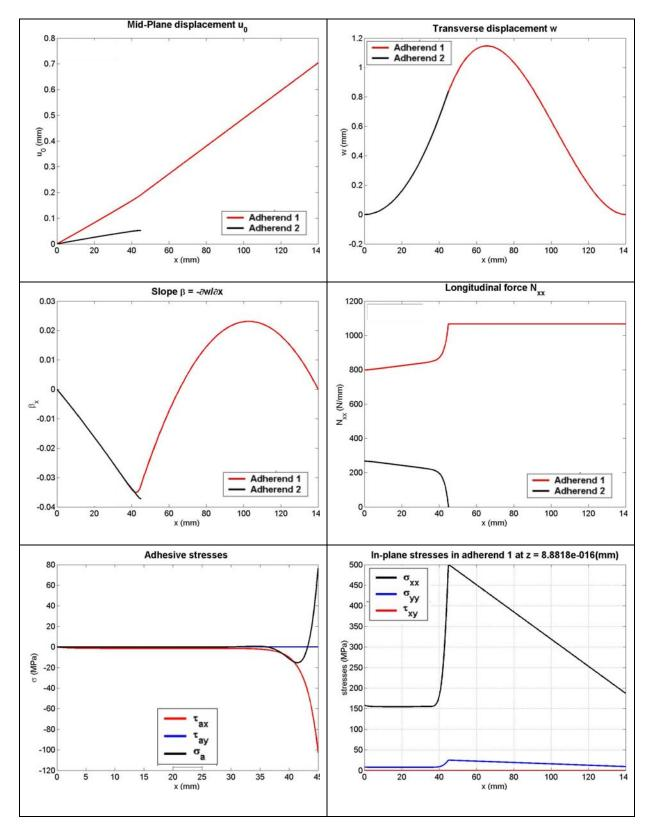
compared to the measured ultimate failure load in the tests. The discrepancy may be due to the progressive damage involved in the experiment and the predicted failure load by *HS-BondJo* only accounts for the damage initiation. Nonlinear analysis predicted a slightly higher failure load, but is still conservative compared to the test data. This is due to the section failure of the adherend being controlled by the in-plane tensile stress, which is less affected by yield of the adhesive layer than the out-of-plane stresses.

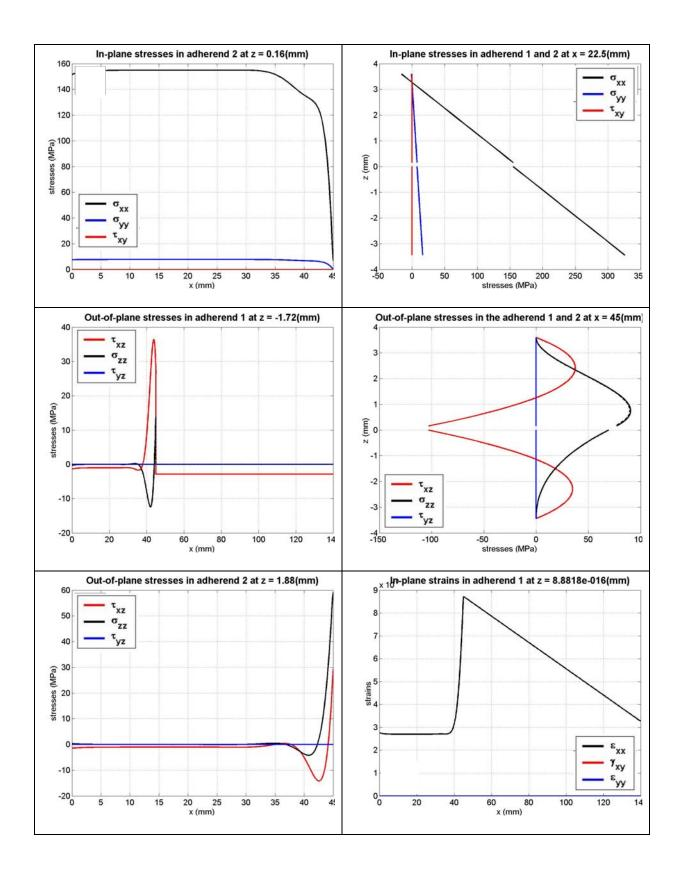
9.6 References

- 9.1 Tong, L., 1997, "An Assessment of Failure Criteria to Predict the Strength of Adhesively Bonded Composite Doubler Lap Joints," *Journal of Reinforced Plastics and Composites*, Vol. 16 (18), pp.698-713.
- 9.2 Cheuk, P. T. and Tong L., (2002), "Failure of adhesive bonded composite lap shear joints with embedded precrack," *Composites Science and Technology*, 62, 1079-1095.
- 9.3 Mortensen, F., (1998), "Development of Tools for Engineering Analysis and Design of High-Performance FRP-composite Structural Elements," Ph.D. Thesis, Institute of Mechanical Engineering, Aalborg University (Denmark), Special Report no. 37.
- 9.4 Cox, B. N. and Flanagan, G., Handbook of Analytical Methods for Textile Composites, NASA contractor report 4750, 1997.

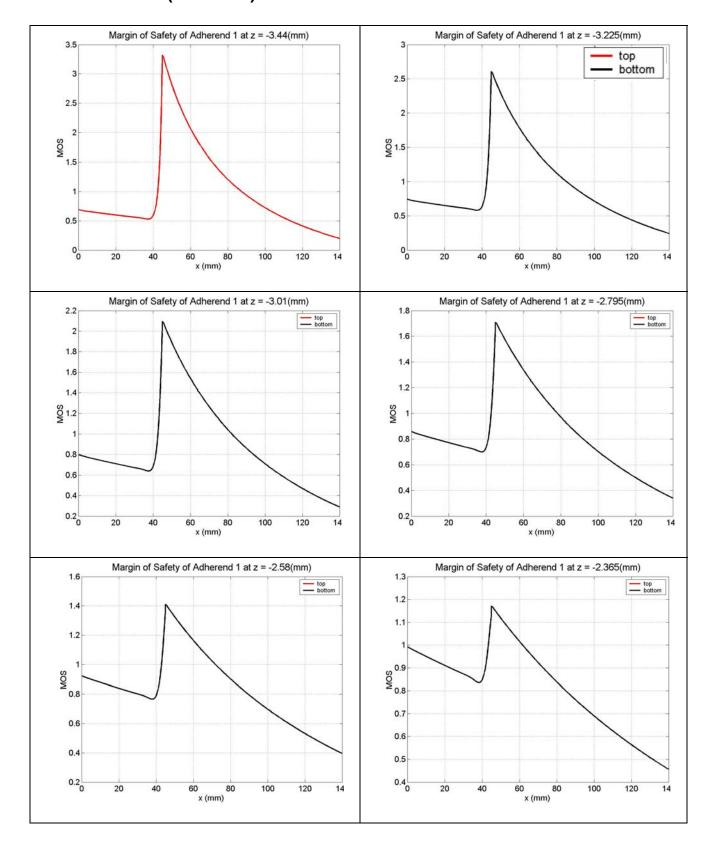
9.7 Supplemental Results

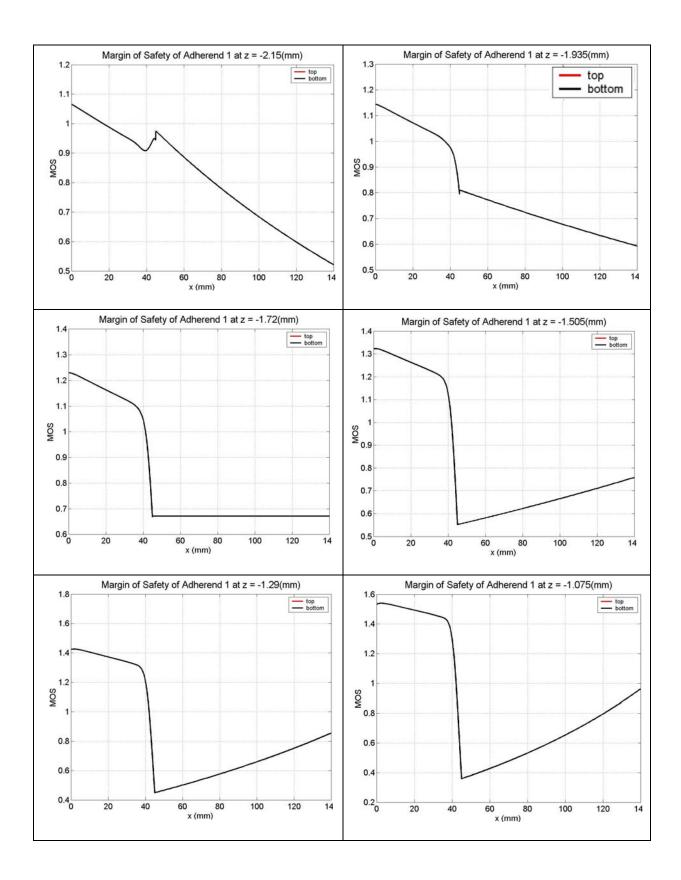
9.7.1 HS-BondJo Stress Analysis Results Using Linear Adhesive (P = 13 kN)

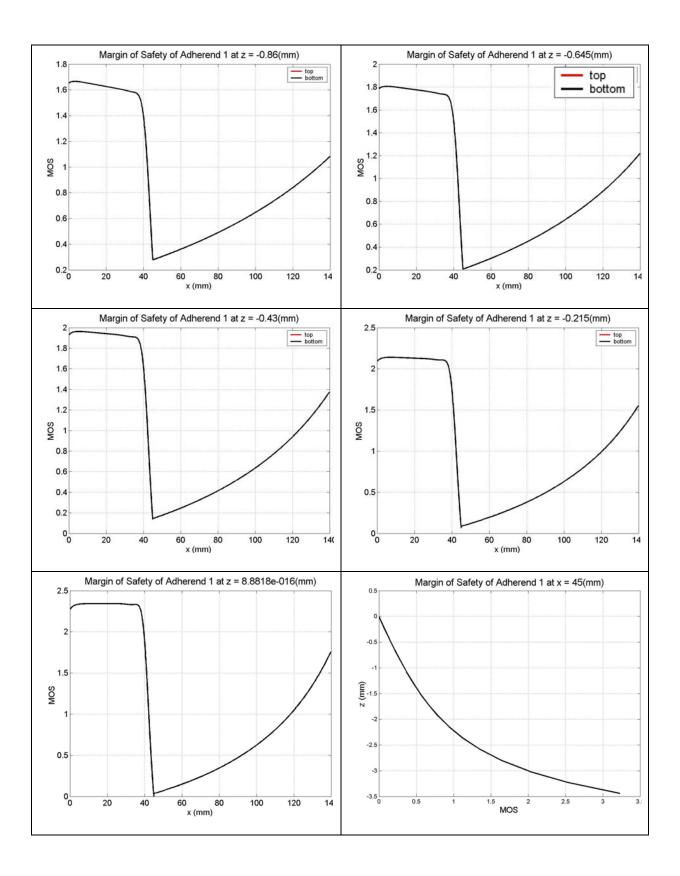


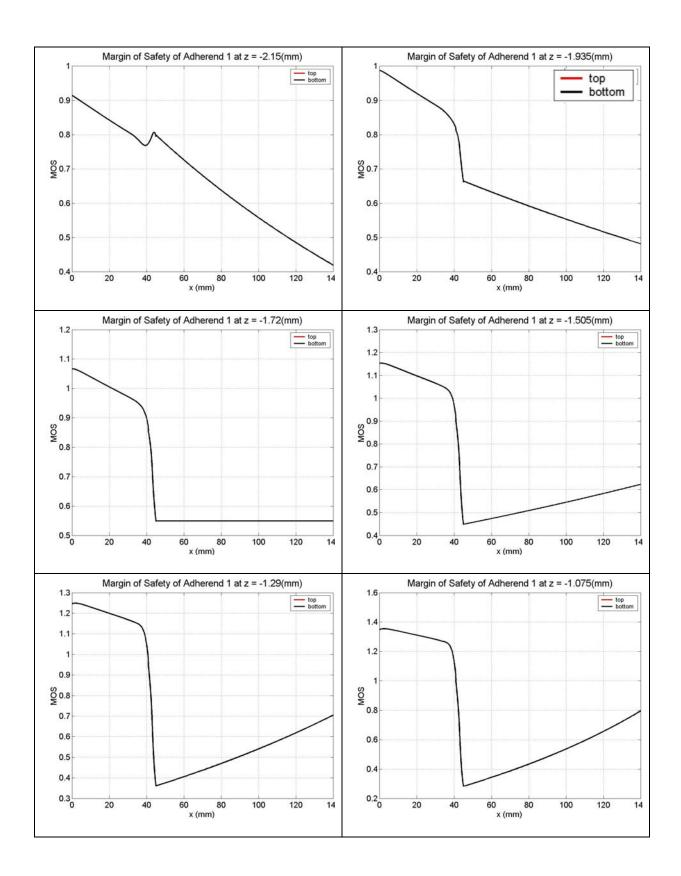


9.7.2 HS-BondJo Calculation of MS in the Adherends using Linear Adhesive (P = 13 kN)

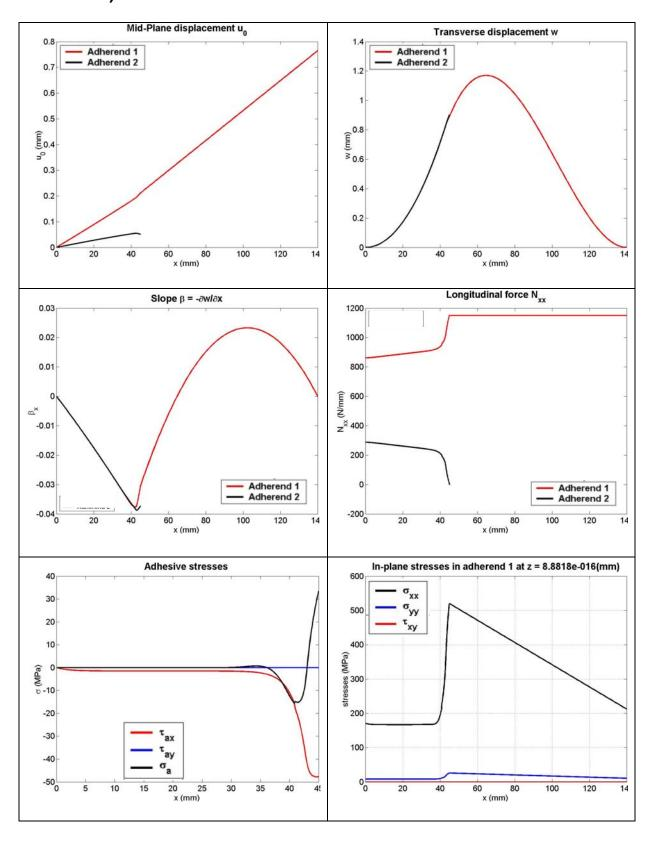


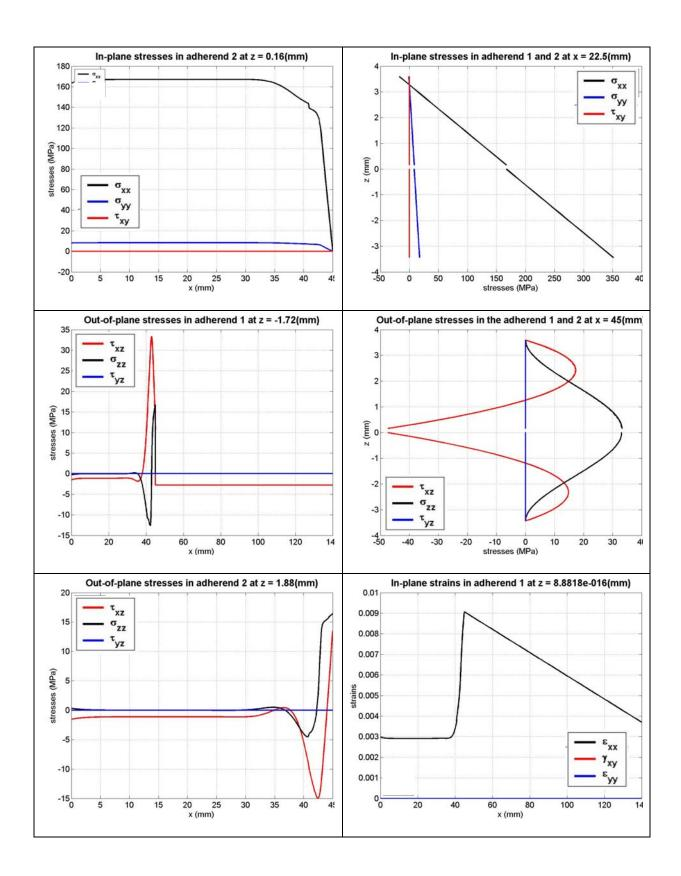




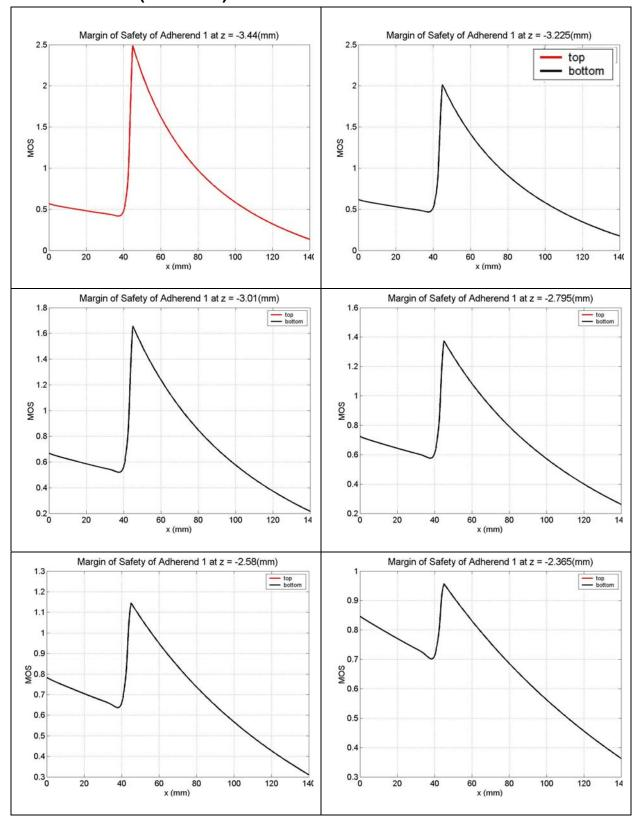


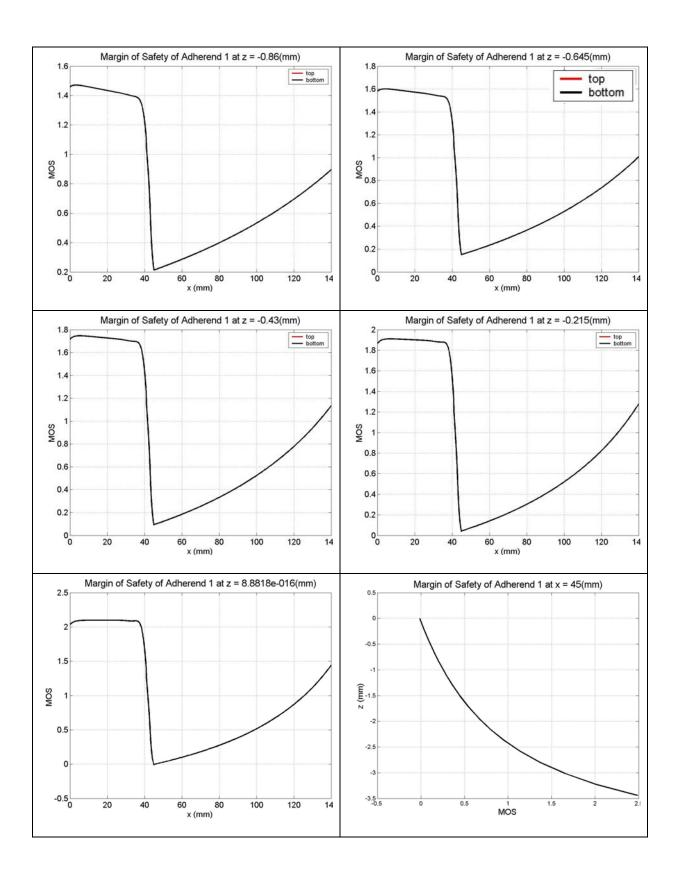
9.7.3 HS-BondJo Stress Analysis Results Using Nonlinear Adhesive (P = 14 kN)





9.7.4 HS-BondJo Calculation of MS in the Adherends using Nonlinear Adhesive (P = 14 kN)





10 Validation – Bonded Doubler Test [0/±45/90] Laminate with Step Taper, NASA Publication

10.1 Summary of Results

Recently, NASA Langley Research Center conducted a series of tests to investigate the failure mechanism of bonded skin/flange configuration [10.2-10.3, 10.6-10.9]. Based on these experiments, NASA researchers also have developed many analytical and numerical models to predict

Note: Results for this Validation Example have been updated in reference 10.13 that shows closer HyperSizer prediction to test.

the failures of skin/stiffener debonding. In particular, the model developed by Krueger et al. [10.2] using delamination fatigue characterization data and a geometric nonlinear finite element analysis correlates well to the test.

The experiment studied by Krueger for bonded composite skin/stringer structures is selected as a validation case for HS-BondJo. Fig. 10.1 shows the failure of the specimen and models of HS-BondJo for this problem. The predicted results and test data are tabulated in Table 10.1.

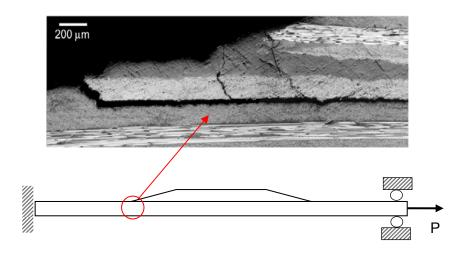


Fig. 10.1, Experiment results and HS-BondJo models for bonded doubler specimen studied by Krueger et al [10.2].

Table 10.1, summary of predicted failure load vs. experimental result

	Experi	ment	BondJo prediction using linear adhesive	BondJo prediction using nonlinear adhesive
Failure load (kN)	No.1	16.2		
	No.2	16.5		
	No.3	18.1		
	No.4	18.3		
	No.5	19.8		
	Average	17.8	24.3	> 27.6

Both linear and nonlinear adhesive properties are considered in this study. The failure criterion of maximum transverse principal stress is used to predict the onset of matrix cracking and the margin of safety is checked at each point of the adherends. The predicted location of damage onset by linear analysis is consistent with experimental observation, while the predicted load for the damage initiation is 24.3 kN, which is about 1.4 times the tested average strength of 17.8 kN. This error may attribute to many factors, such as hygrothermal effect, spew fillet, and so on. Nonlinear analysis shows that soft adhesive will significantly increase the damage resistance of adherend to matrix cracking. Table 10.1 tabulates the predicted failure loads and the test average.

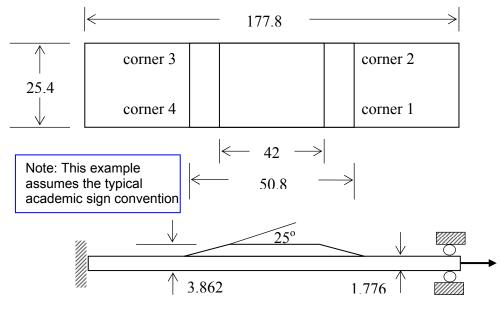
10.2 Problem Definition

The schematic of skin/flange specimen is shown in Fig. 10.2.1. The specimen consists of a tapered flange bonded to the skin. The skin was made of IM7/8552 graphite/epoxy prepreg tape and had a nominal ply thickness of 0.148 mm and a [45/-45/0/-45/45/90/90/-45/45/0/45/-45] layup. The flange was made of an IM7/8552 plain woven fabric, with a lay-up of [45/0/45/0/45/0/45] and nominal thickness of 0.212 mm. The flange was pre-cured, cut to size, machined with a 25° taper along the edges and co-bonded with uncured skin using one ply of grade 5, FM 300 adhesive film. The panel then was cut into 25.4 mm wide by 177.8 mm long specimens. The thickness of the adhesive layer is 0.178 mm. Typical material properties are summarized in Table 10.2.

Quasi-static tension tests were performed in displacement control at a stroke rate of 0.4 mm/min. The specimens were mounted in hydraulic grips with a gage length of 101.6 mm. A total of 4 specimens were tested. A damage onset load was determined at which a small initial load drop was observed prior to flange debonding. The value of the damage onset load was averaged from five tests and determined to be 17.8 kN which was later designed as $P_{100\%}$. The test was terminated when the flange debonded from the skin. The details of the subsequent fatigue test are described in [10.2]. Modeling of fatigue test will not be discussed in this section.

Table 10.2, Linear elastic constants of materials for skin/flange specimens

	IM7/8552 Graphite /Epoxy Prepreg tape	IM7/8552 Plain Woven Fabric	Grade 5 FM300 Adhesive
E ₁ (GPa)	161.0	71.7	1.72
E_2 (GPa)	11.38	71.7	1.72
E ₃ (GPa)	11.38	10.3	1.72
v_{12}	0.32	0.04	0.30
v_{13}	0.32	0.35	0.30
v_{23}	0.45	0.35	0.30
G_{12} (GPa)	5.17	4.48	0.66
G_{13} (GPa)	5.17	4.14	0.66
G_{23} (GPa)	3.92	4.14	0.66



All dimensions in mm

Skin: [45/-45/0/-45/45/90/90/-45/45/0/45/-45] IM7/8552 tape, $t_{ply}=0.148$ Stiffener: [45/0/45/0/45/0/45/0/45] IM7/8552 plain woven fabric, $t_{ply}=0.212$

Adhesive: Grade 5 FM300, thickness = 0. 178 mm

Fig. 10.2.1, Schematics of a skin/flange specimen (bonded doubler) studied by Krueger et al. [10.2].

10.3 Experimental Results

10.3.1 Visualization of Joint Failure

All quasi-static and fatigue tests yielded similar damage patterns. Under quasi-static loading, failure occurred across one flange tip of the specimen only, with no clear preference for corners 1 and 2 or corners 3 and 4. In the static tests, the damage initiated in the form of matrix cracking at the top 45° skin ply and grew into the 45/-45 skin ply interface, as shown in Fig. 10.3.1. Similar damage initiation patterns were observed in the fatigue tests.

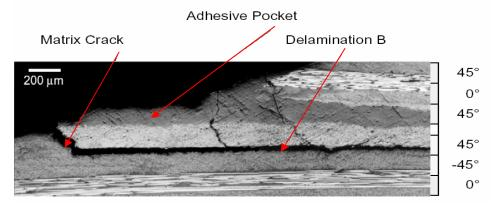


Fig. 10.3.1, Experimental observation of failure modes for boned doubler joint: matrix cracking induced delamination along 45/45 ply interface

10.3.2 Test Data

Krueger et al. [10.2] gave typical results of the five quasi-static tension tests shown as plots of load versus displacement or strain versus load. As shown in Fig. 10.3.2, the load-displacement curves were slightly nonlinear. Possible damage initiation was assumed when a small initial load drop was observed in two of the tests prior to flange debonding. At this point, a crack in one flange tip or even a small delamination along one flange corner was observed. In two specimens, no initial load drop or visible damage could be detected. In general, the initial load drop occurred above 90% of the maximum sustained load.

The tension fatigue failure of the specimens was characterized by plotting the applied tension load versus the number of load cycles at damage onset. The number of cycles to matrix crack onset was plotted for each specimen as shown in Fig. 10.3.3. The static strength values obtained from the quasi-static tests were also added to Fig. 10.3.3 at N=1 to complement the graph. Table 10.3 tabulates the static strength of five specimens and the mean value of static strength for the matrix cracking is $P_{ini} = 17.8 \text{ kN}$.

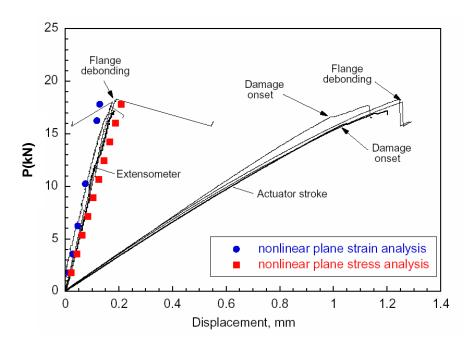


Fig. 10.3.2, Experiment results of load-displacement curves for bonded doubler specimens; The figure shows clearly the damage onset load and final flange debonding load.

Table 10.3, initial damage load of skin/flange specimens

Specimen no.	0-1	0-2	0-3	0-4	0-5	average
Final Failure	16.2	16.5	18.1	18.3	19.8	17.8
load (kN)						

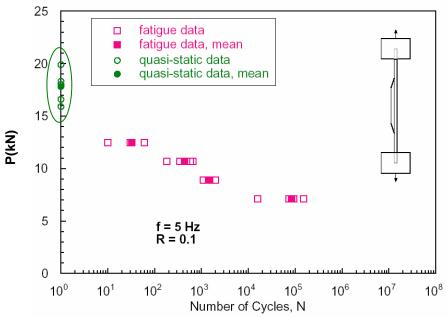


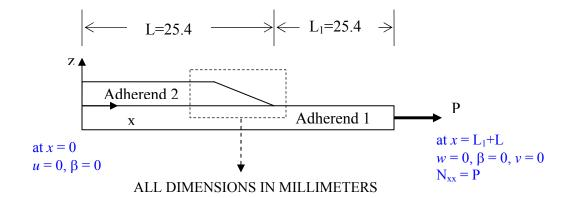
Fig. 10.3.3, Fatigue test data for the bonded doubler specimens. The quasi-static (N=1) points were used for BondJo comparison for damage initiation loads

10.4 HS-BondJo Prediction

10.4.1 HS-BondJo model for analysis

The *HS-BondJo* solution domain of the skin/flange specimen and the boundary conditions applied for this problem are shown in Fig. 10.4.1. The tapered edge of the flange (adherend 2) is modeled with stepped ends with finite thickness. The total number of steps is nine, which is equal to the number of plies in the flange. The thickness of each step is thus equal to the ply thickness; the length of each step is 0.488889 mm.

As shown in Fig. 10.3.1, the initial damage always occurred in the top 45-degree skin ply near the flange tip in form of matrix cracking. Earlier investigations [10.5,10.6] indicated that the matrix cracking occurred when the maximum principal transverse tensile stress attained the transverse tension strength of the material. Thus, the maximum transverse principal stress criterion is adopted herein to predict the initial damage of specimens. The average transverse tensile strength for IM7/8552 was 127 MPa [10.2].



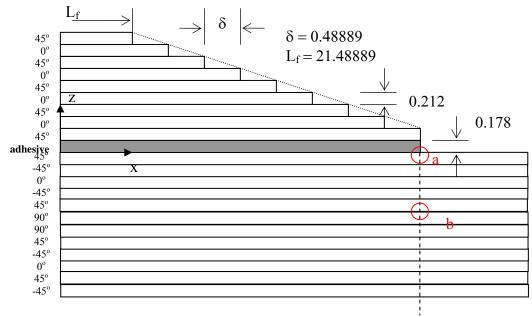


Fig. 10.4.1, Modeling tapered skin/flange specimen by HS-BondJo. The solution domain, boundary conditions are shown in the top; the tapered end is modeled with a stepped-wised end.

10.4.2 Linear analysis

Linear adhesive properties are used in the failure analysis to predict damage initiation load. The margin of safety (MS) was checked at the interface of each ply along the longitudinal direction and through-the-thickness at the free edge, i.e. x = 25.4 mm, where the initial damage occurred. For instance, the margin of safety at the critical point (a) (as shown in Fig. 10.4.1) can be computed according to the following procedure. First, the maximum transverse principal stress is obtained from

$$\sigma_{tt_principal} = \frac{\sigma_{22} + \sigma_{33}}{2} + \sqrt{\left(\frac{\sigma_{22} - \sigma_{33}}{2}\right)^2 + \tau_{23}^2}$$

$$= \frac{84.28 + 72.28}{2} + \sqrt{\frac{\left(84.28 - 72.28\right)^2}{2} + \left(-48.07\right)^2} = 127.1(\text{MPa})$$
(10.4.2.1)

and the MS is given as

$$MS = \frac{Y_t}{\sigma_{tt \text{ principal}}} - 1 = \frac{127}{127.1} - 1 = -7.87 \times 10^{-4}$$
 (10.4.2.2)

Note: Results for this Validation Example have been updated in reference 10.13 that shows additional failure equations

For the NASA stepped bonded doubler example, the failure mode chosen for correlation is the one chosen as the controlling failure mode, "Joint, Bonded, Delamination, Peel, Longitudinal & Transverse Shear, Axial and Transverse" (see Equation 6.5.2.9, Section 6.5 for a description of the joint failure methods). This method is a 3D extension of an equation presented by Tong and predicts delamination failure in the joint when the following interaction relation becomes true,

$$\left(\frac{\sigma_{1}^{2} - \sigma_{1}\sigma_{3}}{X_{t}X_{c}}\right) + \left(\frac{\sigma_{2}^{2} - \sigma_{2}\sigma_{3}}{Y_{t}Y_{c}}\right) + \left(\frac{\sigma_{3}}{Z}\right)^{2} + \left(\frac{\tau_{23}}{Q}\right)^{2} + \left(\frac{\tau_{13}}{R_{13}}\right)^{2} + \left(\frac{\tau_{12}}{R_{12}}\right)^{2} \ge 1$$

$$(Vol2: ref eqn 3.1.1)$$

where X_t , X_c , are the ply allowables in the fiber direction for tension and compression, Y_t , Y_c are the allowables in the transverse direction, and Q, R_{13} , and R_{12} are allowable shear strengths. In HyperSizer the material labels are: (Q = interlaminar Fsu23, $R_{13} = interlaminar Fsu13$, and $R_{12} = In-plane Fsu12$)

Fig. 10.4.2 shows the through-the-thickness distribution of margin of safety in adherend 1 at x = 25.4 mm, where damage initiated. It shows the jumps of MS at the ply interfaces under the predicted failure load P = 960 N/mm (24.3 kN). The MS at the top surface corner (point a) of adherend 1 reaches zero under the axial tensile load of 24.3 kN, indicating that damage initiates at point a under this load. More results of margin of safety in adherend 1 are shown in the section 10.6.

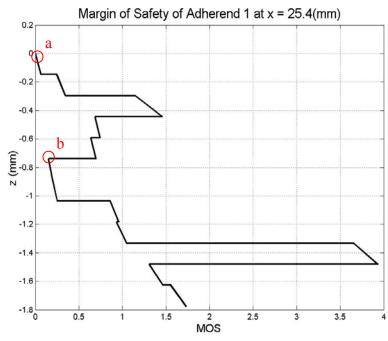


Fig. 10.4.2, Through-the-thickness distribution of the margin of safety of skin at the bondline corner, under longitudinal tension of 24.3 kN.

10.4.3 Nonlinear analysis

HS–*BondJo* can perform the stress analysis for the bonded joints with nonlinear adhesive material. Note that the adhesive used in this problem is Grade 5 FM300, which is assumed linear elastic throughout the analyses performed by Krueger et al. [10.2]. Information about the nonlinear behavior of this adhesive material is not provided. According to limited information found from the internet [10.12], FM300 is a modified epoxy, not a polymer. Thus, the properties of FM300k adhesive should be a reasonable estimate of Grade 5 FM 300. Table 10.4 gives the mechanical properties of FM 300k.

Table 10.4, Mechanical properties of Grade 5 Fm300 adhesive

	Е	v	S_{prop}	S_{ult}	e_{ult}	λ
	(GPa)		(MPa)	(MPa)		
FM 300k	1.72	0.30	25.92	69.88	0.0956	1.0

Note S_{prop} is the proportional limit of adhesive; S_{ult} and e_{ult} are the ultimate stress and strain respectively. λ is the ratio of compressive yield stress to the tensile yield stress of the adhesive. Fig. 10.4.4 plots the experimental stress-strain data for FM 300k along with an approximation using Ramberg-Osgood model [10.11].

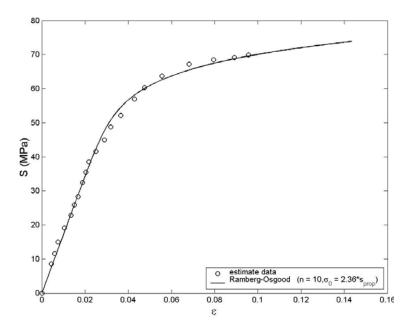


Fig. 10.4.4, Experimental stress-strain data for FM 300k adhesive along with Ramberg-Osgood approximation.

Fig. 10.4.5 shows the adhesive stresses obtained with linear and nonlinear analysis under longitudinal tension P = 27.6 kN (1088 N/mm) respectively. The peak values of adhesive shear and peel stresses are greatly reduced due to yielding of adhesives. The out-of-plane stresses in the surface ply of the skin are reduced as well. According to the failure criteria for matrix cracking, the principal stress on the transverse plane is function of σ_{22} and σ_{33} , so that reduction of out-of-plane stress reduces the transverse principal stress.

Fig. 10.4.6 shows the margin of safety of the skin (adherend 1), obtained with nonlinear adhesive properties, at the bondline corner (x = 25.4 mm). As expected, the margins of safety are all greater than zero even with an escalated load of 27.6 kN. Note that this load is not the damage initiation load. It is also noted that the potential failure location shifts from corner a to the point b (See Fig. 10.4.1), which is the interface of the 45- and 90-degree ply. This may be due to the out-of-plane stresses of the surface ply being affected much more by yielding of the adhesive than those of others far away from the bondline. Continually increasing of loads would cause matrix cracking at point b. This load would be the predicted damage onset load for the bonded skin/flange specimen as a nonlinear adhesive property is considered. Compared to a predicted failure load with a linear adhesive, a soft adhesive will significantly increase the damage resistance of the adherend to matrix cracking. The attempt to find the damage initiation load for nonlinear adhesives was given up at this time because the nonlinear analysis is time consuming, and the value is not important because we have already shown un-conservative predictions for linear adhesive analysis, and nonlinear adhesive prediction will only become more unconservative.

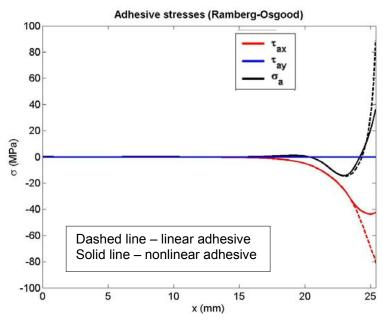


Fig. 10.4.5, Linear (dashed line) and nonlinear adhesive stresses in skin/flange specimen under longitudinal tension of 27.6 kN (1088 N/mm).

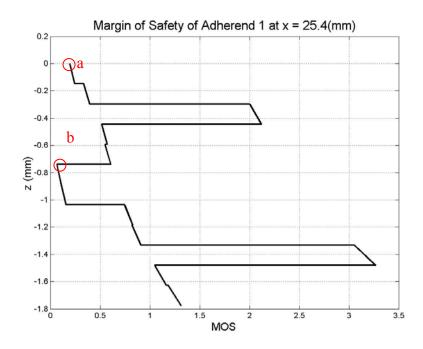


Fig. 10.4.6, Margin of safety of skin obtained with nonlinear adhesive property under longitudinal tension of 27.6 kN (1088 N/mm). This load is not the failure load, but the results show that yielding of adhesive could greatly improve the resistance of bonded doubler to matrix cracking.

10.5 Discussion

10.5.1 Comparison of HS-BondJo and NASA Prediction of Damage Onset

Krueger et al. at NASA used geometric nonlinear finite element analyses along with matrix cracking and delamination fatigue onset characterization data to determine the fatigue life of the composite bonded skin/stringer specimen. The approach used experiments to detect the failure mechanism, computational stress analysis to determine the location and onset of first matrix cracking, and computational fracture mechanics to investigate the potential for subsequent delamination growth. The prediction for matrix cracking onset in the skin/stiffener specimens agreed reasonably well with measured P-N data from the fatigue tests which were included in Fig. 10.5.1. However, significant deviation was noted between measured and predicted onset loads under monotonically increasing (quasi-static) loads. Under the static loading (tension), the damage onset (matrix cracking) load predicted by NASA is about 13 kN. Compared to the tested average strength of 17.8 kN, the error is 27%. According to Krueger et al., better results could be obtained if an alternate characterization test method is used instead of the three-point-bending test of 90-degree laminates.

HS-BondJo used a semi-analytical stress analysis approach along with matrix cracking characterization data to determine the damage initiation load of the composite bonded skin/stringer specimen. Under the static loading (tension), the damage onset (matrix cracking) load predicted by *HS-BondJo* is about 24.3 kN, which is higher than the tested strength of 17.8 kN by 37%. The error could be caused by many factors. Direct comparison of *HS-BondJo* stress results with FEA would be very helpful to clarify this matter. However, these were not available in NASA's report.

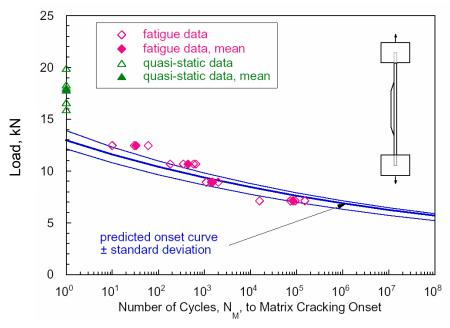


Fig. 10.5.1, NASA predicted load for matrix cracking onset and experimental results. NASA prediction for damage initiation of quasi-static loads is conservative while those of BondJo are unconservative. These difference are still under investigation.

Table 10.5 summarizes the modeling details and predicted failure load by HS-BondJo and NASA's approach.

Table 10.5, Comparison of HS-BondJo and NASA modeling approaches

			HS-BondJo	NASA approach [10.2]
Geometry		Tapered ends of flange	Approximated with finite steps	Modeled exactly
)mc		Spew fillet	Not included	Modeled exactly
Geo			½ of the specimen geometry, with appropriate B.C.	Full model of specimen
lysis		Approach	Semi-analytical	Finite element method (geometric nonlinear)
Stress analysis		Nonmechanical load		Hygrothermal effect is considered
Stre		Characteristic distance	Not used	Not used
4	þ	Linear adhesive	24.3 kN	13 kN
Predict-	ed load	Nonlinear adhesive	>> 27.6 kN	N/A
Test		Damage onset load (under static load)	Average stren	gth is 17.8 kN

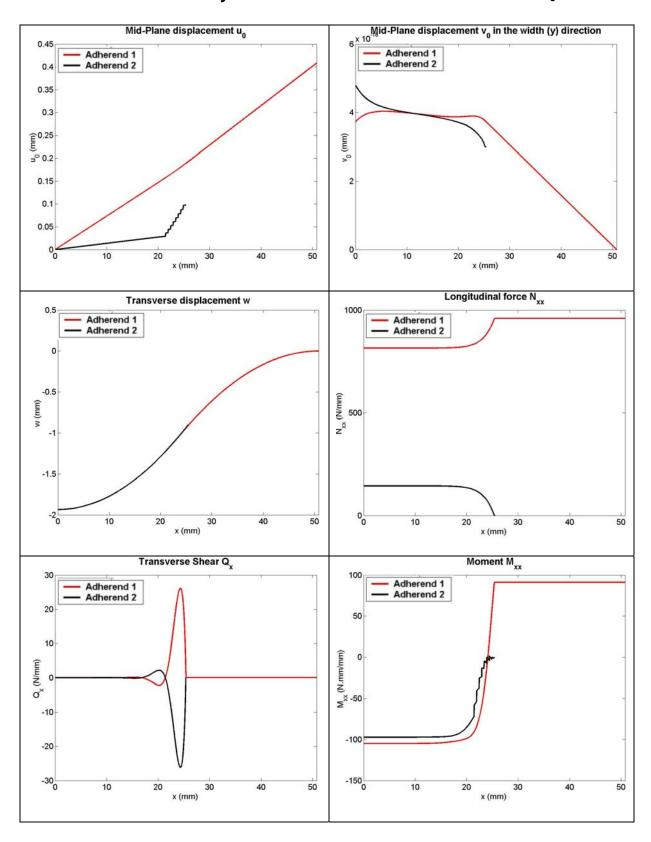
10.6 References

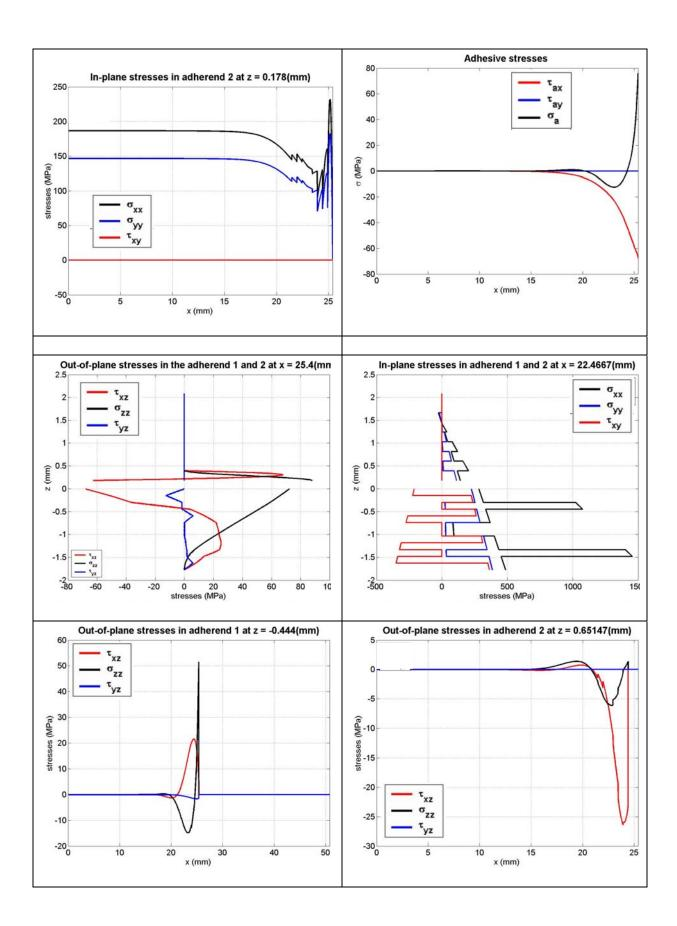
- 10.1 Hoyt, D. M., Ward, S. H., Minguet, P. J., "Strength and Fatigue Life Modeling of Bonded Joints in Composite Structure," *American Society for Composites (ASC) 15th Technical Conference*, September 2000.
- 10.2 Krueger, R., Paris, I. L., O'Brien T. K., and Minguet, P. J., 2001, "Fatigue Life Methodology for Bonded Composite Skin/Stringer Configurations," NASA/TM-2001-210842, ARL-TR-2432.
- 10.3 Krueger, R., Paris, I. L., O'Brien T. K., and Minguet, P. J., 2000, "Testing and Analysis of Composite Skin/Stringer Debonding under Multi-axial Loading," Journal *of Composite Materials*, vol. 34, pp. 1263-1300.
- 10.4 Mortensen, F., (1998), "Development of Tools for Engineering Analysis and Design of High-Performance FRP-composite Structural Elements," Ph.D. Thesis, Institute of Mechanical Engineering, Aalborg University (Denmark), Special Report no. 37.
- 10.5 Minguet, P. J., Fedro, M. J., O'Brien, T. K., Martin, R. H. and Ilcewicz, L. B., "Development of a Structural Test Simulating Pressure Pillowing Effects in Bonded Skin/Stringer/Frame Configuration," in Proceedings of the Fourth NASA/DoD Advanced Composite Technology Conference, Salt Lake City, Utah, 1993.
- 10.6 Minguet, P. J. and O'Brien, T. K., "Analysis of Test Methods for Characterizing Skin/Stringer Debonding Failures in Reinforced Composite Panels," in Composite Materials: Testing and Design (Twelfth Volume), ASTM STP 1274, 1996, pp. 105--124.

- 10.7 Minguet, P. J. and O'Brien, T. K., "Analysis of Composite Skin/Stringer Bond Failures Using a Strain Energy Release Rate Approach," in the Tenth International Conference on Composite Materials, vol. I, A. Poursartip and K. Street, Eds., 1995, pp. 245--252.
- 10.8 Minguet, P. J., "Analysis of the Strength of the Interface Between Frame and Skin in a Bonded Composite Fuselage Panel," in The AIAA/ ASME/ ASCE/ AHS/ ASC Structures, Structural Dynamics and Materials Conference, 1997, pp. 2783--2790.
- 10.9 Cvitkovich, M. K., O'Brien, T. K. and Minguet, P. J., "Fatigue Debonding Characterization in Composite Skin/Stringer Configurations," in Composite Materials: Fatigue and Fracture, Seventh Volume, ASTM STP 1330: American Society for Testing and Materials, 1998, pp. 97-121.
- 10.10 Zhang, J. and Collier, S. C., 2004, "Stress Analysis method for Composite Bonded Joints," CRC internal report.
- 10.11 Zhang, J. and Collier, S. C., 2003, "Procedure of Implementation of Nonlinear Analysis for Adhesively Bonded Joints," CRC internal report.
- 10.12 Internet file, "FM300 High Shear Strength Modified Epoxy Adhesive."
- 10.13 Yarrington, P., Zhang, J., Collier, C., and Bednarcyk, B., "Failure Analysis of Adhesively Bonded Composite Joints," AIAA SDM Conference, April 2005.

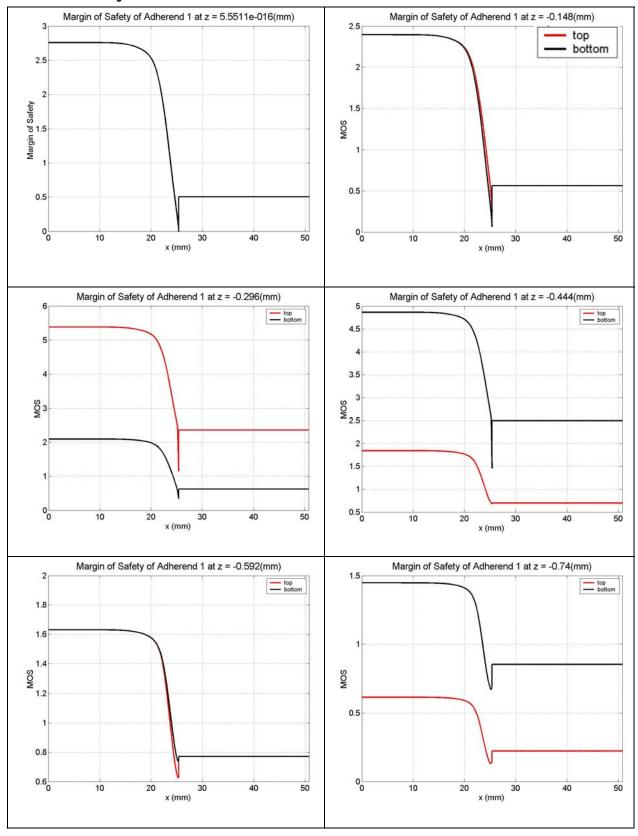
Supplemental Results

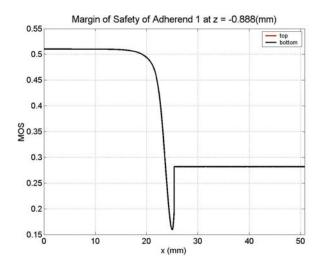
10.6.1 Linear Stress Analysis Results at Predicted Failure Load P_0 = 24.3 kN

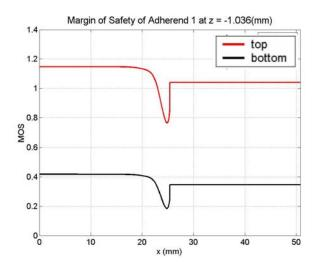


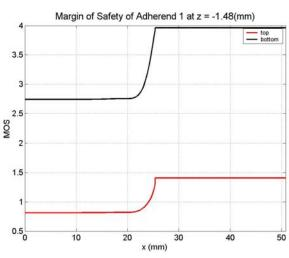


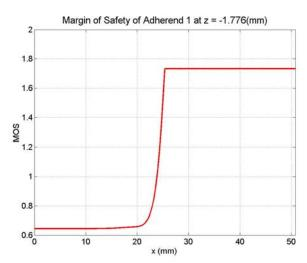
10.6.2 HS-BondJo Calculation of MS in the adherends at Predicted Failure Load P_0 = 24.3 kN

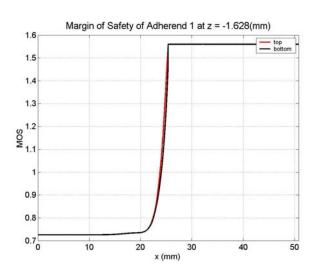












11 Validation - Single Lap Joint, Woven Fabric Laminate, Tong Publication

11.1 Summary of Results

Tong [11.1] conducted an experimental and analytical study to investigate the effect of cracks near the overlap region on failure of adhesively-bonded composite single lap joints. In this study, five groups of specimens were tested and the failure loads and modes for each group were recorded. Fig. 11.1 shows the experimental results for these specimens and the HS-BondJo model. The test and predicted failure loads are tabulated in Table 11.1.

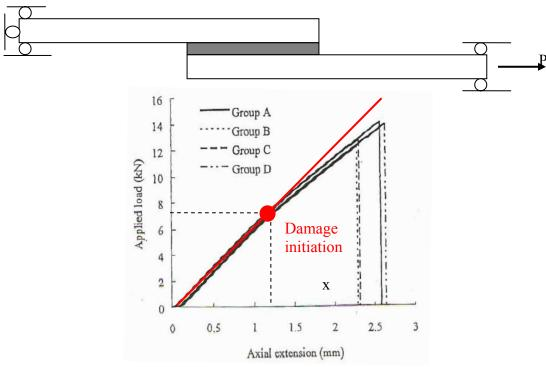


Fig. 11.1, Single lap joint schematic and load-displacement results for single lap joints studied by Tong [11.1].

Table 11.1, summary of predicted failure loads vs. experimental result

	Average value from 18 test specimens	BondJo prediction using linear adhesive	BondJo prediction using nonlinear adhesive
Damage Initiation load (kN)	7.2	6.85	6.82

Both linear and nonlinear analyses were performed to predict failure load of the specimens subjected to longitudinal tension. Max stress criterion is used to predict initial failure of the adherends. The load-displacement curves of the joint specimens (Fig. 11.1) show very pronounced initial damage and damage evolution before ultimate failure. The initial failure location predicted by HS-BondJo matches well with the experimental observations, and the predicted damage initiation load predicted with linear and non-linear analysis (6.85 and 6.82 kN respectively) correlates well with the measured initial failure load of 7.2 kN.

11.2 Problem Definition

The specimens used in this study were adhesively bonded composite single lap joints as shown in Fig. 11.2.1. Composite adherends of 25.4 mm width were cut from 250x250 mm panels manufactured by laminating eight plies of T300/934 plain woven prepreg in 0-deg direction. Before being cut, the two panels were bonded together using FM300-K film adhesive with uniform thickness of 0.16 mm. The material properties of T300/934 plain woven composites and FM300-K are given in Tables 11.2 and 11.3.

Six specimen configurations were considered, and they are referred to as specimen groups A-F, respectively. For all specimens, except those in Group A, two cracks were embedded between the first and second plies 0.215 mm beneath the surface. The location and size of the embedded cracks for all specimens are given in Table 11.4.

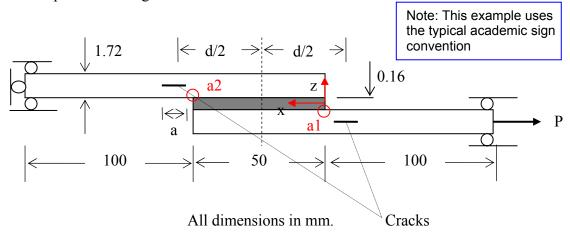


Fig. 11.2.1, Schematic of single lap joints studied by Tong.

Table 11.2, Mechanical properties of a ply of T300/934 carbon/epoxy

plani woven prepreg				
Longitudinal modulus $E_1 = E_2$, MPa	57226			
Transverse modulus E ₃ , MPa	4800			
In-plane shear modulus G ₁₂ , MPa	4481			
Out-of-plane shear modulus $G_{13} = G_{23}$, MPa	4400			
In-plane Poisson ratio v_{12}	0.05			
Out-of-plane Poisson ratio $v_{13} = v_{23}$	0.28			
In-plane tensile strength X_t , MPa	518			

Table 11.3, Mechanical properties of FM300-K adhesive

	E (GPa)	v	S _{prop} (MPa)	S _{ult} (MPa)	e _{ult}	λ
FM300-K	2.40	0.32	25.92	69.88	0.0685	1.0

Note: S_{prop} represents the proportional limit of adhesive; S_{ult} and e_{ult} are the ultimate stress and strain respectively. λ is the ratio of compressive yield stress to the tensile yield

stress of the adhesive. Fig. 11.4.3 plots the actual stress-strain relation of FM300-K adhesive and the approximated stress-strain relation using the Ramberg-Osgood model.

11.3 Experimental Results

11.3.1 Visualization of Joint Failure

There were no cracks in group A. Specimens in groups B, C, and D had two cracks of 4, 6, and 8 mm length, respectively, with an offset distance d of 50 mm between the two crack centers. Specimens in group E had both cracks of 6 mm length embedded outside the joint overlap (d = 60 mm), whereas specimens in group F had both cracks of 6 mm length located inside the joint overlap (d = 40 mm).

All specimens were loaded in axial tension on an Instron testing machine at room temperature. A loading rate of 0.5 mm/min was used for all specimens. The applied load and crosshead displacement were recorded. The measured axial loads increased linearly with the crosshead displacement for all the specimens up to the occurrence of initial damage and then to ultimate failure loads, as shown in the load-displacement curves in Fig. 11.3.1. As noted by the authors, micro-cracking was audible at lower load levels prior to final fracture of the specimens. The authors also indicated that the embedded cracks only cause a slight change in the overall stiffness of the specimen. This information is important to us because it means that stiffness loss shown in the load-displacement curves is mostly due to the damage evolution in the specimens no matter the size or location of the cracks. It can also be deduced that the initial failure load for all specimens should be the same if the initial failure modes and locations are the same.

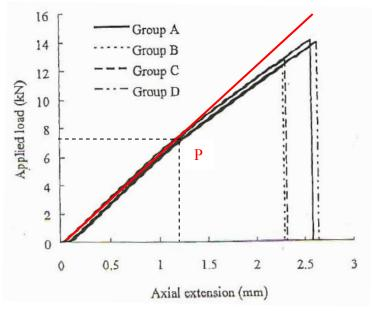


Fig. 11.3.1, Typical curves of applied load vs. crosshead displacement. The load at point P is the damage initiation load where the displacement diverges from linear elastic response (shown with the red line). All groups have similar damage initiation loads as well as damage initiation location (see Table 11.4)

11.3.2 Test Data

Table 11.4 summarizes the ultimate failure loads and the associated failure modes of the specimens tested. Three major failure modes are identified. Failure modes for groups A and E start with initial sectional fracture due to high tensile stress in the surface ply developing into interlaminar delamination leading to final fracture of the remaining cross section. Failure modes for groups B, C and D start with sectional fracture in the surface ply resulting in a final net sectional fracture near the crack tip in the overlap. Failure modes for specimen group F start with sectional fracture in the surface ply and develop into an interlaminar delamination that connects to the embedded crack near the crack tip, then fails in final net sectional fracture. Thus, it can be seen that all specimens experience progressive damage prior to final failure, but more importantly, all specimens have the same initial failure modes, i.e. the sectional fracture of the surface ply near the free edge. This is confirmed from a simple analysis of the load – displacement curves in Fig. 11.3.1. All of the test load-displacement curves diverge from the linear elastic response (shown with the red line) at the same point, P, where damage initiation occurs. Thus, the initial failure load can be estimated from the load-displacement curves as $F_{ini} = 7.2 \text{ kN}$.

Table 11.4, Test data for failure loads and modes

G .		, <u> </u>		ure loads and modes
Specimen	Crack	Final	delamination	Failure modes
	offset	failure	expanded in	
	and	load	width	
	length	(N)	direction	
	(mm)		(mm)	
A2		14,374	6	Surface ply
A3	d = 50	14,064	6-7	failure section
A4	a = 0	14,076	5-6	7-7
Average		14,171		Final fracture section
				Delamination
B1		12,215		
B2	d = 50	12,273	0	
В3	a = 4	12,663	2	
B4		13,628	4	
B5		12,209	3	
Average		12,598		
C1		14,216		
C2	d = 50	12,280	2-3	Precrack
C3	a = 6	12,885	2-3	Surface ply fracture section
C4		12,929	3-4	Tracture section
C5		12,709	2-3	Final fracture
Average		13,004		section
D1		13,051	2-3	
D2	d = 50	13,168	2-5	
D3	a = 8	12,667	0-1	
D4		14,172		
D5		13,916	2-3	
Average		13,395		
E1		13,241		
E2	d = 60	14,852	0-2	Surface ply failure section
E3	a = 6	14,948	2-3	
E4		14,247	0-2	Final fracture
E5		12,812		section Delamination
Average		14,020		
F1		13,773	4-6	Precrack
F3	d = 40	13,169	5-6	Surface ply
F4	a = 6	12,924	5-6	fracture section
F5		13,186	4-5	Final fracture
Average		13,160		section
Avciage		13,203		

11.4 HS-BondJo Prediction

Failure analysis performed by HS-BondJo combines detailed stress analysis and calculation of margin of safety for each point in the adherends. The solution domain of the single-lap joint specimen and the boundary conditions applied for this problem are shown in Fig. 11.2.1. According to Tong, maximum stress is the appropriate failure criterion for initiation of sectional fracture at the surface ply. It is assumed that failure occurs when the average tensile stress in the surface ply attains its in-plane tensile strength, $X_t = 518$ MPa.

11.4.1 Linear Analysis

Linear adhesive properties are used in this analysis. The predicted load for the problem with linear elastic adhesive property is $P_{linear} = 6.85$ kN, which is equivalent to 274 N/mm. Fig. 11.4.1 shows the in-plane stresses in the surface ply of adherend 1. It can be seen that the longitudinal stress at the critical point (Point 'a1', as shown in Fig. 11.2.1) reaches the material strength of 518 MPa. Additional stress analysis are found in Section 11.8.

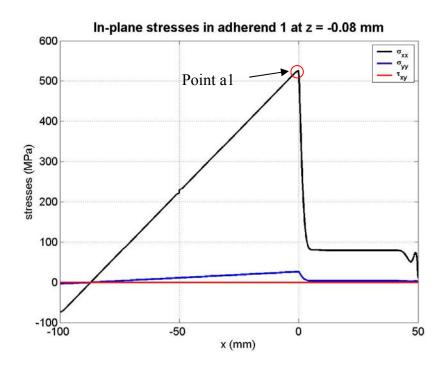


Fig. 11.4.1, In-plane stresses in the surface ply of adherend 1 under tension P = 6.85 kN (274 N/mm) with linear adhesive. The longitudinal stress at the critical point (Point 'a1', as shown in Fig.11.2.1) reaches the material strength of 518 MPa.

The margin of safety (MS) is checked in each ply of both adherends under the predicted failure load. The plots of MS in each ply are not shown here, we give instead the through-the-thickness distribution of the MS along at the reentrant corner of adherend 1. In Fig. 11.4.2, under the longitudinal tension of 6.85 kN, the MS of the surface ply reaches zero at the corner (point 'a1') of the top surface ply of adherend 1, indicating that failure initiates there. Thus, the predicted damage initiation load is 6.85 kN. This is consistent with the experimental observation and correlates well with test data, which is $\mathbf{F_{ini}} = 7.2 \text{ kN}$ for damage initiation.

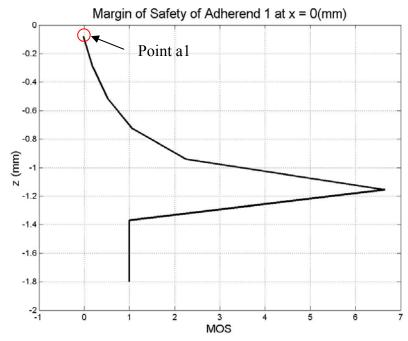


Fig. 11.4.2, Through-the-thickness plot of MS at the free edge (a1) of adherend 1 under tension P = 6.85 kN (274 N/mm) with linear adhesive. The MS at point a1 reaches zero, indicating the location of damage initiation.

11.4.2 Nonlinear Analysis

As the FM 300-K adhesive shows very pronounced nonlinear behavior as shown in Fig. 11.4.3, it is necessary to perform a nonlinear analysis for this problem.

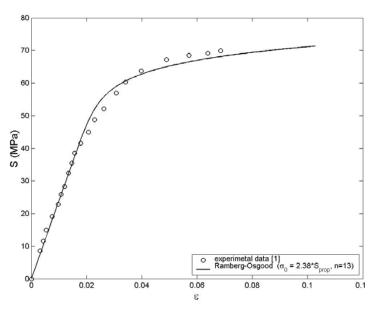


Fig. 11.4.3, The nonlinear stress-strain experimental data for FM 300-K adhesive used in the analysis along with a Ramberg-Osgood approximation of that data.

The predicted failure load with nonlinear analysis is $P_{nl} = 6.82$ kN (268.8 N/mm), which is slightly lower than the one with linear analysis. This is due to the fact that yielding of the adhesive will significantly reduce the peak values of out-of-plane stresses in both adherends but has almost no effect on the in-plane stresses. Fig. 11.4.4 plots the nonlinear adhesive stresses under tension of 6.82 kN. It shows that the maximum values of adhesive peel and shear stress at the free edges are significantly reduced due to softening of the adhesive. Fig. 11.4.5 shows the through-the-thickness distribution of MS in adherend 1 at point a1, one of the bondline free edges. The MS at the corner of the top surface ply of adherend 1 reaches zero, indicating the location of damage initiation.

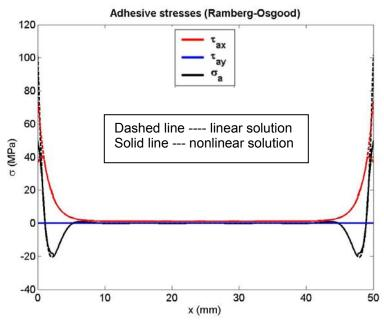


Fig. 11.4.4, Adhesive stresses obtained from nonlinear adhesive model.

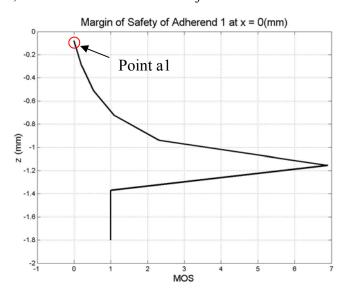


Fig. 11.4.5, Through-the-thickness plot of MS at the lead edge (a1) of adherend 1 under tension P = 6.82 kN (274 N/mm) with nonlinear adhesive. The MS at point a1 reach zero, indicating the location of damage initiation.

More results obtained from linear and nonlinear analysis are appended in Section 11.8.

11.5 Discussion

- 1. The initial failure of the single-lap joint specimens in Tong's paper was neglected by the author so that the recorded failure loads are all for the ultimate failure, which can not be predicted by BondJo correctly because progressive damage analysis is not yet available.
- 2. Whether or not the geometric nonlinearity is an issue in this problem is not clear. First of all, large deformations of specimens seem unlikely because they were clamped at both ends. However, the adherend flexibility, including the ratio of nonoverlap to overlap length, adherend thicknesses and moduli, may cause the overlap region to deform so greatly that it causes an eccentric load path. Finally, the geometric nonlinear FEA by the author shows quite different peak values of the adhesive stresses with BondJo's. Thus, further investigation using our own geometric nonlinear FEA is recommended.
- 3. Tong's FEA analysis and failure prediction are questionable because the final failure loads predicted with the FE results match well with test data without considering progressive failure, which is apparent in the tests.

11.6 Conclusions

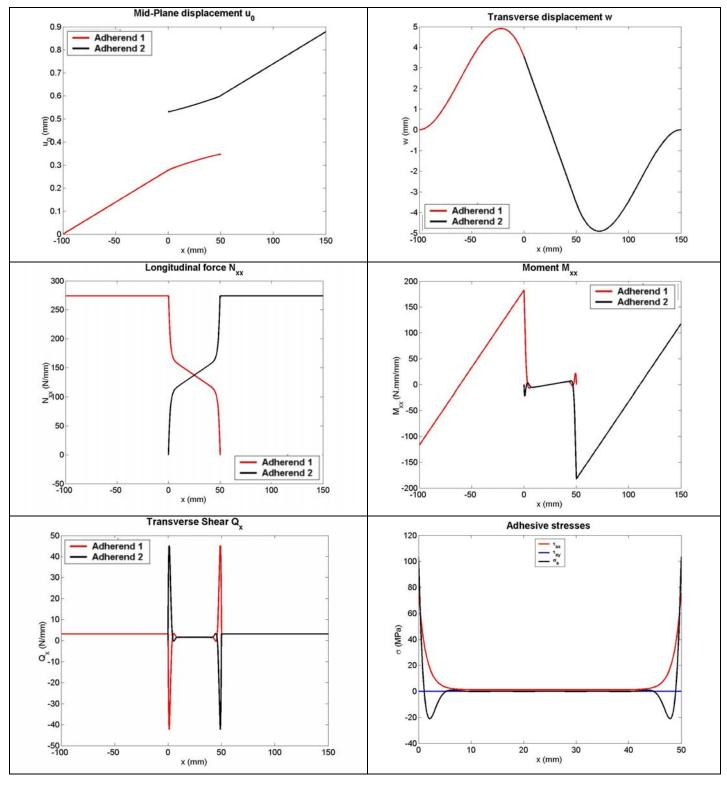
The bonded single-lap joint specimens studied by Tong were used as validation cases for *HS-BondJo*. Both linear and nonlinear analyses were performed to predict the failure load of the specimens subjected to longitudinal tension. Max stress criterion is used for the initial failure of adherends. The load-displacement curves of the joint specimens show very pronounced initial damage and damage evolution process prior to the ultimate failure. The failure location predicted by *HS-BondJo* matches well with the experimental observation, while the damage initiation load predicted with linear and non-linear analyses of 6.85 and 6.82 kN respectively correlate well with the measured initial failure load of 7.2 kN.

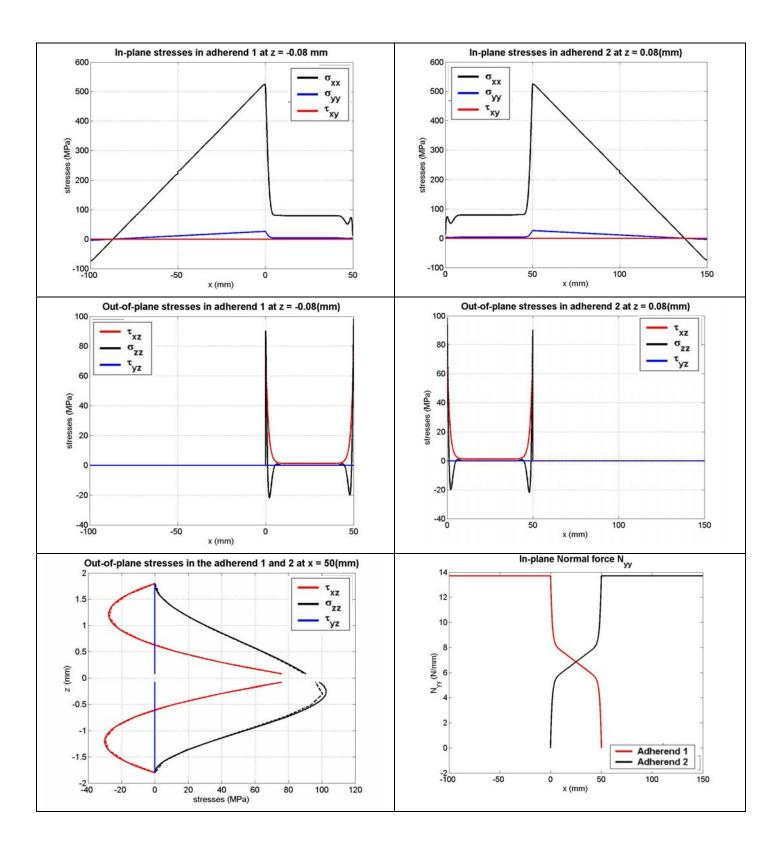
11.7 References

- 11.1 Tong, L., (1998), "Failure of adhesive-Bonded Composite Single Lap Joints with Embedded Cracks," AIAA journal, Vol.36, No.3, pp.448.
- 11.2 Tong, L., 1997, "An Assessment of Failure Criteria to Predict the Strength of Adhesively Bonded Composite Doubler Lap Joints," Journal of Reinforced Plastics and Composites, Vol. 16 (18), pp.698-713.
- 11.3 Mortensen, F., (1998), "Development of Tools for Engineering Analysis and Design of High-Performance FRP-composite Structural Elements," Ph.D. Thesis, Institute of Mechanical Engineering, Aalborg University (Denmark), Special Report no. 37.

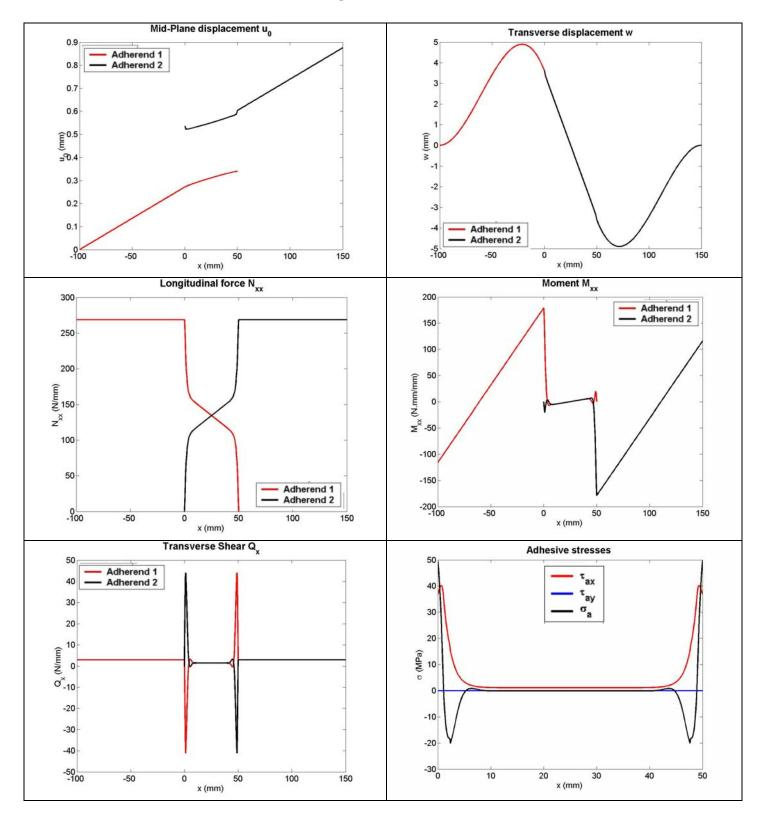
11.8 Supplemental Results

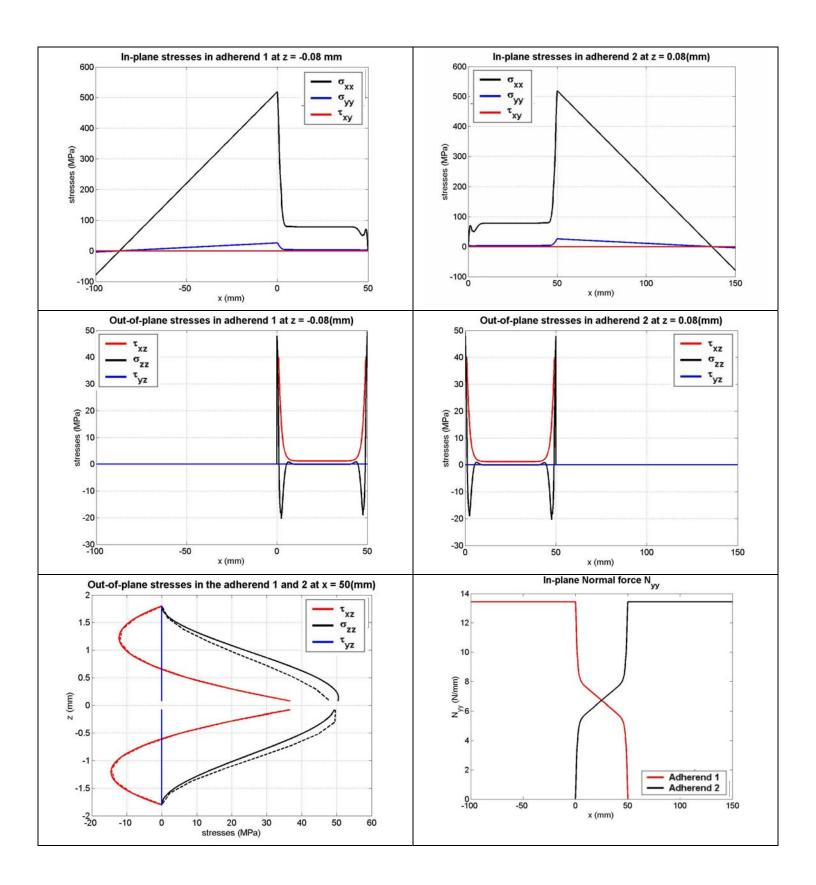
11.8.1 HS-BondJo Stress Analysis Results for Single-lap Joints under Tension N_{xx} = 6.85 kN using Linear Adhesive





11.8.2 HS-BondJo Stress Analysis Results for Single-lap Joints under Tension N_{xx} = 6.82 kN using Nonlinear Adhesive





---Failure Criteria---

HyperSizer Methods and Equations (*.HME)

12 Failure Criteria for Bonded Joints

Composite Bonded Joint Failure Criteria

```
Failure Analysis methods:
      160= Joint, Bonded, Edge Delamination Onset
      161= Joint, Bonded, Edge Delamination
      162= Joint, Bonded, Fracture, Principal Transverse
      163= Joint, Bonded, Fracture, Max Stress 1 direction
      164= Joint, Bonded, Delamination, Peel Dominated
      165= Joint, Bonded, Delamination, Peel and Transverse Shear
      166= Joint, Bonded, Delamination, Peel and Transverse Shear 2
      167= Joint, Bonded, Delamination, Tong, Peel, Transverse Shear & Axial, 1
      168= Joint, Bonded, Delamination, Tong, Peel, Transverse Shear & Axial, 2
      169= Joint, Bonded, Delamination, Tong, Peel, Transverse Shear & Axial, 3
      170= Joint, Bonded, Delamination, Tong, Peel, Transverse Shear & Axial, 4
      171= Joint, Bonded, Delamination, Tong, Peel, Transverse Shear & Axial, 5
      172= Joint, Bonded, Delamination, Tong, Peel, Transverse Shear & Axial, 6
      173= Joint, Bonded, Delamination, Peel, Longitudinal & Transverse Shear
      174= Joint, Bonded, Delamination, Peel, Longitudinal & Transverse Shear,
           Axial and Transverse
      175= Joint, Bonded, Adhesive, Peel Dominated
      176= Joint, Bonded, Adhesive, Von Mises Strain
      177= Joint, Bonded, Adhesive, Maximum Principal Stress
      178= Joint, Bonded, Adhesive, Peel, Longitudinal & Transverse Shear
      179= Joint, Bonded, Adhesive, Longitudinal & Transverse Shear Stress
      180= Joint, Bonded, Adhesive, Longitudinal & Transverse Shear Strain
```

12.1 Bonded Joint Failure Theory Classifications

The following classifications of bonded joint failure theories were identified by Heslehurst and Hart-Smith [12.1] and are included in HyperSizer's failure prediction. Margins-of-safety are computed based on recently published failure criteria. Failure methods are classified into two broad groups, adherend failures (blue) and adhesive failures (orange).

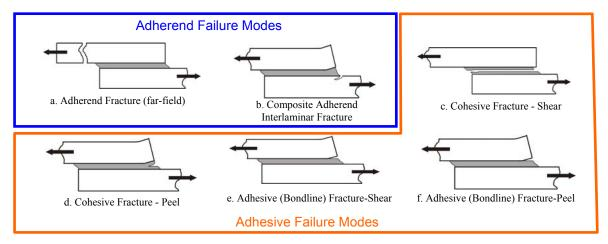


Fig. 12.1, Failure modes in adhesively bonded joints identified by Heslehurst and Hart-Smith 12.1]

The failure modes depicted in Fig. 12.1 are represented by the equations described in Section 12.2:

- a. Equations (162), (163)
- b. Equations (164)-(174)
- c. Equations (176), (179), (180)
- d. Equations (175) (178)
- e. Equations (179)-(180)
- f. Equations (175), (178)

12.2 Adherend Failure Methods

12.2.1 Sectional Fracture

ID	Failure mode	Failure criteria	Description
162	+	$\frac{\sigma_{tt_principal}}{Y_t} = 1$	162. Adherend fracture caused by matrix cracking [12.2, 12.3, 12.4].
163	Adherend Fracture (far field)	$\frac{\sigma_{11}}{X_t} = 1 \text{ or } \frac{\varepsilon_{11}}{\varepsilon_1^{ult}} = 1$	163. This type of failure occurs as the longitudinal stress or strain exceed their allowables [12.5].

12.2.2 Interlaminar Delamination

ID	Failure mode	Failure criteria	Description
164		$\frac{\sigma_3}{Z} = 1$	164. Eqn.(103), proposed by Adams [12.6], regards the interfacial peel
165		$\left(\frac{\sigma_3}{Z}\right)^2 + \left(\frac{\tau_{13}}{R}\right)^2 = 1$	stress is the major contributor to the delamination failure.
166		$\frac{\sigma_3}{Z} + \left(\frac{\tau_{13}}{R}\right)^2 = 1$	165-166. Interactive failure criterion for interlaminar
167	Composite Adherend	$\frac{\sigma_1(\sigma_1 - \sigma_3)}{X_t^2} + \left(\frac{\sigma_3}{Z}\right)^2 + \left(\frac{\tau_{13}}{R}\right)^2 = 1$	delamination, caused mainly by interlaminar peel and shear stresses.
168	Interlaminar Fracture	$\frac{\sigma_1(\sigma_1 - \sigma_3)}{X_t^2} + \left(\frac{\sigma_3}{Z}\right) + \left(\frac{\tau_{13}}{R}\right)^2 = 1$	Eqn. 165 proposed by Long[12.7], Eqn. 166 proposed by Hoyt [12.8].
169		$\left(\frac{\sigma_1}{X_t}\right)^2 + \left(\frac{\sigma_3}{Z}\right)^2 + \left(\frac{\tau_{13}}{R}\right)^2 = 1$	167-172. Tong [12.9] proposed 6 interactive criteria for interlaminar
170		$\left(\frac{\sigma_1}{X_t}\right)^2 + \left(\frac{\sigma_3}{Z}\right) + \left(\frac{\tau_{13}}{R}\right)^2 = 1$	fracture of adherends that consider the contribution of axial stresses
171		$\left(\frac{\sigma_1^2 - \sigma_1 \sigma_3}{X_t X_c}\right) + \left(\frac{\sigma_3}{Z}\right)^2 + \left(\frac{\tau_{13}}{R}\right)^2 = 1$	causing fiber breakage.

172	$\left(\frac{\sigma_1^2 - \sigma_1 \sigma_3}{X_t X_c}\right) + \left(\frac{\sigma_3}{Z}\right) + \left(\frac{\tau_{13}}{R}\right)^2 = 1$	173. Camanho et al. [12.10] proposed this criterion for onset
173	$\int \left(\frac{\sigma_{33}}{Z}\right)^{2} + \left(\frac{\tau_{23}}{Q}\right)^{2} + \left(\frac{\tau_{13}}{R}\right)^{2} = 1 \sigma_{33} > 0$	of delamination based on the work of Hashin-Rotem.
	$\left\{ \left(\frac{\tau_{23}}{Q}\right)^2 + \left(\frac{\tau_{13}}{R}\right)^2 = 1, \qquad \sigma_{33} < 0 \right\}$	174. This is a 3D stress state extension of Tong's failure criteria (171). This
174	$\left(\frac{\sigma_1^2 - \sigma_1 \sigma_3}{X_t X_c}\right) + \left(\frac{\sigma_2^2 - \sigma_2 \sigma_3}{Y_t Y_c}\right) + \left(\frac{\sigma_3}{Z}\right)^2$	criteria accounts for the contribution of full stress components for interlaminar
	$+\left(\frac{\tau_{23}}{Q}\right)^2 + \left(\frac{\tau_{13}}{R}\right)^2 + \left(\frac{\tau_{12}}{R}\right)^2 = 1$	fracture composite adherends.

12.2.3 Matrix Cracking

ID	Failure mode	Failure criteria	Description
162	Adherend Fracture (far-field) Matrix cracking (initial damage of adherends) Composite Adherence Interlaminar Fracture	$\frac{\sigma_{tt_principal}}{Y_t} = 1$ where $\sigma_{tt_principal} = \frac{\sigma_{22} + \sigma_{33}}{2} + \sqrt{(\frac{\sigma_{22} - \sigma_{33}}{2})^2 + \tau_{23}^2}$	115. Matrix cracking is considered as a major damage mode in the laminated adherends. Minguet et al. [12.11, 12.12]. investigated composite Skinstiffener debonding and believed that maximum tensile stress in the matrix is the major cause of the matrix cracking.

12.3 Adhesive Failure Methods

12.3.1 Cohesive Failures

ID	Failure mode	Failure criteria	Description
175		$\left(\frac{\sigma_{33}}{F_{peel}}\right) = 1 \text{ as } \sigma_{33} > 0$	175. Failure criterion for peel dominant cohesive failure
176		$\frac{\varepsilon_{eqv.}}{S_{eqv.}} = 1$	176.Adhesives are more susceptible to failure due to tensile strain than pure shear
17X		$\left(\frac{U_{II}}{U_{IIC}}\right)^{\alpha} + \left(\frac{U_{I}}{U_{IC}}\right)^{\beta} = 1$	and compression. For some adhesives, the nonlinear behavior dominates and strain to failure can exceed 100%
177	Cohesive Fracture - Shear	$\frac{\sigma_{principal}}{F_{\text{max}}} = 1$	17X. Tong [12.13] proposed a criterion that calculates strain energy density in the adhesive. This is not implemented in
178	Cohesive Fracture - Peel	$ \left\{ \left(\frac{\sigma_{33}}{F_{peel}} \right)^2 + \left(\frac{\tau_{13}}{F_{shear}} \right)^2 + \left(\frac{\tau_{23}}{F_{shear}} \right)^2 = 1, \ \sigma_{33} > 0 \right. $ $ \left(\left(\frac{\tau_{13}}{F_{shear}} \right)^2 + \left(\frac{\tau_{23}}{F_{shear}} \right)^2 = 1, \ \sigma_{33} < 0 $	HyperSizer. 177. Considers adhesive spew fillet. As shown by Adams [12.6], the initial damage in the adhesive spew fillet is caused by the maximum principal stress.
179		$\left(\frac{\sqrt{\tau_{13}^2 + \tau_{21}^2}}{F_{shear}}\right) = 1$	178. For general failure of decohesion, empirical interactive
180		$\left(\frac{\sqrt{\varepsilon_{13}^2 + \varepsilon_{21}^2}}{\gamma_{shear}^{ult}}\right) = 1$	failure was proposed [12.14]. Note that F _{peel} and F _{shear} are the bondline peel and shear strength, which can be measured in a tensile shear experiment.
			179-180. Failure criteria for shear dominant cohesive failure

12.4 Adhesive – Adherend Bondline Failures

The criteria for adhesive-adherend bondline failure are repeated from the cohesive failures given above. While in theory, the F_{peel} and F_{shear} allowable strengths are different for bondline versus cohesive failures, practically, these allowables are never distinguished in experiments. Generally only one of the two values will be available. If values for bondline and cohesive allowables are both available, the lower of the two values should be entered for each criterion.

ID	Failure mode	Failure criteria	Description
175		$\left(\frac{\sigma_{33}}{F_{peel}}\right) = 1 \text{ as } \sigma_{33} > 0$	175, 178, 179. For adhesive-adherend bondline failure, empirical interaction
170	Adhesive (Bondlone) Fracture – Shear	$\int \left(\frac{\sigma_{33}}{F_{peel}}\right)^{2} + \left(\frac{\tau_{13}}{F_{shear}}\right)^{2} + \left(\frac{\tau_{23}}{F_{shear}}\right)^{2} = 1, \ \sigma_{33} > 0$	failure criteria are given. The equations have the same forms as those for cohesive failure. Note that F_{peel} and F_{shear} are the peel
178		$\left(\frac{\tau_{13}}{F_{shear}}\right)^{2} + \left(\frac{\tau_{23}}{F_{shear}}\right)^{2} = 1, \ \sigma_{33} < 0$	and shear strength of adhesive/adherend interface.
179	Adhesive (Bondline) Fracture - Peel	$\left(\frac{\sqrt{\tau_{13}^2 + \tau_{21}^2}}{F_{shear}}\right) = 1$	

12.5 Joint Failure Location Checks

The Joint failure margins-of- safety are calculated at multiple points in the vicinity of the bonded flange (doubler) for stiffened panels.

The full stress tensor is calculated at multiple stations as shown in Fig. 12.2. Each adherend and each ply are broken into a userdefined number of y and locations, \mathbf{Z} represented by the green dots. The full stress state is evaluated each of these locations. For a full description of HyperSizer's stress calculation within bonded joints, see Volume 2, Section 6.

Once the stress state is known, margins of safety are calculated using the failure criteria described in Sections 12.2 – 12.4.

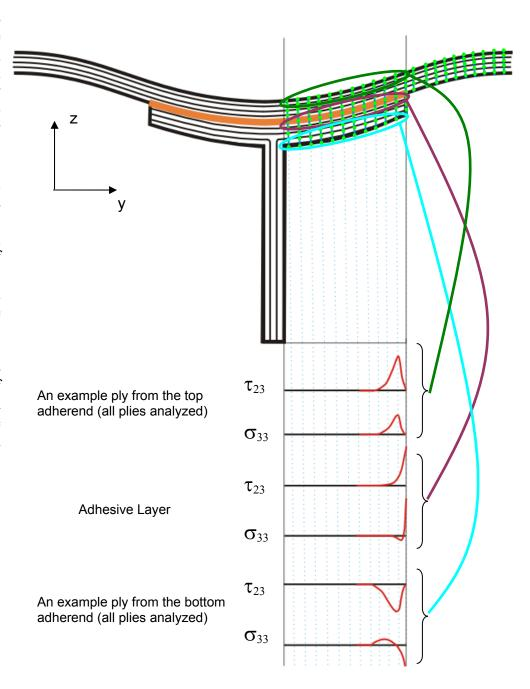


Fig. 12.2, The full stress state within the bonded joint is calculated by HyperSizer at a user-defined number of y and z locations. At each of these locations, margins of safety are calculated using the failure criteria described in Sections 12.2 – 12.4.

12.6 Symbols

- Normal stress in ply/material coordinates σ_1 , σ_2 , σ_3 - Normal stress in laminate/global coordinates σ_x , σ_y , σ_z $au_{12}\,,\,\, au_{23}\,,\,\, au_{13}$ - Shear stress in ply/material coordinates - Shear stress in laminate/global coordinates τ_{xy} , τ_{xz} , τ_{yz} - Normal strain in ply/material coordinates \mathcal{E}_{11} , \mathcal{E}_{22} , \mathcal{E}_{33} - Normal strain in laminate/global coordinates ε_{xx} , ε_{yy} , ε_{zz} - Shear strain in ply/material coordinates \mathcal{E}_{12} , \mathcal{E}_{13} , \mathcal{E}_{23} - Shear strain in laminate/material coordinates ε_{xy} , ε_{xz} , ε_{yz} - Interlaminar transverse shear stress τ_{23} , τ_{yz} $\sigma_{I,}$ $\sigma_{II,}$ σ_{III} - Principal stresses - Max principal transverse stress transverse $\sigma_{_{tt_principal}}$ X_t, X_c - Ultimate tensile and compressive longitudinal strength - Ultimate tensile and compressive transverse strength Y_t, Y_c \boldsymbol{Z} - Interlaminar (peel) tensile strength - Interlaminar longitudinal shear strength R 0 - Interlaminar transverse shear strength - Ultimate tensile strength of the adhesive $S_{eqv.}$ - Von Mises strain in the adhesive $\mathcal{E}_{eqv.}$ α and β - Empirical constants for bond strain energy failure method U_I , U_{II} - Bond strain energies for pure peel and shear respectively U_{IC}, U_{IIC} - Critical bond strain energies for pure peel and shear respectively - Tensile strength of bulk adhesive F_{max} - Bondline or cohesive peel strength F_{peel} - Bondline or cohesive shear strength F_{shear}

- Tensile ultimate strain in the fiber direction

- Shear ultimate strain in the adhesive

12.7 References

 γ_{shear}^{ult}

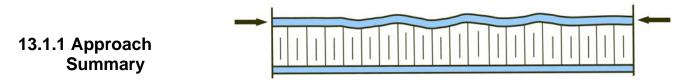
12.1 R. Heslehurst and J. Hart-Smith, The Science and Art of Structural Adhesive Bonding, SAMPE Journal, Vol. 38, No. 2, March/April 2002.

- 12.2 Krueger, R., Paris, I. L. and O'Brien, T. K., 2000, "Fatigue life methodology for bonded composite skin/stringer configurations," Proceedings of the American Society for Composites, 15th Technical Conference, pp.729-736.
- 12.3 Minguet, P. J. and O'Brien, T. K., "Analysis of Test Methods for Characterizing Skin/Stringer Debonding Failures in Reinforced Composite Panels," Composite Materials: Testing and Design (Twelfth Volume), ASTM STP 1274, 1996, pp. 105-124.
- 12.4 Minguet, P. J. and O'Brien, T. K., "Analysis of Composite Skin/Stringer Bond Failures Using a Strain Energy Release Rate Approach," in the Tenth International Conference on Composite Materials, vol. I, A. Poursartip and K. Street, Eds., 1995, pp. 245--252.
- 12.5 Cheuk, P. T. and Tong L., (2002), "Failure of adhesive bonded composite lap shear joints with embedded precrack," Composites Science and Technology, 62, 1079-1095.
- 12.6 Adams, R. D. and Wake, W. C., 1984, Structural Adhesive Joints in engineering. London: Elsevier Applied Science Publishers.
- 12.7 Long R. S., (1991), "static strength of adhesively bonded ARALL-1 joints," J. Composite Materials, 25, 391-415.
- 12.8 Hoyt, D. M., Ward, S. H., Minguet, P. J., "Strength and Fatigue Life Modeling of Bonded Joints in Composite Structure," American Society for Composites (ASC) 15th Technical Conference, September 2000.
- 12.9 Tong, L. (1997), "An assessment of failure criteria to predict the strength of adhesively bonded composite double lap joints," J. Reinforced Plastics and Composites, 16,699-713.
- 12.10 Camanho, P.P. and Matthews, F. L., (1999), "Delamination Onset Prediction in Mechanically Fastened Joints in Composite Laminates," J. Composite Materials, Vol.33, No.10, pp906-927.
- 12.11 Minguet, P. J. and O'Brien, T. K., "Analysis of Test Methods for Characterizing Skin/Stringer Debonding Failures in Reinforced Composite Panels," in Composite Materials: Testing and Design (Twelfth Volume), ASTM STP 1274, 1996, pp. 105--124.
- 12.12 Minguet, P. J. and O'Brien, T. K., "Analysis of Composite Skin/Stringer Bond Failures Using a Strain Energy Release Rate Approach," in the Tenth International Conference on Composite Materials, vol. I, A. Poursartip and K. Street, Eds., 1995, pp. 245--252.
- 12.13 Tong, L., (1997), "Strength of Adhesively Bonded Single-lap and Lap-shear Joints,"Int. J. Solids Structures, Vol.35, No.20, pp.2601-2616.
- 12.14 Tong, L. and Steven, G. P., Analysis and Design of Structural Bonded Joints, Kluwer Academic Publishers, 1999.

13 Failure Criteria for Sandwich Panels

This failure analysis documentation is included because honeycomb analysis is one of the failure modes that is included in the LRSA airframe example.

13.1 Wrinkling



Sandwich structures with thin facesheets and lightweight cores are prone to a type of local failure known as facesheet wrinkling. The term wrinkling refers to local, short wavelength buckling phenomenon of the facesheet, with mode shapes having wavelengths up to the thickness of the core. The small buckling wavelength of the wrinkling mode results in the allowable load being insensitive to structural boundary conditions and curvature. Sandwich structures exhibit little or no post-wrinkling load carrying capability, therefore failure of these structures by wrinkling is typically catastrophic. As a consequence, accurate prediction of wrinkling is important to quantifying structural integrity of sandwich structures.

There are two distinct wrinkling modes: symmetrical and antisymmetrical. The following equations handle both.



Two Equations

There are two primary mathematical models from which wrinkling equations are derived. The first is general and based on solid isotropic cores [13.2.1, 13.2.4]

$$\sigma_{wr} = k_1 \left(E_f \ E_c \ G_c \right)^{\frac{1}{3}} \tag{13.1.1}$$

The second is suitable for honeycomb cores (anti-plane math model), [13.2.1, 13.2.3].

$$\sigma_{wr} = k_2 E_f \sqrt{\frac{E_c t_f}{E_f t_c}}$$
(13.1.2)

Table 3 of reference 13.2.1 provides the suggested factors to use with the wrinkling allowable stress equations, which are:

$$k_1 = 0.63$$

 $k_2 = 0.82$

The factors k_1 and k_2 are not empirically derived from test data but are rather theoretically based values that are derived from the physics of sandwich facesheet wrinkling.

Composite Materials

Wrinkling equations are based on isotropic materials. Reference [13.2.1], equation (15) includes terms for specially orthotropic composite facesheets. However, as implied in Reference [13.2.1], a better approach is to use the validated isotropic equations and substitute for E_f , not an equivalent membrane Young's modulus,

$$E_f = \frac{1}{{\bf A}_{11}^{-1} t_f}$$

but rather an equivalent flexural modulus based on the Dij of the laminate, (Reference [13.2.1], equation (18)). HyperSizer computes this term using the D_{II}^{-1} term from the inverted 6x6 A, B, D matrix.

$$E_f = \frac{12}{D_{11}^{-1} t_f^3}$$

Effect of Adhesive

Reference [13.2.2], shows that including the effect of a 0.005" thick adhesive layer on the theoretical wrinkling stress of a 0.010" thick facesheet on a 1.0" thick core was to increase this wrinkling stress by 50%. Since analyses do not include the effect of an adhesive layer (if such a layer exists) the wrinkling stress of sandwich panels with very thin facesheets are likely overly conservative.

Combined Loads

Most test data validation is performed on a "strut" specimen loaded uniaxially. Little research or test data exists for combined biaxial loading with or without shear. One procedure to predict wrinkling caused by combined loads is to use the maximum principal facesheet compressive stress. This approach requires that not only major and minor principal stresses be computed, but also the major and minor principal stress allowables. Another procedure is to rotate the actual stresses into a coordinate system with axes parallel to the core ribbon and transverse directions. This approach takes on the interaction equation of the following form:

$$\frac{\left(\sigma_x^3 + \sigma_y^3\right)^{\frac{1}{3}}}{K\sigma_{wr}} + \left(\frac{\tau_{xy}}{\sigma_{wr}}\right)^2 = 1 \tag{13.1.3}$$

HyperSizer implements this approach but extends it by determining allowable wrinkling stresses in the two directions: $\sigma_{x,wr}$ and $\sigma_{y,wr}$. Below the procedure is described in more detail, and how to properly determine the margin-of-safety (MS).

13.1.2 Symbols

 E_c = Through-the-thickness elastic modulus of core

 E_f = Elastic modulus of facesheet

 $E_{f,x}$ = x direction, elastic modulus of facesheet

 $E_{f,y}$ = y direction, elastic modulus of facesheet

 k_1 = Wrinkling factor for equation 13.1.1 k_2 = Wrinkling factor for equation 13.2.2 σ = Stress

 σ_{wr} = Wrinkling stress allowable

 τ_{xy} = In-plane shear stress of facesheet

 t_f = Facesheet thickness

 t_c = Core thickness

 R_a = Membrane stress ratio (applied / allowable) of facesheet

 R_s = Shear stress ratio (applied / allowable) of facesheet Fcw_x = Wrinkling stress allowable due to biaxial loads

Fcw = Wrinkling stress allowable due to loads in the ribbon direction

Fsw = Wrinkling allowable stress due to inplane shear loads

K = Factor on wrinkling allowable due to ribbon vs. transverse strength of

core

Note, unless otherwise noted, x direction is the core ribbon direction.

Equations

Equations 13.1.1 and 13.1.2 show the wrinkling stress as an allowable. Below are the corresponding margin-of-safety equations (MS). MS equations for combined stresses are presented in the Appendix.

Analysis_ID= 90 Analysis_ID= 91 (Eqn #1, wrinkling isotropic cores) (Eqn #2, wrinkling honeycomb cores)

Generic

$$MS = \frac{k_1 (E_f E_c G_c)^{\frac{1}{3}}}{\sigma} - 1$$

$$MS = \frac{k_1 (E_f E_c G_c)^{\frac{1}{3}}}{\sigma} - 1 \qquad MS = \frac{k_2 E_f \sqrt{\frac{E_c t_f}{E_f t_c}}}{\sigma} - 1$$
 (13.1.4)

HyperSizer

x direction

$$MS = \frac{k_1 (E_{f,x} E_c G_c)^{\frac{1}{3}}}{\sigma_x} - 1$$

$$MS = \frac{k_1 (E_{f,x} E_c G_c)^{\frac{1}{3}}}{\sigma_x} - 1 \qquad MS = \frac{k_2 E_{f,x} \sqrt{\frac{E_c t_f}{E_{f,x} t_c}}}{\sigma_x} - 1 \qquad (13.1.5)$$

y direction

$$MS = \frac{K_{hc} k_1 (E_{f,y} E_c G_c)^{\frac{1}{3}}}{\sigma_y} - 1 \qquad MS = \frac{K_{hc} k_2 E_{f,x} \sqrt{\frac{E_c t_f}{E_{f,x} t_c}}}{\sigma_y} - 1 \qquad (13.1.6)$$

where:

 $K_{hc} = 1$ isotropic (e.g. foam) core $K_{hc} = 0.95$ honeycomb core

Biaxial Loads with Shear

In this case, x is the direction (either ribbon or transverse) of greatest *compressive* stress and y is the direction with least compressive (or tensile) stress. The form of the MS equation depends on whether σ_y is compressive or tensile.

$$\sigma_{y} \text{ compressive:} \qquad MS = \frac{2}{\left(\sigma_{x}^{3} + \sigma_{y}^{3}\right)^{\frac{1}{3}} + \sqrt{\left(\sigma_{x}^{3} + \sigma_{y}^{3}\right)^{\frac{1}{3}}} + 4\left(\sigma_{xy}^{3}\right)^{\frac{1}{3}}} + 4\left(\sigma_{xy}^{3}\right)^{\frac{1}{3}}} + 4\left(\sigma_{xy}^{3}\right)^{\frac{1}{3}}$$

$$\sigma_{y} \text{ tension:} \qquad MS = \frac{2}{\frac{\sigma_{x}}{K \sigma_{wr}} + \sqrt{\left(\frac{\sigma_{x}}{K \sigma_{wr}}\right)^{2} + 4\left(\frac{\sigma_{xy}}{\sigma_{wr}}\right)^{2}}} - 1 \qquad (13.1.8)$$

where σ_{wr} is the wrinkling allowable in the ribbon direction and is either given by Equation (13.1.1) or (13.1.2) above depending on whether the core is isotropic (e.g. foam) or honeycomb.

If the facesheet material is orthotropic, the effective stiffness in the x and y direction are different. Therefore, σ_{wr} is obtained by combining the effective wrinkling allowable from equation (13.1.1) or (13.1.2) by an average weighted by the σ_y and σ_y loads.

$$\sigma_{wr} = \frac{\sigma_x \sigma_{wr,x} + \sigma_y \sigma_{wr,y}}{\sigma_x + \sigma_y}$$
 (13.1.9)

13.1.3 References

- 13.2.1 Ley, R. P., Lin, W., Mbanefo, U., "Facesheet Wrinkling in Sandwich Structures", NASA CR-1999-208994, 1999.
- 13.2.2 Gutierrez, A.J. and Webber, J.P.H., "Flexural Wrinkling of Honeycomb Sandwich Beams with Laminated Faces," *International Journal of Solids and Structures*, Vol. 16, 1980, pp. 645-651.
- 13.2.3 Hexcel, "The Basics of Bonded Sandwich Construction," TSB 124, 1982.
- 13.2.4 Bruhn, E.F., "Analysis & Design of Flight Vehicle Structures", January 1965, C12.5.3.
- 13.2.5 Zhang, J.Z., Collier, C.S., "Margin of Safety from Interaction Equation", *Collier Research Internal Document*, February 12, 2004.

13.1.4 Interaction Equation for Wrinkling due to Biaxial Loads with Shear

The following is a derivation of the interaction equation for wrinkling (Equation 13.1.3) based on references [13.2.1] and [13.2.4]. For combined (x, y, xy) loading of a facesheet, HyperSizer assumes the following interaction equation suggested by Bruhn [13.2.4, p. 12.11 – 12.13]:

$$R_a + R_s^2 = 1$$
 (C 12.5.16) (13.2.1)

Where R_a and R_s are stress ratios of the form:

$$R_a = \frac{\sigma_x}{Fcw_x} \qquad R_s = \frac{\sigma_{xy}}{Fsw} \tag{13.2.2}$$

In these stress ratios, the x direction is either the ribbon direction or the transverse direction, whichever has the higher magnitude of compressive stress.

From Bruhn, C12.5.3.3; Fcw_x is given by:

$$\sigma_{y} \text{ compressive:} \qquad Fcw_{x} = \frac{Fcw}{\sqrt[3]{1 + \left(\frac{\sigma_{y}}{\sigma_{x}}\right)^{3}}} = \frac{Fcw \sigma_{x}}{\sqrt[3]{\sigma_{x}^{3} + \sigma_{y}^{3}}}$$
(13.2.3)

$$\sigma_{y}$$
 tensile: $Fcw_{x} = Fcw$

Therefore,

$$\sigma_{y}$$
 compressive: $R_{a} = \frac{\sqrt[3]{\sigma_{x}^{3} + \sigma_{y}^{3}}}{Fcw}$ (13.2.4) σ_{y} is tensile: $R_{a} = \frac{\sigma_{x}}{Fcw}$

According to section C12.5.3.2:

$$Fsw = Fcw \tag{13.2.5}$$

So the interaction equation becomes:

$$\sigma_y$$
 compressive:
$$\frac{\left(\sigma_x^3 + \sigma_y^3\right)^{\frac{1}{3}}}{Fcw} + \left(\frac{\sigma_{xy}}{Fcw}\right)^2 = 1$$
 (13.2.6)

$$\sigma_{y}$$
 tensile: $\frac{\sigma_{x}}{Fcw} + \left(\frac{\sigma_{xy}}{Fcw}\right)^{2} = 1$

Fcw is the allowable stress of a panel loaded in pure compression along the ribbon direction. Bruhn's form of this allowable is:

$$F_{cw} = \eta_2 (.43) \sqrt[3]{E_f E_c G_c} = k_1 \sqrt[3]{E_f E_c G_c} = \sigma_{wr}$$
 (13.2.7)

This has the same form as that suggested by [13.2.1], where the suggested value of k_1 is 0.63.

Bruhn also suggests that if the panel is principally loaded in the transverse direction, this allowable should be adjusted by a factor of 0.95. This is applied using a multiplication factor on the allowable, K. The final interaction equation becomes:

$$\sigma_{y} \text{ compressive:} \qquad \frac{\left(\sigma_{x}^{3} + \sigma_{y}^{3}\right)^{\frac{1}{3}}}{K \sigma_{wr}} + \left(\frac{\sigma_{xy}}{\sigma_{wr}}\right)^{2} = 1$$

$$\sigma_{y} \text{ tension:} \qquad \frac{\sigma_{x}}{K \sigma_{wr}} + \left(\frac{\sigma_{xy}}{\sigma_{wr}}\right)^{2} = 1$$
(13.2.8)

Where K = 1 for loading dominated in ribbon direction; K = 0.95 for loading dominated in transverse direction

To go from the interactive equation to an equation for Margin of Safety, the following margin of safety equation is derived from the interaction equation (see [13.2.4, equation C12.5.11] and [13.2.5, equation 4]):

$$MS = \frac{2}{R_a + \sqrt{R_a^2 + 4R_s^2}} - 1 \tag{13.2.9}$$

Therefore, using equations 13.2.2-13.2.7, the MS for facesheet wrinkling due to biaxial loading with shear becomes:

$$\sigma_{y} \text{ compressive: } MS = \frac{2}{\left(\sigma_{x}^{3} + \sigma_{y}^{3}\right)^{\frac{1}{3}} + \sqrt{\left[\left(\sigma_{x}^{3} + \sigma_{y}^{3}\right)^{\frac{1}{3}}\right]^{2} + 4\left(\frac{\sigma_{xy}}{\sigma_{wr}}\right)^{2}} - 1 \quad (13.2.10)$$

$$\sigma_{y} \text{ tension: } MS = \frac{2}{\left(\sigma_{x}^{3} + \sigma_{y}^{3}\right)^{2} + 4\left(\frac{\sigma_{xy}}{\sigma_{wr}}\right)^{2}} - 1$$

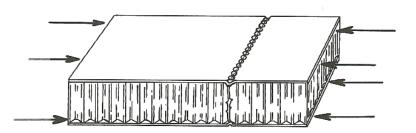
13.2 Dimpling

13.2.1 Summary approach

Intracell Dimpling, or Intracell buckling, is a failure specific to honeycomb sandwich concepts that is caused by local instability of the facesheets. If the face thickness of a honeycomb sandwich is reduced while cell size and material are held constant, a thickness will eventually be reached at which the facesheet will buckle between the cell walls. A typical Intracell dimpling failure is shown in the figure below.

Allowable Equation

The Intracell dimpling allowable stress is primarily a function of facesheet material stiffness, thickness and honeycomb cell size. The equation used to determine this stress is from [13.4.1].



$$\sigma_{dp} = \frac{2E_f}{\left(1 - \nu^2\right)} \left(\frac{t_f}{S}\right)^2 \tag{13.3.1}$$

Composite Materials

The above defined Intracell dimpling equation is based on isotropic materials and is based on the facesheet elastic modulus, E_f . However, in order to use the validated isotropic equation (13.3.1) for orthotropic materials, the assumption is that it is a better approach to substitute for E_f , not an equivalent membrane Young's modulus,

$$E_f = \frac{1}{{\mathbf{A}_{11}}^{-1} t_f}$$

but rather an equivalent flexural modulus based on the Dij of the laminate. HyperSizer computes this term using the D_{ii}^{-1} terms from the inverted 6x6 ABD matrix.

$$E_{f,x} = \frac{12}{D_{11}^{-1} t_f^3}; \ E_{f,y} = \frac{12}{D_{22}^{-1} t_f^3}$$

In addition, to account for the orthotropic nature of the material, the Poison's ratio term $(1-v_2)$ is replaced by the equivalent Poisson's ratio term for orthotropic materials, $(1-v_{12} \ v_{21})$.

Combined Loads

Most test data validation is performed on a "strut" specimen loaded uniaxially. Little research or test data exists for combined biaxial loading with or without shear. The approach used here is suggested by Bruhn [13.4.2]. The procedure is to rotate the actual stresses into a coordinate

system with axes parallel to the core ribbon and transverse directions. This approach takes on the interaction equation of the following form:

$$\frac{\left(\sigma_x^n + \sigma_y^n\right)^{\frac{1}{n}}}{\sigma_{dp}} + \left(\frac{\tau_{xy}}{0.8\sigma_{dp}}\right)^2 = 1$$
(13.3.2)

where n is a function of the ratio, (S/t_f) . HyperSizer implements this approach but extends it by determining allowable dimpling stresses in the two directions: $\sigma_{dp,x}$ and $\sigma_{dp,y}$. The Equation section describes the procedure in more detail, and how to properly determine the margin-of-safety (MS) from the interaction equation.

13.2.2 Symbols

 ν = Poisson's Ratio

 t_f = Thickness of facesheet

S = Cell size

 σ = Normal stress in facesheet

 $E_{f,x}$ = x direction, flexural modulus of facesheet

 $E_{f,y}$ = y direction, flexural modulus of facesheet

 σ_x = Facesheet stress in x (ribbon) direction

 σ_{v} = Facesheet stress in y (transverse) direction

 A_{11} , A_{22} D_{11} , D_{22}

= Stiffness terms from A, B, D matrix for facesheet

13.2.3 Equations

Generic
$$MS = \frac{2E_f}{(1-v_{12} v_{21})} \left(\frac{t_f}{S}\right)^2 - 1$$
 (13.3.3)

HyperSizer

x Direction
$$MS = \frac{2E_{f,x}}{(1 - v_{12} v_{21})} \left(\frac{t_f}{S}\right)^2 - 1$$
 (13.3.4)

y Direction
$$MS = \frac{2E_{f,y}}{(1 - v_{12} v_{21})} \left(\frac{t_f}{S}\right)^2 - 1$$
 (13.3.5)

For isotropic facesheets: $v_{12} = v_{21} = v$ and $E_{f,x} = E_{f,y} = E_f$

For composite facesheets:

mposite facesheets:
$$E_{f,x} = \frac{12}{D_{11}^{-1} t_f^{-3}}; E_{f,y} = \frac{12}{D_{22}^{-1} t_f^{-3}}$$
Effective Laminate Flexural Moduli

Biaxial Loads with Shear

In this case, x is the direction (either ribbon or transverse) of greatest *compressive* stress and y is the direction with least compressive (or tensile) stress. The form of the MS equation depends on whether σ_v is compressive or tensile and the magnitude of the (S/t_f) ratio. Margins of safety for biaxial and shear loads are given in terms of the dimpling allowable stress, σ_{dp} , which is computed independently in the x and y directions from Equation (13.3.1).

$$\sigma_{y} \text{ compressive:} \quad MS = \frac{2}{\left(\sigma_{x}^{n} + \sigma_{y}^{n}\right)^{\frac{1}{n}} + \sqrt{\left[\left(\sigma_{x}^{n} + \sigma_{y}^{n}\right)^{\frac{1}{n}}\right]^{2} + 4\left(\frac{\sigma_{xy}}{0.8\sigma_{dp}}\right)^{2}}} + 4\left(\frac{\sigma_{xy}}{0.8\sigma_{dp}}\right)^{2}$$

 $S/t_f > 15.63$: n = 3

$$S/t_f < 15.63$$
: $n = 2 + (15.63 / (S/t_f))^2$

 $\sigma_{y} \text{ tension:} \qquad MS = \frac{2}{\frac{\sigma_{x}}{\sigma_{dp}} + \sqrt{\left(\frac{\sigma_{x}}{\sigma_{dp}}\right)^{2} + 4\left(\frac{\sigma_{xy}}{0.8\sigma_{dp}}\right)^{2}}} - 1 \qquad (13.3.7)$

If the facesheet material is orthotropic, the effective stiffness in the x and y direction are different. Therefore, σ_{dp} is obtained by combining the effective wrinkling allowable from equation (13.3.1) by an average weighted by the σ_y and σ_y loads.

$$\sigma_{dp} = \frac{\sigma_x \sigma_{dp,x} + \sigma_y \sigma_{dp,y}}{\sigma_x + \sigma_y}$$
(13.3.8)

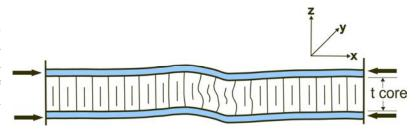
13.2.4 References

- 13.4.1 Hexcel, "The Basics of Bonded Sandwich Construction," TSB 124, 1982.
- 13.4.2 Bruhn, E.F., "Analysis & Design of Flight Vehicle Structures", January 1965, C12.5.3.
- 13.4.3 Zhang, J.Z., Collier, C.S., "Margin of Safety from Interaction Equation", Collier Research Internal Document, February 12, 2004.

13.3 Shear Crimping

13.3.1 Summary approach

Shear Crimping is a general panel instability failure mode which manifests as a short wavelength buckle. This failure is caused by the low shear modulus of the sandwich core.



Allowable Equation

The shear crimping allowable force is a function of the core depth (t_{core}), the shear stiffness in the direction of loading and the facesheet thickness. There are several different approaches to shear crimping in the literature. Reference [13.6.1] uses only the core thickness and shear stiffness in its allowable calculation.

$$N_{allowable} = Gt_{core} (13.5.1)$$

References [13.6.2] and [13.6.3] begin to account for the moment of inertia of both the facesheets and core by providing alternate allowable calculations:

Reference [13.6.2]:
$$N_{allowable} = G(t_{core} + 2t_f)$$
 (13.5.2)

Reference [13.6.3]:
$$N_{allowable} = 0.75G_c \frac{(t_{core} + 2t_f)^2}{t_{core}}$$
 (13.5.3)

We believe that neither of these forms fully accounts for the effects of facesheet flexibility on the shear crimping strength. Because crimping is a short wave phenomena, it does not seem that Equation 13.5.2 or 13.5.3 properly account for the facesheets, especially if their thickness is large in comparison to the core. If this is the case, the bending and shear resistance of the facesheets must be accounted for in the shear crimping calculation. In other words, the energy required for the facesheets to obtain the crimping deformation should be included. This energy is the lesser of the out-of-plane shearing (short-beam) or the cylindrical bending deformation of the facesheet. We suggest the following equation for shear crimping:

$$N_{allowable} = K_c G_c t_{core} + K_f \left[\frac{(2G_f t_f)(2D_{11,f})}{2G_f t_f + 2D_{11,f}} \right]$$

where K_c and K_f are factors that specify the proportions to which facesheet and core affect the crimping allowable. By inspection, this is a more general equation to account for the facesheet contribution. As we collect shear crimping test data, these factors will be determined. For now, the default calculation in HyperSizer only accounts for the core, therefore $K_c = 1$ and $K_f = 0$.

13.3.2 Symbols

G = Out-of-plane shear modulus of core

 G_{ℓ} = Out-of-plane shear modulus of core in ribbon direction

 G_{ω} = Out-of-plane shear modulus of core in transverse direction

 t_{core} = Core thickness of core

 θ = Angle between ribbon direction and principal loading direction

N = Force per unit length

 N_x = Force per unit length in x (ribbon) direction N_y = Force per unit length in y (transverse) direction N_I = Force per unit length in principal coordinates

13.3.3 Equations

Generic
$$MS = \frac{G t_{core}}{N} - 1$$
 (13.5.4)

HyperSizer

x direction:
$$MS = \frac{G_{\ell} t_{core}}{N_{x}} - 1$$
 (13.5.5)

y direction:
$$MS = \frac{G_{\omega} t_{core}}{N_{y}} - 1$$
 (13.5.6)

Biaxial Loads with Shear

If in-plane shear is present, the loads are rotated into principal coordinates using Mohr's circle approach. So from Nx, Ny, we get the principal stresses, N_L , N_{II} , which are the major and minor principal stresses respectively. Rotate the out-of-plane shear term into the direction of principal coordinates according to:

$$G_{Iz} = \sin^2 \theta G_{\omega} + \cos^2 \theta G_l \tag{13.5.7}$$

where θ is the angle between the ribbon direction and the principal loading direction.

Biaxial with shear:
$$MS = \frac{G_{Iz} t_{core}}{N_I} - 1$$
 (13.5.8)

13.3.4 References

- 13.6.1 Hexcel, "The Basics of Bonded Sandwich Construction," TSB 124, 1982.
- 13.6.2 Bruhn, E.F., "Analysis & Design of Flight Vehicle Structures", January 1965, C12.5.3.
- 13.6.3 Boeing, "Advanced Composite Design Handbook," Rev B, p 4.6-12

13.4 Core Crushing

13.4.1 Approach Summary

There are three different types of loadings that can cause core crushing. The first is from a concentrated load. The second is caused by flexural bending moments. The third is caused by joint support loads.

For all three types of loadings, the choice will be available for the user to compare calculated core compressive stress to either: crush, bar, or stabilized material allowables.

$$User Choice \ of (Fcu_{crush}, Fcu_{bare}, Fcu_{stablized})$$

The HyperSizer default is to take the lowest of these three core material allowables.

13.4.2 Symbols

d = sandwich depth between facesheet neutral axis (sheet midplanes)

 D_{ii} = sandwich bending stiffness

 f_{cc} = compressive core stress in the normal (Z axis)

 Fcu_{crush} = compressive, through-thickness crush strength of core (strength after

exceeding initial ultimate failure, a constant post failure load allowable)

 Fcu_{haro} = compressive, through-thickness bare strength of core (higher than the

crush

strength but lower than facesheet stabilized strength)

 $Fcu_{stabilized}$ = compressive, through-thickness stabilized strength of core (higher than

crush or bare allowable)

p = unit pressure loading

 Q_x = out-of-plane shear load in x Q_y = out-of-plane shear load in y

 W_{eff} = effective width of support bearing upon sandwich panel

 Z_c = compressive, through-thickness strength of core (general term)

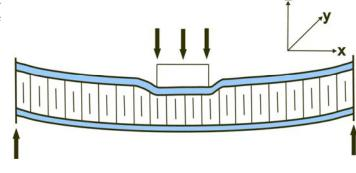
Core Crushing Concentrated Load, Analysis ID = 100

This type of failure occurs when a concentrated load (pressure) bears down in the normal direction, reference [13.8.1].

Equations

Generic

$$MS = \frac{Z_c}{p} - 1$$



HyperSizer

$$MS = \frac{\min(Fcu_{crush}, Fcu_{stablized})}{p} - 1$$

* Software will calculate MS from minimum of Fcu_{crush} or $Fcu_{stabilized}$. User controls which allowable is considered by creating alternate materials with either crush or stabilized properties removed.

Core Crushing Flexural Bending Load, Analysis ID = 101

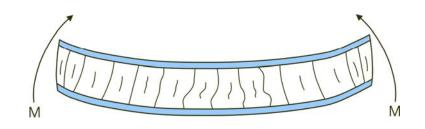
This type of failure occurs when bending moment is high and the facesheet is thick and the core is weak. This type of failure is uncommon in airframe structures [13.8.2].

Equations

Generic

$$f_{cc} = \frac{M \, \text{max}^2}{d \, Dij}$$

$$MS = \frac{Z_c}{f_{cc}} - 1$$



HyperSizer

$$MS = \frac{\min(Fcu_{crush}, Fcu_{stablized})}{f_{cc}} - 1$$

* Software will calculate MS from minimum of Fcu_{crush} or $Fcu_{stabilized}$. User controls which allowable is considered by creating alternate materials with either crush or stabilized properties removed.

Core Crushing Joint Support Load, Analysis ID = 102

This type of loading occurs when a sandwich panel is continuous across and supported underlying by substructure such as wing spars and ribs, or by fuselage ringframes or shape control members, Fig. 13.7.1. This is in contrast to joint designs that have closeouts or rampdowns at the sandwich panel edges, such as in Fig. 13.7.2, in which case the out-of-plane Qx and Qy shear loads do not cause concentrated compressive core stresses.

Failure mode of Fig. 13.7.1 is HyperSizer a default toggled on analysis. It uses the FEA computed shell element Q_x and Q_y forces to obtain an

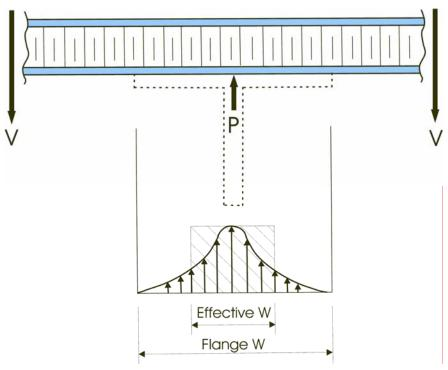


Fig. 13.7.1, Compressive stress on sandwich panel from support bearing load P.

appropriate concentrated load. In many cases of high out-of-plane (normal) pressure loading, this failure mode will control the optimization. If this failure mode is toggled off, consideration should be given to the extra weight required to obtain a panel edge closeout, such as Fig. 13.7.2. HyperSizer does not yet perform rampdown closeout analysis.

Panel out-of-plane edge forces Q_x and Q_y (V) are equivalent to a running (unit) "P" force. This force "P" is mostly concentrated in the vicinity of the stiffener, with less force exerted by the more flexible flanges. This applied force distribution is represented by the curve of Fig.

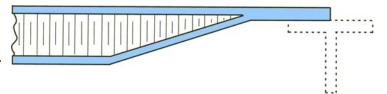


Fig. 13.7.2, Sandwich Rampdown closeout design.

13.7.1, where the length of the upward pointing vertical lines indicate a relative magnitude. The area under this curve is equal to "P". Another representation is to assume the "P" force is supported by an effective width of the stiffener. The same peak stress times the effective width is depicted by the rectangle, and this area also equals "P". The key being that the peak compressive stress equals the same for both representations, and is the value used for failure prediction. An appropriate effective width for aerospace joints is assumed to be 1".

Equations

Generic

$$f_{cc} = \frac{p}{Weff}$$

$$MS = \frac{Z_c}{f_{cc}} - 1$$

HyperSizer

$$f_{cc} = \frac{Max\left(Q_{x}, Q_{y}\right)}{Weff}$$

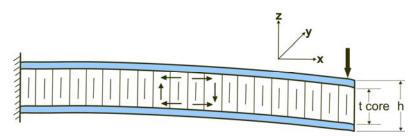
$$MS = \frac{\min(Fcu_{crush}, Fcu_{stablized})}{f_{cc}} - 1$$

* Software will calculate MS from minimum of Fcu_{crush} or $Fcu_{stabilized}$. User controls which allowable is considered by creating alternate materials with either crush or stabilized properties removed.

13.4.3 References

- 13.8.1 Hexcel, "The Basics of Bonded Sandwich Construction," TSB 124, 1982.
- 13.8.2 Boeing, "Advanced Composite Design Handbook," Rev B, p 4.6-12.

13.5 Shear Strength



13.5.1 Summary approach

The shear strength failure calculation is a comparison of the shear strength in the core to the out-of-plane shear loads

induced by cantilevered loads (as shown here) or pressure loads, which are common in aerospace applications. In the case of coupling of HyperSizer with FEA, the shear loads in the panels, Q_x and Q_y are extracted directly from the element forces of the FEA results.

Allowable Equation

The shear strength allowable is the shear strength in the core multiplied by a shear strength correction factor, which is derived from vendor data. The form of the shear strength allowable is taken from Reference [13.10.1].

$$Q_{allowable} = R K_{sscf} h ag{13.9.1}$$

13.5.2 Symbols

R = Out-of-plane shear strength of core

 K_{sscf} = Shear strength correction factor

Q = Out-of-plane shear load per unit length

 Q_x = Out-of-plane shear load per unit length in x (ribbon) direction

 Q_y = Out-of-plane shear load per unit length in y (transverse) direction

h = Total panel height (core & facesheets)

 Fsu_{ℓ} = Out-of-plane ultimate shear strength of core in ribbon direction

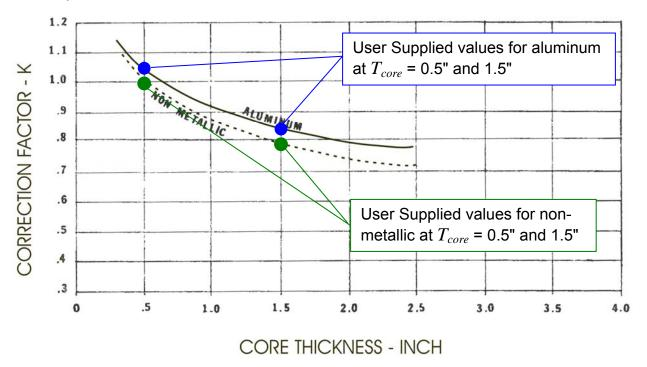
 Fsu_{ω} = Out-of-plane ultimate shear strength of core in transverse direction

 t_{core} = Core thickness

13.5.3 Shear Strength Correction Factor

The shear strength correction factor is a modification of the shear strength allowable based on the thickness of the core. The shape of the curve is generic, but the specific curve is material dependent and should be supplied by the honeycomb vendor. The figure below shows some typical curves for aluminum and "non-metallic" taken from Ref. [13.10.1]. The important thing to remember is the user has complete freedom to enter a correction factor for their own material systems.

In HyperSizer, the generic material depend curve is approximated with a bilinear curve fit based on user supplied values for shear strength correction factors at two core thicknesses ($t_{core} = 0.5$ " and 1.5").



13.5.4 Equations

Generic

$$MS = \frac{R K_{sscf}}{\frac{Q}{h}} - 1$$

HyperSizer

$$MS_{x} = \frac{Fsu_{\ell} K_{sscf}}{\frac{Q_{x}}{h}} - 1$$

$$MS_{y} = \frac{Fsu_{\omega} K_{sscf}}{\frac{Q_{y}}{h}} - 1$$

13.5.5 References

13.10.1 Hexcel, "The Basics of Bonded Sandwich Construction," TSB 124, 1982.

14 Failure Criteria for Laminates

Refer to Volume 2, Chapter 7 for details on the equations. Omitted from here.

15 How to compute Margin-of-Safety for complex loading and failure interactions

The following table summarizes the margin of safety of selected interactive equations.

Table 15, Summary of margin of safety of selected interactive equations

No.	Interactive equations	Margin of safety (MOS)
1	$\mathbf{R}_1 + \mathbf{R}_2 = 1$	$MOS = \frac{1}{R_1 + R_2} - 1$
2	$\mathbf{R}_1^2 + \mathbf{R}_2^2 = 1$	$MOS = \frac{1}{\sqrt{R_1^2 + R_2^2}} - 1$
3	$\mathbf{R}_{1}^{n} + \mathbf{R}_{2}^{n} + \mathbf{R}_{3}^{n} + \mathbf{R}_{k}^{n} = 1$ (k =1,2N)	$MOS = \frac{1}{(R_1^n + R_2^n + R_3^n +R_k^n)^{1/n}} - 1$
4	$\mathbf{R}_1^2 + \mathbf{R}_2 = 1$	$MOS = \frac{2}{R_2 + \sqrt{R_2^2 + 4R_1^2}} - 1$
5	$\mathbf{R}_1^2 + \mathbf{R}_2 + \mathbf{R}_3 = 1$	$MOS = \frac{2}{(R_2 + R_3) + \sqrt{(R_2 + R_3)^2 + 4R_1^2}} - 1$
6	$\mathbf{R}_1^2 + \mathbf{R}_2^2 + \mathbf{R}_3 = 1$	$MOS = \frac{2}{R_3 + \sqrt{R_3^2 + 4(R_1^2 + R_2^2)}} - 1$
7	$(\mathbf{R}_{1}^{2} + \mathbf{R}_{2}^{2} + \mathbf{R}_{3}^{2} + \mathbf{R}_{m}^{2}) + (\mathbf{R}_{m+1} + \mathbf{R}_{m+2} + \mathbf{R}_{m+3} + \mathbf{R}_{m+n}) = 1 $ $(\mathbf{n} = 1, 2, N), (\mathbf{m} = 1, 2, P)$	$MOS = \frac{2}{\sum_{k=m+1}^{m+n} R_k + \sqrt{\left(\sum_{k=m+1}^{m+n} R_k\right)^2 + 4\left(\sum_{k=1}^{m} R_k^2\right)}} - 1$
8	$(\mathbf{R}_{1}\mathbf{R}_{2} + \mathbf{R}_{2}\mathbf{R}_{3} + \mathbf{R}_{3}\mathbf{R}_{4} + + \mathbf{R}_{m-1}\mathbf{R}_{m}) + (\mathbf{R}_{m+1} + \mathbf{R}_{m+2} + \mathbf{R}_{m+3} +\mathbf{R}_{m+n}) = 1$ $(\mathbf{n} = 1, 2, N), (\mathbf{m} = 1, 2, P)$	$MOS = \frac{2}{\sum_{k=m+1}^{m+n} R_k + \sqrt{\left(\sum_{k=m+1}^{m+n} R_k\right)^2 + 4\left(\sum_{k=1}^{m} R_{k-1} R_k\right)}} - 1$
9	$\mathbf{R}_1^2 + \mathbf{R}_2^2 = \left(1 - \mathbf{R}_3\right)^2$	$MOS = \frac{1}{R_3 + \sqrt{(R_1^2 + R_2^2)}} - 1$

15.1 Interactive form of failure criteria

The failure criteria are generally given in an interactive fashion, as

$$\mathbf{R}_{1}^{x} + \mathbf{R}_{2}^{y} + \mathbf{R}_{3}^{z} + \dots = 1 \tag{15.1.1}$$

where

 \mathbf{R}_1 , \mathbf{R}_2 , \mathbf{R}_3 = stress ratio (applied stress or load /allowables) for various loadings such as compression, bending, shear, etc.

x, y, z = exponents defining interaction relationships

15.2 Definition of margin of safety (MOS)

Considering only two loading conditions, Equation (15.1.1) can be plotted as a single interaction curve as R_1 against R_2 . When three or more loading conditions exist, the interaction equation represents an interaction surface.

Now take an interaction curve with only two loading conditions (R_1 and R_2), as shown in Fig. 15.2.1.

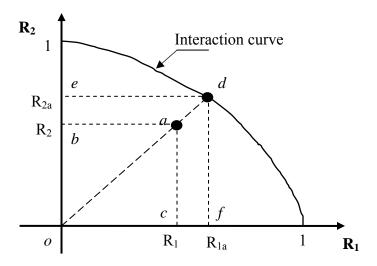


Fig. 15.2.1, Definition of MOS for a failure criterion with two interactive terms.

In Fig. 15.2.1, arbitrary point "a" given by (R_1, R_2) represents a positive margin of safety, because it locates inside the curve. Then the *Margin of Safety* (MOS) [15.5.1, 15.5.2] is defined as

$$MOS = \frac{od}{oa} - 1 = \frac{of}{oc} - 1 = \frac{oe}{ob} - 1 \text{ or } MOS = \frac{od}{oa} - 1 = \frac{R_{1a}}{R_1} - 1 = \frac{R_{2a}}{R_2} - 1$$
 (15.2.1)

Equation (15.2.1) also implies the following universal relations

$$\frac{od}{oa} = \frac{R_{1a}}{R_1} = \frac{R_{2a}}{R_2} = \delta \tag{15.2.2}$$

Extending the above definition to three or more loading conditions, we have

$$MOS = \frac{od}{oa} - 1 = \frac{R_{1a}}{R_1} - 1 = \frac{R_{2a}}{R_2} - 1 = \frac{R_{3a}}{R_2} - 1 = \dots = \frac{R_{na}}{R_n} - 1$$
 (15.2.3)

and

$$\frac{od}{oa} = \frac{R_{1a}}{R_1} = \frac{R_{2a}}{R_2} = \frac{R_{3a}}{R_3} = \dots = \frac{R_{na}}{R_n} = \delta$$
 (15.2.4)

15.3 Calculation of margin of safety Examples

For the same order interactive relations, i.e. exponent is same for each term, the MOS could be solved analytically; while for those with different exponents (>=3) for each term, numerical methods are usually used to obtain the solutions of MOS. In the following, we give some commonly used interactive equations and show the detailed solution procedure of obtaining MOS analytically.

Example 1.

$$\mathbf{R}_1 + \mathbf{R}_2 = 1 \tag{15.3.1}$$

Solution:

According to Equation (15.2.2), we have the following universal relations hold

$$\frac{R_{1a}}{R_1} = \delta \tag{15.3.2}$$

$$\frac{R_{1a}}{R_1} = \delta \tag{15.3.2}$$

$$\frac{R_{2a}}{R_2} = \delta \tag{15.3.3}$$

The point (R_{1a}, R_{2a}) is always on the curve, so it should satisfy Equation (15.3.1),

$$R_{1a} + R_{2a} = 1 ag{15.3.4}$$

Solving Equations $(15.3.2)\sim(15.3.4)$ together yields

$$\delta(R_1 + R_2) = 1 \qquad \Rightarrow \qquad \delta = \frac{1}{R_1 + R_2} \tag{15.3.5}$$

Thus, MOS is obtained from Equation (15.2.1),

$$MOS = \delta - 1 = \frac{1}{R_1 + R_2} - 1$$
 (15.3.6)

Example 2

$$\mathbf{R}_{1}^{2} + \mathbf{R}_{2}^{2} = 1 \tag{15.3.7}$$

Solution 1 (Method 1)

According to the original definition of MOS, Equation (15.2.1)

$$MOS = \frac{od}{oa} - 1 \tag{15.3.8}$$

where od represents the distance between the origin and the points (R_{1a} , R_{2a}) on the interaction curves, as shown in Fig. 15.2.1; oa represents the distance between an arbitrary point and the origin. Since Equation (15.3.7) represents a circle with origin at (0,0) and radius of 1, od is always equal to 1. That is

$$od = 1 \tag{15.3.9}$$

and

$$oa = \sqrt{R_1^2 + R_2^2} \tag{15.3.10}$$

Thus

$$MOS = \frac{1}{\sqrt{R_1^2 + R_2^2}} - 1 \tag{15.3.11}$$

Solution 2 (Method 2)

This method follows the general procedure described in Example 1. It start with the following universal relations

$$\frac{R_{1a}}{R_1} = \delta \qquad \Rightarrow \qquad R_{1a} = R_1 \delta
\frac{R_{2a}}{R_2} = \delta \qquad \Rightarrow \qquad R_{2a} = R_2 \delta$$
(15.3.12)

and

$$R_{1a}^2 + R_{2a}^2 = 1 ag{15.3.13}$$

Solving Equations (15.3.12) and (15.3.13), yields

$$\delta = \frac{1}{\sqrt{R_1^2 + R_2^2}} \tag{15.3.14}$$

so that

$$MOS = \frac{1}{\sqrt{R_1^2 + R_2^2}} - 1 \tag{15.3.15}$$

Example 3

Equations (15.3.1) and (15.3.7) are the two-term polynomial functions with the same order, we can easily extend them into the multiple terms, as

$$\mathbf{R}_{1}^{n} + \mathbf{R}_{2}^{n} + \mathbf{R}_{3}^{n} + ... \mathbf{R}_{k}^{n} = 1$$
 (k=1,2....N) (15.3.16)

Following the procedure described in Example 1 and 2, we can readily obtain the MOS for Equation (15.3.16). It is

$$MOS = \frac{1}{(R_1^n + R_2^n + R_3^n + ...R_k^n)^{1/n}} - 1$$
 (15.3.17)

Obviously, the interactive functions in example 1 and example 2 are the special cases of Equation (15.3.16) when n = 1 and 2, k = 2.

In the following, we give some simple examples for the interactive functions with different orders.

Example 4

$$\mathbf{R}_{1}^{2} + \mathbf{R}_{2} = 1 \tag{15.3.18}$$

We can see that in Equation (15.3.18), the exponents for term R1 and term R2 are different. Nevertheless, we still start with the universal relations

$$\frac{R_{1a}}{R_1} = \delta \qquad \Rightarrow \qquad R_{1a} = R_1 \delta \qquad \Rightarrow \qquad (R_{1a})^2 = (R_1 \delta)^2$$

$$\frac{R_{2a}}{R_2} = \delta \qquad \Rightarrow \qquad R_{2a} = R_2 \delta$$
(15.3.19)

$$R_{1a}^2 + R_{2a} = 1 ag{15.3.20}$$

Substituting Equation (15.3.19) into (15.3.20) yields

$$\delta^2 \cdot R_1^2 + \delta \cdot R_2 - 1 = 0 \tag{15.3.21}$$

Solving δ from Equation (15.3.21), we have

$$\delta_{1,2} = \frac{-R_2 \pm \sqrt{R_2^2 + 4R_1^2}}{2R_1^2} \tag{15.3.22}$$

Taking the positive root of Equation (15.3.22), we obtain δ

$$\delta = \frac{-R_2 + \sqrt{R_2^2 + 4R_1^2}}{2R_1^2} \tag{15.3.23}$$

It also can be written as an alternative form

$$\delta = \frac{-R_2 + \sqrt{R_2^2 + 4R_1^2}}{2R_1^2} = \frac{\left(-R_2 + \sqrt{R_2^2 + 4R_1^2}\right) \cdot \left(-R_2 - \sqrt{R_2^2 + 4R_1^2}\right)}{2R_1^2 \cdot \left(-R_2 - \sqrt{R_2^2 + 4R_1^2}\right)}$$

$$= \frac{R_2^2 - R_2^2 - 4R_1^2}{2R_1^2 \cdot \left(-R_2 - \sqrt{R_2^2 + 4R_1^2}\right)} = \frac{2}{R_2 + \sqrt{R_2^2 + 4R_1^2}}$$
(15.3.24)

$$MOS = \delta - 1 = \frac{2}{R_2 + \sqrt{R_2^2 + 4R_1^2}} - 1$$
 (15.3.25)

Example 5

$$\mathbf{R}_{1}^{2} + \mathbf{R}_{2} + \mathbf{R}_{3} = 1 \tag{15.3.26}$$

Using the universal relations, we have

$$\frac{R_{1a}}{R_1} = \delta \qquad \Rightarrow \qquad R_{1a} = R_1 \delta \qquad \Rightarrow \qquad (R_{1a})^2 = (R_1 \delta)^2$$

$$\frac{R_{2a}}{R_2} = \delta \qquad \Rightarrow \qquad R_{2a} = R_2 \delta$$

$$\frac{R_{3a}}{R_3} = \delta \qquad \Rightarrow \qquad R_{3a} = R_3 \delta$$
(15.3.27)

$$R_{1a}^2 + R_{2a} + R_{3a} = 1 ag{15.3.28}$$

substituting Equation (15.3.27) into (15.3.28), yields

$$\delta^2 \cdot R_1^2 + \delta \cdot (R_2 + R_3) - 1 = 0 \tag{15.3.29}$$

Solving Equation (15.3.29) and taking the positive root, yields

$$\delta = \frac{-(R_2 + R_3) + \sqrt{(R_2 + R_3)^2 + 4R_1^2}}{2R_1^2}$$
 (15.3.30)

After some algebraic operation described in Equation (15.3.24), we finally obtain the expression for the margin of safety of Equation (15.3.16). It is given as

$$MOS = \delta - 1 = \frac{2}{(R_2 + R_3) + \sqrt{(R_2 + R_3)^2 + 4R_1^2}} - 1$$
 (15.3.31)

Example 6

$$\mathbf{R}_{1}^{2} + \mathbf{R}_{2}^{2} + \mathbf{R}_{3} = 1 \tag{15.3.32}$$

Solution:

Using the universal relations, we have

$$\frac{R_{1a}}{R_1} = \delta \qquad \Rightarrow \qquad R_{1a} = R_1 \delta \qquad \Rightarrow \qquad (R_{1a})^2 = (R_1 \delta)^2$$

$$\frac{R_{2a}}{R_2} = \delta \qquad \Rightarrow \qquad R_{2a} = R_2 \delta \qquad \Rightarrow \qquad (R_{2a})^2 = (R_2 \delta)^2$$

$$\frac{R_{3a}}{R_3} = \delta \qquad \Rightarrow \qquad R_{3a} = R_3 \delta$$
(15.3.33)

$$R_{1a}^2 + R_{2a}^2 + + R_{3a} = 1 (15.3.34)$$

substituting Equation (15.3.33) into (15.3.34), yields

$$\delta^2 \cdot (R_1^2 + R_2^2) + \delta \cdot (R_3) - 1 = 0 \tag{15.3.35}$$

Solving Equation (15.3.35) and taking the positive root, yields

$$\delta = \frac{-R_3 + \sqrt{R_3^2 + 4(R_1^2 + R_2^2)}}{2(R_1^2 + R_2^2)}$$
(15.3.36)

After some algebraic operation described in Equation (15.3.24), we finally obtain the expression for the margin of safety of Equation (15.3.32). It is given as

$$MOS = \delta - 1 = \frac{2}{R_3 + \sqrt{R_3^2 + 4(R_1^2 + R_2^2)}} - 1$$
 (15.3.37)

Example 7

Extending example 6 and example 7 into a more general case, we write the following interactive polynomial

$$\left(\mathbf{R}_{1}^{2} + \mathbf{R}_{2}^{2} + \mathbf{R}_{3}^{2} + ... + \mathbf{R}_{m}^{2}\right) + \left(\mathbf{R}_{m+1} + \mathbf{R}_{m+2} + \mathbf{R}_{m+3} + ... \mathbf{R}_{m+n}\right) = 1 \quad (n = 1, 2, ... N), (m = 1, 2, ... P)$$
(15.3.38)

Following the same procedure described in examples 6 and 7, we can have the MOS

$$MOS = \frac{2}{\sum_{k=m+1}^{m+n} R_k + \sqrt{\left(\sum_{k=m+1}^{m+n} R_k\right)^2 + 4\left(\sum_{k=1}^{m} R_k^2\right)}} - 1$$
 (15.3.39)

Note that the margin of safety for the following interactive relation is also easily calculated,

$$(\mathbf{R}_{1}\mathbf{R}_{2} + \mathbf{R}_{2}\mathbf{R}_{3} + \mathbf{R}_{3}\mathbf{R}_{4} + ... + \mathbf{R}_{m-1}\mathbf{R}_{m}) + (\mathbf{R}_{m+1} + \mathbf{R}_{m+2} + \mathbf{R}_{m+3} + ...\mathbf{R}_{m+n}) = 1$$
 (15.3.40)

We can see the summation of the orders of each terms in the first bracket is same, so MOS is

$$MOS = \frac{2}{\sum_{k=m+1}^{m+n} R_k + \sqrt{\left(\sum_{k=m+1}^{m+n} R_k\right)^2 + 4\left(\sum_{k=1}^{m} R_{k-1} R_k\right)}} - 1$$
 (15.3.41)

There are many other variation of Equation (15.3.38), but we can still easily find their MOS, by putting the same-order terms in groups and then substituting them into Equation (15.3.39).

Example 8

$$\mathbf{R}_{1}^{2} + \mathbf{R}_{2}^{2} = (1 - \mathbf{R}_{3})^{2} \tag{15.3.42}$$

Expanding Equation (15.3.42), yields

$$\mathbf{R}_{1}^{2} + \mathbf{R}_{2}^{2} - \mathbf{R}_{3}^{2} + 2\mathbf{R}_{3} = 1 \tag{15.3.43}$$

Starting with the universal relations, we have

$$\frac{R_{1a}}{R_1} = \delta \qquad \Rightarrow \qquad R_{1a} = R_1 \delta \qquad \Rightarrow \qquad (R_{1a})^2 = (R_1 \delta)^2$$

$$\frac{R_{2a}}{R_2} = \delta \qquad \Rightarrow \qquad R_{2a} = R_2 \delta \qquad \Rightarrow \qquad (R_{2a})^2 = (R_2 \delta)^2$$

$$\frac{R_{3a}}{R_3} = \delta \qquad \Rightarrow \qquad R_{3a} = R_3 \delta \qquad \Rightarrow \qquad (R_{3a})^2 = (R_3 \delta)^2$$

$$(15.3.44)$$

and

$$R_{1a}^2 + R_{2a}^2 - R_{3a}^2 + 2R_{3a} = 1 (15.3.45)$$

Substituting Equation (15.3.44) into (15.3.45), yields

$$\delta^{2}(R_{1}^{2} + R_{2}^{2}) - (\delta R_{3} - 1)^{2} = 0$$
 (15.3.46)

Solving Equation (15.3.46), we have

$$\delta \sqrt{(R_1^2 + R_2^2)} = \pm (\delta R_3 - 1) \tag{15.3.47}$$

Taking the positive root of δ , we finally get

$$MOS = \delta - 1 = \frac{1}{R_3 + \sqrt{(R_1^2 + R_2^2)}} - 1$$
 (15.3.48)

15.4 Summary

The Margin of safety of interactive failure criteria was defined and the procedure for calculating MOS was described in general and details. For the same order interactive relations, i.e. exponent is same for each term, the MOS could be solved analytically; while for those with different exponents (>= 3) for each term, numerical methods are usually used to obtain the solutions of MOS. Eight types of interactive failure criteria are given as examples to demonstrate the procedure of calculation of MOS.

15.5 References

- 15.5.1 Niu, M. C. Y., Airframe stress analysis and sizing, 1997, Hong Kong Conmilit Press Limited.
- 15.5.2 Aircraft products group, Structures Manual.

16 How to back out Margin-of-Safety from %reliability, and %reliability from MS

Refer to Vol 1, Ch 11.2. Omitted from here.

---Automation---

17 HyperSizer and Automation through Web Services

17.1 Meeting Notes and Design Document for HyperSizer Web Services

A meeting was held at AFRL in October 2003 with Phil Yarrington(CRC), Craig Collier(CRC), Duane Veley (AFRL), and Ray Kolonay (AFRL) to discuss the possibilities of developing a web-services based environment that could either call HyperSizer and/or allow HyperSizer to call other analysis codes. As a result of this Collier Research proposed and partially carried out an activity to investigate .NET and web services and how they can be used with HyperSizer to establish an enterprise-wide engineering environment. This environment should allow industry and government designers and analysts to easily access best-in-class software tools (both newly developed and legacy tools) regardless of geographic location or computer platform.

17.2 Background and Purpose of Prototype

The commercially available structural analysis and sizing tool, HyperSizer, has a built-in object model that exposes much of its functionality through Windows COM / ActiveX. This allows HyperSizer processes to be automated, called as part of a batch process, and integrated into a larger design environment. For example, we have successfully integrated HyperSizer's detail optimization with a global vehicle optimization using the non-linear solver capability of Microsoft Excel. HyperSizer was also integrated into a multi-disciplinary design environment using ModelCenter from Phoenix Integration as part of NASA's HPCCP (High Performance Computing and Communications Program).

The capabilities of the HyperSizer Object Model are described in some detail in the white paper "Using the HyperSizer Object Model for Software Integration", which is downloadable from the HyperSizer.com website.

http://hypersizer.com/pdf/wp01_using_the_hyperSizer_object_model_for_software_integration.pdf

In the development of the proposed prototype, we will leverage HyperSizer's automation capability and demonstrate its usefulness to an Enterprise wide aerospace vehicle design environment in two capacities.

- 1. Establish HyperSizer as a WEB SERVICE that can be called from any platform and included as part of a Web Service Process.
- Use HyperSizer's structural analysis specific database and infrastructure as a hub that
 exposes best-in-class structural legacy codes to an industry and government wide user
 base through web services.

17.3 AFRL/VA Background and Interest

The AFRL technical lead for this prototype development has a strong background with JAVA and network computing. One possible model for this new system is called the Federated

Intelligent Product Environment (FIPER), which was developed at GE, and uses JAVA JINI, which builds on and extends JAVA RMI (Remote Method Invocation). Collier Research has some experience with these methods from its work with NASA HPCCP (High Performance Computing and Communications Program).

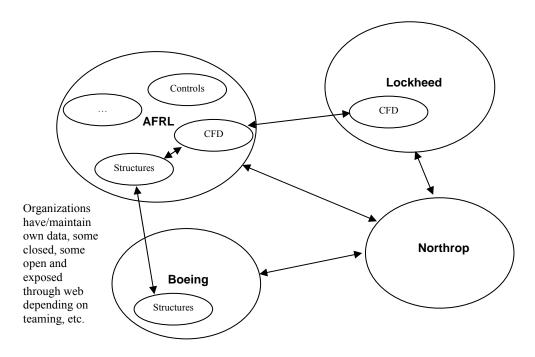
In FIPER, only limited amounts of Meta-data were "injested" (i.e. imbedded in objects that are passed directly through ports opened by RMI) while larger blocks of data were passed around through URL web links. In other words, when objects were passed around, subroutines invoked, etc. there were no large arrays of data passed through the calling arguments, rather data like this was passed through files with web downloads, http, ftp, etc.

AFRL's interest is in "Network Computing" for engineering analyses analogous to these technologies emerging in Business to Business (B2B) systems. Engineering analysis methods should be combined over a network, allowing engineers to access tools from anywhere without needing specifics of their implementation or needing to maintain their software (i.e. If a change is made to the software on the web, it should automatically be available to the end users without any action on their part.). This environment should be implemented for heterogeneous networks.

In our prototype, AFRL asked us to explore .NET, XML, SOAP, web services and their viability as an engineering environment. This should be an Object Oriented Design Environment over a heterogeneous network. They know of no existing .NET project that we can reference as a successful model for the type of prototype we want to build.

17.4 AFRL/VA Grand Vision

The ultimate objective of integrating tools together is to create an engineering environment as shown in the below figure. The system should allow engineers and designers at different sites and organizations within each site to access each other's data and software as required by partnership agreements, etc, be secure and be easy to maintain.



The attributes of this vision:

- There is communication of data and programs between disciplines (e.g. structures to CFD), between companies, and between government and industry
- Organizations control the extent to which their own data and programs are shared with other companies and/or the government
- No transfer of data through flat files
 - o E.g. Data files to removable media, hard drives, files transmitted over internet, etc.
 - Eliminate the current paradigm where if an engineer wants data or a program, he would have to contact an individual or organization and they then have to fill out paperwork, collect data, build an installation for a program, send him instructions for how to install it, and he would have to get IT people to give him administrative privilege, etc.
- No porting of codes Example: Structures needs access to CFD results but doesn't want to:
 - o see/maintain source code
 - o know how to run code
 - o know how it is implemented
- The clients or software consumers in the system only need to know the interfaces for what data is sent to programs and what is returned.

In the long term, we want to have a mature distributed analysis process with the following attributes that were present in the FIPER system. All of these attributes may or may not necessarily be available in our prototype demonstration.

- Create Process
- Submit individual jobs
- Monitor individual jobs and entire process
- Interactive Debugger

- Ability to pause process
- Retrieve intermediate results
- Edit
 - o Data
 - Process
- Restart process from anywhere

17.5 Advantages of .NET for Distributed Engineering Analysis

AFRL/VA is not too interested at this point in the .NET CLR (Common Language Runtime) implementation, but said that they might be later. The idea behind CLR is essentially the same as the Java Virtual Machine (JVM).

.NET has the following qualities:

- Provides an extensive communications infrastructure backed by Microsoft (meaning that it can't be ignored)
- Has strong built-in security (this is a REALLY big deal)
- *Corporate acceptance

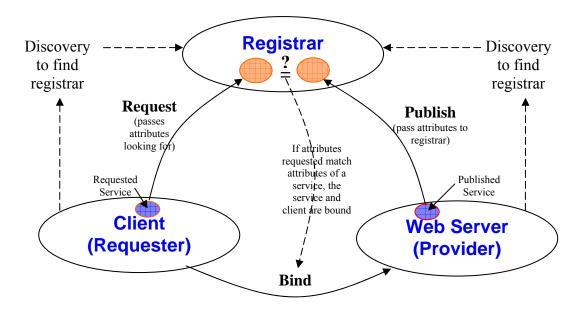
Our technical lead's opinion is that the Java JINI/RMI solution, such as was used in FIPER, is just as good as .NET (if not better), however the big problem they had with their system is that they required opening of non-standard (i.e. not http, ftp, etc) ports to link up their systems, and the IT people in the companies were unwilling to allow these holes in their firewalls. Thus, while they had a good system, it could not gain acceptance at the corporate level.

.NET and Web Services hopefully get around these problems by using port 80 (standard http://web browser port) or the secure equivalent of this (port 443 or similar).

.NET is becoming the de facto communications architecture and his opinion is that as time goes on it will become more and more accepted by the big corporations. JAVA/ RMI/ JINI is not a viable corporate option and .NET is going to prevail.

17.6 Service Oriented or Peer-to-Peer (P2P) Computing

The model that AFRL would like to adopt follows the modern peer-to-peer (P2P) model of distributed computing instead of the more traditional client-server approach. The primary difference is that in P2P any machine on the network can serve as client, server, or both simultaneously, and the client does not necessarily know a priori which machine will be a server. In traditional client-server networks, server locations are generally well-defined and clients and servers do not switch roles. The generic model for P2P computing is shown below.



The WEB SERVER publishes its services to a registrar. This means that it sends to the registrar a complete description of its service with attributes. (Registrar in web services through UDDI - Universal Description, Discovery, and Integration)

The process of finding a registrar is called "DISCOVERY" and can be *static*, meaning that the registrar is known a priori or *dynamic*, meaning that the registrar must be found. With static discovery, the address and port number of the register must be specified in advance, which is a disadvantage because this location can change over time. The registrar itself is a web service.

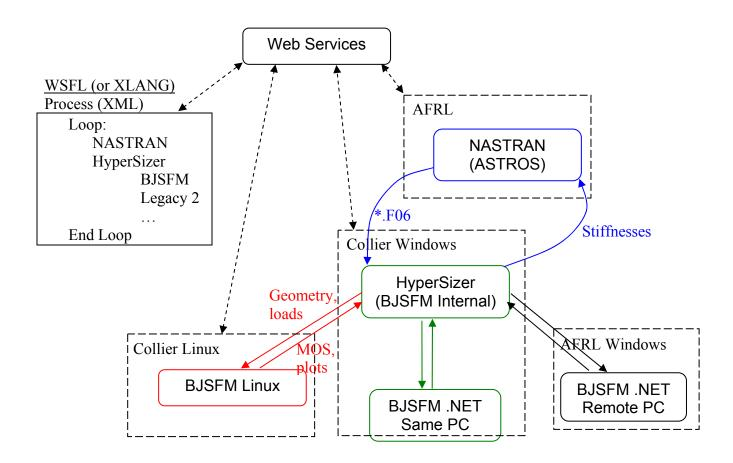
The process that FIPER used for discovery was called multi-cast, which basically sent out packets on the web looking for a registrar – and stopped looking after 15 router jumps. This was implemented in a JAVA JINI process called "Dynamic Discovery and Join."

The CLIENT also must find a registrar through discover (static or dynamic) and it then passes to the registrar a description (attributes) of a service that it is looking for. If the requested attributes match those of a published service, then the client and web service are BOUND.

267

HyperSizer Specific Proposed Tasks and Data Flow

Our intention is to construct a prototype web-service process that has HyperSizer as a web service and HyperSizer able to call other web services. This entire procedure will be tied together using Web Service technology as shown in the diagram below.



The development of our prototype will follow a series of increasingly complex steps that are outlined in detail in the following section, HyperSizer Web Service.

In general terms the steps are:

17.6.1 Scenario Level 1: Demonstrate a web service using simple functions that can be called from a client

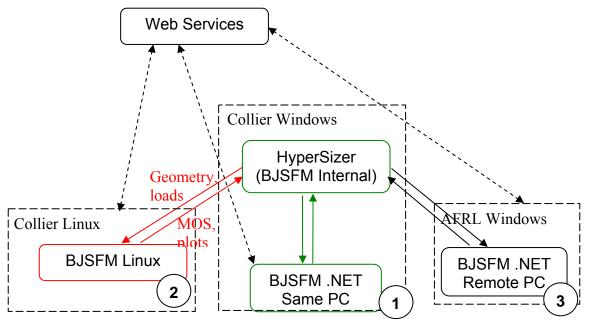
The purpose of this step is mainly to allow us to learn about the various technologies involved and how they are implemented on Windows or other platforms. We will be using very simple functions for the demonstration such as the traditional "Hello World" program. We will follow a progression from building the web service and calling from a web page to building a client program on a) the same computer b) the same platform (but different computer) and c) a different platform.

268

17.6.2 Scenario Level 2: Demonstrate Peer-to-Peer, WSFL/Scripting file to control the process

Here we will still be using the simple "Hello World" functions but investigating how to publish, request, bind, etc. using the tools provided in the .NET environment, as well as learning about the different web service technologies such as WSDL (Web Services Description Language), WSFL (Web Services Flow Language), and UDDI (Universal Description, Discovery, and Integration).

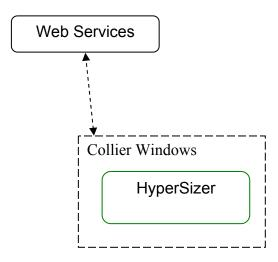
17.6.3 Scenario Level 3: BJSFM legacy bolt program web service



Using lessons learned in Levels 1 and 2 we will implement the legacy BJSFM code as a web service and begin the integration of that service into HyperSizer. This will also be done in a progression of steps starting with 1) building the BJSFM web service with the MS .NET fortran compiler and calling it from the same PC in the Collier office or from another local Windows PC in our office. 2) we will demonstrate the heterogeneous capability by installing BJSFM as a web service on a Linux workstation, but still in our office within our firewall. 3) Finally, we may try to implement this web service on a completely remote computer, possibly within AFRL to demonstrate its flexibility. In this step, HyperSizer itself is not yet a web service.

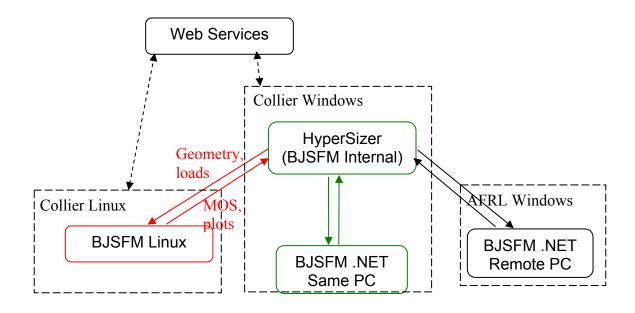
269

17.6.4 Scenario Level 4: HyperSizer as web service



Create and test a web service and calling client that calls the HyperSizer Object model. Begin with calling this web service from a Windows workstation and progress to possibly calling this web service from a client on a Linux workstation or from a client running on an AFRL computer.

17.6.5 Scenario Level 5: HyperSizer as web service calling BJSFM as a web service



We will basically combine steps 3 and 4 into one process where HyperSizer as a web service exposes the BJSFM service to the network. One possibility that we may pursue is to devise a general way for legacy analysis (through web services) to be plugged into HyperSizer and then for HyperSizer to publish these services that are available under itself to the network.

17.6.6 Practice Level 6: Learn how to use the FEMAP COM/API

Because we do not have access to command line NASTRAN in-house, but rather access NASTRAN through the FEMAP interface of NASTRAN for Windows, we propose to start our automation of the HyperSizer-NASTRAN iteration using the FEMAP built-in COM API/object model. This exposes the functionality of FEMAP in the same way that HyperSizer's object model exposes HyperSizer functionality. In Level 6, we will simply study and learn the steps necessary to implement the NASTRAN procedure using COM through VBA. In other words, in this step, we will not attempt to use Web services.

17.6.7 Scenario Level 7: Develop the process we need for automated HyperSizer FEA iteration *** Demonstrate FEMAP/NASTRAN web service

In this step, we will take lessons learned from Level 6 and previous lessons from steps 1-5 to implement FEMAP/NASTRAN as a web service, and demonstrate this service on our in-house Windows PCs. After establishing this procedure with our in-house FEMAP/NASTRAN tool, the final piece of the puzzle will be to work with Ray Kolonay to wrap the AFRL in-house FEA tool (ASTROS) as a web service which accepts data generated by HyperSizer and sends data back to HyperSizer.

17.6.8 Scenario Level 8: Establish iterative HyperSizer-NASTRAN procedure using WSFL

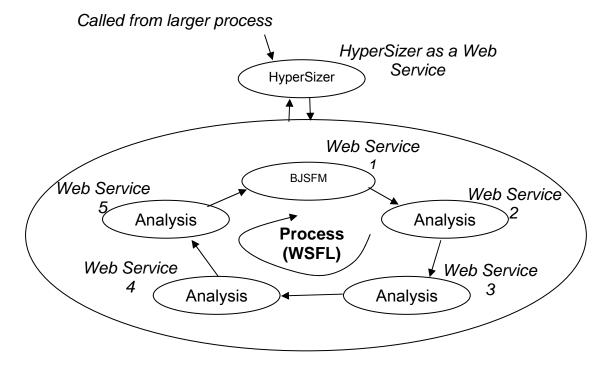
Completion of this step will bring together the "whole picture" for the prototype. Essentially it is just a matter of assembling all of the pieces and lessons learned from all previous steps into a web **process** (controlled by WSFL)

17.7 Overview of Technologies

17.7.1 Web Services

Aspect of .NET that AFRL is most interested in is "Web Services". We are to investigate how to **CREATE NEW / PUBLISH / DISCOVER** EXISTING web services. We are also to explore how to set up HyperSizer as a web service – how to call web services from HyperSizer and how to build a process by tying together web services using Web Services Flow Language (WSFL) through XML (described below). This flow process (one pass through a series of web services) is referred to as a "transaction".

In AFRL's view of what our goal should look like, we need to enable HyperSizer to call a web service (by definition, if it is a web service, it is callable from anywhere and could reside anywhere, even on another platform). Possibly it should go as far as being able to create and execute a process with WSFL that basically is a series of web processes (see below diagram)



In addition to this modification, we will pursue how to expose HyperSizer itself as a web service.

Overview for web services

http://www.gotdotnet.com/team/XMLwebservices/default.aspx

XML Web services are the fundamental building block in the move to distributed computing on the Internet. Open standards and the focus on communication and collaboration among people and applications have created an environment where XML Web services are becoming the platform for application integration. Applications are constructed using multiple XML Web services from various sources that work together regardless of where they reside or how they were implemented.

XML Web services are built on XML, SOAP, WSDL (Web Services Description Language) and UDDI (Universal Description, Discovery, and Integration) specifications. These constitute a set of baseline specifications that provide the foundation for application integration and aggregation. From these baseline specifications, companies are building real solutions and getting real value from them.

Standards organization for ensuring that Web Services are universally compatible is called WS-I or Web Services Interoperability Organization)

Also see the "Global XML Web Services Architecture" white paper at http://www.gotdotnet.com/team/XMLwebservices/gxa_overview.aspx

Another Overview:

http://www.llnl.gov/CASC/workshops/components 2001/viewgraphs/FranciscoCurbera.pdf

http://msdn.microsoft.com/webservices/understanding/webservicebasics/default.aspx

17.7.2 Web Services Description Language (WSDL)

The Web Services Description Language (WSDL) provides an XML grammar for describing these details. WSDL picks up where XML Schema left off by providing a way to group messages into operations and operations into interfaces. It also provides a way to define bindings for each interface and protocol combination along with the endpoint address for each one. A complete WSDL definition contains all of the information necessary to invoke a Web service. Developers that want to make it easy for others to access their services should make WSDL definitions available.

Excellent overview of WSDL and how it interacts with XML and WebServices: http://msdn.microsoft.com/webservices/understanding/webservicebasics/default.aspx?pull=/library/en-us/dnwebsrv/html/understandwsdl.asp

17.7.3 Web Services Flow Language (WSFL)

The Air Force is very interested in setting up web services and processes. Discussed "Web Service Flow Language" from IBM... Also mentioned a similar competing language called XLANG from Microsoft. WSFL differs from WSDL in that where WSDL describes completely the interface for a web service, WSFL provides a way to describe a process made up of one or more web services

Overview (http://www.ebpml.org/wsfl.htm)

The Web Services Flow Language (WSFL) is an XML language for the description of Web Services compositions as part of a business process definition. It was designed by IBM to be part of the Web Service technology framework and relies and complements existing specifications like SOAP, WSDL, XMLP and UDDI. WSFL considers two types of Web Services compositions:

The first type specifies an executable business process known as a flowModel. The second type specifies a business collaboration known as a globalModel.

Flow model

The unit of work in WSFL is an activity - activities represent nodes in a linked graph. The dataLink and controlLink represent the data flow and the control flow between these activities.

Global Models

The Global Model provides a facility to model interactions between business partners. Notice that, as in the case of XLANG, a global model is merely a mapping between inputs and outputs.

"Official" WSFL Specification:

http://www-3.ibm.com/software/solutions/webservices/pdf/WSFL.pdf

XLANG (Microsoft):

http://www.gotdotnet.com/team/xml wsspecs/xlang-c/default.htm

17.7.4 Universal Description, Discovery, and Integration (UDDI)

UDDI stands for Universal Description, Discovery and Integration. The UDDI specification enables businesses to quickly, easily, and dynamically find and transact with one another. UDDI enables a business to (i) describe its business and its services, (ii) discover other businesses that offer desired services, and (iii) integrate with these other businesses.

UDDI Website, descriptions and white papers: http://www.uddi.org

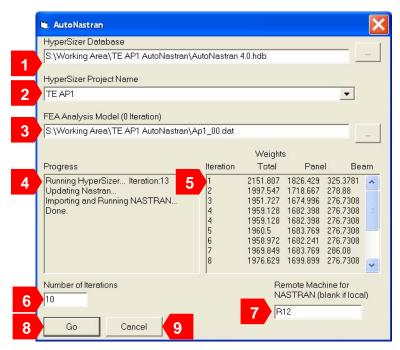
18 HyperAutoFEA/AutoNastran

18.1 Introduction

A procedure has been developed using the COM/ActiveX object models built into HyperSizer and MSC.visualNastran (FEMAP) that automates iterations of the finite element solution between HyperSizer, which determines structural masses and stiffnesses, and MSC/NASTRAN, which determines internal loads. The code that implements this procedure is called "AutoNastran". This new automation capability was developed completely under this contract and the code description and example described below are not yet in the HyperSizer User Manual documents.

18.2 AutoNastran Interface

AutoNastran is a standalone application that controls both the HyperSizer and FEMAP applications given the filenames and project names controlling the process. The entries on the AutoNastran form are described below.

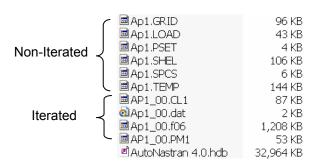


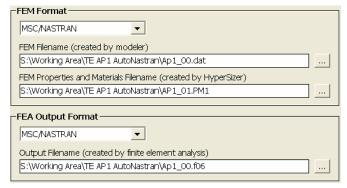
- 1. HyperSizer database containing the model to be iterated.
- 2. Drop-down combo containing the name of all projects in the specified database. The contents of this combo are updated whenever the database name is changed.
- 3. The name of the root or 0th iteration finite element model that is to be analyzed using NASTRAN. This finite element model file is not necessarily the same as that specified on the Setup tab of the HyperSizer project being iterated. AutoNastran expects the name of this finite element model to end with "_00.DAT". If the NASTRAN job is to be executed on a different computer, this file name should reside on a network drive accessible by both the computer running AutoNastran and the computer running NASTRAN.

- 4. The progress window shows the currently running operation in the iteration procedure. When all operations are complete, "Done" will appear in this window.
- 5. The weight window summarizes the panel, beam and total structure weight after every iteration.
- 6. Number of iterations to run when the "Go" button is pressed. Iterations are cumulative. For example, if AutoNastran is run for 3 iterations and then submitted again for 5 iterations, the code will automatically start where it left off and generate weights for iterations 4-8.
- 7. If MSC.visualNastran for Windows is installed on a remote computer, it can be activated remotely through DCOM. Type the name of the remote computer in this box. If the MSC.visualNastran job is run locally, leave this box blank. If the computer name in this box is invalid, or the computer is unavailable, an error will occur. See the appendix for instructions on preparing a remote computer to run MSC.visualNastran unattended.
- 8. Press "Go" to start the iteration procedure.
- 9. The cancel button will stop the process after completion of the current iteration (NOT CURRENTLY OPERATIONAL). If no iterations are running, this button will close the AutoNastran window.

18.3 Example Problem

The example used to demonstrate AutoNastran is the AP1 training example. The AP1 finite element mesh is shipped with the HyperSizer installation and used extensively in the HyperSizer Pro User Manual. For a complete description of the AP1 data files, see the Introduction of the Tutorial Examples section of the Pro User's Manual. The file structure and HyperSizer Setup form are shown below. The filenames that end with "_00" are files that changed from iteration to iteration. That is, new files with extensions _01, _02, etc. will be created as each iteration takes place. The remainder of the files (e.g. Ap1.GRID, Ap1.LOAD, etc.) do not change from iteration to iteration.





Because this demonstration is to be iterated over a distributed network (with NASTRAN running on a remote machine), all data files were copied to a network shared folder, "S:\Working Area\TE AP1 AutoNastran\". In the "master" finite element file, "Ap1_00.dat", absolute paths pointing to this folder were added for all include files.

This procedure assumes that the finite element model has been analyzed at least one time, meaning that the file, "Ap1_00.F06" exists. To start the iteration procedure, all components are assigned into a single group. For this example, we begin with a Titanium honeycomb group where the number of sections is limited to 50 candidate designs to speed up execution.

The examples discussed here are contained in the HyperSizer database, "AutoNastran 4.0.hdb"

- 1. Open the database containing the TE AP1 project. On the Project Setup form, set the paths to the FEM, PM1 and FEA files as shown above. Open the sizing form, assign all panel components in the project to Unstiffened Family: Group 1. Depending on the current state of this project, this might require removing the components from another group.
- 2. Start AutoNastran. Fill in the database name, and FEA Analysis model using the data shown in the previous section
- 3. For the number of iterations, leave the default value of 4. Leave the "Remote Machine" name blank for now. This assumes that NASTRAN can be run on the local computer.
- 4. Press the "Go" button.

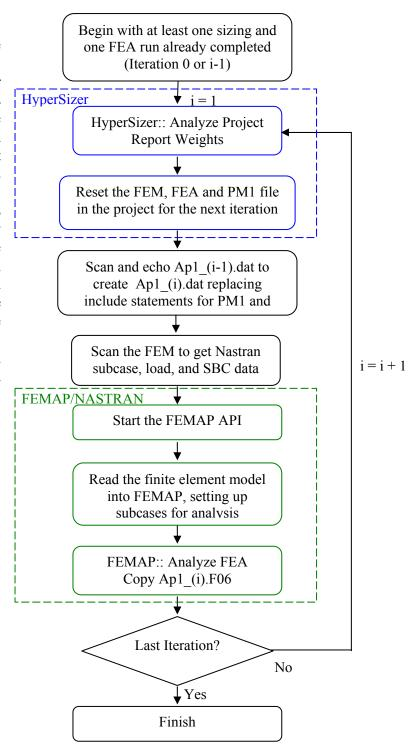
After the first four iterations, the weights for the structure are converged. Now, we want to change the structure to that of a uniaxially stiffened structure. The stiffnesses for a uniaxial structure are very different than those of honeycomb, as the transverse membrane and bending stiffnesses are orders of magnitude lower than the longitudinal. Therefore changing to uniaxial should result in a large change in the overall weight and cause a need to iterate again.

- 5. On the sizing form, remove all components from Group 1, and assign them to Uniaxial Family: Group 4.
- 6. Go back to AutoNastran. Change the number of iterations to 6. Press Go

AutoNastran should pick up where it left off and perform iterations 5-10. Once the process is complete, the convergence of the iterations can easily be plotted in Excel. Simply swipe the contents of the Weights window, right click and select "Copy" and then go to Excel and paste the contents into a spreadsheet.

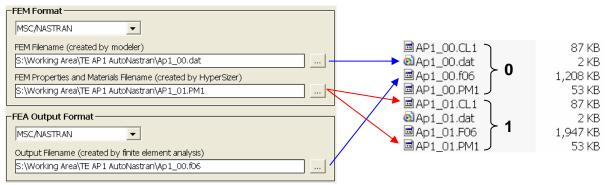
18.4 Process

The process carried about in the iteration process is shown here. Starting from iteration 0 (or continuing on from a previous state), AutoNastran first sizes the components with HyperSizer and prepares HyperSizer for the next iteration by changing the names of the FEM, FEA and PM1 files. The current iteration number is determined by AutoNastran by reading and parsing the FEM file name on the Project Setup form to extract the previous iteration For example, for the number. **FEM** file Ap1 03.dat, iteration number would be 3. Several iterations through discussed AutoNastran are below.



First Iteration

The input files to HyperSizer containing the finite element model and resultant element forces (*.dat and *.F06) are from the previous iteration. In this case, this is the 0th iteration. When HyperSizer runs, the properties and materials file and the CBAR offset file are generated for the current iteration (Ap1 01.PM1 and Ap1 01.CL1 respectively).



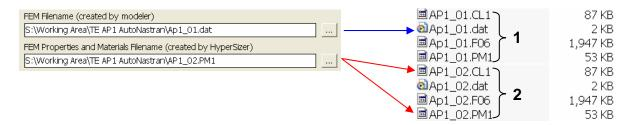
After HyperSizer generates new properties, materials and beam offsets, AutoNastran then creates a new finite element model file (Ap1_01.dat) by reading and echoing the previous iteration finite element model (Ap1_00.dat). During this echo, the "INCLUDE" statements referencing the PM1 file are changed to reflect the current iteration.

```
$ Include HyperSizer generated property and material data to represent
$
     panel thermoelastic stiffness changes that occur during sizing
$
     iterations.Provides the updated PSHELL, PBAR, MAT2, and MAT1 data.
$
     *_00=starting point properties, *.01=first sizing iteration properties,
INCLUDE 'S:\Working Area\TE AP1 AutoNastran\Ap1_01.PM1'
                                                      In the first iteration, this
$ Include HyperSizer generated CBAR beam element da
                                                      file name is changed from
$
     Provides beam offset vectors to represent neut
$
     occur during sizing iterations.
                                                      "Ap1 00.PM1" to
$
     *._00=starting point properties, *.01=first si
                                                      "Ap1 01.PM1".
etc.
INCLUDE 'S:\Working Area\TE AP1 AutoNastran\Ap1_01.CL1'
```

This new finite element file is used for the NASTRAN finite element analysis.

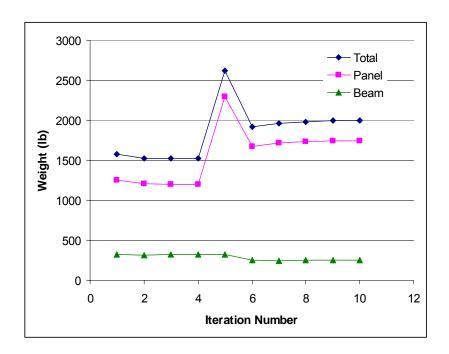
Second Iteration

At the end of the first iteration, the "FEM filename" and "FEM Properties and Materials Filename" for the project are updated by AutoNastran to reflect the next iteration. Again, HyperSizer uses the finite element model and results from the previous iteration, in this case the 1st, and generates properties and materials data for the current.



18.5 Results

In the procedure described above the weight initially converges for the titanium honeycomb case but peaks when the structural concept changes from honeycomb to uniaxial. In this case, the FEA loads from the honeycomb structure are used to size the uniaxial panels, and because the transverse and longitudinal loads are on the same order, the uniaxial panels size up substantially. As the iterations continue, the weight immediately drops off with the next iteration as the effect of the uniaxial structure is felt in the FEA.



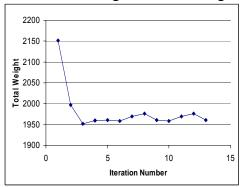
Distributed Analysis

Running distributed is simply a matter of entering a machine name on which to execute FEMAP/NASTRAN. There are some steps required to set the remote computer up for automation which are detailed in the appendix. AutoNastran makes no distinction between FEMAP/NASTRAN running on the local computer or running on a remote computer.

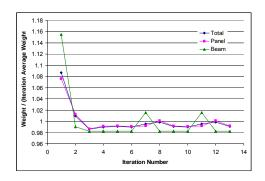
There is some overhead involved in running HyperSizer and NASTRAN over the network. As a comparison, if all files are located on a workstation's local hard drive (i.e. HyperSizer database and all FE files) and all processes run on that hard drive, the process runs for **54** seconds per iteration. If the database and FE files are moved to a central server hard drive, even if the entire process runs on the same workstation, then the process is slowed somewhat by file IO across the network. In this test, the process takes **67** seconds per iteration. Finally when running AutoNastran and HyperSizer on a local workstation and FEMAP/NASTRAN on a separate workstation, the process takes **63** seconds per iteration. The relative speeds of the two computers for the NASTRAN job has not been quantified, however, the second computer has dual processors, therefore this may account for the slight speedup in the last case.

Convergence Not Guaranteed

The iterations are not guaranteed to converge exactly. For this example, if the iterations start from zero and attempt to size the AP1 vehicle with uniaxial structure, it was observed that a small repeating oscillation occurs in the convergence of the weight as shown here.



Shown below is the plot of weight per iteration for the total structure, panel, and beam normalized against their average values. This is a repeating pattern, therefore the weight will never converge exactly, however the change in total weight from iteration to iteration is only on the order of 1%.



However, other applications did converge to just a single number. This particular application had only 50 candidate designs, i.e. relatively big incremental jumps in optimization sizes available to choose from. It is believed that if more candidate designs were made available, as in most optimizations we do, if the oscillation were to still be present, the change in weight between iterations would likely be less than 0.1%.

In the future, we might want to look for ways to make this convergence more robust. Perhaps when going from one iteration to the next we could limit the change in stiffness for each component.

18.6 Conclusions

This AutoNastran procedure is currently restricted to running the finite element model by going through the MSC.visualNastran / FEMAP interface. However, the finite element models that are used and updated by HyperSizer are actually self-contained NASTRAN bulk data files, and if we have access to MSC/NASTRAN or perhaps the NX/NASTRAN command line programs in the future, it would be very easy to simply plug those programs into this process. In addition, if ASTROS reads in bulk data files, generates F06 force data, and supports all of the relevant features (such as ABD matrices entered through MAT2 cards) then it may be able to plug in fairly easily as well.

Finally, the distributed portion of this procedure currently only works in a homogeneous computing environment where there is a shared file structure. If this is to be extended to a heterogeneous environment, then some sort of more generic distributed computing tool such as JAVA/RMI or Web Services must be used to spawn the remote processes. The current implementation uses DCOM which only works in an all Windows environment. In addition, if there is no shared file structure between the platforms, then a method for transferring data files before runs must be developed as well.

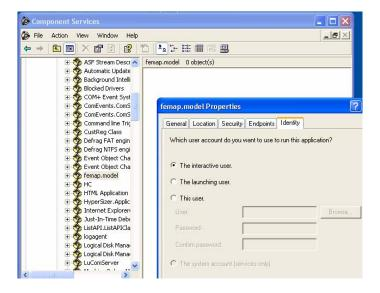
18.7 Setting up MSC. VisualNastran2003 (FEMAP 8.2) for Automation

Several steps must be executed to allow the MSC.visualNastran for Windows process to successfully run.

- 1. Apparently MSC.visualNastran2003 installs with an environment variable which can cause the analysis runs to fail. Open up the computer "Environment Variables" (located on the control panel "System" applet, Advanced tab. If Nastran is licensed using a dongle instead of a FlexLM license string, remove the environment variable, "MSC LICENSE FILE".
- 2. The finite element files to be run must reside in a location available to both the AutoNastran process and the FEMAP/NASTRAN process. In the TE AP1 example outlined above, the finite element model files were located on the network share drive, S:.
- 3. Locate and open the file, FEMAP.ini. This should be located in the folder, "C:\Mscvn4w2003\modeler". Add the line "ISN4W=1" in the [User] section of the file:

[User]
N4WINI=mscvn4w2003.ini
N4WVER=2003
ISN4W=1

- 4. The FEMAP API seems to have trouble if it is not allowed to run in "interactive" mode. Meaning that the FEMAP window pops up to the screen while the process is running. By default, remote processes under DCOM are run in the background with a GUI. Therefore, to run the process remotely, an adjustment needs to be made to the DCOM settings of FEMAP to allow it to run interactively.
 - a. Be sure that you are logged in with Administrative privilege.
 - b. On the machine with the FEMAP installation, open the DCOM configuration utility (WinXP: Start | App Programs | Administrative Tools | Component Services)
 - c. Expand the Component Services | Computers | My Computer | DCOM Config branch of the Console Tree. (Answer No to the warning messages that pop up regarding recording of some missing ClsIDs)
 - d. Right click on the node, femap.model, and select properties. On the resulting dialog, select the "Identity" tab.
 - e. Change the user account on which to run the application to "The interactive user". Press the Apply and OK button to dismiss this form.



- 5. The user executing AutoNastran on the local computer must: a) have an account and be logged in to the remote computer; b) have an active license and privilege to run FEMAP/NASTRAN on the remote computer. If the computer console is "locked" the process will still run. Unfortunately, because the FEMAP API requires the interactive GUI, the FEMAP window will pop up periodically as the finite element analysis is required. If no one is logged into the target computer, an error will occur and the AutoNastran iterations will stop.
- 6. FEMAP/NASTRAN seems to require a relatively simple file structure for its input files. Having special characters ("~", ",") in the filename or pathname seems to trip up the analysis, therefore when AutoNastran runs, it uses a "TEMP" folder for running the FE analysis. It uses the same drive where the HyperSizer database resides and if a <Drive>:\AutoNastran\ folder does not exist, it creates one and then deletes it when the process completes.